FRP STRENGTHENING OF NON-FLEXURAL REINFORCED CONCRETE MEMBERS BASED ON STRUT-AND-TIE MODELLING

ZHAO YUJIE

NATIONAL UNIVERSITY OF SINGAPORE

2016

FRP STRENGTHENING OF NON-FLEXURAL REINFORCED CONCRETE MEMBERS BASED ON STRUT-AND-TIE MODELLING

ZHAO YUJIE

(B.Eng., M.Eng.)

A THESIS SUBMITTED

FOR DEGREE OF DOCTOR OF PHILOSOPHY

DEPARTMENT OF CIVIL AND ENVIRONMENTAL ENGINEERING

NATIONAL UNIVERSITY OF SINGAPORE

2016

DECLARATION

I hereby declare that this thesis is my original work and it has been written by me in its entirety. I have duly acknowledged all the sources of information which have been used in the thesis.

This thesis has also not been submitted for any degree in any university previously.

ZhaoYujie

Zhao Yu Jie

30 June 2016

Acknowledgement

I would like to take this opportunity to express my deepest appreciation to my supervisor, Prof. Tan Kiang Hwee, for his systematic supervision and patience guidance throughout the course of my study and research. He spent numerous hours to make an impact on my life and to craft me into a better researcher. Prof. Tan has always been ready to answer my doubts and offered me materials that would help in my study and research. His knowledge and experience has been my guiding star throughout this endeavor. I am forever indebted to my supervisor Prof. Tan Kiang Hwee for the enormous amount of patience he has shown during my study and research.

I would also like to thank the staff of the Concrete & Structural Laboratory for their help and advice. This research would not be possible if not for the laboratory technicians, especially Mr. Wong Kah Wai (Huang Jiawei), Mr. Choo Peng Kin, Mr Koh Yian Kheng, Mr Ang Beng Oon, Mr Ishak Bin A. Rahman and Mr Kamsan Bin Rasman, who have assisted and guided me tremendously in the experiments.

I would also like to acknowledge the National University of Singapore for providing all necessary financial and academic support without which my Ph.D. programme would not have been possible. I am grateful to my lecturers, relatives and friends who have supported the study in many ways. I would like to give heartfelt thanks to my seniors, Dr. Du Hongjian in particular, for his kind help with my experiments and encouragement throughout the study.

This page is intentionally left blank.

Table of Contents

Chapter 3. FRP Strengthening of Tie Members 47

Chapter 4. FRP Strengthening of Strut Members 95

Summary

Non-flexural structural concrete members such as deep beams, corbels, pile caps, brackets and connections are commonly seen in reinforced concrete (RC) structures. To strengthen such non-flexural RC members with discontinuity regions (D-regions), a fibre-reinforced polymer (FRP) strengthening approach based on strut-and-tie modelling would be appropriate. This involves the strengthening of struts, tie members and nodal zones where required. However, very limited studies have been conducted in this area.

This thesis presents both experimental and analytical investigations on the FRP strengthening of tie members and strut members. A case study of RC corbels strengthened with FRP systems based on strut-and-tie modelling was also conducted.

To study the strengthening of tie members using FRP systems, a total of eight short tie specimens and seven long tie specimens were fabricated and tested to failure under direct tension. The specimens were strengthened with externally bonded (EB) carbon FRP sheets and/or near-surface-mounted (NSM) carbon FRP rods in various quantities. Test results indicated that the ultimate axial load capacity was increased in proportion to the reinforcement parameter of the FRP reinforcement. The most efficient FRP configuration consisted of a combination of EB-FRP sheets and NSM-FRP rods.

To investigate the strengthening of struts using FRP systems, a total of twenty-seven isolated prismatic, partial bottle-shaped or full bottle-shaped strut specimens were tested to failure under monotonically increasing compressive load. Test results indicated that the ultimate load capacity of strut members was substantially increased when strengthened by transverse EB-FRP sheets and the failure mode of partial bottle-shaped struts changed from tensile splitting failure of concrete to the crushing of concrete at the end of the strut. No significant enhancement in ultimate load capacity was obtained for partial bottle-shaped struts strengthened with NSM-FRP rods only. The predicted axial load capacities of FRP strengthened strut members based on a confinement model showed reasonably good agreement with the test results.

To verify the effectiveness of FRP strengthening system and validity of the proposed approach based on strut-and-tie modelling for non-flexural reinforced concrete members, fourteen reinforced concrete corbels, strengthened with EB-FRP sheets and/or NSM-FRP rods, were fabricated and tested to failure. The test variables were the shear span to depth ratio, concrete strength, main reinforcement ratio and FRP strengthening system. Test results revealed that the loss in ultimate load capacity of RC corbels due to insufficient concrete strength or steel reinforcement could be restored by using FRP strengthening systems designed based on strut-and-tie modelling.

Keywords: corbels; discontinuity region (D-region); fibre-reinforced polymer (FRP); strut-and-tie model (STM); strut; tie; ultimate load capacity.

List of Tables

List of Figures

List of Notations

Symbols, which appear more than once, as defined as follows:

A = total area of concrete section / cross-sectional area of prismatic strut;

A_b = area of the bearing support / area of loading area;

A_c = cross-sectional area of tie member;

A_e = effective confinement area;

A_{FRP} = cross-sectional area of FRP reinforcement;

$A_{FRP,r}$ = cross-sectional area of a FRP rod;

A_s = cross-sectional area of steel bar;

A_{strut} = effective cross-sectional area of strut;

A_{node} = effective cross-sectional area of nodal zones;

a = width of loading area, or effective shear span;

b = width of member section;

b_1 = width of loading plate;

b_2 = width of support;

b_{ef} = effective width of bottle-shaped strut;

B = width of strut specimen;

D = diameter of an equivalent circular cross section for noncircular cross sections;

d = effective corbel depth on the corbel-column interface;

E_c = elastic modulus of concrete;

$E_{FRP,s}$ = elastic modulus of FRP sheet;

$E_{FRP,r}$ = elastic modulus of FRP rod;

E_s = elastic modulus of steel bar;

F_{strut} = compressive load capacity of strut member;

F_{tie} = tensile load capacity of tie member;

F_T = tensile resistance provided by concrete and FRP reinforcement;

F_{node} = load bearing capacity of nodal zone;

f'_c = cylinder compressive strength of concrete;

f'_{co} = unconfined compressive strength of concrete;

f'_{cc} = confined compressive strength of concrete;

f_{FRP} = ultimate tensile strength of FRP;

f_{strut} = design compressive strength of strut member;

f'_{strut} = effective compressive strength of strut member;

f_{tie} = design strength of tie member;

f_l = confining pressure;

f_{node} = design strength of nodal zone;

f'_{node} = effective strength of nodal zone;

f_y = yield strength of steel reinforcement;

H = height of strut member;

h = height of member section;

k_1 = efficient factor of concrete (see **Table 2.5**);

L = length of horizontal FRP rods, or length of corbel protrusion from face of column stump;

l_b = width of the support bearing plate;

m = number of FRP rods per side;

n = number of ply of FRP sheets per side;

P = applied load of tie members or strut members or corbels;

$P_{FRP,r}$ = compressive load capacity of vertical FRP rods;

P_u = ultimate load;

$P_{u,d}$ = design ultimate load;

$P_{u,Test}$ = experimental ultimate load;

$P_{u,Pred}$ = predicted ultimate load;

r = corner radius of section's corner;

t = thickness;

$t_{FRP,s}$ = thickness of one layer of FRP sheet;

v = total number of vertical FRP rods;

$w_{FRP,s}$ = width of FRP sheet;

w_{strut} = width of strut member;

β_s = efficient factor (see **Table 2.2**);

β_n = efficient factor (see **Table 2.5**);

ε = strain;

ε_c = compressive strain in concrete;

ε_{ct} = tensile strain in concrete;

ε_{cu} = ultimate compressive strain of concrete;

$\varepsilon_{cracking}$ = cracking strain of concrete;

ε_{eff} = effective strain of FRP reinforcement at failure;

$\varepsilon_{FRP,s}$ = longitudinal tensile strain of FRP sheet;

$\varepsilon_{FRP,r}$ = longitudinal tensile strain of FRP rod;

$\varepsilon_{FRP,ru}$ = rupture strain of FRP reinforcement;

$\varepsilon_{FRP,s,ru}$ = rupture strain of FRP sheet;

$\varepsilon_{FRP,r,ru}$ = rupture strain of FRP rod;

ε_s = strain of steel reinforcement;

$\varepsilon_{s,ru}$ = rupture strain of steel reinforcement;

ε_y = yield strain of steel reinforcement;

η = efficient factor (see Equation 2.7);

θ = angle between strut and tie;

v = efficient factor (see Equation 2.1);

v' = efficient factor (see **Tables 2.2** and **2.5**);

v_1 = efficient factor (see Equation 2.3);

v_2 = efficient factor (see Equation 2.3);

ρ = steel reinforcement ratio;

ϕ = partial safety factor (see Equations 2.2, 2.5 and 2.8);

χ_s = longitudinal reinforcement index of steel bar;

χ_{FRP} = longitudinal reinforcement index of FRP reinforcement;

ω_{FRP} = total reinforcement parameter of FRP reinforcement;

$\omega_{FRP,s}$ = reinforcement parameter of FRP sheet;

$\omega_{FRP,r}$ = reinforcement parameter of FRP rod;

$\omega_{FRP,h}$ = horizontal FRP strengthening parameter.

Chapter 1. Introduction

1.1 Background

A significant number of structures were constructed during the first half of the 20th century using reinforced or pre-stressed concrete. Many of these structures have now reached the end of their planned service life, and deterioration in the form of steel corrosion, concrete cracking, and spalling is observed frequently. In addition, some structures that were originally constructed for a specific use are now being renovated or upgraded for a different application that may require a higher load-carrying capacity. As a result of these higher load demands, existing structures need to be reassessed and may require structural strengthening to meet heavier load requirements.

Non-flexural reinforced concrete (RC) members such as deep beams, corbels, pile caps, brackets, and connections are very common in reinforced concrete structures. These members constitute what is known as discontinuity regions (D-regions), in which the strain distribution over their cross-section depth is complex in nature and not well-defined by simple rules, even in the elastic stage (Schlaich and Schäfer 1991; Wight and Macgregor 2011). Various examples of D-regions are illustrated in **Figure 1.1**. A D-region generally expands a distance equal to the member height from a force or geometric discontinuity. Regions between D-regions are known as B-regions in which bending theory is generally valid.

Figure 1.2 shows two typical examples of RC structures which need structural strengthening: (i) The Leon County Courthouse Parking Garage: It is a cast-in-place concrete structure with a capacity of more than 500 vehicles. It consists of five below-grade parking levels and a five-floor office structure above the parking levels. Tests revealed that the existing reinforcement was inadequate to carry the load from the monument. Additional inspection showed signs of serious cracking on all floor levels - leading the owner to pursue and implement a comprehensive structural evaluation and strengthening program. The ultimate goal for the County was a cost-effective and comprehensive solution to restore and improve the capacity of the structural elements of the garage while keeping the entire facility operational; (ii) Martin Springs Drive Bridge: The bridge is a three-span simply supported reinforced concrete slab with no transverse steel reinforcement, load posted and located on Martin Spring Outer Road in Phelps County, MO. The original construction combined with the presence of very rigid parapets caused the formation of a wide longitudinal crack which resulted in the slab behaving as two separate elements. Structural strengthening was required to avoid further cracking and such that the transverse flexural capacity was higher than the cracking moment.

However, structural strengthening of non-flexural RC members is not as simple and straightforward as normal slabs, beams and columns since traditional bending theory and shear design do not apply.

1.2 FRP strengthening systems

The structural strengthening of concrete structures can be achieved using one of many different strengthening methods such as span shortening, externally bonded steel plates, external or internal post-tensioning systems, section enlargement, fiber-reinforced polymer (FRP) reinforcement or a combination of these techniques. The primary considerations are economy, constructibility, durability, and aesthetics.

Originally developed in Japan and Europe in the 1980s, the use of FRP systems to strengthen concrete structures has gained popularity in the world and had become one of the most widely adopted solutions (Teng *et al.* 2002; Lam and Teng 2003). FRPs are made of filaments of high performance fibers such as glass, carbon and aramid which are impregnated with an epoxy resin to form fabric sheets and rods. They are bonded or mounted to concrete members to increase their load carrying capacity. Important characteristics of FRPs for structural strengthening applications include their non-corrosive properties, speed and ease of installation, lower cost, and aesthetic appeal.

Figure 1.3 illustrates the application of Externally Bonded FRP (EB-FRP) strengthening systems. EB-FRP systems involve either a pre-cured (that is, prefabricated) system or a wet layup application. In the wet layup method, the fiber sheets are saturated with resin and applied to the concrete surface, and then the system is allowed to cure in-place. Conversely, pre-cured sheets (or shells) are manufactured in a controlled environment and then later adhered to the concrete structure. As with any other externally bonded system, the bond between the FRP system and the existing concrete is critical, and surface preparation is very important. Typically, installation is achieved by applying an epoxy adhesive to the prepared surface, installing the FRP reinforcement and, when required, applying a second layer of the epoxy adhesive.

In the application of Near Surface Mounted FRP (NSM-FRP) reinforcement (as shown in **Figure 1.3**), slots are cut into the concrete cover of a reinforced concrete member, typically using a diamond cutting disc, and an FRP bar, strip, or tape is inserted, and bonded with an epoxy adhesive. This strategy of strengthening is very attractive due to the simple application procedure and the possibility of mitigating the risk of premature de-bonding failure of FRP. In general, NSM-FRP system provides some advantages compared to EB-FRB system as follows: (a) the improved utilization of FRP reinforcement permits higher loads to be applied, leading to reduced cross sectional area of FRP reinforcement; (b) the quality of the substrate (tensile strength of the surface) is less important; NSM-FRP reinforcement can also transfer loads into substrates with a low bearing capacity such as brickwork and masonry; (c) NSM-FRP reinforcement is more economical as leveling and roughening is not required unlike surface-applied sheets and laminates; (d) the NSM-FRP reinforcement is protected against mechanical damage; better performance is achieved in the event of a fire, thus reducing the cost of fire protection measures.

1.3 Strengthening design approaches

FRP strengthening systems could be effectively used to increase the load bearing capacity of non-flexural structural concrete members such as deep beams, dapped-end beams, beams with openings and corbels. To strengthen non-flexural RC members, a rational approach based on strut-and-tie modelling would be appropriate (Tan 2004). The strut-and-tie method (STM) is an elegant design tool to model and detail discontinuity regions (D-regions) in concrete structures (ACI 318 2011; Eurocode 2 2004; Marti 1985; Schlaich *et al.* 1987; Schlaich and Schäfer 1991). By using strut-and-tie models, the real stress fields in a structural member are represented in a discrete way. STMs consist of concrete compression struts, steel tension ties and nodal zones (as shown in **Figure 1.4**), so the strengthening work should involve the FRP strengthening of ties, strut members and nodal zones where required.

However, very limited studies have been conducted with regards to FRP strengthening of RC non-flexural members based on strut-and-tie modelling. Studies by Lim (2006), Muhammad (2007) and Tan (2001, 2004) have shown that the strut-and-tie model is a suitable method to predict the load capacity of such members strengthened with FRP reinforcement. However, a systematic study on the capacities of FRP-strengthened tie members and strut members and the effect of FRP strengthening on the load carrying capacity of non-flexural RC members is desirable and currently not available.

1.4 Research objective and scope of work

The main objective of this study is therefore to investigate and evaluate the applicability and effectiveness of FRP strengthening method based on strut-and-tie modelling for non-flexural RC members, as shown in **Figure 1.5**. To achieve the research objectives, both experimental and analytical works were carried out. The scope of work included the following parts:

1. ***FRP strengthening of RC tie members.*** Tests were carried out to investigate the effectiveness of FRP strengthening systems on the tensile load capacity of tie member and an analytical model was proposed for the determination of the tensile load capacity of FRP strengthened tie members;

2. ***FRP strengthening of strut members.*** Tests were carried out to investigate the effectiveness of FRP strengthening systems on the axial compressive load capacity of strut members. An analytical model was also proposed for the determination of the axial load capacity of FRP strengthened struts;

3. ***Case study on FRP strengthening of corbels.*** As an example of the application of the proposed approach, tests were carried out on under-strength corbels due to insufficient concrete strength or amount of tensile steel reinforcement. The deficient strut or tie members were strengthened following the findings on FRP-strengthened strut and tie members to restore the ultimate load carrying capacity of the corbels.

1.5 Structure and organization of thesis

This thesis consists of six chapters. Chapter 1 introduces the background of the current work on FRP strengthening of non-flexural RC structures based on strut-and-tie modelling. In addition, the research objectives and scope of study are highlighted.

Chapter 2 reviews the related research findings on FRP strengthening of non-flexural RC members based on strut-and-tie modelling in the literature, to identify research gaps in the areas of study.

Chapter 3 presents an investigation on the behavior and strength of FRP strengthened reinforced concrete tie members under axial tensile loading. The experimental results are presented and discussed. An analytical model is proposed to determine the ultimate load capacity of FRP strengthened tie members and comparison with observed experimental results is made.

Chapter 4 presents an investigation on the behavior and strength of FRP strengthened plain concrete strut members under axial compressive loading. An analytical model is proposed for the determination of the ultimate load capacity of FRP strengthened struts and comparison with the observed test results is made.

Chapter 5 presents a case study on the FRP strengthening of reinforced concrete corbels based on the findings of Chapters 3 and 4. The applicability of the proposed method to restore the strength of corbels deficient in concrete strength or steel reinforcement is discussed.

Chapter 6 summaries the research work carried out and draws conclusions based on the experimental and analytical investigations. In addition, recommendations for further research are made.

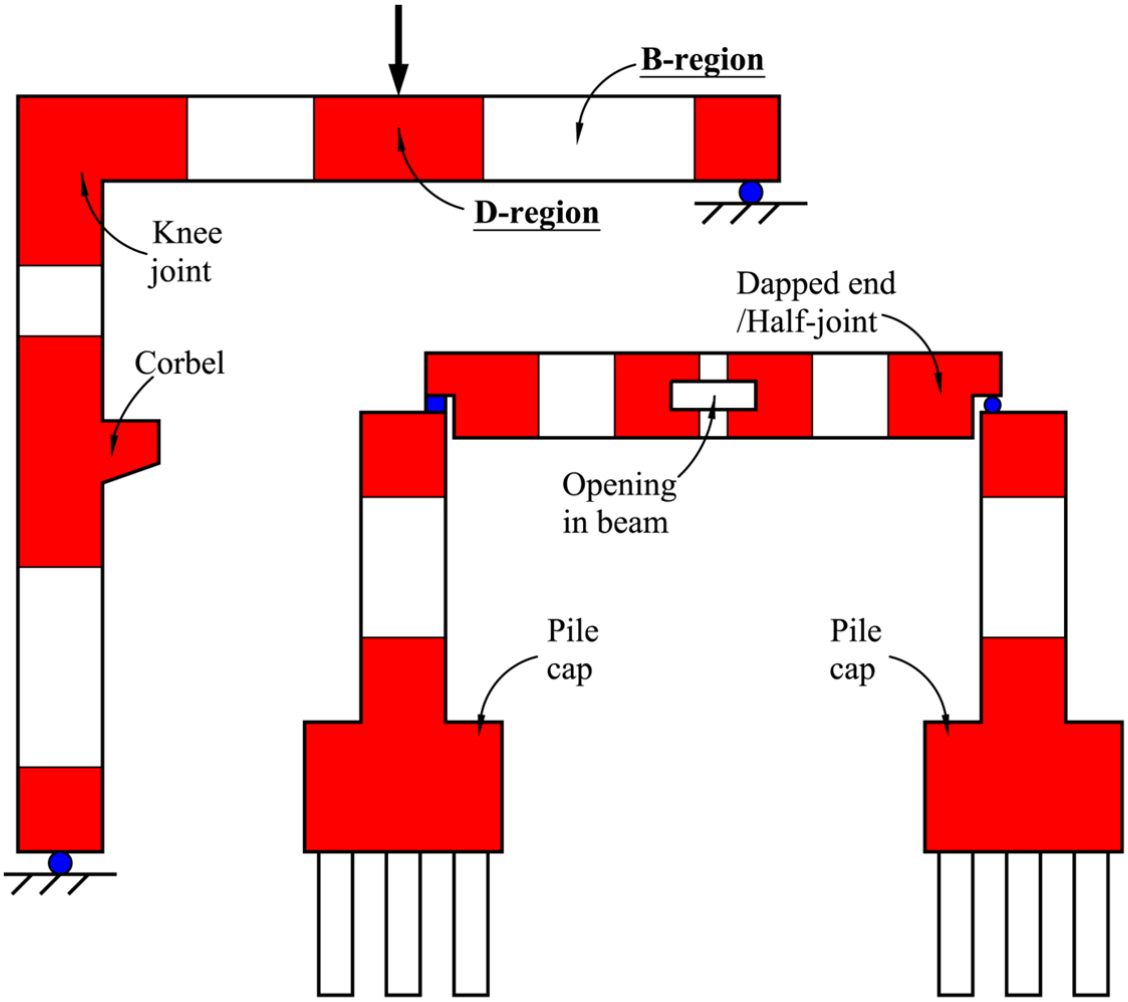

Figure 1.1: B-regions and D-regions of non-flexural RC structures

(a) Leon county courthouse parking garage-1

(b) Leon county courthouse parking garage-2

(c) Martin springs drive bridge-1

(d) Martin springs drive bridge-2

(e) Typical crack at dapped end member

(f) Spalled reinforced concrete corbel

Figure 1.2: Examples of non-flexural RC structures needing strengthening

(a) EB-FRP strengthening of beams

(b) EB-FRP strengthening of slabs

(c) EB-FRP strengthening of columns

(d) NSM-FRP strengthening of bridge deck

(e) NSM-FRP strengthening of beams

(f) NSM-FRP strengthening of slabs

Figure 1.3: FRP systems for structural strengthening

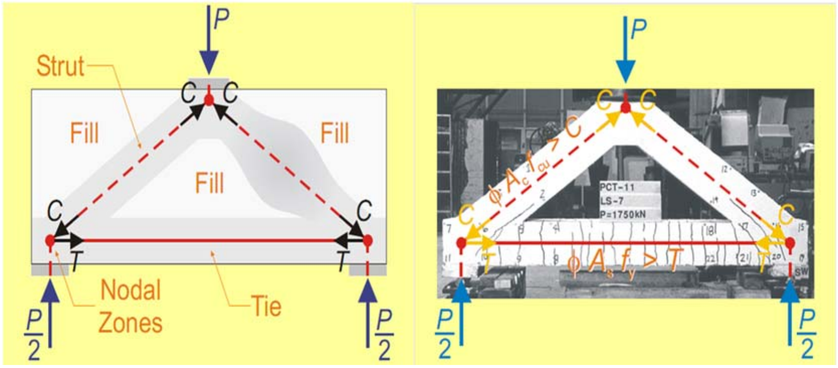

(a) Strut-and-tie model for deep beam

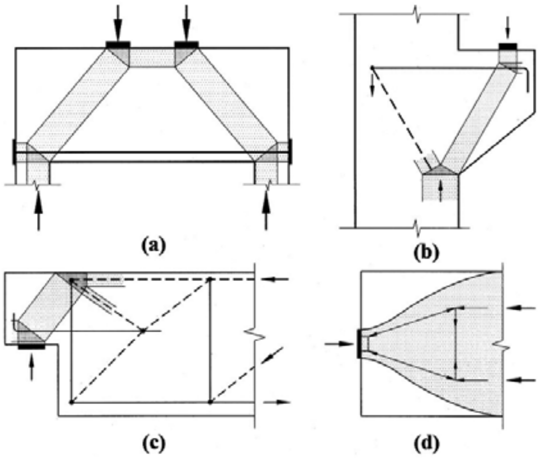

(b) Strut-and-tie models for non-flexural RC members (Foster and Malik 2002)

Figure 1.4: Typical strut-and-tie models for non-flexural members

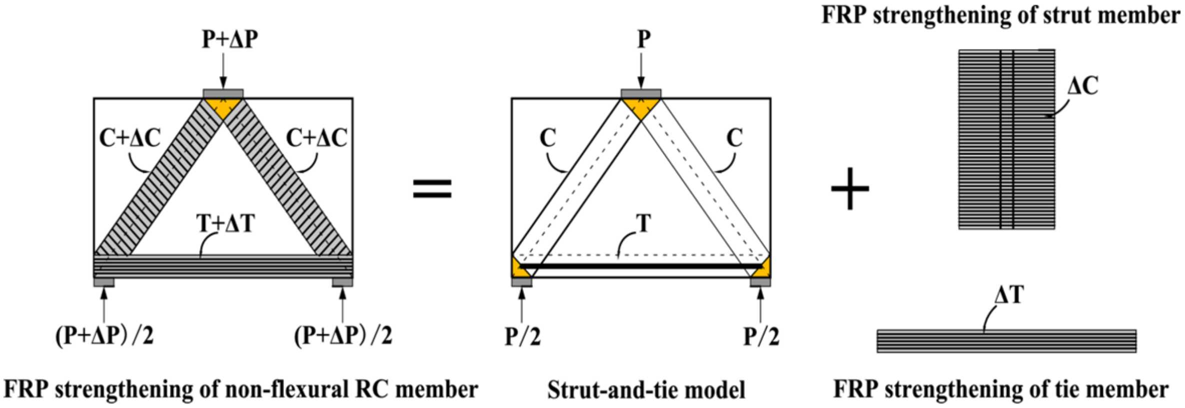

Figure 1.5: FRP strengthening of non-flexural members based on strut-and-tie modelling

Chapter 2. Literature Review

2.1 General

This chapter first reviews previous research works that were carried out on FRP strengthening of discontinuous regions (D-regions) or non-flexural RC members. Next, the principle of strut-and-tie modelling is reviewed. Subsequently, the application of strut-and-tie models in FRP strengthening of non-flexural RC members is discussed in the light of the present study.

2.2 FRP strengthening of non-flexural RC members

The application of fiber reinforced polymer (FRP) systems has been shown to be a competitive method in structural strengthening. The method has been used for several decades, yet most research work undertaken have been focused on conventional RC members, with limited application in non-flexural RC members with discontinuous regions (D-regions), such as deep beams, dapped-end beams, beams with openings, corbels and others.

Islam *et al.* (2005)'s study explored the prospect of strengthening structurally deficient deep beams by using an externally bonded FRP system, as shown in **Figure 2.1**. Test results showed that the use of a bonded FRP system led to a much slower growth of the critical diagonal cracks and enhanced the load-carrying capacity of the beam to a level quite sufficient to meet most of the practical upgrading requirements. Although FRP grids placed in normal orientation (as shown by Gird 1 in **Figure 2.1c**) was found to be the most effective system as far as the amount of material used in strengthening is concerned, other systems were found to be almost equally effective. An enhancement of shear strength in the order of about 40%, as achieved in this study, represented more than what was usually needed in a practical situation.

Sas *et al.* (2014) presented a parametric investigation, based on non-linear finite element modelling, to identify the most effective configuration of carbon fiber-reinforced polymers (FRP) for strengthening reinforced concrete (RC) dapped-end beams, as shown in **Figure 2.2**. Following a field application and laboratory tests, it focused on the effect of different configurations of externally bonded FRP (EB-FRP) reinforcement and near surface mounted FRP (NSM-FRP) reinforcement on the capacity and failure mode of dapped-end beams. The investigated parameters were the mechanical properties of the carbon FRP, the strengthening procedure and the inclination of the fibers with respect to the longitudinal axis. Two failure scenarios were considered: rupture and de-bonding of the FRP reinforcement. The results indicated that high-strength NSM FRPs can considerably increase the capacity of dapped-end beams and the strains in reinforcement can be substantially reduced by using high modulus fibers.

Huang and Nanni (2006) investigated the use of externally bonded carbon FRP laminates for the strengthening of the dapped-end of RC members. Five specimens were tested: two one-ply carbon FRP reinforced specimens and one steel reinforced specimen with a loading span of 2.4 m, and one two-ply FRP reinforced specimen and one steel reinforced specimen with a loading span of 1.5 m. Two types of failure for the carbon

FRP reinforced specimens were noted: carbon FRP delamination and fiber rupture failure. The two-ply carbon FRP reinforced specimen using U-anchor increased the shear capacity and ensured fiber rupture at failure. This study verified that FRP reinforcement can increase the capacity of dapped-end beams and the proposed method for strengthening dapped-end beams with FRP reinforcement was found to be satisfactory and conservative.

Nagy-György (2012) presented experimental and numerical assessments of the effectiveness of strengthening dapped-end reinforced concrete beams using externally bonded carbon fiber reinforced polymers (CFRPs), as shown in **Figure 2.3**. Four similar specimens were tested: one un-strengthened reference specimen, two strengthened with high-strength carbon FRP plates and one with high-modulus carbon FRP sheets. The specimens strengthened with plates had slightly higher load carrying capacity than the reference element, but failed by de-bonding, while the specimens strengthened with sheets showed no increase in capacity and failed by fiber rupture. Nonlinear finite element analysis of the specimens under the test conditions indicated that: (a) de-bonding was more likely to occur at the inner end of dapped-ends; and (b) the capacity could have been increased by up to 20% if the plates had been mechanically anchored.

Amorn Pimanmas (2010) studied the application of externally installed FRP rods to strengthen RC beams with openings, as shown in **Figure 2.4**. A total of thirteen beams with circular or square opening were tested. Two patterns of strengthening by FRP rods were investigated: one was to place FRP rods around the opening and the other was to place FRP rods diagonally throughout the entire depth of the beam. When FRP rods were placed throughout the entire beam depth, a significant improvement in loading capacity and ductility was achieved. The flexural failure mode was restored in such beams.

Elgwady M. A. *et al.* (2005) carried out an experimental study on six corbels strengthened by carbon fiber reinforced plastic (CFRP) to study the effectiveness of using carbon FRP as an external strengthening method to increase the load carrying capacity of corbels, as shown in **Figure 2.5**. Laminates of carbon FRP were bonded to the corbels using a two-component epoxy. Different strengthening configurations were used. The test results indicated that the proposed technique had the potential in improving the ultimate load carrying capacity of the short cantilever. Using the carbon FRP reinforcement enhanced the load carrying capacity of the corbels and the increase in ultimate load ranged between 8% to 70% compared to the control specimen.

Ozden and Atalay (2011) investigated the strength and post-peak performance of reinforced concrete corbels strengthened with epoxy bonded glass fiber reinforced polymer (GFRP) overlays, as shown in **Figure 2.6**. The test variables were the shear span to depth ratio, main reinforcement ratio, and the number and orientation of the GFRP fibers. In total, 24 normal strength concrete, one-third scale, corbel specimens, without hoop reinforcement, were tested to failure under quasi-static gravity loading. GFRP wraps with different layers and different orientations were used in strengthening of the corbel specimens. One-and three-layer patterns for diagonal GFRP wrapping (with fiber oriented at 45 degrees to the horizontal) was applied, whereas only three-layer pattern was used for horizontal GFRP configuration. Test results revealed that GFRP wrapping can be considered as an easy-to-apply and effective way for the enhancement of corbel load bearing capacity, depending on the fiber orientation. The increase in ultimate strength of corbels using GFRP wrapping ranged between 40% and 200%. The main reinforcement ratio and the number of GFRP plies were found to be the two main variables affecting the magnitude of strength gain in the corbel specimens.

2.3 Strut-and-tie method for non-flexural RC members

The strut-and-tie method (STM) provides a rational and conservative approach for the design of disturbed regions (D-regions) where the conventional plane bending theory does not hold. By transferring the applied loads to the supports using a system of strut and tie members, the method can be applied to structural concrete members with complex geometrical and loading conditions. The governing provisions of this approach consist of dimensioning rules, concrete efficiency factors, reinforcement limits, and anchorage requirements. The model promotes a better understanding of load transfer mechanisms and structural behavior and it improves the designers' abilities to handle unusual circumstances. It has therefore been included as a design approach in major design codes (CSA 1994; CEB-FIP 1993; AASHTO 2008; ACI 318 2011; EC2 2004).

In the early development of practical design procedures for reinforced concrete at the end of the nineteenth century, it was rapidly recognized that the simple theories of flexure were inadequate to handle regions which were subjected to high shear. A rational design approach was developed, primarily by Ritter (1899) and Mörsch (1920, 1922), based on an analogy with the way a steel truss carries loads. The truss analogy promoted the subsequent use of transverse reinforcement as a means of increasing the shear capacity of beams. Rausch (1929) extended the plane-truss analogy to a space-truss analogy and thus proposed the torsion-resisting mechanism of reinforced concrete beams. More sophisticated truss models were then proposed (Slater *et al.* 1927; Richart and Larsen 1927) where inclined stirrups were used and the compressive struts were oriented at angles other than 45°. The method was further refined and expanded (Kupfer 1964; Leondardt 1965). Only in the past two decades, after the work of Marti (1985), Collins and Mitchell (1986), Rogowsky and Macgregor (1986), and Schlaich *et al.* (1987), has the design procedure been systematically derived and successfully applied to solve various reinforced concrete problems.

The work by Schlaich *et al.* (1987) extended the beam-truss model to allow application to nearly all parts of the structure in the form of strut-tie systems. Schlaich (1987) suggested a load-path approach aided by the principal stress trajectories, based on a linear elastic analysis of the structure. The principal compressive stress trajectories can be used to select the orientation of the strut members of the model. The strut-and-tie system was completed by placing the tie members so as to furnish a stable load-carrying structure. This model was applied to the design of deep-pile caps, and the accuracy was found to be better than the conventional method suggested in the ACI Building Code (Adebar and Zhou 1996).

A significant number of research articles dealing with strut-and-tie modelling have been reported. They can be categorized as those dealing with: (a) the general principles of strut-and-tie modelling; (b) the determination of strength of struts, ties, and nodes; and (c) the application of strut-and-tie models to specific structural elements including serviceability requirements.

2.3.1 General principles of strut-and-tie modelling

The general principles of strut-and-tie modelling have been most extensively studied. Generally, these studies include the procedure for determining discontinuous-regions (D-regions), determining boundary conditions, development of strut-and-tie model, solution for member forces, choice and detailing of reinforcement, and checking of the stress conditions in nodes and strut members. Work done by Marti (1985), Collins and Mitchell (1986), and Schlaich *et al.* (1987) are some of the most complete and informative works of this type. In addition to outlining the strut-and-tie model procedure, these researches also give suggestions for strut and node strengths and show basic models for some simple structural elements. Some research articles (Foster *et al.* 1996; Maxwell and Breen 2000) present more experiments on strut and node strengths, detailing and anchorage requirements for reinforcement, and strut-and-tie models for increasingly complex structural members.

2.3.2 Design criteria

Researchers have tried to determine the appropriate effective strengths for the different types of nodes and struts through both laboratory testing and analytical work. The strengths of struts, ties and nodes have been investigated both experimentally and analytically. Despite the vast amount of research done in this area, there is no clear consensus among researchers on the strength of struts and nodes. This is also reflected in the different design specifications as described here (CSA 1994; CEB 1993; AASHTO 2008; ACI 318 2011; EC2 2004).

(a) Strength of strut

The strut-and-tie method incorporates the lower-bound plasticity theory, assuming concrete and steel to be elastoplastic. Concrete, however, does not behave as a plastic material, and full internal stress redistribution does not occur. The geometrical shape of a strut is highly dependent upon the force path. As discussed by Schlaich and Schäfer (1991), there are three basic shapes for struts: prismatic, bottle-shaped, and fan-shaped (**Figure 2.7**). The major factors affecting the compressive strength of a strut are: (1) the concrete compressive strength f_c'; (2) the orientation of cracks in the strut; (3) the width and the extent of cracks; and (4) the degree of lateral confinement. To account for the above factors, the effective compressive strength of a strut may be written as:

$$f_{strut}' = \nu f_c' \tag{2.1}$$

where f_c' is the cylinder compressive strength of concrete and v (≤1.0) is an efficiency factor to account for the lack of plasticity in concrete. The proposed values of v, along with the recommended values by other researchers, are listed in **Table 2.1**. It is noted that strain incompatibility is likely to occur when the angle between the compressive strut and tie is less than 30°. Therefore, the angle between the strut and the yielded tie θ should be assumed greater than 30° for typical STM. The typical values of v vary between 0.85 for an un-cracked strut with uniaxial compressive stress, to 0.55 for a skewed severely cracked strut. The minimum value is around 0.35.

The design compressive strength of strut member is usually expressed as:

$$f_{strut} = \phi f'_{strut} = \phi v f_c' \tag{2.2}$$

where ϕ is the partial safety factor. The codified strengths for concrete strut are listed in **Tables 2.2**.

The Canadian Code (CSA 1994) gives the design strength of strut as a function of the strut orientation as well as the strains of both concrete and steel. However, this formula does not take into account the brittleness of concrete with increasing strength. Su and Chandler (2001) adopted the approach of MacGregor (1997), taking the efficiency factor for struts as a product of two partial safety factors (v_1 and v_2) which account for: (i) the orientation of the strut-tie; (ii) the brittleness of concrete with increasing strength; (iii) the strain state of both concrete and steel; and (iv) the strength state of the node boundary; that is:

$$f_{strut} = \phi v_1 v_2 f'_c \tag{2.3}$$

where ϕ is a partial safety factor, equal to 0.67, $v_1 = \dfrac{1}{1.14 + 0.75\cot^2\theta}$, and $v_2 = 1.15(1 - f'_c/250)$, in which θ is the angle between the strut member and tie member. The first partial safety factor v_1 originated from the modified Collins and Mitchell relation (1986), taking into account the types of stress fields, orientation and the extent of cracks in the strut and the presence of transverse reinforcement. The second partial safety factor v_2 was adopted to incorporate the brittleness of the higher strength concrete.

The design compressive load capacity of strut is:

$$F_{strut} = f_{strut} \cdot A_{strut} = f_{strut} \cdot w_{strut} t \tag{2.4}$$

where A_{strut} is the effective cross-sectional area of strut. The value of A_{strut} shall be determined by considering both the available concrete area and the anchorage conditions at the ends of the strut. The width of a strut w_{strut} is determined by the equation $w_{strut} = l_b \cos\theta + t\sin\theta$, where l_b is the width of the support bearing plate; and t is the thickness of compression strut. In dimensioning the width of a strut where support or load plate is not used, l_b is assumed to be equal to t.

Schlaich *et al.* (1987) observed that the shape of the compressive strut is bowed and, as a result, transverse tensile forces exist within the strut. The bottle-shaped stress field with its bulging stress trajectories develops considerable transverse stresses; resulting in compression near the bottle neck and tension further away. The transverse tension can cause longitudinal cracks and initiate an early failure of the member. It is therefore necessary to reinforce the stress field in the transverse direction, when determining the failure load of the strut. It is also important that a minimum quantity of reinforcement is provided to avoid cracking of the compressive strut due to the induced tensile forces so as to ensure the efficiency of the strut.

(b) Strength of tie

Ties are members that are subjected to tensile forces. As concrete is known to have a small tensile capacity, only reinforcing or pre-stressing steel are considered to provide the axial tensile capacity of a tie member. The codified tensile capacity of ties specified in different codes is given in **Table 2.3**. The partial safety factor ϕ for ties is generally 0.87, except for the suggested value of 0.70 by the Australian Code (AS 3600-1994), which is substantially conservative. In most of the design specifications, the capacity of a tie composed of reinforcing steel is determined as the product of the area of the reinforcing steel, A_s, the partial safety factor, ϕ, and the yield strength of the steel, f_y. Therefore, the design strength and design axial capacity of a tie member are, respectively, given by:

$$f_{tie} = \phi f_y \tag{2.5}$$

$$F_{tie} = f_{tie} \cdot A_s = \phi f_y A_s \tag{2.6}$$

where ϕ is the partial safety factor, f_y is the yield strength of the reinforcing steel, A_s is the cross-sectional area of steel reinforcement in tie member. It should be noted that a designer must properly detail the anchorage of the steel reinforcement to ensure that the tie member develops its design axial capacity.

(c) Strength of node

The strength of the nodal zones depends on a number of factors: (1) the confinement of the zones due to reaction forces, compression struts, anchorage plates for pre-stressing, reinforcement from the adjoining members, and hoop reinforcement; (2) the effects of strain discontinuities within the nodal zone when ties are anchored in, or cross, a compressed nodal zone; and (3) the splitting stresses and hook-bearing stresses resulting from the anchorage of the reinforcing bars of a tension tie in, or immediately behind, a nodal zone. The limiting compressive strength of a node is typically taken as the product of the concrete compressive strength and a reduction factor. The reduction factor depends on the node type. Most design specifications recognize three major node types: CCC, CCT, and CTT nodes. A CCC node is bounded by only strut members. A CCT node anchors one tie, and a CTT node anchors two or more ties. The geometry of a node is determined by bearing conditions, the details of anchored reinforcement, and the geometry of struts connected to node. **Figure 2.8** illustrates the different node types (Mitchell *et al.* 2004).

The effective strength of a node may be expressed as:

$$f'_{node} = \eta f'_c \tag{2.7}$$

where f_c' is the cylinder compressive strength of concrete and η is the strength efficiency factor for a node ($\eta \leq 1.0$), the values of which, proposed by different researchers, are shown in **Table 2.4**. It can be observed that a small variation of η exists for different types of node. The typical values of CCC, CCT and CTT nodes are 0.85, 0.68 and 0.6, respectively. Schlaich *et al.* (1987) increased the value of η from 0.85 to 0.94 for CCC node under two or three dimensional compressive stresses in the nodal region. Experimental study of concrete nodes by Jirsa *et al.* (1991) reported that the minimum strength of CCT and CTT nodes was $0.80 f_c'$.

The design strength and design bearing capacity of a node are, respectively, given by:

$$f_{node} = \phi f'_{node} \tag{2.8}$$

$$F_{node} = f_{node} \cdot A_{node} = \phi f'_{node} \cdot A_{node} \tag{2.9}$$

where ϕ is the partial safety factor, A_{node} is the effective area of node. **Table 2.5** shows the codified strength for a concrete node.

(d) Anchorage

Safe anchorage of tie reinforcement in the node has to be assured; to achieve this, minimum ratio of bent bars and anchorage lengths of bars may be selected following the ACI code recommendations (ACI 318-11) for example. The tension tie reinforcement must be uniformly distributed over an effective area of concrete at least equal to the tie force divided by the concrete stress limits for the node. The anchorage must be located within and 'behind' the nodes. The bar must extend to the other end of the node region. If this length is less than required by the code, the bar may be extended beyond the node region. The tensile forces introduced behind the node can resist the remaining forces developed within the nodal regions.

2.4 FRP strengthening of non-flexural RC structures based on STM

Limited studies have been conducted with regards to the application of strut-and-tie model on the design of the FRP strengthening strategy for non-flexural reinforced concrete structures with D-regions.

2.4.1 Deep beams

Park and Aboutaha (2009) presented a practical analysis and design process for carbon FRP strengthened deep RC members using the strut-and-tie model, as shown in **Figure 2.9**. In addition, seven effective factor models accounting for reduction of strength in cracked concrete were also evaluated. A total of 17 experimental deep beam test results were compared with the proposed STM approach results. It has been shown that the proposed STM approach with an effective factor model depending on the strut angle provides the best agreement with the test results.

2.4.2 Dapped-end beams

In the study of Tan (2001), several schemes for the strengthening of dapped-end beams with carbon FRP plates in shear to cater for increased imposed loads were investigated, as shown in **Figure 2.10**. In all, seven single-load tests using four 2.25

meter long beams were carried out. One beam was un-strengthened while the other three beams were strengthened with carbon FRP plate (CP), carbon fibre sheets (CS), or glass fibre fabrics (GS). For each of the strengthened beams, the FRP system was installed with different anchorage systems on two ends. After failing the beam on the weaker side, the failed section was enlarged with additional reinforcement and the beam was re-tested to evaluate the effectiveness of the FRP system at the other end. All the beams failed in shear, with diagonal cracks propagating from the reentrant corner to the flange of the beam in most cases. Beams strengthened with FRP systems exhibited a delay in diagonal cracking, increase in stiffness and an increase in ultimate load compared to the un-strengthened beam. Results indicated an increase in ultimate load of 43%, 75% and 80% for the CP, CS and GS systems respectively. The use of an anchorage bolt in the CP system at the critical location further enhanced the strength by 16%, while the use of bonded transverse fabric led to further strength increase of 33% and 41% respectively for the CS and GS systems respectively. A strut-and-tie model, consisting of two sub-models to evaluate the increased shear capacities due to vertical and diagonal reinforcement, was found suitable for the evaluation of the increased shear capacity due to the FRP system.

2.4.3 Stepped beams (non-prismatic beams)

Tan (2004)'s study dealt with the application of the strut-and-tie models in the analysis and design of non-prismatic reinforced concrete beams, as shown in **Figure 2.11**. Test results showed that the ultimate loads exceeded the design loads for all beams. Non-prismatic beams with a recess through the web performed satisfactorily, compared to beams with equivalent transverse rectangular openings. For non-prismatic beams with a recess at the bottom, an increase in the recess width resulted in a decrease in the stiffness and an increase in the beam deflection. Non-prismatic beams with a recess in the compression zone performed better with regards to cracking but not deflection, compared to beams with a recess in the tensile zone. Also, beams strengthened with carbon fibre-reinforced polymer plates performed satisfactorily with regard to strength; however, the deflection and crack widths increased rapidly thereafter, leading to a sudden and non-ductile failure of the beam. The strut-and-tie method of design was shown to be suitable for application in non-prismatic beams as (a) the crack pattern and measured strains in the reinforcement agreed with the strut-and-tie model; (b) the strut-and-tie model gave lower bound values for the ultimate load; and (c) the method offered a simple and straightforward solution that was based on established principles to an otherwise complicated problem.

Afefy *et al.* (2013) presented both experimental and analytical investigations undertaken to evaluate the ability of externally bonded (EB) carbon FRP strips and sheets to restore the ultimate capacity of defectively detailed stepped beams, as shown in **Figure 2.12**. The strengthening strategy of these beams was based on analyzing their stepped joints using strut-and-tie model with all possible arrangements of tension and compression members and then applying the strengthening strips and sheets parallel to the obtained tension ties. The common feature of the four strengthened beams was that all beams were strengthened using carbon FRP strips of dimensions 25 mm width, 1.2 mm thickness and 1200 mm length extended from the tension side of the upper portion to the lower portion and centered at the middle part of the beam. These carbon FRP strips were mounted at both faces of the beam and were used to compensate for the insufficient bond length of the main tension steel of the upper portion. For beam BS1, two 100 mm wide by 0.13 mm thick orthogonal carbon FRP sheets were used at the stepped part in order to trace the main ties according to strut-and-tie model I. Both layers were U-shaped, while the horizontal sheet extended 700 mm along the beam axis and the vertical U-shaped extended 425 mm perpendicular to the beam axis. Finally, two 100 mm width anchorage U-shaped sheets were used at the both ends of the carbon FRP strips in order to prevent the premature peeling of the strips in addition to the horizontal sheet. The vertical sheet had a double duty, in addition to strengthening the beam in the vertical direction, it worked as U-shaped anchorage for the horizontal strips. Strengthening configuration complying with strut-and-tie model II was used for beams BS2, BS3, and BS4. For beam BS2, one 100 mm width carbon FRP sheet was used to strengthen the joint in the vertical direction while an 100 mm carbon FRP sheet inclined at 45° was used to trace the inclined tie. A horizontal 100 mm U-shaped sheet was used for beam BS3. In addition, the inclined carbon FRP sheet of beam BS2 was replaced by carbon FRP strips for beam BS3. The considered configuration of beam BS4 was similar to that of beam BS3 except that a concrete haunch was used in case of beam BS4. In all cases, 100 mm wide U-shaped anchorage sheets were used at both ends of the carbon FRP strips.

Test results showed that, contrary to the observed behavior of the correctly detailed beams, the un-strengthened defected beam exhibited premature splitting failure due to slippage of the main reinforcement and, its load carrying capacity was decreased by about 77% compared with that of the correctly detailed beam. However, strengthening the defected beams with EB-carbon FRP had not only restored the defected beams flexural capacity but also prevented the early steel reinforcement de-bonding and consequently enhanced the flexural performance of the strengthened beams. Based on the proposed strut-and-tie model, the adopted carbon FRP strengthening system can restore the ultimate capacity of defected beam and outperform the behavior of such beam when compared to the properly detailed stepped beam by about 15%. It was however not guaranteed that the carbon FRP strengthening technique always increases the ultimate capacity of defected beam. The affirmative effect always happens if only the proper configuration is chosen based on rigorous analysis. The performance of beam BS2 was just as promising, if not more so, due to the fact that the proposed strengthening configuration based on the second strut-and-tie model (Model II) was able to increase its load-carrying capacity to 62.03 kN, approximately five times higher than that of the control beam B0.

2.4.4 Beams with opening

Lim (2006) investigated the application of FRP strengthening systems using strut-and-tie method in the analysis and design of reinforced concrete beams with openings. Seven beams were designed, fabricated and tested. This included a solid beam of the same dimensions but without openings. The main parameters of the other beams investigated included the size and location of the openings and the type of FRP strengthening system. The test results were also compared with past studies on beams originally designed with openings. Test results showed that the ultimate loads exceeded the design load. With the openings sufficiently reinforced, the beams showed comparable performance with a solid beam in terms of deflection and cracking characteristics in the region of the beams away from the openings. External FRP strengthened beams also exhibited performance comparable to beams with openings originally designed for. The strut-and-tie method proved to be suitable for application in strengthening beams with openings as it gave a conservative design.

Muhammad (2007) presented a study on the behavior of T-beams with openings under the influence of GFRP strengthening systems based on strut-and-tie modelling. Test results showed all the T beams with openings presented comparable performance in terms of deflection, crack width and ultimate load after being strengthened with glass FRP compared to a solid T beam without opening. The strut-and-tie model proved to be a suitable method to predict the stress flow at the D-regions for all the six beams and gave a lower bound solution.

2.4.5 Remarks

To sum up, the strut-and-tie model could be applied readily to FRP reinforcement. For FRP strengthened structural concrete, FRP reinforcements are considered as additional tensile ties. **Figure 2.10b** shows the way by which diagonal and vertical FRP plates and fabrics/sheets are replaced by tie members (Tan 2001). The capacity of the tie members is equal to the cross sectional area multiplied by the yield or effective strength of the reinforcement. The tensile capacity of FRP strengthened tie member is given by:

$$F_{tie} = f_y A_s + E_{FRP} \varepsilon_{eff} A_{FRP} \tag{2.10}$$

where f_y is the yield strength of the reinforcing steel, ε_{eff} is the effective strain of FRP reinforcement, A_s and A_{FRP} are the cross-sectional area of steel reinforcement and FRP reinforcement in the tie member. Theoretically, it is very difficult to accurately estimate the effective strain because of the complex bonding mechanism between the FRP reinforcement and the concrete surface. Several effective strain models for FRP have been proposed by various technical committees and researchers. Based on ACI 440's recommendation (ACI 440, 2008), the effective FRP strain at failure can be taken as: $\varepsilon_{eff} = 0.004 \leq 0.75\varepsilon_{FRP,ru}$, where $\varepsilon_{FRP,ru}$ is the rupture strain of FRP reinforcement. For carbon FRP plates, the plate would de-bond before the full potential of its tensile strength is reached. Based on Tan's study (2001), an effective strength of 0.45 times the rupture strength may be used.

In these studies, the FRP strengthening strategy based on strut-and-tie modelling was based on analyzing non-flexural RC members using strut-and-tie model with all possible arrangements of tension and compression members and then applying the FRP reinforcement parallel to the obtained tension ties. The FRP reinforcement required to carry an additional load is obtained by dividing the induced force by an effective tensile strength of the FRP reinforcement (Tan 2001).

$$A_{FRP} = \Delta F_{tie} \big/ E_{FRP}\varepsilon_{eff} \tag{2.11}$$

where ΔF_{tie} is the additional load of the tie member. When dimensioning the area of FRP ties, only 75% of FRP is considered to be effective, i.e., the strength reduction factor is equal to 0.75, which reflects the uncertainties in carbon FRP strengthening due to carbon FRP de-bonding (Park and Aboutaha 2009).

However, FRP strengthening of strut members and nodal zones was not considered in these studies. Further efforts should be put into this area.

2.5 Summary

A literature review on the FRP strengthening of non-flexural reinforcement concrete structures based on strut-and-tie modelling was presented.

First, previous works on FRP strengthening of non-flexural RC members with D-regions were reviewed. Research findings revealed that FRP strengthening systems could effectively enhance the load-carrying capacity of non-flexural RC members.

Next, a brief introduction and description of strut-and-tie model was presented. The concept behind strut-and-tie modelling and their limitations were discussed. Available design codes and models were also presented and summarized. Several theoretical and experimental studies about strut members and tie members have been done, giving clear indications of the structural behavior of these disturbed regions. However, little experimental information is available for the FRP strengthening of isolate ties or struts and there is no consensus amongst current design codes or the literatures on the method of FRP strengthening for tie members and strut members.

Finally, typical studies on FRP strengthening of non-flexural reinforced concrete structures based on strut-and-tie modelling were presented in this chapter. Test results showed that the strut-and-tie method proved to be suitable for the application in FRP strengthening of non-flexural reinforcement concrete structures. However, very limited studies have been conducted with regards to the use of strut-and-tie model to design the FRP strengthening strategy for reinforced concrete structures with D-regions. Thus, a systematic study on this area is needed.

Table 2.1: Effective factor for concrete strut

References	**Efficiency factor *v* for strut**
Uncracked strut with uniaxial state of compressive stress	
Nielsen *et al.* (1978)	(0.7- f_c' /200), $f_c' \le 60$ MPa
Rogowsky & MacGregor (1986)	0.85
Schlaich *et al.* (1987)	0.85
Alshegeir & Ramirez (1992)	0.80~0.95
Warwick & Foster (1993)	0.85
Foster & Gilbert (1997)	0.85
Cracks parallel to the strut with normal crack width	
Schlaich *et al.* (1987)	0.68
Alshegeir & Ramirez (1992)	0.75
Warwick & Foster (1993)	$1.25- f_c'/500-0.72 \cot\theta+0.18\cot^2\theta \le 0.85$
Foster & Gilbert (1997)	$1/(1.14+0.75\cot^2\theta)$
Cracks skewed to the strut with severe crack width	
Schlaich *et al.* (1987)	0.51
Alshegeir & Ramirez (1992)	0.50
Warwick & Foster (1993)	$1.25- f_c'/500-0.72 \cot\theta+0.18\cot^2\theta \le 0.85$
Foster & Gilbert (1997)	$1/(1.14+0.75 \cot^2\theta)$
Minimum strength of strut (assuming $\theta \le 30°$)	
Schlaich *et al.* (1987)	0.34
Alshegeir & Ramirez (1992)	0.2~0.25
Warwick & Foster (1993)	$0.53- f_c'/500$
Foster & Gilbert (1997)	$1/(1.14+0.75 \cot^2\theta)$

Note: θ represents the angle between strut and horizontal tie.

Table 2.2: Codified strength of concrete strut member

Design standard	**Partial safety factor**	**Codified strength of strut**
CEB-FIP: 1990	ϕ =0.67 f_c' ≤80 MPa	$\phi\, 0.85(1\text{-}\, f_c'/250)\, f_c'$; un-cracked strut $\phi\, 0.60(1\text{-}\, f_c'/250)\, f_c'$; cracked strut
EN 1992-1-1: 2004 (EC 2)	ϕ =0.67 f_c' ≤50 MPa	$\phi f_c'$ struts without transverse tension $0.6\phi v' f_c'$ struts with transverse tension v' =(1.0- f_c' /250)
CSA A23.3-94	ϕ =0.6 f_c' ≤80 MPa	$\phi f_c'/(0.8+170\, \varepsilon_1) < 0.85\, \phi f_c'$ $\varepsilon_1 = \varepsilon_s + (\varepsilon_s + 0.002)\cot^2\theta$ ε_s is the yield strain of horizontal steel ties at ultimate state.
AS 3600-1994	ϕ =0.70 f_c' ≤50 MPa	$\phi\,(0.8\text{-}\, f_c'/200)\, f_c'$
ACI 318-2011	f_c' ≤55 MPa	$0.85\beta_s f_c'$ $\beta_s = 1.0$, for a strut of uniform cross-sectional area over its length; $\beta_s = 0.75$, for bottle-shaped strut with transverse reinforcement satisfying A.3.3; $\beta_s = 0.60$, for bottle-shaped strut without transverse reinforcement satisfying A.3.3 (normal-weight concrete); $\beta_s = 0.4$, for struts in tension members, or the tension flanges of members; $\beta_s = 0.60$, for all other cases (normal-weight concrete).

Note: ε_1 and ε_2 are the major and minor principal strains of the concrete; ε_s is the yield strain of horizontal steel ties at ultimate state; θ represents the angle between strut and horizontal tie.

Table 2.3: Codified strength for tie member

Design standard	**Partial safety factor ϕ**	**Codified strength of tie**
CEB-FIP: 1990	0.87	$0.87f_y$
EN 1992-1-1: 2004 (EC 2)	0.87	$0.87f_y$
CSA A23.3-94	0.85	$0.85f_y$
NZS 3101: Part 2: 1995	0.87	$0.87f_y$
AS 3600-1994	0.70	$0.70f_y$

Table 2.4: Effective factor for concrete node

References	**Efficiency factor η for node**		
	CCC node	**CCT node**	**CTT node**
Collins & Mitchell (1986)	0.85	0.75	0.60
Schlaich *et al.* (1987)	0.94	0.68	0.68
MacGregor (1997)	0.85	0.65	0.50
Jirsa *et al.* (1991)	—	0.80	0.80
Bergmeister *et al.* (1991)	2.50 (Triaxially confined nodes) 0.76 (Unconfined nodes) 0.8, if $f_c' \leq 27.6$ MPa $(0.9-0.25 f_c'/69)$, if $27.6 \leq f_c' \leq 69$ MPa 0.65, if $f_c' \geq 69$ MPa	—	—

Table 2.5: Codified strength for concrete node

Design Standard	**Partial safety factor**	**Codified strength of node**
CEB-FIP: 1990	ϕ =0.67 $f_c' \leq$80 MPa	$\phi\, 0.85(1- f_c'/250)\, f_c'$ CCC $\phi\, 0.60(1- f_c'/250)\, f_c'$ CCT and CTT
EN 1992-1-1: 2004 (EC 2)	ϕ =0.67 $f_c' \leq$50 MPa	$\phi k_1 v' f_c'$ k_1 =1.0 CCC k_1 =0.85 CCT k_1 =0.75 CTT v' =(1.0- f_c'/250)
CSA A23.3-94	ϕ =0.6 $f_c' \leq$80 MPa	0.85 $\phi f_c'$; CCC 0.75 $\phi f_c'$; CCT 0.65 $\phi f_c'$; CTT
NZS 3101: Part2: 1995	ϕ =0.8 $f_c' \leq$70 MPa	0.65 $\phi f_c'$; CCC 0.55 $\phi f_c'$; CCT 0.45 $\phi f_c'$; CTT
AS 3600-1994	ϕ =0.70 $f_c' \leq$50 MPa	ϕ (0.8- f_c'/200) f_c'
ACI 318-2011	$f_c' \leq$55 MPa	$0.85\beta_n f_c'$ $\beta_n = 1.0$; CCC $\beta_n = 0.80$; CCT $\beta_n = 0.60$; CTT

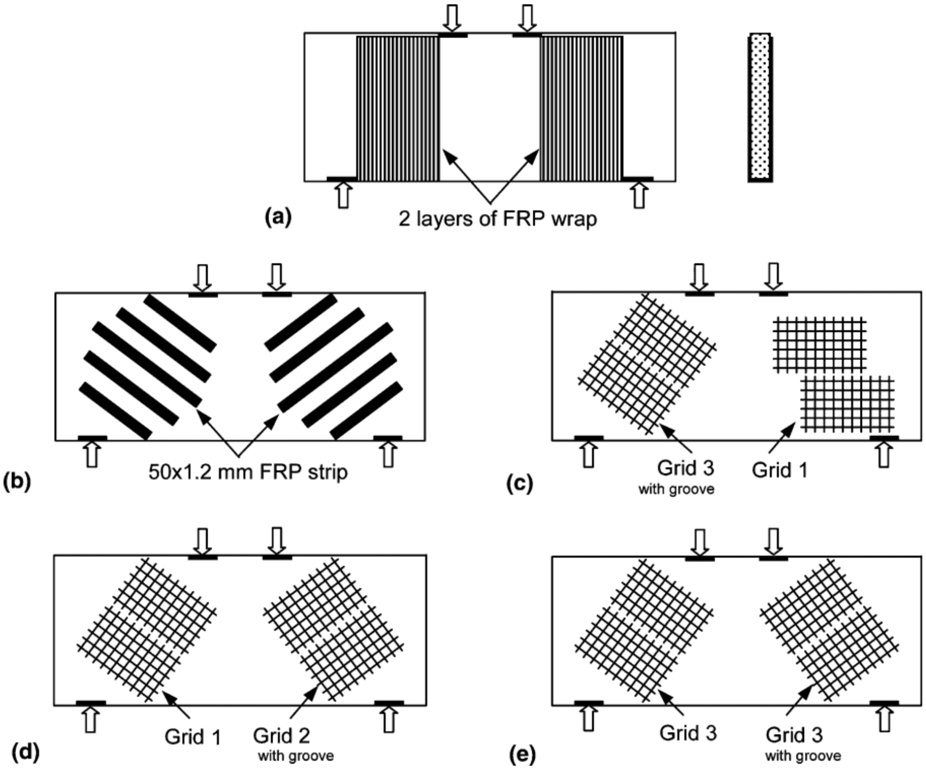

Figure 2.1: Arrangement of externally bonded FRP systems (Islam *et al.* 2005)

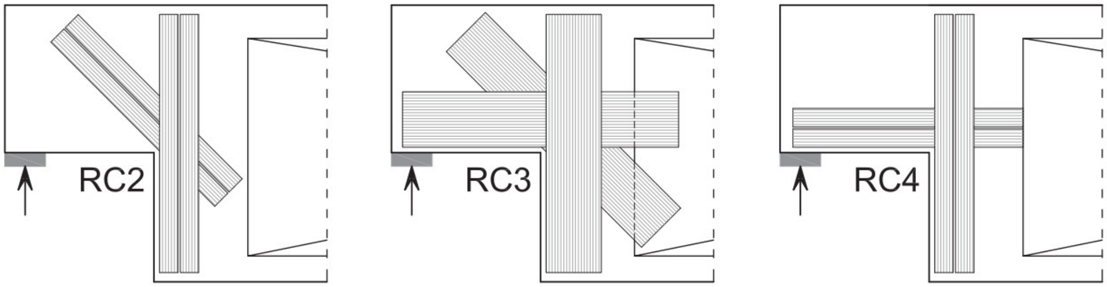

Figure 2.2: Schematic illustration of the tested strengthening systems (Sas *et al.* 2014)

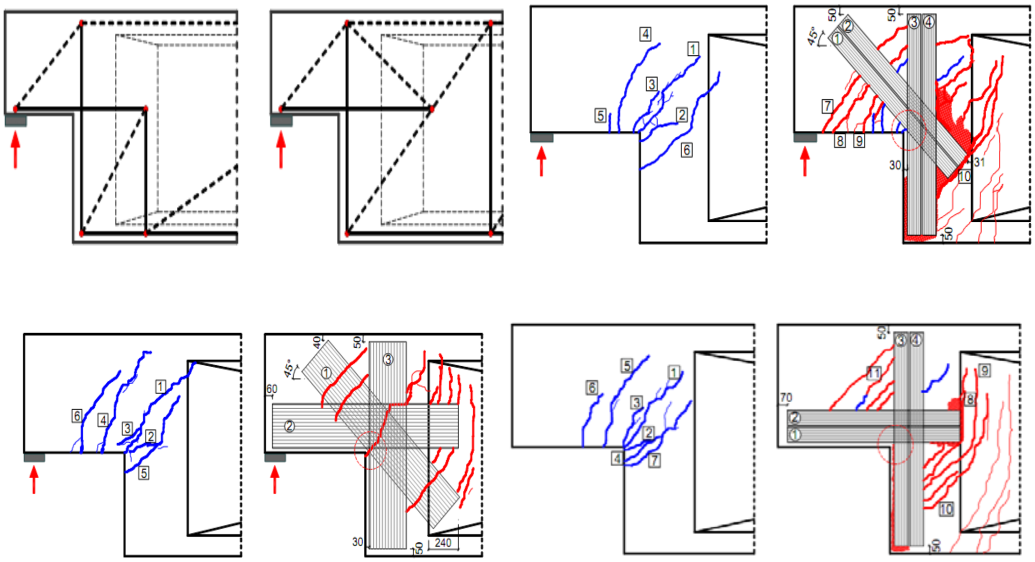

Figure 2.3: Strut-and-tie models and FRP strengthening systems for dapped-end RC beams (Nagy-György 2012)

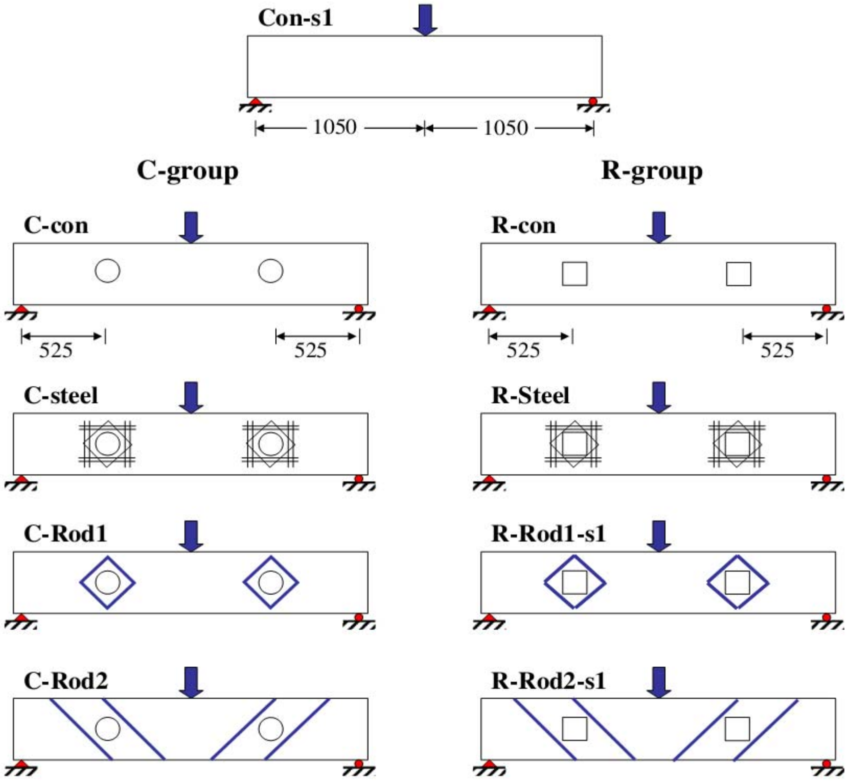

Figure 2.4: Strengthening RC beams with opening by externally installed FRP rods (Amorn Pimanmas 2010)

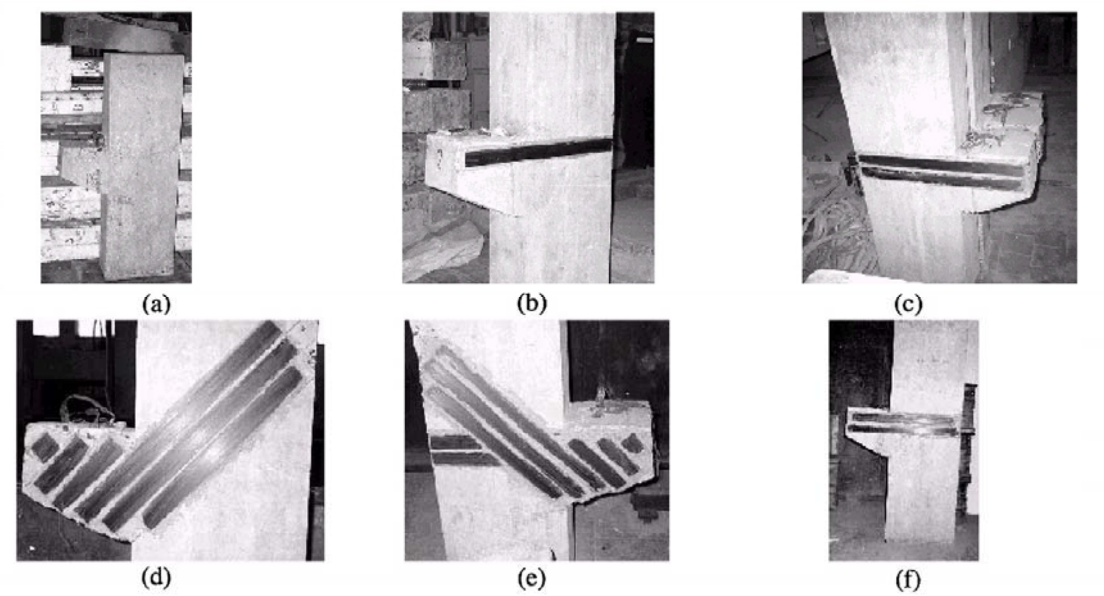
(a) (b) (c) (d) (e) (f)

Figure 2.5: FRP strengthening of corbels (Elgwady M. A. *et al.* 2005)

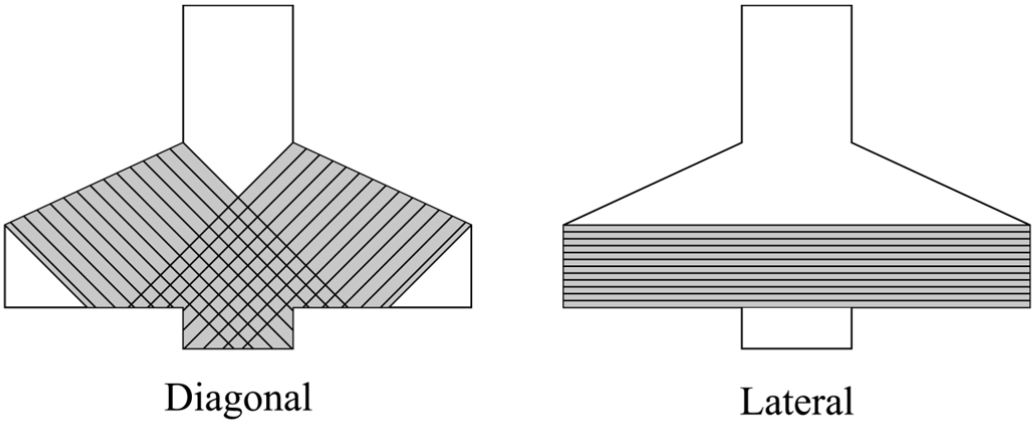

Figure 2.6: FRP strengthening configurations of corbels (Ozden and Atalay 2011)

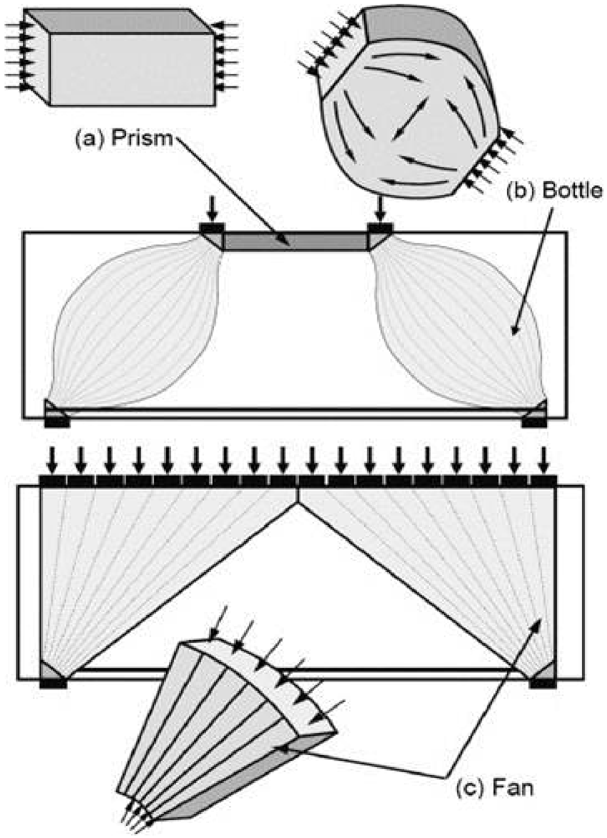

Figure 2.7: Geometric shapes of struts (Schlaich and Schäfer 1991)

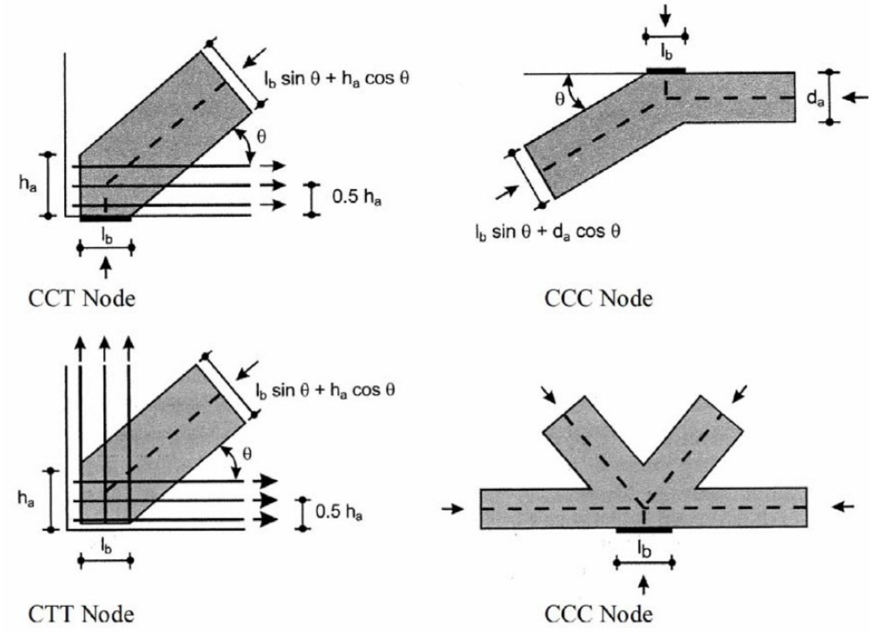

Figure 2.8: Types of strut-and-tie model nodes (Mitchell *et al.* 2004)

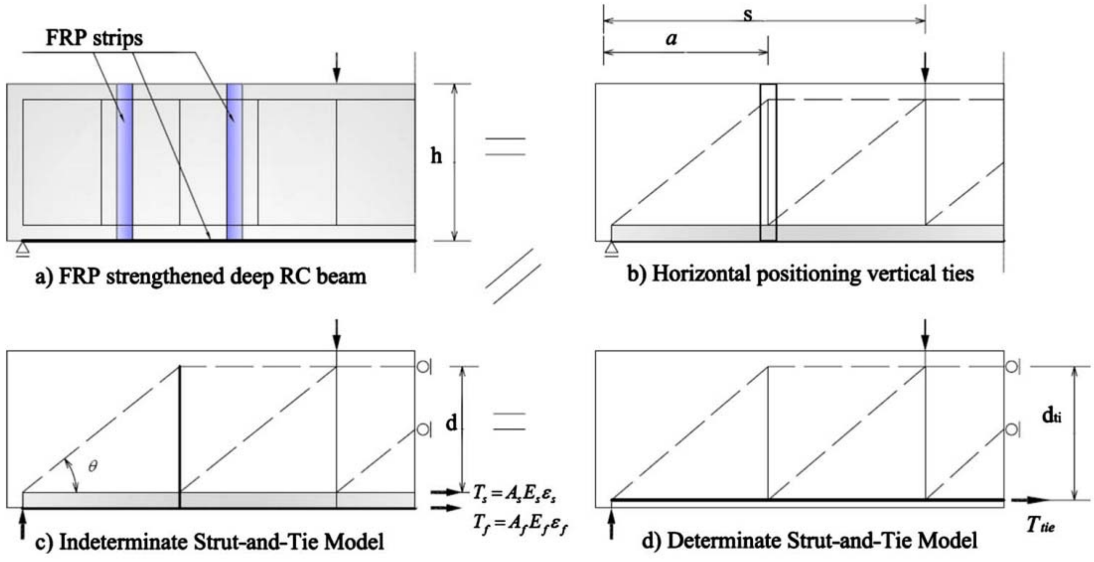

Figure 2.9: Strut-and-tie models and FRP strengthening systems for deep RC beams (Park and Aboutaha 2009)

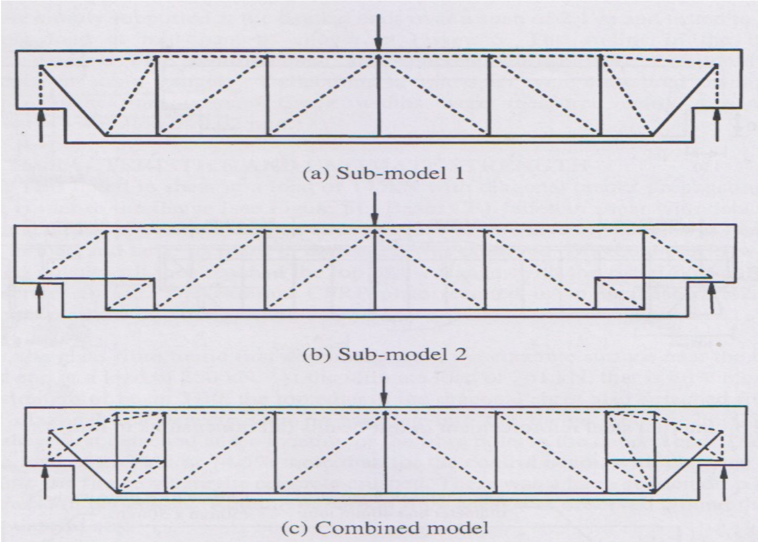

(a) Strut-and-tie model

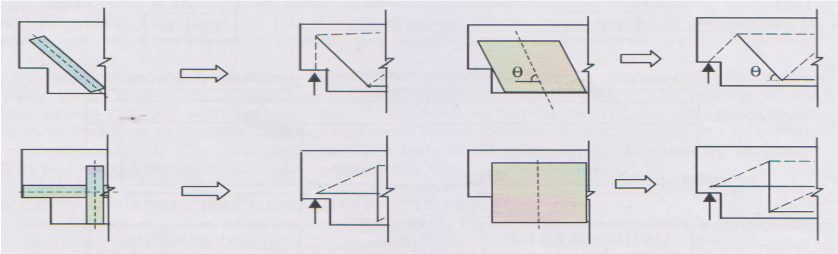

(b) Modelling for FRP reinforcement

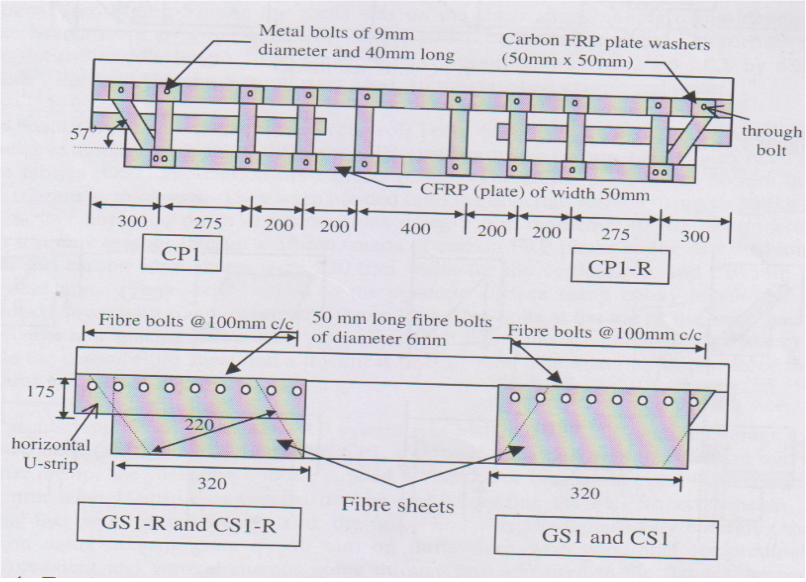

(c) FRP strengthening systems

Figure 2.10: Strut-and-tie models and FRP strengthening systems for dapped beams (Tan 2001)

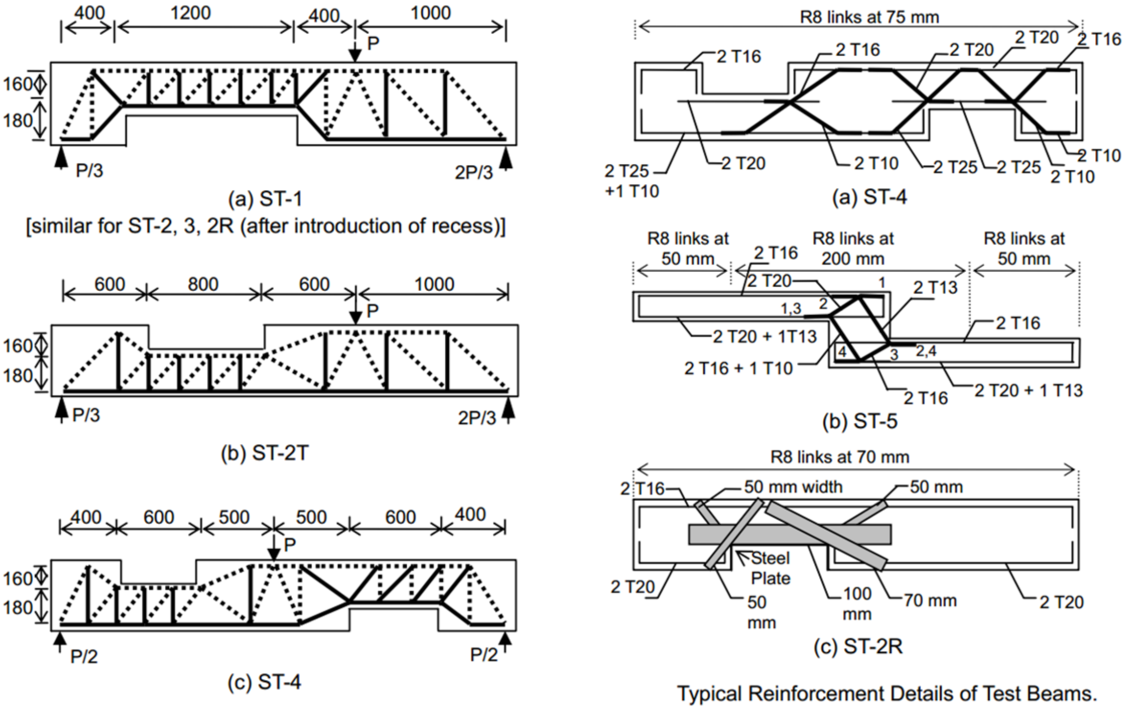

Figure 2.11: Strut-and-tie models and FRP strengthening systems of non-prismatic RC beams (Tan 2004)

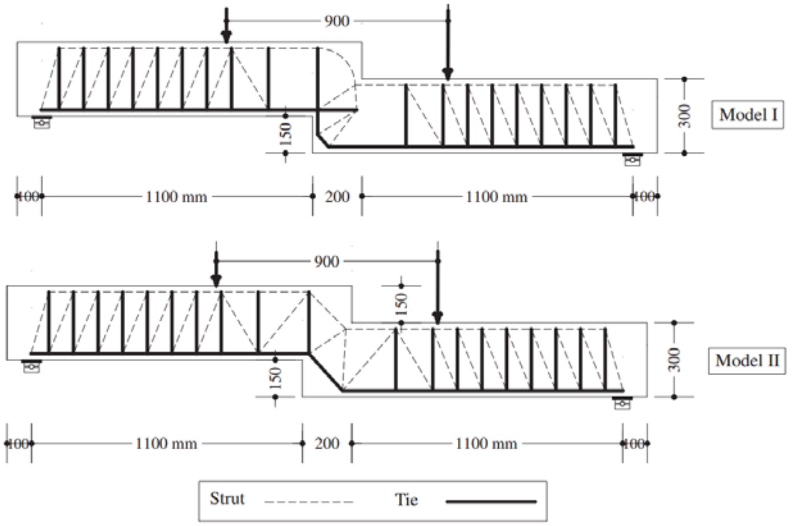

(a) Adopted strut-and-tie models

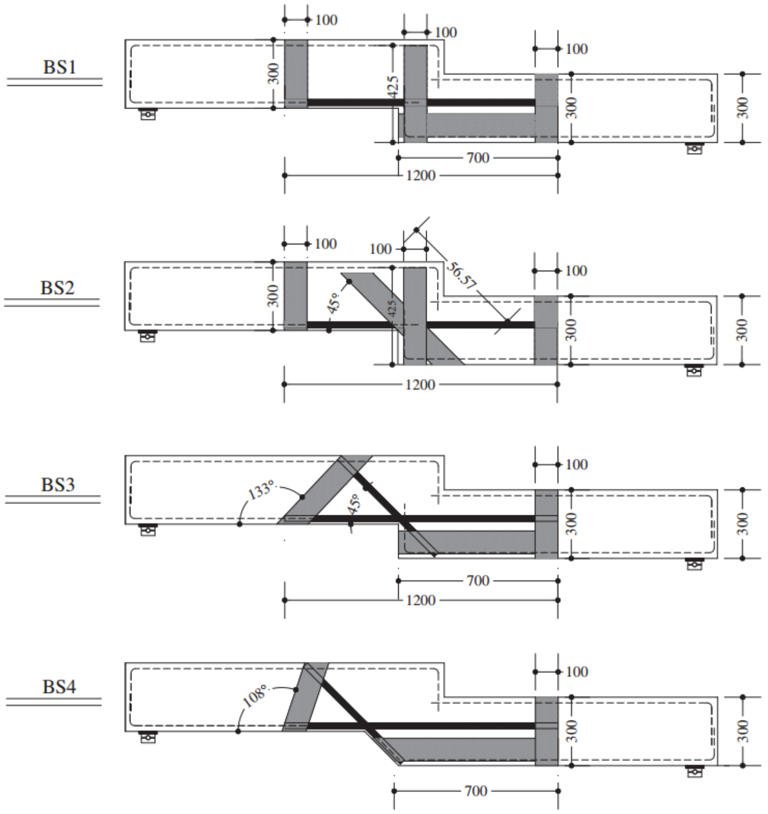

(b) Strengthening configurations using carbon FRP sheets and carbon FRP strips for the strengthened beams

Figure 2.12: Rehabilitation of defected RC stepped beams using carbon FRP (Afefy *et al.* 2013)

Chapter 3. FRP Strengthening of Tie Members

3.1 General

This chapter presents the investigation on the behavior and ultimate load of FRP strengthened reinforced concrete tie members under axial tensile loading. Tests were carried out with the FRP reinforcement configuration of tie specimens as the main parameter. Test results are discussed and an analytical model is proposed to determine the ultimate load capacity of FRP strengthened tie members. The analytical predictions are then compared with experimental values.

3.2 Test program

In order to verify the applicability and effectiveness of FRP strengthening systems, the strength and behavior of reinforced concrete tie members, strengthened with epoxy bonded carbon fiber reinforced polymer (EB-FRP) sheets and near-surface-mounted carbon fiber reinforced polymer (NSM-FRP) rods, were experimentally investigated. Focus was placed on the enhancement in ultimate load capacity of RC tie members due to FRP reinforcement.

3.2.1 Test specimens

Figure 3.1 shows a typical strut-and-tie model. Tie members are significant elements within the strut-and-tie models that carry tension forces. The tie member can be taken as a prismatic member symmetrically reinforced with longitudinal bars with a width twice the cover to the centroid of the steel reinforcement. Specimens of two different lengths were considered so as to confirm that the test results are independent of the specimen length.

In total, two series, consisting of eight short tie specimens and seven long tie specimens respectively, were fabricated and tested to failure. **Figure 3.2** shows the geometry and reinforcement details for the specimens. The test parameters are given in **Table 3.1**. The main parameters were the carbon FRP strengthening configuration and the reinforcement parameter. Except for the control un-strengthened Specimens T00 and LT00, each specimen was strengthened with externally-bonded carbon FRP sheets or near-surface-mounted carbon FRP rods or both. The specimens were designated as T*xy* for Series T specimens and LT*xy* for Series LT specimens, where *x* denotes the number of ply of longitudinal EB-FRP sheets and *y* the number of NSM-FRP rods, on each face of the specimen. For Specimen T10, two tests were conducted to verify the repeatability of the test results, and they were designated as T10a and T10b.

All the short tie specimens in Series T had the same length of 500 mm and cross section measuring 100 mm in width and 70 mm in thickness. The longitudinal steel reinforcement in the test region consisted of one 12 mm diameter deformed steel bar which corresponded to a steel reinforcement ratio of about 1.62%. The clear concrete cover was 29 mm. Mild steel stirrups of 6 mm diameter were spaced at 20 mm spacing at the two ends of the specimens. The steel bars were welded together to form the steel cage. The ends of the FRP strengthened tie specimens were wrapped with 100 mm wide carbon FRP sheets after the corners were rounded to a minimum radius of 12 mm to prevent stress concentration in the FRP sheets. These carbon FRP sheets had a dual role; in addition to strengthening the ends of the tie members, it helped to anchor the longitudinal carbon FRP sheets and rods and delay de-bonding of the FRP reinforcement.

All the long tie specimens in Series LT had a length of 1200 mm and a cross section measuring 100 mm in both width and thickness. The longitudinal steel reinforcement in the test region consisted of one 12 mm diameter deformed steel bar which corresponded to a steel reinforcement ratio of about 1.13%. The clear concrete cover was 44 mm. Mild steel stirrups of 6 mm diameter were spaced at 20 mm spacing at the two ends of the specimens. The steel bars were again welded together to form the steel cage.

3.2.2 Materials

3.2.2.1 Concrete

To reflect the likely condition in strengthening works where the concrete compressive strength is low, the concrete cylinder compressive strength at 28 days was targeted at 30 MPa. Several trial mixes were carried out and a mix proportion of 1: 2.18: 2.62: 0.69 by weight of Ordinary Portland Cement, natural sand, crushed granite of a maximum size of 10 mm and water was adopted. The corresponding weights of cement, fine aggregate, coarse aggregate, and water were 343, 748, 898 and 240 kg/m^3. The main properties of the concrete are shown in **Table 3.2**.

The short tie specimens were cast in two batches, the first batch for Specimens T0 and T10a, and the second batch for the other six specimens. The long tie specimens were cast in three batches, the first batch for Specimens LT00, LT10 and LT20, the second batch for Specimens LT01, LT02 and LT11, and the third batch for Specimen LT22. For each batch, six concrete cylinders (100 mm diameter × 200 mm height) and six concrete cubes (100 mm in side dimension) were cast for the determination of the concrete strength on the day of specimen test.

3.2.2.2 Internal steel reinforcement

Reinforcement details of the specimens are shown in **Figure 3.2**. Two types of steel reinforcements were used: (1) 12-mm diameter deformed steel bars as longitudinal steel reinforcement; and (2) 6-mm mild diameter steel links as transverse reinforcement at the ends of the specimens. Tensile tests were carried out on three samples for each type of steel bars. The mechanical properties of the steel bars are shown in **Table 3.3**. The longitudinal steel bars had an average yield strength of 570 MPa. The yield strength of transverse steel bars was about 583 MPa. The moduli of elasticity for the two types of reinforcements were 201.1 GPa and 208.7 GPa respectively.

3.2.2.3 FRP materials

The mechanical properties of the carbon FRP sheets, carbon FRP rods according to the supplier's specifications are shown in **Table 3.4**. The material properties of the carbon FRP were provided by the carbon FRP manufacturers and the key parameters of carbon FRP were verified by the test of carbon FRP coupons. The unidirectional carbon FRP sheets had a thickness of 0.176 mm with a weight of 330 g/m^2, and had a specified tensile strength of 3800 MPa, a tensile elastic modulus of 240 GPa and an ultimate elongation to rupture of 1.55 percent. A 3-part resin was used to install the carbon FRP sheets. The carbon FRP rods were 10 mm by 1.4 mm in cross-section, and had a specified tensile strength of 1000 MPa at 0.6% strain, elastic modulus of 165 GPa and ultimate elongation of 0.8 to 1.0 percent. They were inserted into slots approximately 5 mm wide and 15 mm deep, which were then filled with epoxy adhesive.

3.2.3 Specimen preparation

Six steel moulds were used to cast the short tie specimens (Series T). Three wooden moulds were fabricated for the casting of long tie specimens (Series LT). The steel bars were first cut and bent. The steel reinforcement cages for the specimens were then assembled with the bars held in position by short transverse bars of 6 mm diameter and welded together. Before casting, two 10 mm strain gauges (Type FLA-10-11) were fixed on the longitudinal bars for the measurement of longitudinal strains and were water-proofed using silicone. Lead wires were soldered to the gauges and guided along the steel bar out to the exposed top of the formwork. After the moulds were oiled, the steel reinforcement cages were placed inside. Then concrete were mixed and placed in the moulds. The specimens were cast in five batches with accompanying cubes and cylinders as described earlier for determining the concrete strengths at the time of specimen testing. The formwork was removed after one day, and the specimens were then covered with damp gunny sacks for a week. Thereafter, they were left in the laboratory under ambient conditions. The accompanying cubes and cylinders were cast and cured in the same manner. All test specimens were white washed before the test in order to trace the crack patterns.

3.2.4 Installation of FRP strengthening systems

The FRP strengthening schemes are shown in **Figure 3.3**. The FRP strengthening systems were applied on fully cured, surface-dry specimens. The specimens were cured for more than 28 days before FRP strengthening so that full strength of concrete could be developed.

3.2.4.1 Externally bonded carbon FRP sheets

A three-part resin was used to bond the FRP sheets on to the concrete. The sheets were cut to the required length and width using an ordinary cutting blade. The concrete surface was ground to remove dust, grease, disintegrated materials, loose particles and other bond inhibiting materials before the sheets were bonded to the specimens. The resin was applied on the required surface using a roller, followed by application of the resin-coated carbon FRP sheets. To ensure proper bonding, an aluminum roller was used to press the carbon FRP sheets down. The procedure was repeated for each ply of carbon FRP sheets.

3.2.4.2 Near-surface-mounted carbon FRP rods

The FRP flat rods were installed into slots on both faces of tie members. A concrete saw was first used to cut slots approximately 5 mm wide and 15 mm deep into the concrete substrate. The slots were filled with the epoxy adhesive, and the FRP rods were placed into the slots.

3.2.5 Test setup

Figure 3.4 shows the typical locations of strain gauges placed on the specimens. To measure steel strains, 10 mm FLA-10-11 strain gauges were installed on to the reinforcing bars. Proper installation and surface preparation of the steel bars ensured effective strain measurement. First, the ribs of deformed bars were ground away until a smooth surface was achieved. It is important not to reduce the bar diameter during the grinding process. Next, strain gauges and terminals were installed on the ground surface using an adhesive. Wires were soldered to the gauges for connection to the data logger. After checking the strain gauges for proper functioning using the strain meter, the strain gauges were protected with a thick layer of silicone, which was then left to harden for at least one day before casting of concrete. Also, 30 mm PFL-30-11 strain gauges were used to measure the concrete strain distribution on the surface of the specimens during the test. They were attached onto the concrete surface using adhesive. The concrete surface was cleaned using acetone solution for better bonding between the gauges and the concrete surface. In addition, 10mm PFL-10-11 strain gauges were used to measure the strain distribution in the carbon FRP sheets and rods. The sides of specimen were white washed so that cracks could be spotted easily.

Figure 3.5 shows the test set-up. Two Linear Variable Differential Transducers (LVDTs) of 100 mm range were mounted on the concrete surface in the longitudinal direction to measure the longitudinal elongation of the test zone. They were placed one each at the front and back of the specimen.

3.2.6 Test procedure

All specimens were tested under monotonically increasing axial tension load. Tests were conducted using the universal servo-hydraulic closed-loop testing machine with a calibrated 500 kN load cell, as shown in **Figure 3.5**. Strain gauges and transducers were connected to the TML TDS-302 data logger and data were recorded automatically.

The specimens were gripped and leveling of the specimen was carried out using a spirit level. Following the fixing of specimens, the specimen was subjected to about 1 kN tensile force which was about the self-weight of the specimen. Adjustments were then made until eccentricity with the grips was minimized as indicated by the LVDTs and strain gauge readings.

The load was applied monotonically in small increments to eliminate the potential effects of sudden loading. The initial load was applied at a rate of 0.10 mm/min. After yielding of the internal steel bar, the loading rate was increased to 0.3 mm/min and kept constant up to failure of the specimen. The loads, displacements and strain readings were read using an automatic data logger unit (TML TDS-302). Cracks were monitored and traced out. Crack widths were also measured using a hand-held microscope. The load at which cracks appeared was recorded.

3.3 Test results and discussion

The concrete strengths at the time of testing the specimens are shown in **Table 3.2**. The cylinder compressive strength varied from 26.2 MPa to 40.9 MPa with an average of

33.9 MPa, whereas the cube compressive strength varied from 30.2 MPa to 46.8 MPa with an average of 40.6 MPa. The test results are summarized in **Table 3.5**. The failure was defined as the sudden and excessive loss of load bearing capacity of the test specimen. Specimens LT02 and LT10 were subjected to accidental eccentricity during loading, leading to unreliable test results which were therefore not shown here.

3.3.1 Overall behavior and failure modes

Figure 3.6 shows the appearance of the test specimens after they were tested to failure. Tension cracks inevitably happened at the neck of the short tie specimens, which connected the enlarged, steel reinforced end.

3.3.1.1 Un-strengthened specimens

The overall behavior of the un-strengthened specimens (T00 and LT00) was similar. First, horizontal cracks were observed in the short specimen near the mid-length section (about 50 mm away from the mid-length) at around 13 kN (see **Figure 3.6a**). For the long specimens, horizontal cracks were first observed at the "neck" section which was 200 mm away from the end face at around 21 kN (see **Figures 3.2b** and **3.6b**). Then, cracks started to appear within the test zone with increasing load. The elongation of specimen was small before yielding of the steel bar. When the steel bar yielded, the cracks near the mid-length section started to widen extensively and the elongation increased quickly. After that, the load increased slowly to the peak load which was maintained with further elongation.

3.3.1.2 EB-FRP strengthened specimens

The behavior of all EB-FRP strengthened specimens (T10a, T10b, T20 and LT20) was similar to un-strengthened specimens at the early stage of loading. First, one or two horizontal cracks appeared at the neck and middle sections and a very small elongation of the specimens was observed. Upon further loading, noises related to the cracking of concrete and stretching of the carbon FRP sheets could be heard. With further increase in tensile load, the cracks began to widen and the elongation of specimens increased. The yielding of longitudinal steel bar was observed from the strain reading. The loading ended with sudden de-bonding in most specimens or rupture of carbon FRP sheets in Specimen LT20, upon which the load would drop steeply to the yield capacity of the internal steel bar (about 70~80 kN). After that, the tensile cracks widened extensively.

3.3.1.3 NSM-FRP strengthened specimens

For specimens strengthened by NSM-FRP rods (T01, T02 and LT01), the increase in elongation and development of cracks were much slower than that of EB-FRP strengthened specimens and no cracking sound was heard during the test. The horizontal crack widths and longitudinal elongations of NSM-FRP strengthened specimens were quite small even near the ultimate load compared to EB-FRP strengthened specimens. An inclined crack (about 45 degree to the longitudinal axis) began to form from the transverse cracks at one end and propagated towards to the other end. For long tie specimen (LT01), no diagonal cracks occurred. The steel bar yielded simultaneously and the applied tensile load dropped to the yield load capacity of the internal steel bar. Finally, NSM-FRP strengthened specimens failed with total de-bonding of carbon FRP rods at one end of the specimens.

3.3.1.4 Specimens strengthened with both EB-FRP and NSM-FRP reinforcement

The behavior of Specimens T11, T22, LT11 and LT22 was a combination of those of EB-FRP strengthened and NSM-FRP strengthened specimens. That was, during the early loading stage, one or two horizontal cracks gradually appeared at the neck sections and only very small elongation was observed. The elongation increased with increasing load and the steel bar was observed to yield. The widths of the cracks and elongations of specimens were small even at high loads, due to the presence of FRP reinforcement. Failure occurred suddenly, due to simultaneously de-bonding and rupture of carbon FRP sheets was observed, except T22, where failure was due to de-bonding of the FRP sheet. The failure was quite brittle in nature and the cracks were observed to widen extensively, as shown in **Figures 3.6a** and **3.6b**.

3.3.2 Load-elongation relations

Figure 3.7 shows the relationships between the load and axial elongation for all test specimens.

It is evident that Specimens T00 and LT00 exhibited a bilinear behavior before failure. The first part of the curves was roughly linear up to the yield strength of steel bar. During this stage, the load would experience some small drops when cracks occurred at various locations. The second part of the curve continued with a lower stiffness until it reached the ultimate state. The load was then maintained at the peak level with an increase in elongation until failure occurred with a sudden drop in the applied load.

For all FRP strengthened specimens except for T10b, the curves show a similar load-elongation behavior till sudden failure occurred. The load-elongation relation was linear up to the ultimate load with almost the same stiffness as the un-strengthened specimen. When the specimens failed due to de-bonding or rupture of FRP reinforcement, the load dropped suddenly to between 70 and 80 kN which corresponded to the yield capacity of the steel bar. The loads were maintained at this load level with increasing elongation. Finally, the loads dropped steeply when the specimens totally failed.

3.3.3 Effect strain at ultimate

The failure strains in FRP reinforcement are shown in **Figure 3.8** and **Table 3.6**. All FRP strengthened tie specimens failed at about the same strain level of approximately $3000\text{-}4000\times10^{-6}$ mm/mm. For short specimens, the failure strains varied from 2400×10^{-6} mm/mm to 6300×10^{-6} mm/mm with an average of 4900×10^{-6} mm/mm, whereas the failure strains of long specimens varied from 2800×10^{-6} mm/mm to 3500×10^{-6} mm/mm with an average of 3200×10^{-6} mm/mm. Based on the test observation, the effective tensile strain was therefore in the order of 3000×10^{-6} mm/mm to 5000×10^{-6} mm/mm. Following ACI 440 (2008)'s recommendation, to ensure integrity of the confined concrete, the effective FRP strain at failure can therefore be taken as: $\varepsilon_{eff} = 0.004 \leq 0.75\varepsilon_{FRP,ru}$, where $\varepsilon_{FRP,ru}$ is the rupture strain of FRP reinforcement.

3.3.4 Effect of FRP systems

As shown in **Figure 3.9** and **Tables 3.5**, compared to the un-strengthened specimens, the ultimate load capacity of the strengthened specimens was increased by 15.7% in Specimen LT01 to 98.50% in Specimen T22 due to the FRP strengthening systems.

The ultimate load of Specimens T10a, T10b and T20, which were strengthened by EB-FRP sheets only, was about 23-25% higher compared to the un-strengthened specimen (T00). Whereas, the failure load of long tie specimens (LT20) was 24.6% higher compared to the un-strengthened specimen (LT00). Due to the de-bonding of carbon FRP sheets and rods, the high tensile strength of FRP reinforcement was not fully utilized.

For Specimens T01, T02 and LT01, strengthened with NSM-FRP rods only, the ultimate load increase was 30-43% which was higher than that of EB-FRP strengthened specimens. Moreover, at service load level, Specimens T01, T02 and LT01 exhibited lower elongations and smaller crack widths compared to Specimens T10a, T10b, T20 and LT20.

For specimens provided with both EB-FRP and NSM-FRP reinforcement (T11, T22 LT11 and LT22), the ultimate load increased by as much as 73%~98.5%. The key factor affecting the strengthening effectiveness was the cracking of concrete. The cracks would impair the bond between concrete and FRP reinforcement severely, causing de-bonding of FRP reinforcement. The NSM-FRP rods could led to a slow growth of the cracks and reduce the crack widths effectively, therefore the de-bonding of FRP could be delayed. Thus the tensile strength of the carbon FRP sheets and rods can be utilized better and a better strengthening effectiveness can be achieved in specimens with both EB-FRP sheets and NSM-FRP rods.

3.3.5 Comparison with theoretical analysis

The axial tensile capacity of the specimen was evaluated using the principles of equilibrium and compatibility, as shown in **Figure 3.10**. This calculation considered the partial contribution of concrete (before cracking), tensile steel bar, carbon FRP sheets and carbon FRP rods. The strain in the concrete and FRP reinforcement was taken equal to the strain of the steel reinforcement at the same level. The tensile strength of concrete was ignored after cracking. EB-FRP sheets and NSM-FRP rods were modeled as elastic materials, and steel reinforcing bars were modeled as an elastic-plastic material. As shown in **Figure 3.11**, P-ε relations are given as:

1. Before cracking of concrete ($0 < \varepsilon \le \varepsilon_{ct}$)

$$P = \left(E_s A_s + E_c A_c + 2nE_{FRP,s} t_{FRP.s} w_{FRP,s} + 2mE_{FRP,r} A_{FRP,r} \right) \varepsilon \qquad (3.1)$$

2. After cracking of concrete, and before yielding of steel bar ($\varepsilon_{ct} < \varepsilon \le \varepsilon_y$)

$$P = \left(E_s A_s + 2nE_{FRP,s} t_{FRP.s} w_{FRP,s} + 2mE_{FRP,r} A_{FRP,r} \right) \varepsilon \qquad (3.2)$$

3. After yielding of steel bar, and before de-bonding or rupture of FRP sheets or rods ($\varepsilon_y < \varepsilon \le \varepsilon_{eff} = 0.004$)

$$P = f_y A_s + \left(2nE_{FRP,s} t_{FRP.s} w_{FRP,s} + 2mE_{FRP,r} A_{FRP,r}\right)\varepsilon \qquad (3.3)$$

4. After de-bonding or rupture of FRP sheets, ($\varepsilon_{eff} < \varepsilon \le \varepsilon_{s,ru}$)

$$P = f_y A_s \qquad (3.4)$$

where P is the applied tensile load of the tie member; E_s and A_s are the elastic modulus and cross-sectional area of steel reinforcements, respectively; E_c is the elastic modulus of concrete; A_c is the cross-sectional area of tie specimen; n is the number of ply of FRP sheets per side; m is the number of longitudinal FRP rods per side; $t_{FRP,s}$ is the thickness of one layer FRP sheets; $w_{FRP,s}$ is the width of FRP sheets; $E_{FRP,s}$ is the elastic modulus of FRP sheets; $E_{FRP,r}$ is the elastic modulus of FRP rods; $A_{FRP,r}$ is the cross-sectional area of a FRP rods, ε is the strain; ε_{ct} is the ultimate tensile strain of concrete; ε_y is the yield strain of steel bar; ε_{eff} is the effective strain of FRP reinforcement at failure, which is taken as 0.004; and $\varepsilon_{s,ru}$ is the rupture strain of the steel bar.

Figure 3.12 compares the experimental load-strain curves and theoretical load-strain curves. The theoretical curves show a good prediction of the overall load-tensile strain response for both control specimens and FRP-strengthened specimens. However, all the theoretical load-strain curves overestimated the ultimate load capacity of specimens and the theoretical curves were stiffer than the experimental load-strain curves due to the ideal assumption that the bond between concrete and FRP was perfect.

Based on the above analysis, the ultimate load capacity, P_u, of FRP strengthened tie members can be taken by:

$$P_u = f_y A_s + \left(2nE_{FRP,s}t_{FRP.s}w_{FRP,s} + 2mE_{FRP,r}A_{FRP,r}\right)\varepsilon_{eff} \tag{3.5}$$

The ultimate load capacities of FRP strengthened tie member were calculated using the effective strain of 0.004 based on the findings in Section 3.3.3. The predicted ultimate loads of FRP-strengthened struts are compared with the observed failure loads in **Table 3.6** and **Figure 3.13**. The observed ultimate load carrying capacity of FRP strengthened tie members was found to be within 20 percent of the design value. The mean and standard deviation values of the ratio of $P_{u,Test}/P_{u,Pred}$ of the 11 specimens were 0.90 and 0.12 respectively, showing good agreement between the predicted failure load and observed failure load. In general, the predicted failure loads were higher than the observed failure loads.

3.3.6 Effect of reinforcement index and parameter

From **Equation 3.5**, the normalized ultimate tensile load capacity can be obtained by dividing by bhf_c'; that is,

$$\begin{aligned}\frac{P_u}{bhf_c'} &= \frac{f_y A_s}{bhf_c'} + \frac{2nt_{FRP,s}w_{FRP,s}}{bh}\cdot\frac{E_{FRP,s}\varepsilon_{eff}}{f_c'} + \frac{2mA_{FRP,r}}{bh}\cdot\frac{E_{FRP,r}\varepsilon_{eff}}{f_c'} \\ &= \chi_s + \omega_{FRP,s}\cdot\varepsilon_{eff} + \omega_{FRP,r}\cdot\varepsilon_{eff} = \chi_s + \chi_{FRP} = \chi_s + \omega_{FRP}\cdot\varepsilon_{eff}\end{aligned} \tag{3.6}$$

$$\frac{P_u}{bhf_c'} - \chi_s = \chi_{FRP} = \left(\omega_{FRP,s} + \omega_{FRP,r}\right)\cdot\varepsilon_{eff} = \omega_{FRP}\cdot\varepsilon_{eff} \tag{3.7}$$

where *b* is the width of the tie member, *h* is the height of the tie member and *f'ₖ* is the cylinder compression strength of concrete. In addition, $\chi_s = \dfrac{f_y A_s}{bhf_c'}$ is defined as the longitudinal reinforcement index of the steel bar, $\chi_{FRP} = \omega_{FRP} \cdot \varepsilon_{eff}$ is defined as the longitudinal reinforcement index of the FRP reinforcement, $\omega_{FRP} = \omega_{FRP,s} + \omega_{FRP,r}$ is defined as the longitudinal reinforcement parameter of FRP reinforcement, where $\omega_{FRP,s} = \dfrac{2nt_{FRP,s}w_{FRP,s}}{bh} \cdot \dfrac{E_{FRP,s}}{f_c'}$ and $\omega_{FRP,r} = \dfrac{2mA_{FRP,r}}{bh} \cdot \dfrac{E_{FRP,r}}{f_c'}$. Also, ε_{eff} is the effective strain of FRP reinforcement at failure.

The relationship between the ultimate tensile load and FRP reinforcement parameter is shown in **Figure 3.14**. **Figure 3.14** presents that the gain in the ultimate load resulting from carbon FRP reinforcement was proportional to the reinforcement parameter which shows a linear relationship between the ultimate tension strength and the reinforcement parameter. To sum all the results up, similar conclusion could be drawn. The following equation could be derived to model this relationship:

For short tie specimens,

$$\frac{P_u}{bhf_c'} - \chi_s = \chi_{FRP} = 0.0035\omega_{FRP} \tag{3.8}$$

For long tie specimens,

$$\frac{P_u}{bhf_c'} - \chi_s = \chi_{FRP} = 0.0030\omega_{FRP} \tag{3.9}$$

For all tie specimens,

$$\frac{P_u}{bhf_c'} - \chi_s = \chi_{FRP} = 0.0033\omega_{FRP} \tag{3.10}$$

Based on these equations, the effective strain in the FRP reinforcement ε_{eff} would be 0.0033.

3.4 Summary

In an attempt to study the behavior of tie members strengthened with FRP systems under axial tensile loading and check the effectiveness of different FRP strengthening strategy, eight short tie specimens and seven long tie specimens were fabricated and tested to failure. The effect of FRP strengthening systems and reinforcement parameter was investigated and discussed. The following conclusions may be drawn from this study carried out:

(a) The ultimate tensile load capacity was substantially increased. Failure of the FRP-strengthened tie specimens was sudden and non-ductile due to de-bonding and rupture of FRP reinforcement.

(b) The strengthening effectiveness of NSM-FRP rods was better than EB-FRP sheets while the most effective FRP strengthening system consisted of a combination of NSM-FRP rods and EB-FRP sheets.

(c) The effective strain in the FRP reinforcement was found to be about 0.003 to 0.005.

(d) The theoretical load-strain curves based on de-bonding of FRP reinforcement matched the test results well, although the axial stiffness was higher than observed due to the assumption that the bond of concrete and FRP was perfect.

(e) The gain in the ultimate load due to FRP strengthening systems was proportional to the FRP reinforcement parameter.

Table 3.1: Design parameters of specimens

Series	**Specimens**	**Parameters**			
		f'_c(MPa)	**EB-FRP sheets/side**	**NSM-FRP rods/side**	**Remarks**
T	T00	30.4	0	0	Control specimen
	T10a	30.4	1	0	1 layer CFRP sheet on each side
	T10b	26.2	1	0	1 layer CFRP sheet on each side
	T20	26.2	2	0	2 layers CFRP sheet on each side
	T01	26.2	0	1	1 CFRP rod on each side
	T02	26.2	0	2	2 CFRP rods on each side
	T11	26.2	1	1	1 layer CFRP sheet and 1 CFRP rod on each side
	T22	26.2	2	2	2 layers CFRP sheet and 2 CFRP rods on each side
LT	LT00	39.5	0	0	Control specimen
	LT10	39.5	1	0	1 layer CFRP sheet on each side
	LT20	39.5	2	0	2 layers CFRP sheet on each side
	LT01	40.9	0	1	1 CFRP rod on each side
	LT02	40.9	0	2	2 CFRP rods on each side
	LT11	40.9	1	1	1 layer CFRP sheet and 1 CFRP rod on each side
	LT22	32.4	2	2	2 layers CFRP sheet and 2 CFRP rods on each side

Note: Series T specimens measured 70 mm in height by 100 mm in width by 500 mm in length, and Series LT specimens measured 100 mm in height by 100 mm in width by 1200 mm in length.

Table 3.2: Main properties of concrete

Concrete batch	**Average cube compressive strength (MPa)**	**Average cylinder compressive strength (MPa)**	**Tensile strength (MPa)**	**Elastic modulus (GPa)**
C1 (T00, T10a)	40.3	30.3	2.38	30.7
C2 (T10b, T20,T01) (T02, T11, T22)	30.2	26.2	2.08	29.4
C3 (LT00, LT20)	43.9	39.5	2.99	33.2
C4 (LT01, LT11)	46.8	40.9	3.08	33.6
C5 (LT22)	41.6	32.4	2.52	31.3

Table 3.3: Main properties of reinforcing steel

Reinforcing bar	**Diameter, *d* (mm)**	**Cross-sectional area, A_s (mm^2)**	**Elastic modulus, E_s (GPa)**	**Yield strength, f_y**		**Ultimate strength, f_u**	
				MPa	**kN**	**MPa**	**kN**
Mild steel bar	6	28.3	208.7	583	16.5	671	19
Deformed steel bar	12	113	201.1	570	64.5	715.8	80.9

Table 3.4: Main properties of carbon FRP sheet and carbon FRP rod

Main properties	**Carbon FRP Sheet**	**Carbon FRP rod**	
Tensile strength (MPa)	3800	1000 (6‰)	1300(8‰)
Elastic modulus (GPa)	240	165	
Ultimate elongation	1.55%	8-10‰	
Design thickness (mm)	0.176	1.4	
Design width (mm)	70	10	

Table 3.5: Test results and failure modes

Specimens	**Cylinder compressive strength, *f'c* (MPa)**	**First cracking load (kN)**	**Ultimate load (kN)**	**Failure modes**	**Ultimate load increase (%)**
T00	30.3	13.3	70.7	Y	-
T10a	30.3	15.5	87.0	YD	+23.2%
T10b	26.2	11.5	85.1	YD	+20.4%
T20	26.2	13.5	88. 5	YD	+25.2%
T01	26.2	15.0	101.3	YD	+43.4%
T02	26.2	10.5	91.8	YD	+30.0%
T11	26.2	18.0	108.5	YR	+53.5%
T22	26.2	20.1	140.2	YD	+98.5%
LT00	39.5	21.0	83.5	Y	-
LT20	39.5	21.7	104.0	YR	+24.6%
LT01	40.9	24.2	96.6	YD	+15.7%
LT11	40.9	25.9	102.0	YR	+22.1%
LT22	32.4	24.1	145.1	YR	+73.0%

Y: yielding of steel bar;

YD: FRP de-bonding following steel yielding;

YR: FRP rupture following steel yielding.

Table 3.6: Reinforcement parameter of specimens

Series	**Specimens**	**Ultimate load (kN)**	**Theoretical ultimate load (kN)**	$P_{u,test}$ / $P_{u,Pred}$	**FRP strain at failure (mm/mm)**	**FRP reinforcement parameter**
T	T00	70.7	80	0.88	-	-
	T10a	87.0	93.8	0.93	0.0063	27.9
	T10b	85.1	93.8	0.91	0.0050	32.2
	T20	88.5	117.5	0.75	0.0024	64.5
	T01	101.3	88.7	1.14	0.0064	25.2
	T02	91.8	107.1	0.86	0.0051	50.4
	T11	108.5	112.3	0.97	0.0060	57.4
	T22	140.2	154.8	0.91	0.0036	114.9
LT	LT00	83.5	83.0	1.00	-	-
	LT20	104.0	138.2	0.75	0.0028	42.8
	LT01	96.6	89.1	1.08	0.0033	11.3
	LT11	102.0	122.8	0.83	0.0035	31.9
	LT22	145.1	175.1	0.83	0.0032	80.6

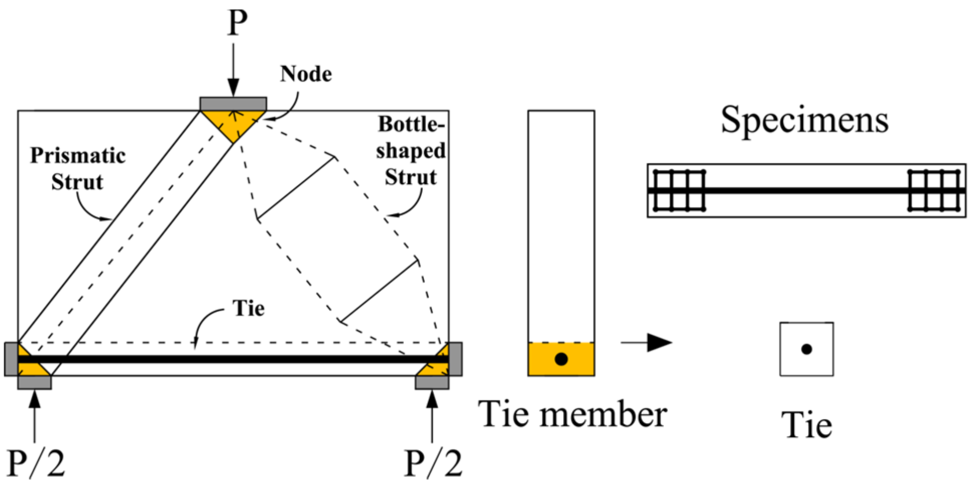

Figure 3.1: Idealization of tie member

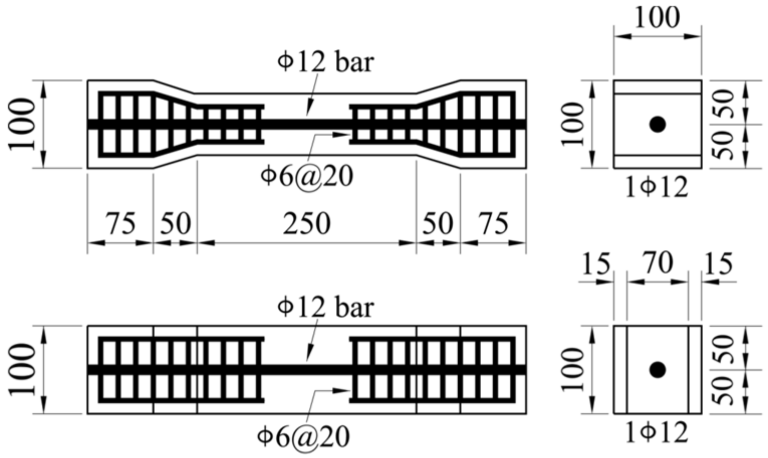

(a) Short tie specimens

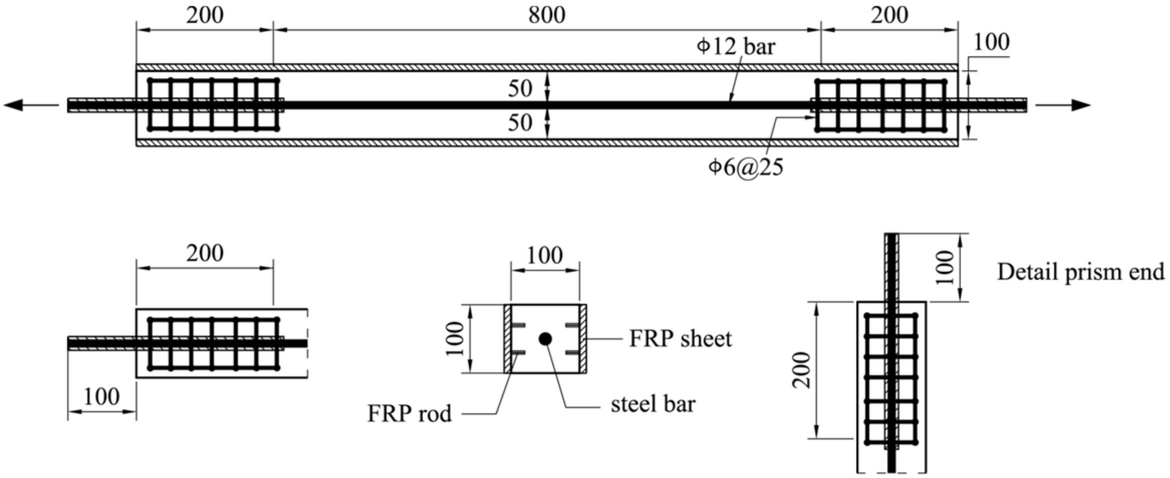

(b) Long tie specimens

Figure 3.2: Geometry and reinforcement details of test specimens (dimensions in mm)

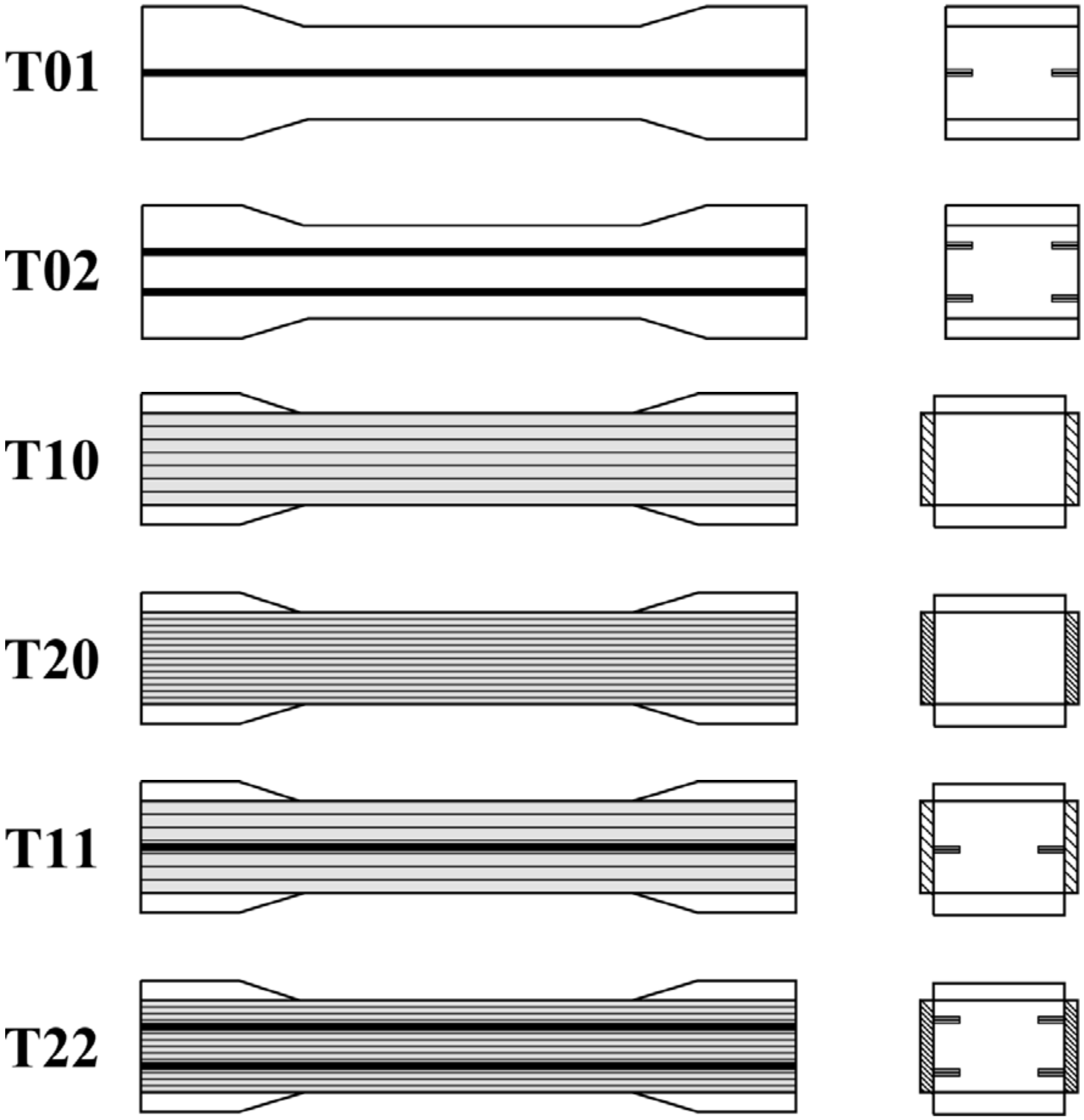

(a) Short tie specimens

Figure 3.3: FRP strengthening systems (cont.)

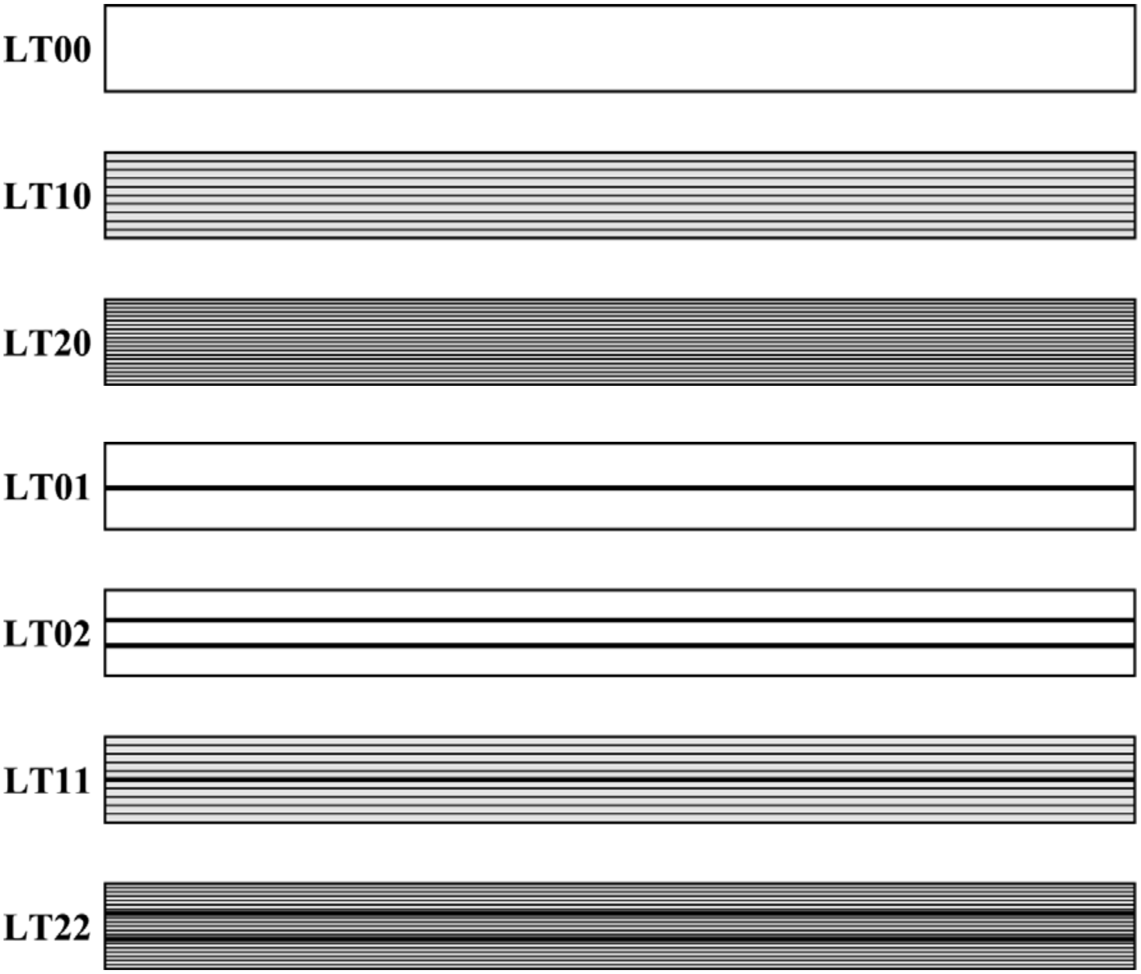

(b) Long tie specimens

Figure 3.3: FRP strengthening systems

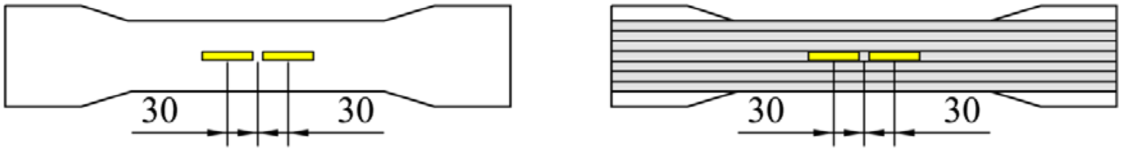

Concrete Surface

FRP sheet

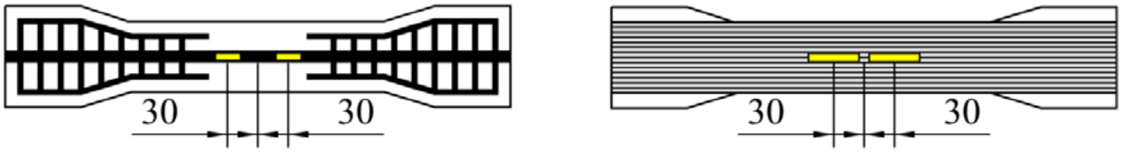

Steel bar

FRP sheets

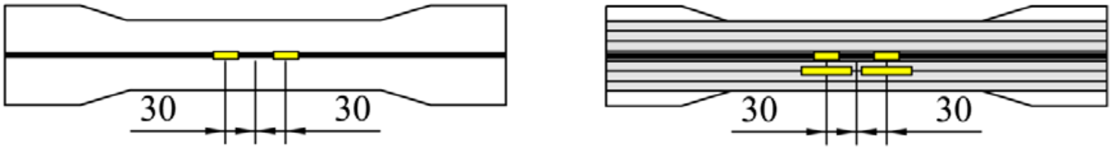

FRP rod

FRP sheets and rods

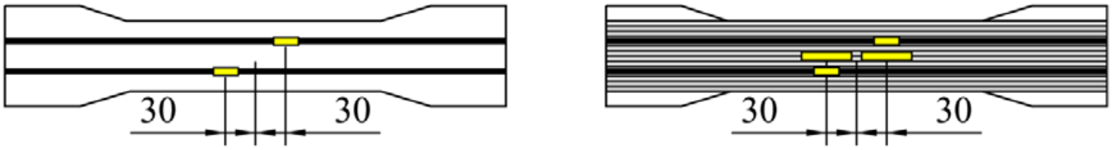

FRP rods

FRP sheets and rods

(a) Short tie specimens

Figure 3.4: Arrangement of strain gauges (cont.)

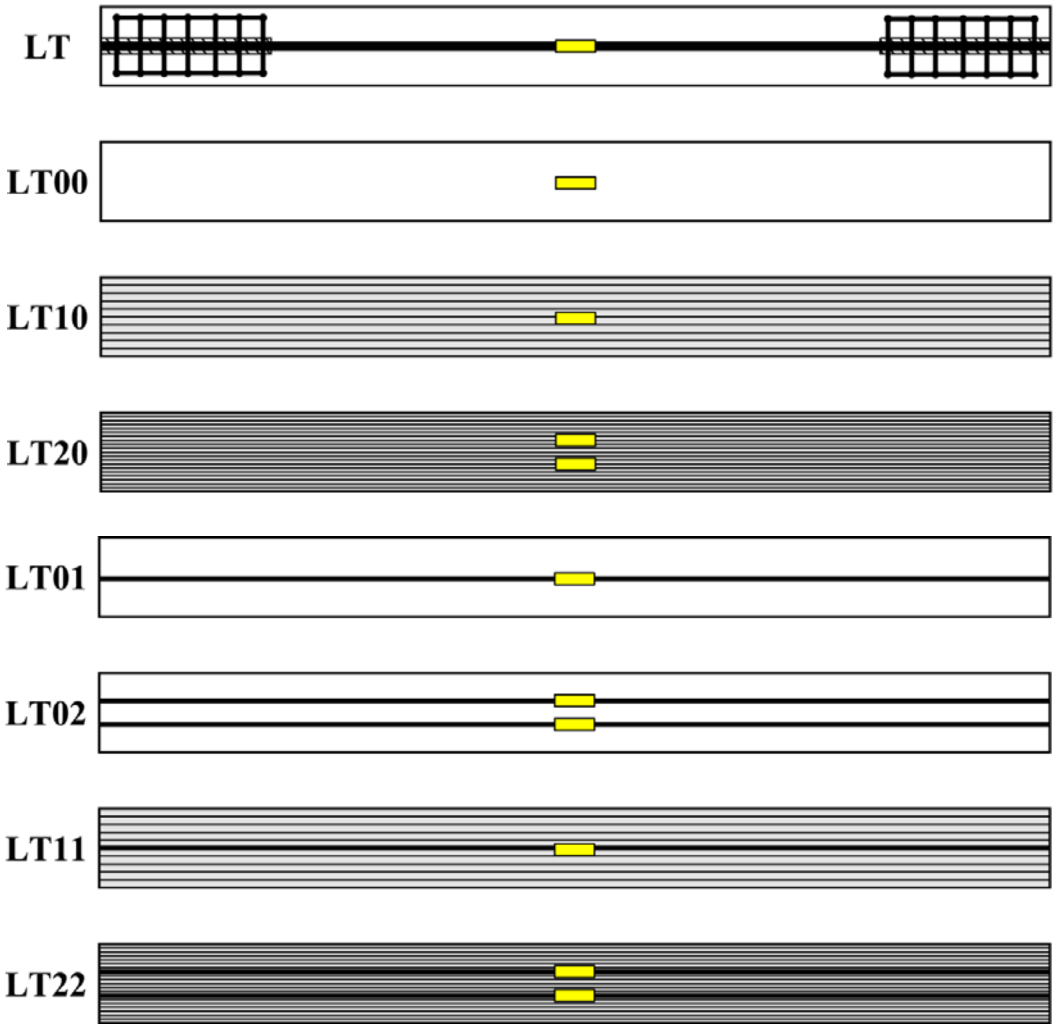

(b) Long tie specimens

Figure 3.4: Arrangement of strain gauges

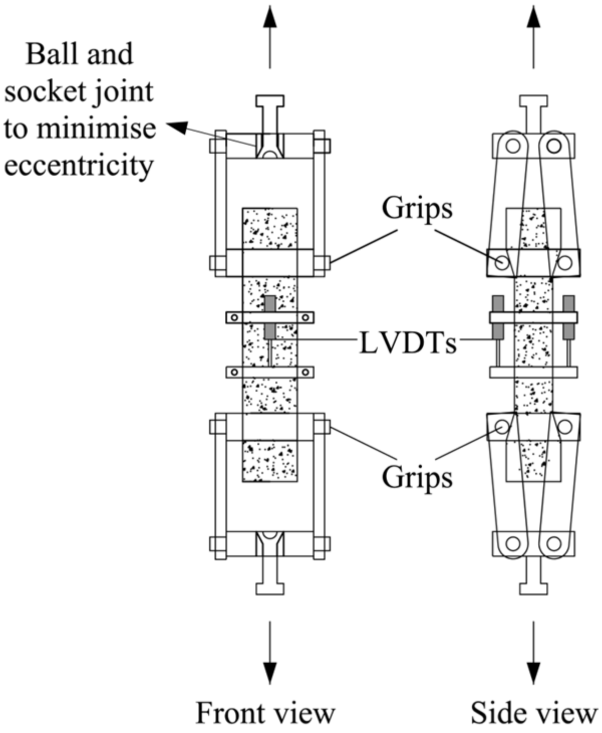

(a) Test setup for short tie specimen

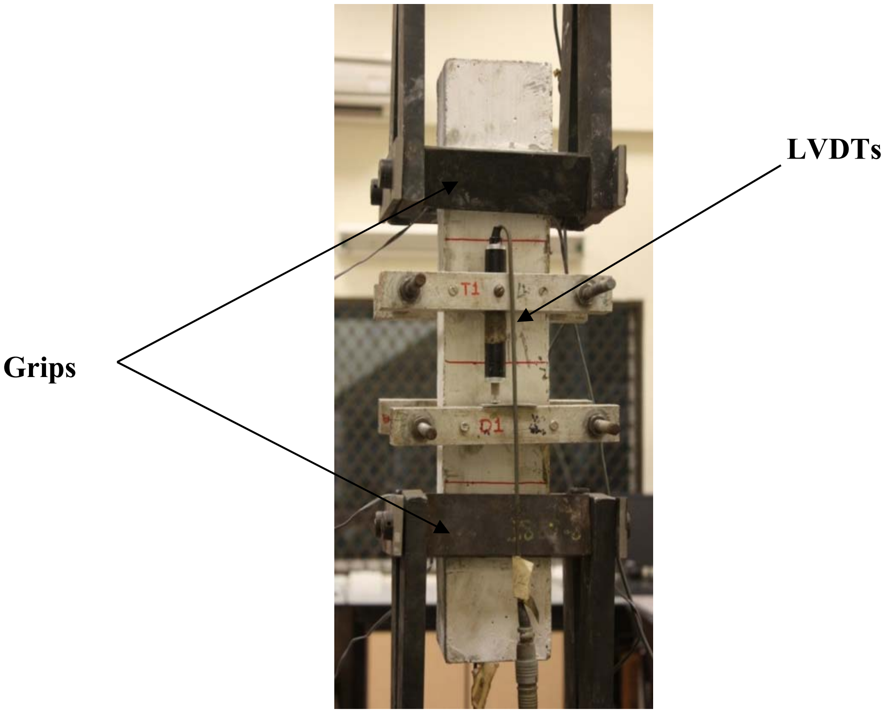

(b) Test setup for short tie specimens (front view)

Figure 3.5: Tension test set up (cont.)

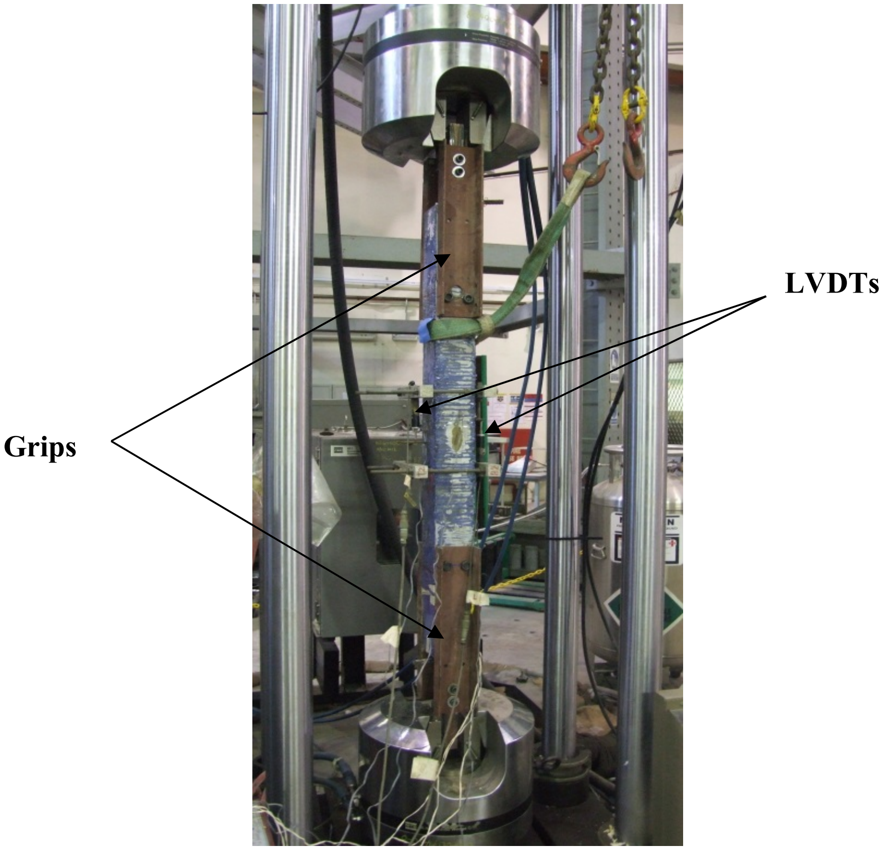

(c) Test setup for long tie specimens

Figure 3.5: Tension test set up

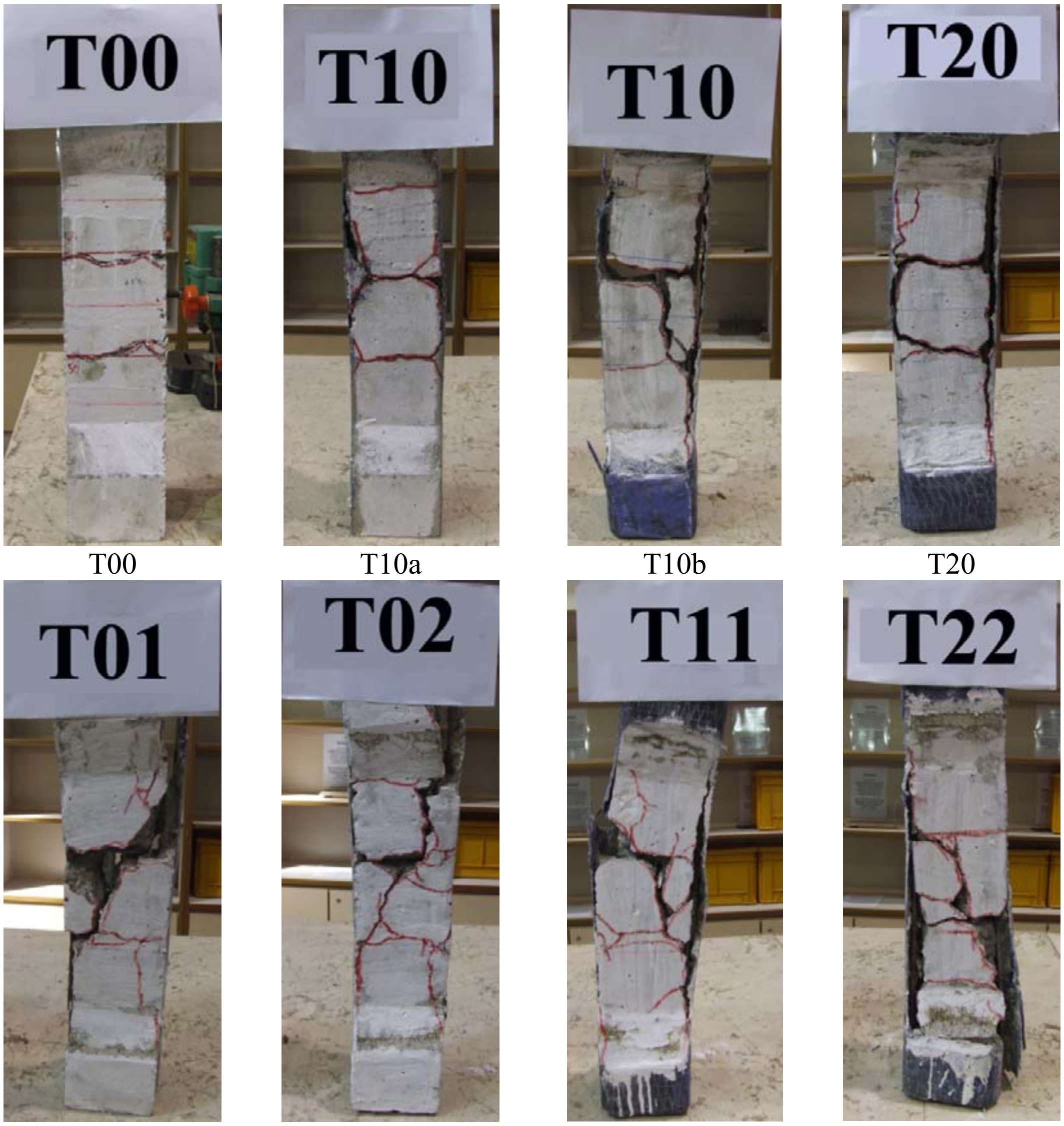

T00 T10a T10b T20

T01 T02 T11 T22

(a) Short tie specimens

Figure 3.6: Close-up views of specimens after failure (cont.)

LT00

LT01

LT20

LT11

LT22

(b) Long tie specimen

Figure 3.6: Close-up views of specimens after failure

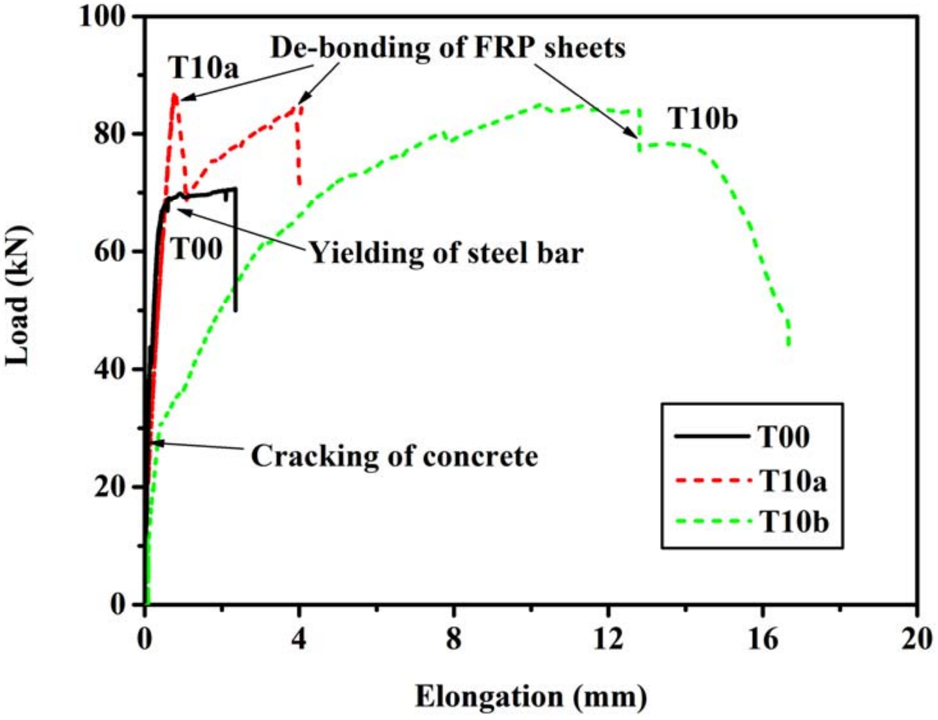

(a) Specimens T00, T10a, T10b

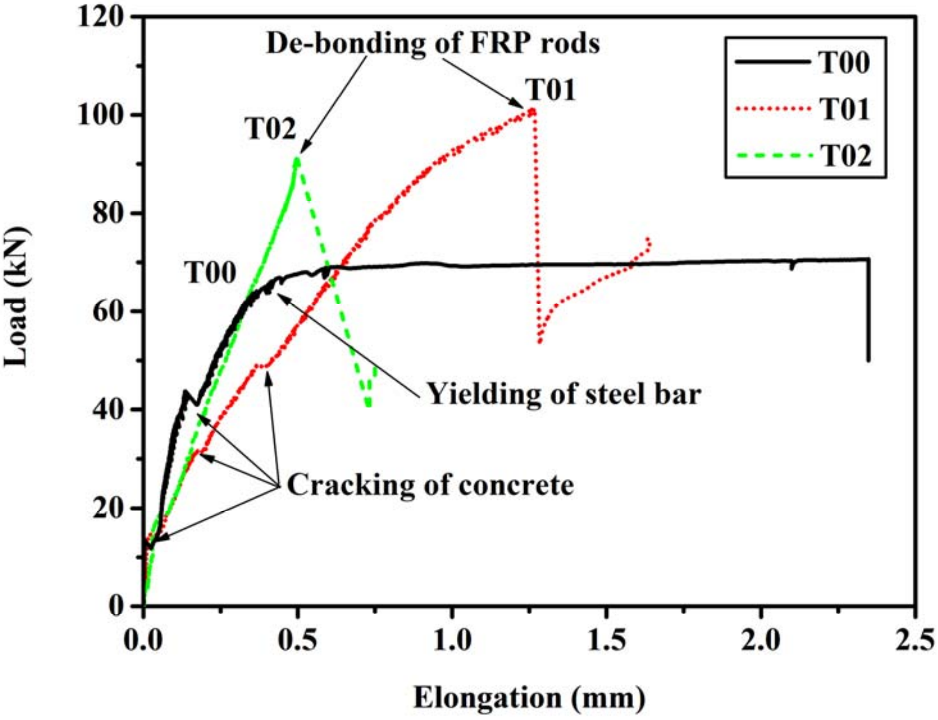

(b) Specimens T00, T01, T02

Figure 3.7: Load-elongation curves of specimens (cont.)

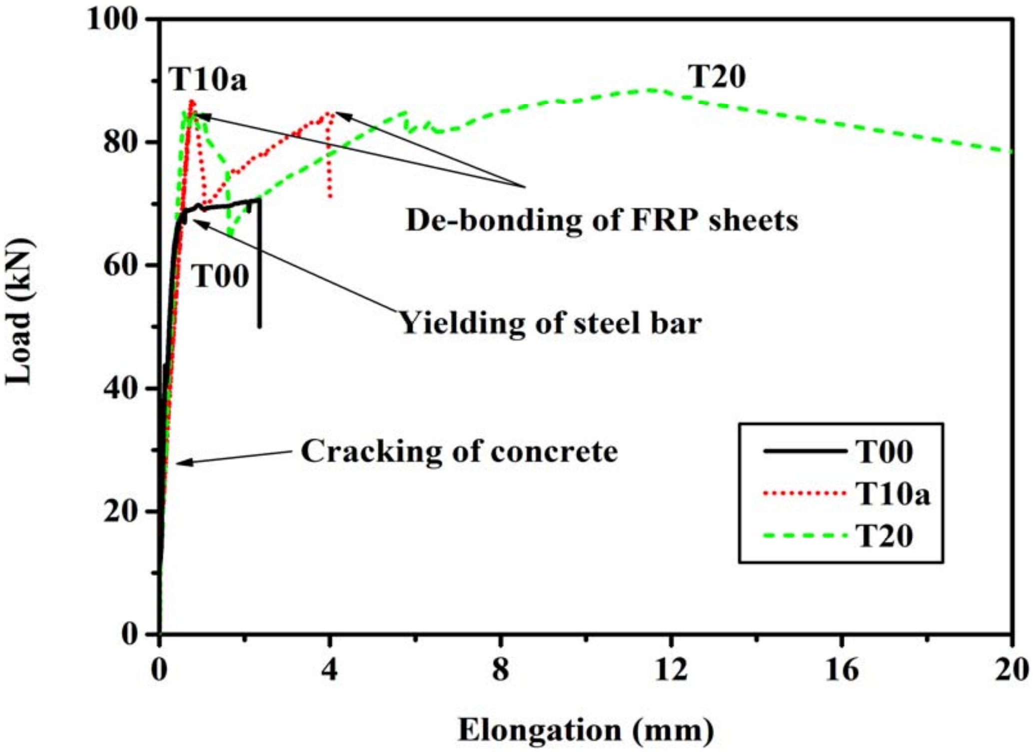

(c) Specimens T00, T10a, T20

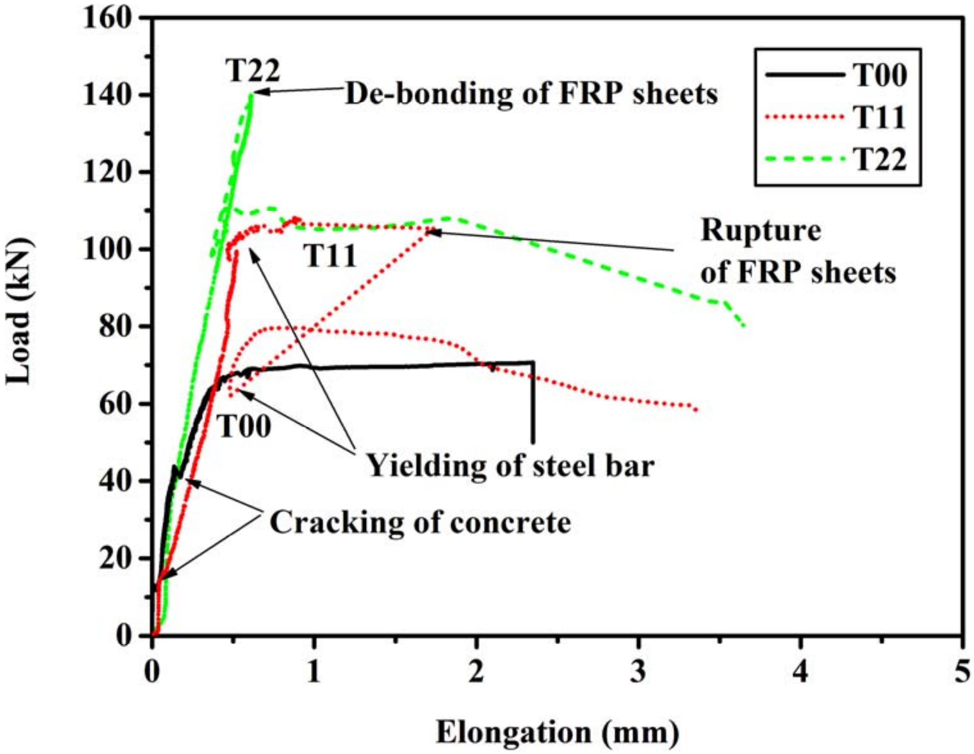

(d) Specimens T00, T11, T22

Figure 3.7: Load-elongation curves of specimens (cont.)

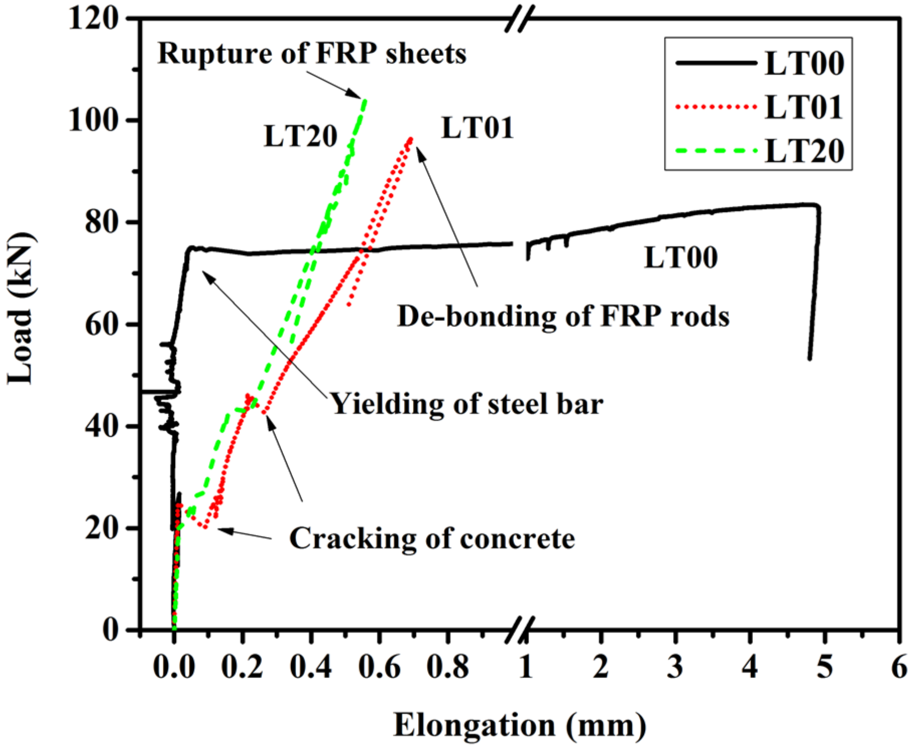

(e) Specimens LT00, LT01, LT20

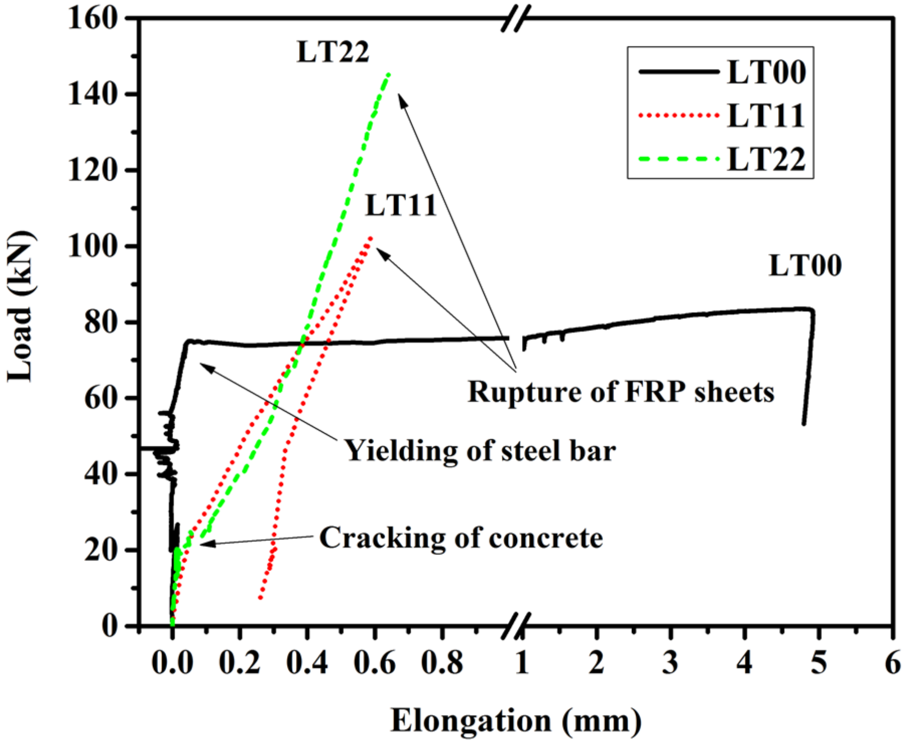

(f) Specimens LT00, LT11, LT22

Figure 3.7: Load-elongation curves of specimens

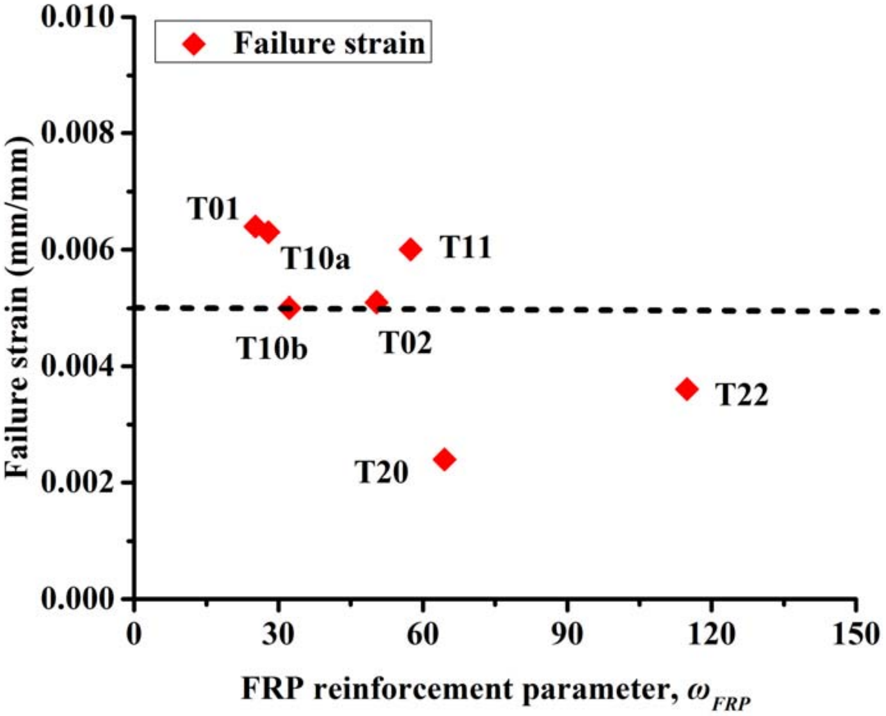

(a) Short tie specimens

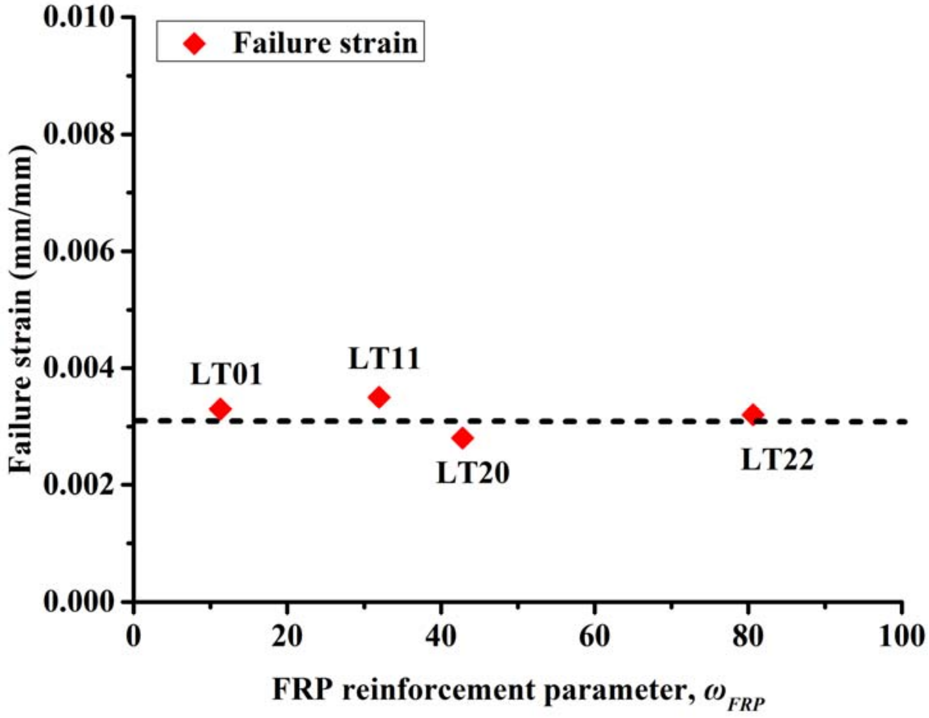

(b) Long tie specimens

Figure 3.8: Failure strains of FRP strengthened specimens

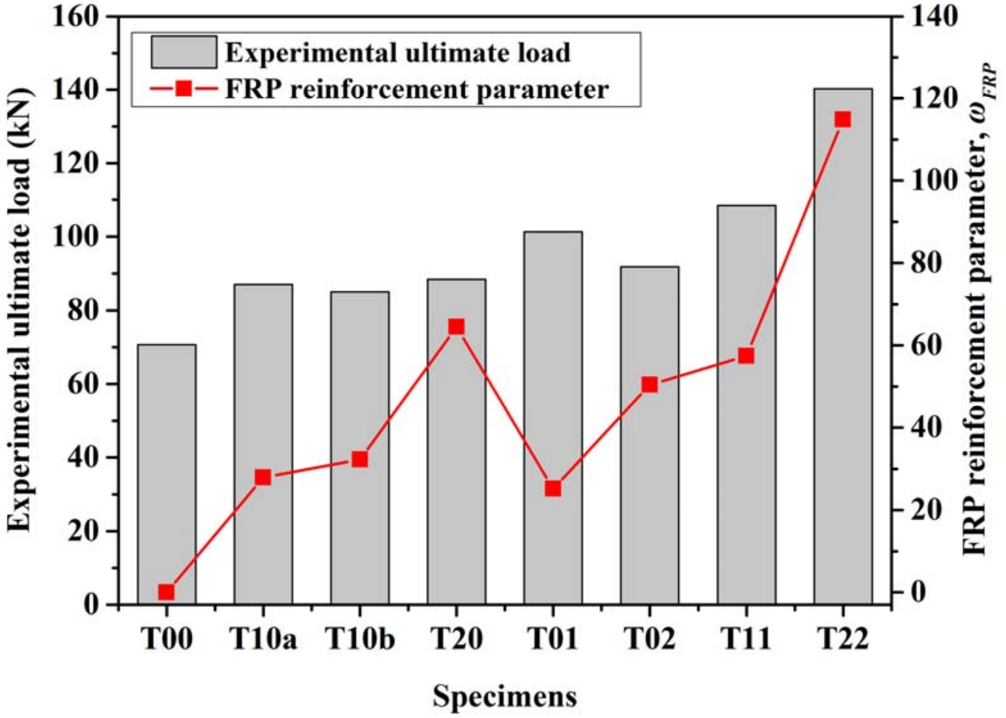

(a) Short tie specimens

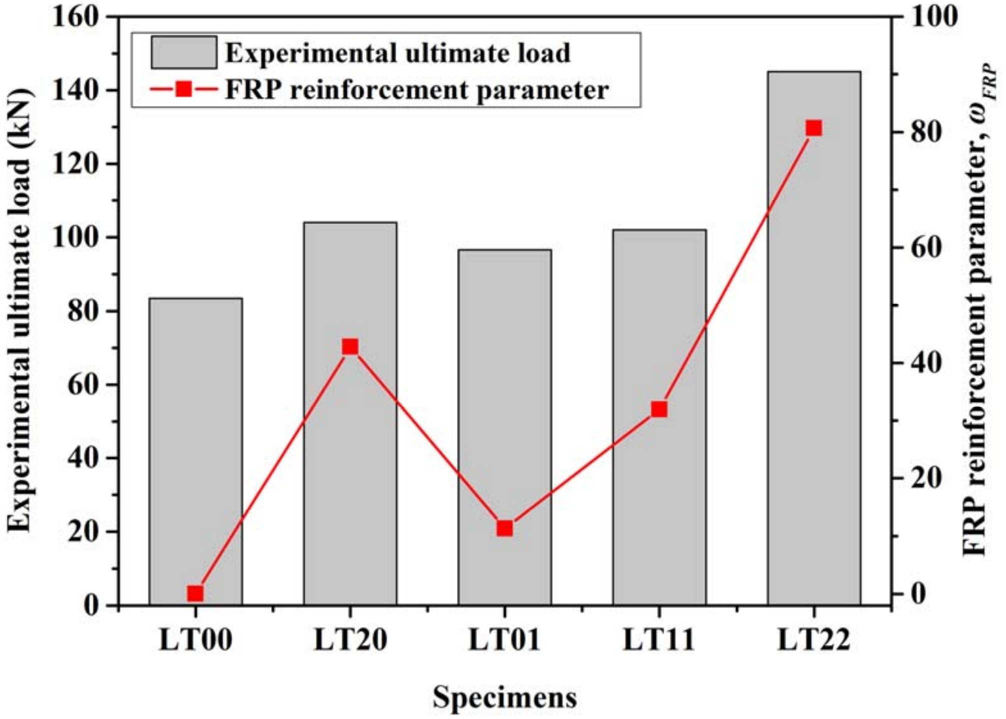

(b) Long tie specimens

Figure 3.9: Experimental ultimate load VS FRP reinforcement parameter

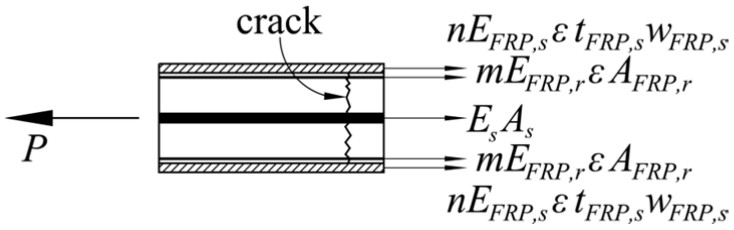

(a) Short tie specimens

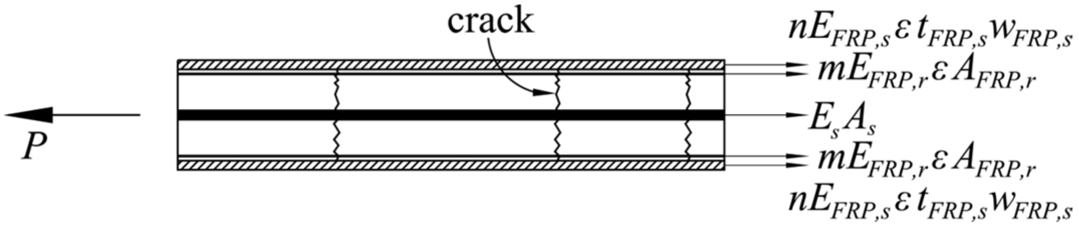

(b) Long tie specimens

Figure 3.10: Stress analysis

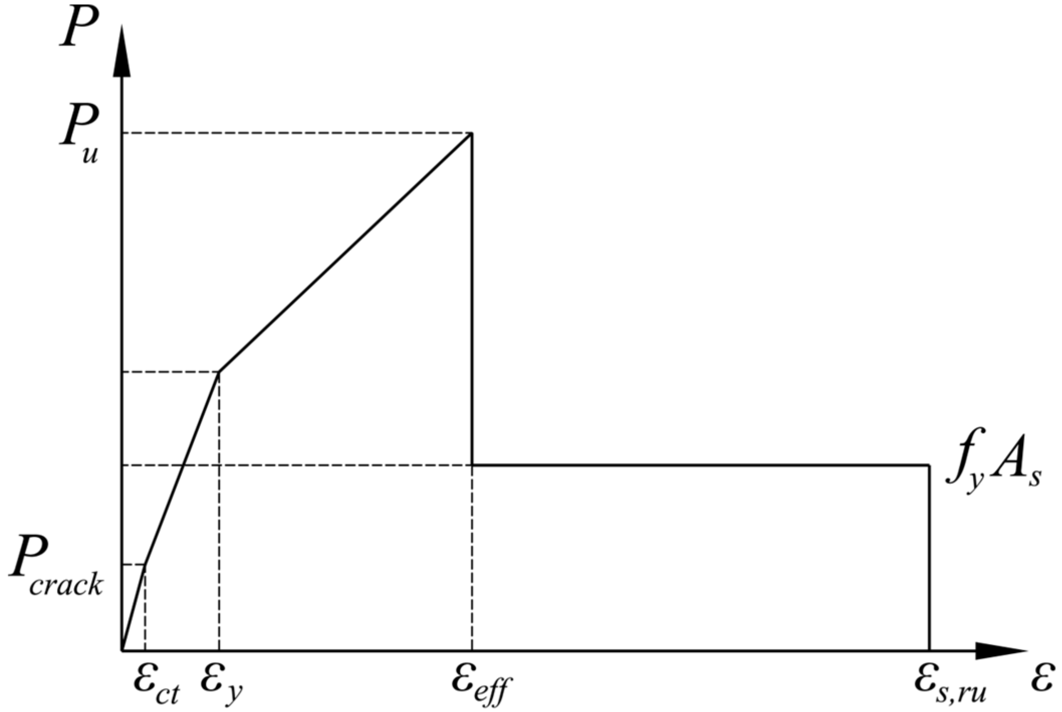

Figure 3.11: Theoretical load-strain curves

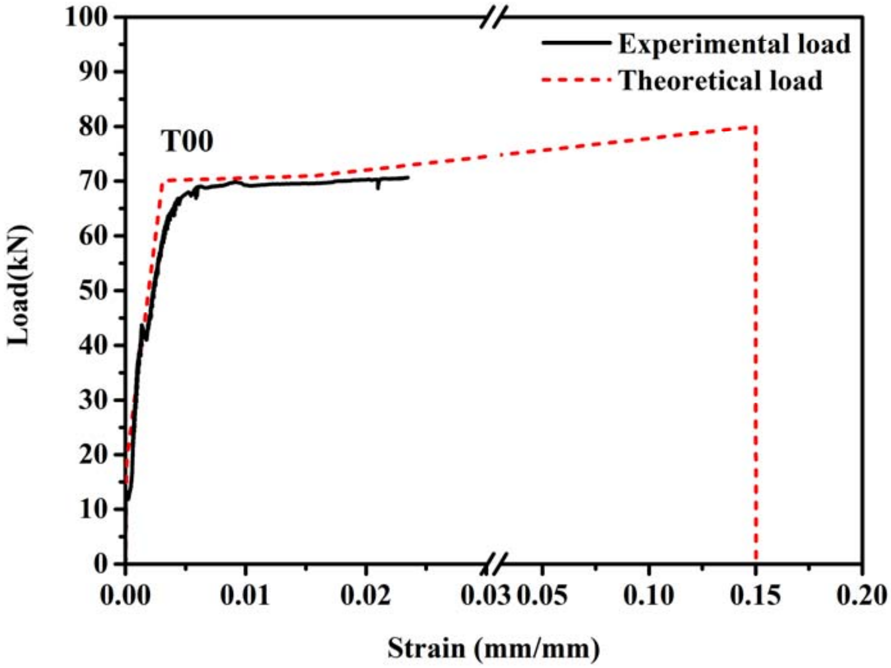

(a) Specimen T00

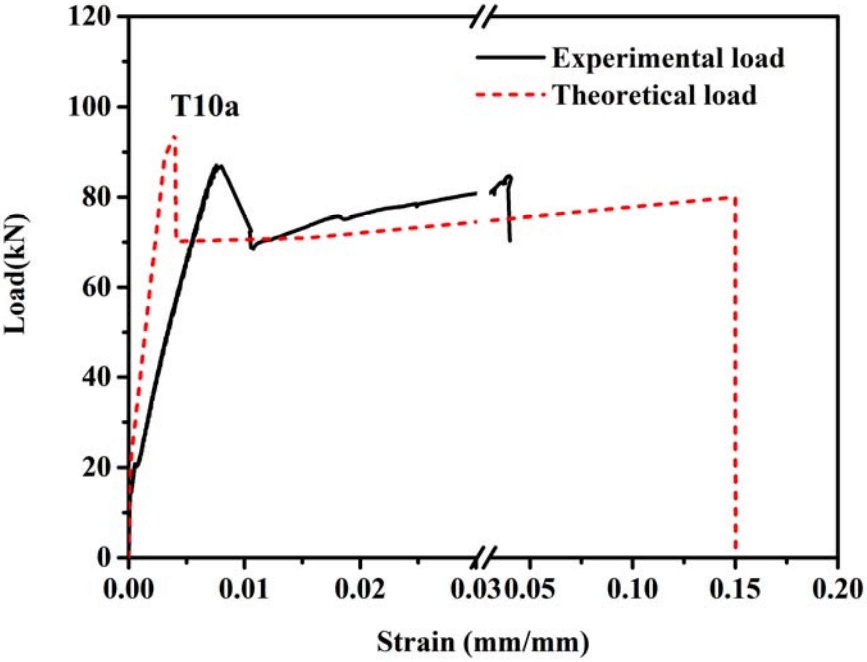

(b) Specimen T10a

Figure 3.12: Comparison between experimental load-strain curves and theoretical load-strain curves (cont.)

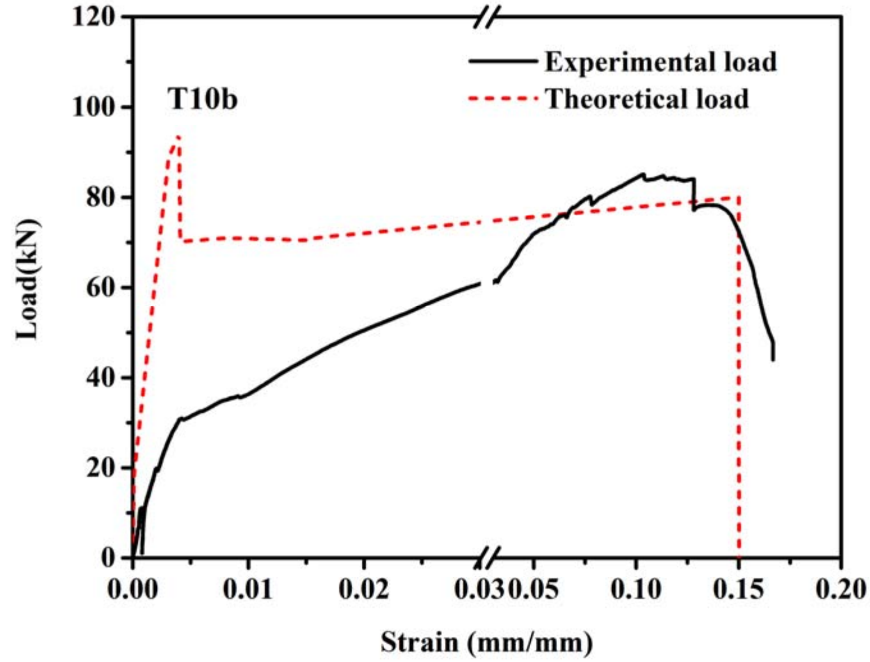

(c) Specimen T10b

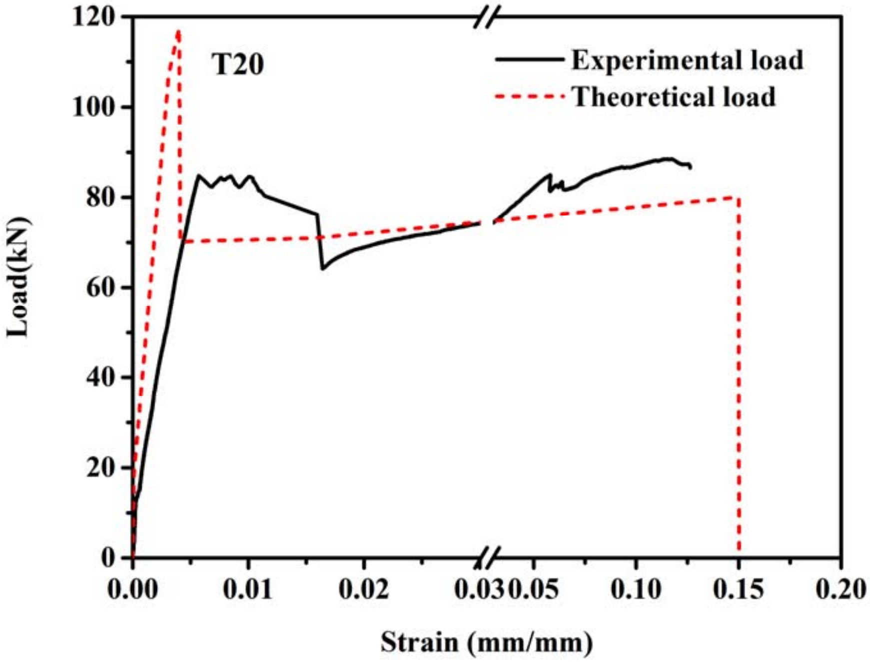

(d) Specimen T20

Figure 3.12: Comparison between experimental load-strain curves and theoretical load-strain curves (cont.)

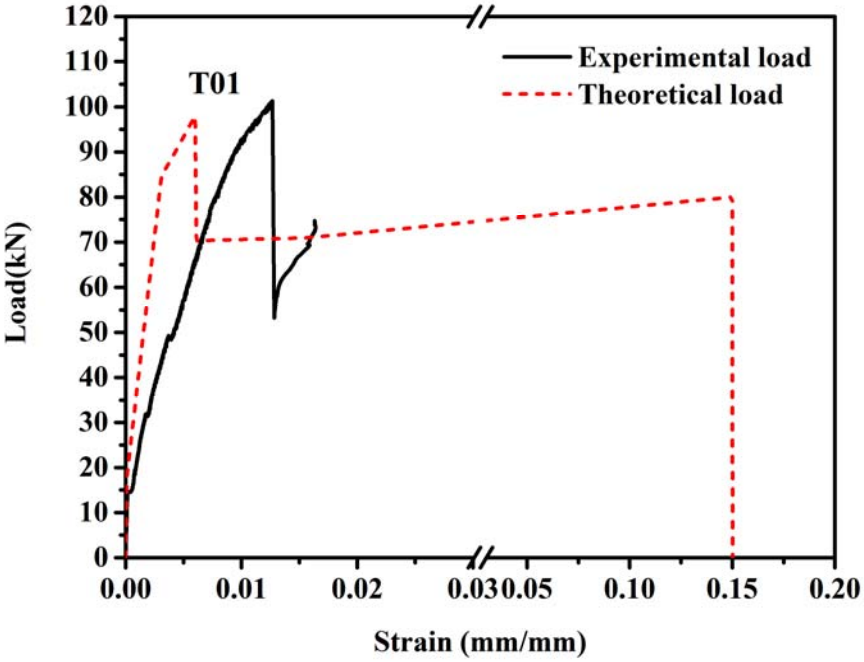

(e) Specimen T01

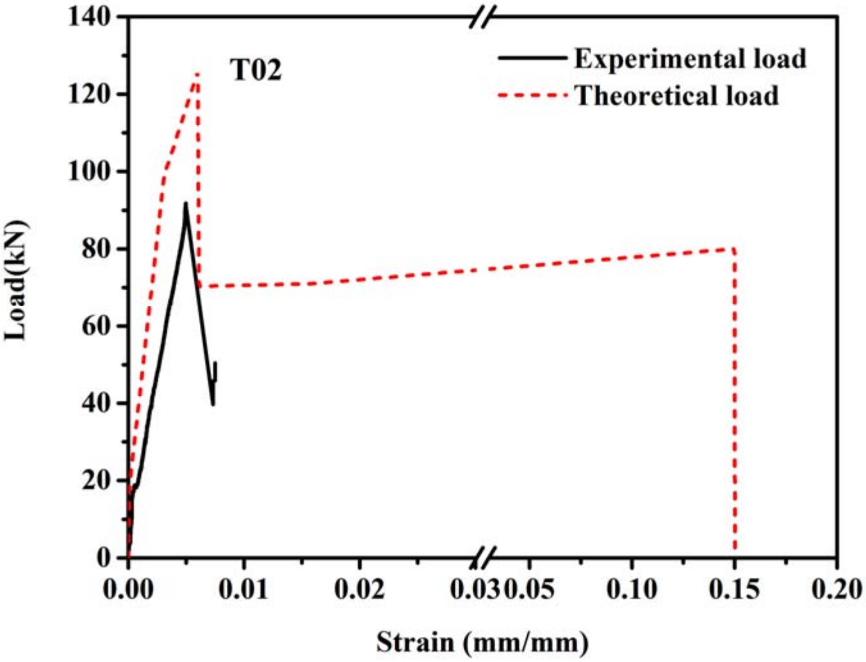

(f) Specimen T02

Figure 3.12: Comparison between experimental load-strain curves and theoretical load-strain curves (cont.)

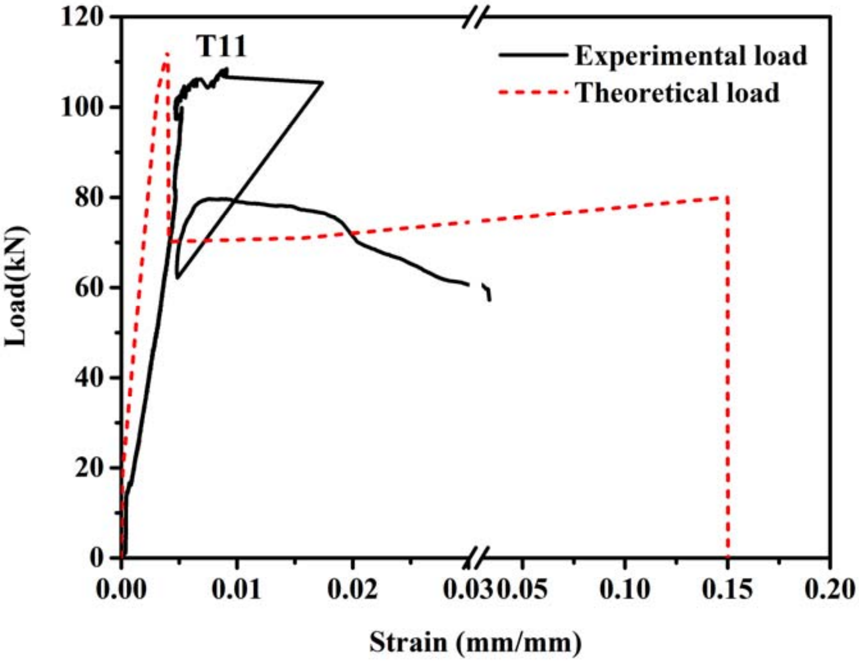

(g) Specimen T11

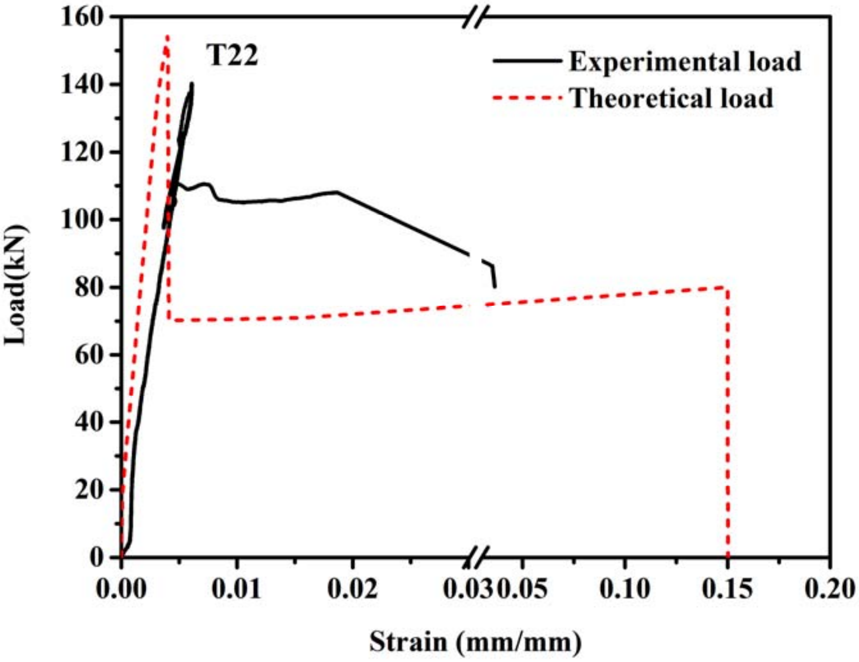

(h) Specimen T22

Figure 3.12: Comparison between experimental load-strain curves and theoretical load-strain curves (cont.)

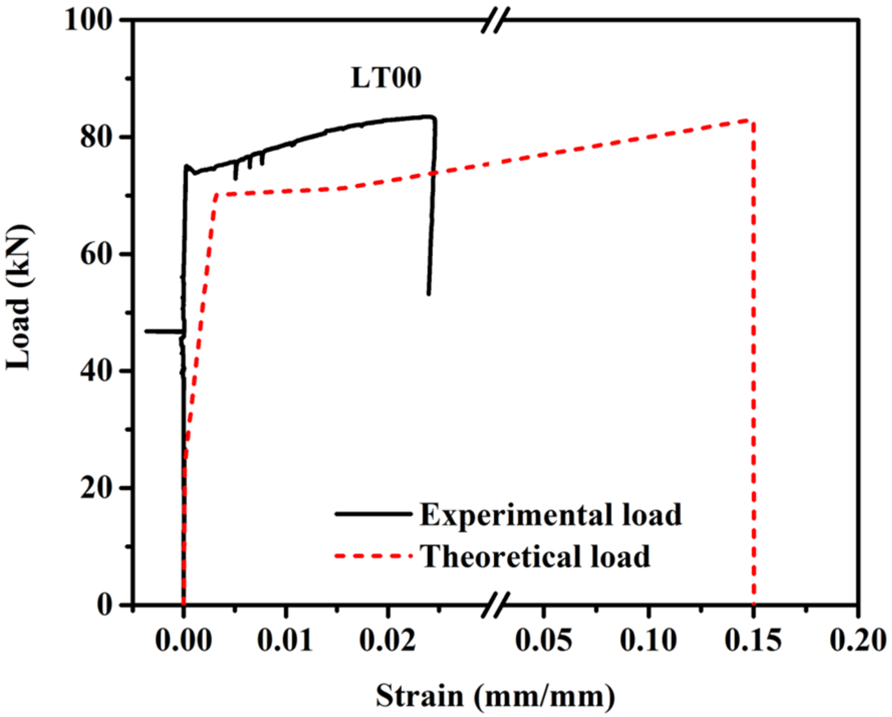

(i) Specimen LT00

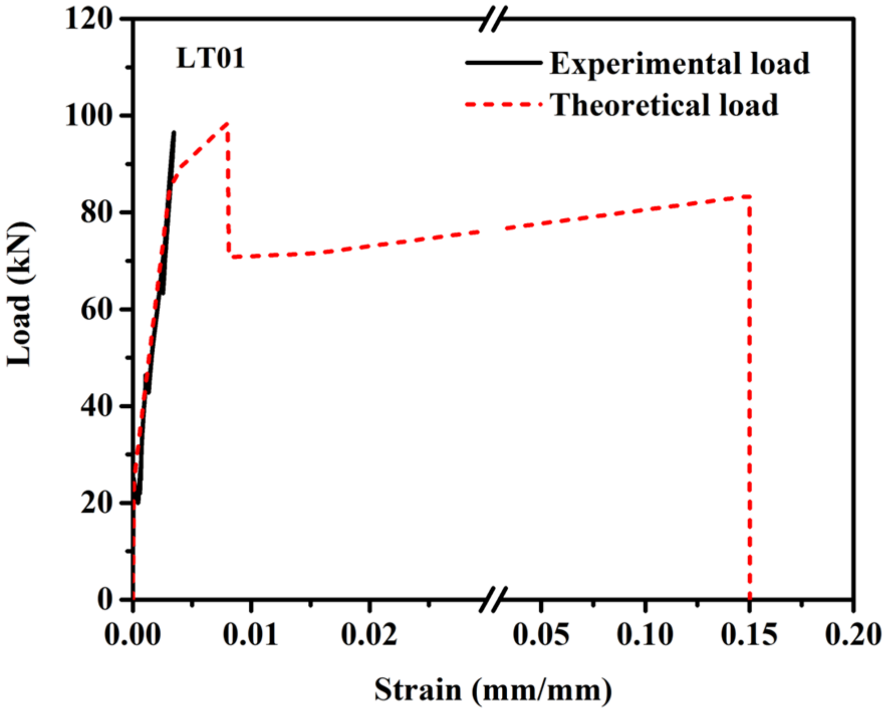

(j) Specimen LT01

Figure 3.12: Comparison between experimental load-strain curves and theoretical load-strain curves (cont.)

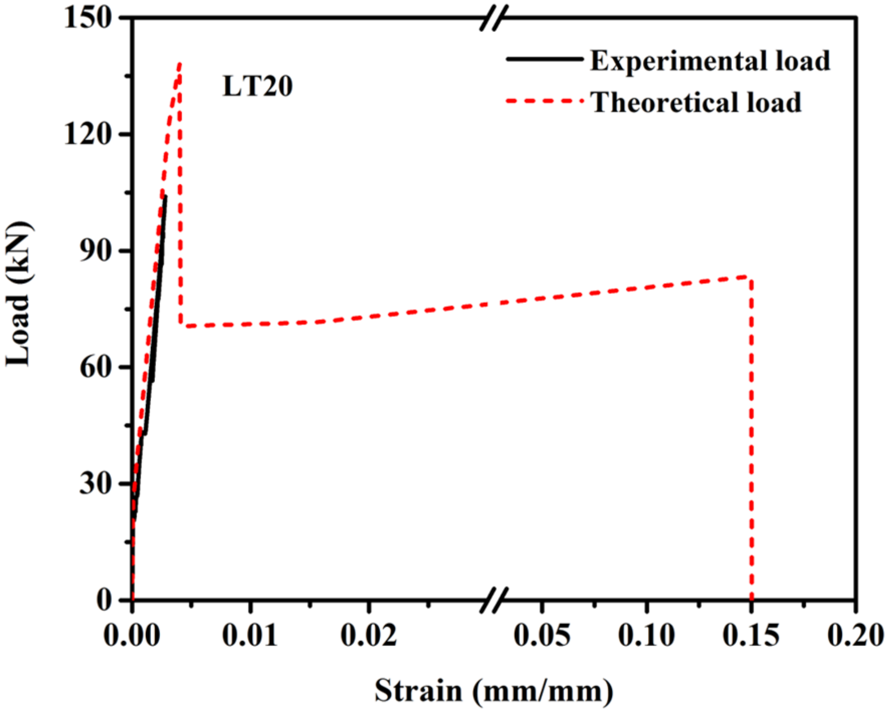

(k) Specimen LT20

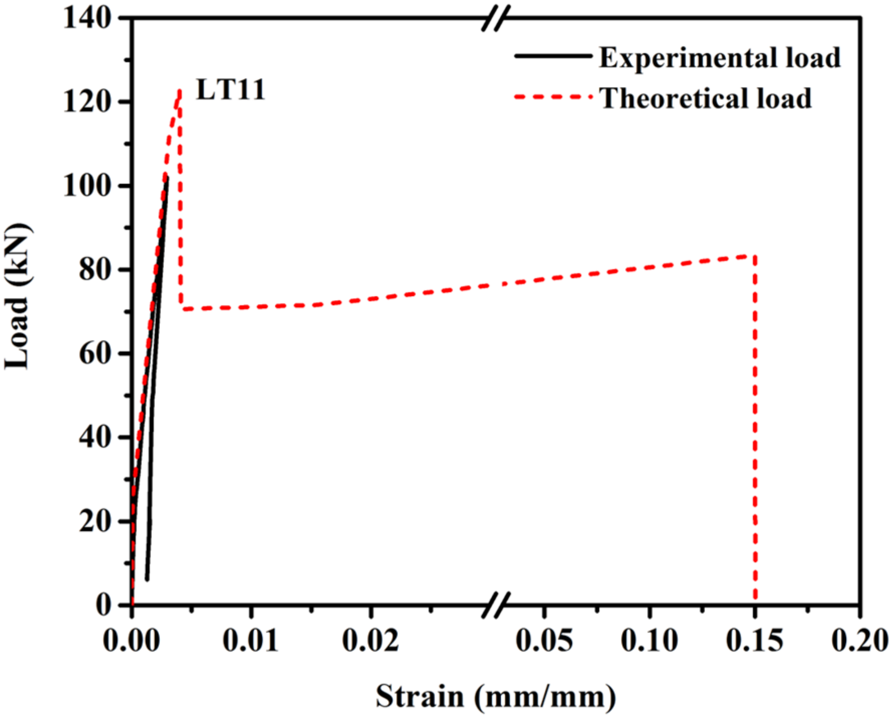

(l) Specimen LT11

Figure 3.12: Comparison between experimental load-strain curves and theoretical load-strain curves (cont.)

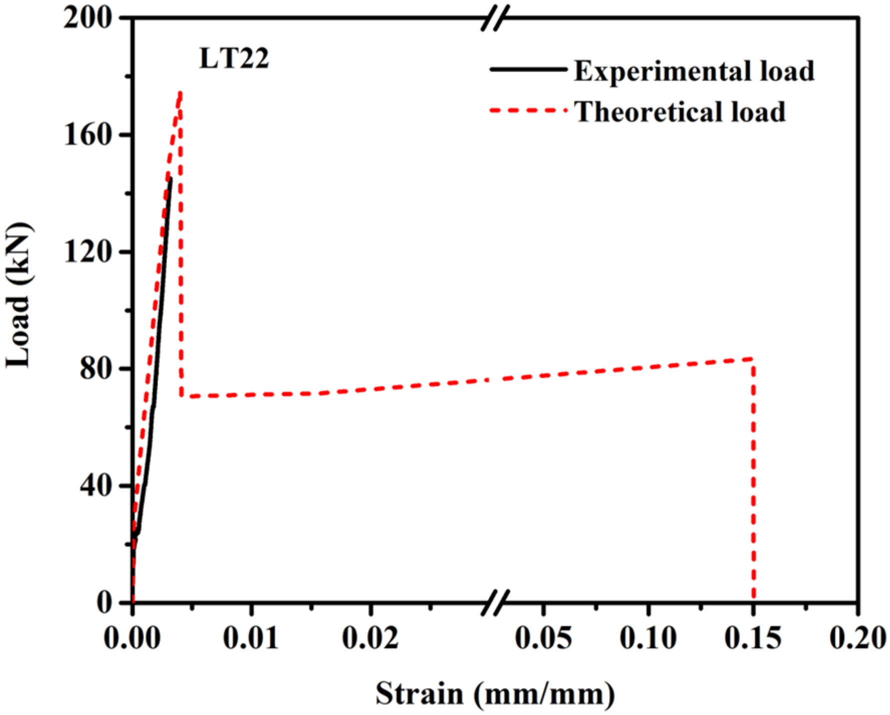

(m) Specimen LT22

Figure 3.12: Comparison between experimental load-strain curves and theoretical load-strain curves

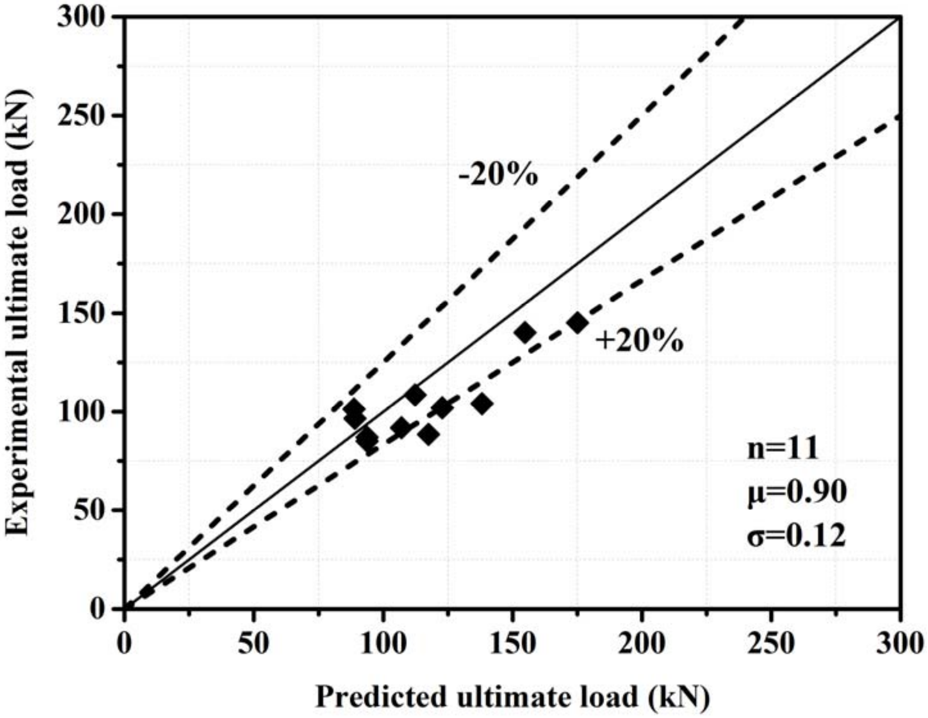

Figure 3.13: Comparison between experimental ultimate load and predicted ultimate load

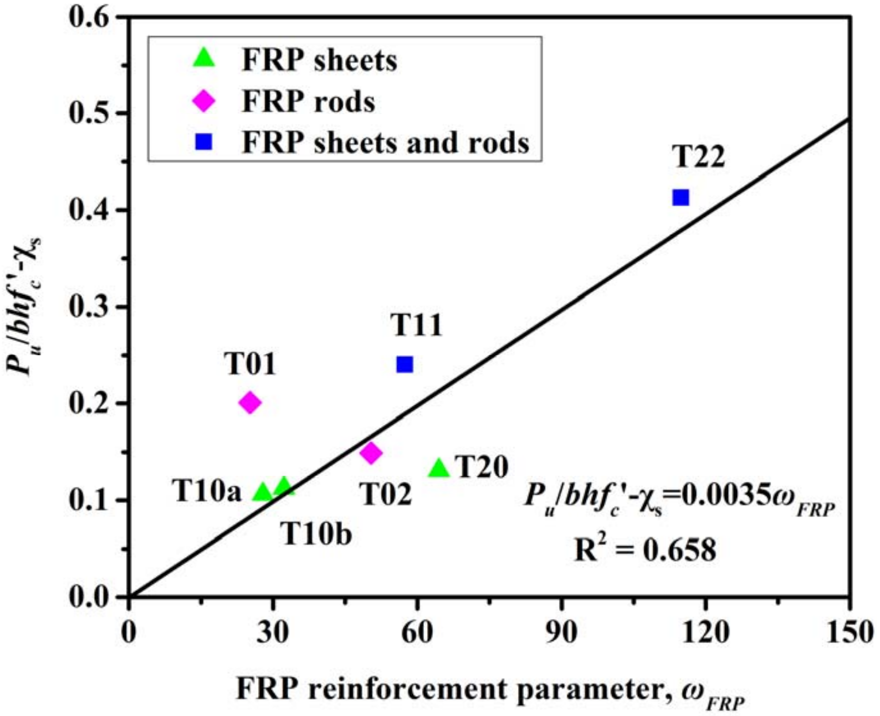

(a) Short tie specimens

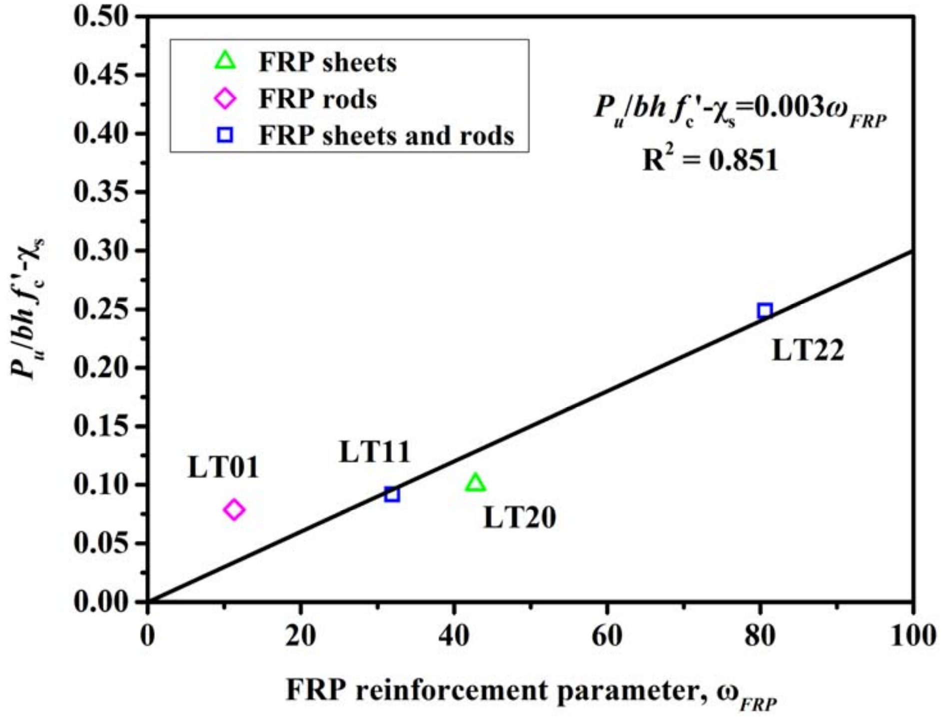

(b) Long tie specimens

Figure 3.14: Relation of experimental ultimate load and FRP reinforcement parameter (cont.)

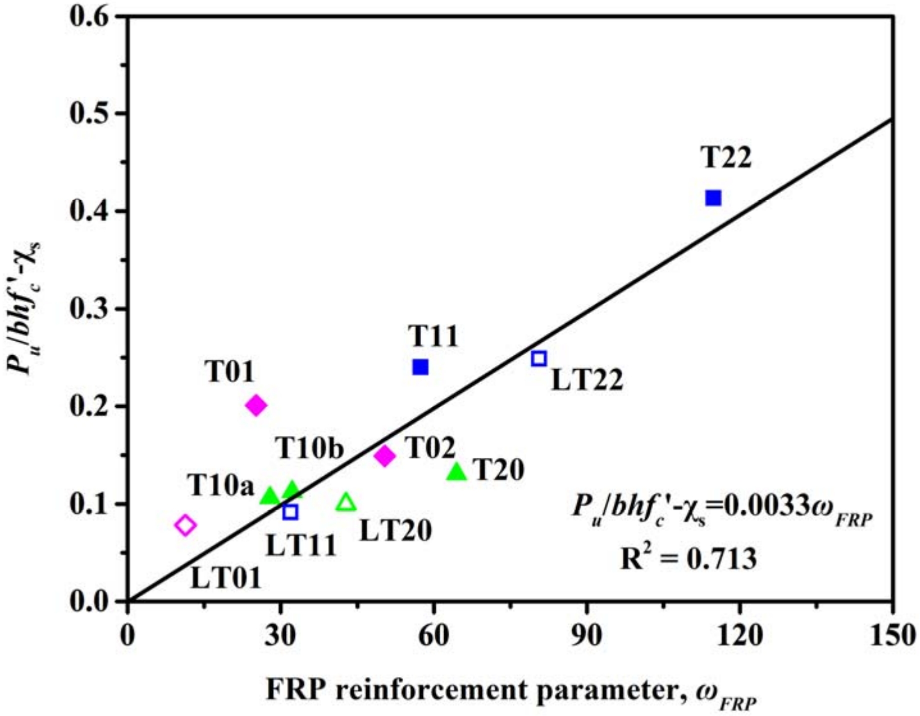

(c) All specimens

Figure 3.14: Relation of experimental ultimate load and FRP reinforcement parameter

Chapter 4. FRP Strengthening of Strut Members

4.1 General

This chapter presents the study on the behavior and ultimate load of FRP strengthened plain concrete strut members under axial compressive loading. A test program was carried out to investigate the effect of FRP strengthening systems on the ultimate load capacity of prismatic, partial bottle-shaped, and bottle-shaped struts. In total, twenty-seven specimens were tested to failure under quasi-static loading. An analytical model was proposed to determine the ultimate load capacity of FRP strengthened struts and test results were compared with the analytical predictions.

4.2 Analytical considerations

Struts are elements in the strut-and-tie models that carry compressive forces, as shown in **Figure 4.1**. They are usually classified by the profile of its outermost stress trajectories (**Figure 4.2**). The most basic type is a prismatic strut, which has straight outlines with a uniform cross section throughout its length. A bottle-shaped strut has a convex outer profile with a non-uniform cross section. A fan-shaped strut has straight outlines with a uniformly tapering cross section.

Bottle-shaped struts are formed when load is applied to a relatively small area of a member and the resulting compressive stress field spreads laterally as the forces flow through the member because extra width is available in the concrete member on either side of the strut axis beyond the node-strut interface. As the compressive stress field in a bottle-shaped strut disperses, the stress trajectories change direction and form an angle with the axis of the strut, thereby developing a tensile force in a bottle-shaped strut to balance the lateral component of the outwardly curving compressive stress trajectories, as shown in **Figure 4.3**. The internal force system within a bottle-shaped strut can be modeled by a strut-and-tie sub-model, depending on the height-to-width ratio of the strut. This model is composed of transverse ties, diagonal and longitudinal struts. The dispersion of compressive stress is indicated by the inclination angle of the diagonal strut, as shown in **Figure 4.4**. Regardless of whether a one-tie or a two-tie model is adopted, the sum total of transverse tension in the strut is the same and is directly proportional to the applied axial compression. The strut-and-tie models suggest that the stability and strength of a bottle-shaped strut is dependent on the tensile resistance offered by the transversely oriented tie, that is:

$$P_{strut} = \left(\sum F_{tie}\right)\tan\theta \tag{4.1}$$

where P_{strut} is the axial load carried by the strut, F_{tie} the effective tensile force in the transverse tie and $\tan\theta$ is the slope of stress dispersion.

Transverse tension is an inevitable component of the internal force system in a strut member. In order to increase the load capacity of the strut, a rational approach is to provide sufficient transverse FRP reinforcement to resist the tensile force developed. The purpose of FRP strengthening in struts is therefore to furnish the desired tensile resistance and maintain static equilibrium, thereby enabling the strut to carry higher load beyond cracking and preventing a brittle failure.

Several studies on bottle-shaped strut have been done recently (Arabzadeh1 *et al.* 2012; Brown and Bayrak 2006, 2008; Brown *et al.* 2006; Foster and Malik 2002; Sahoo *et al.* 2008; Sahoo *et al.* 2009 a, b; Sahoo *et al.* 2011; Low 2013), giving clear indications of the structural behavior of these disturbed regions. Some studies have also been carried out to explain the FRP strengthening of deep RC members using strut-and-tie model (Tan 2004; Park and Aboutaha 2009). However, little experimental information is available for the FRP strengthening of isolated bottle-shaped struts and there is no consensus amongst current design codes or the literatures on the method of FRP strengthening for bottle-shaped struts. With this aim, an experimental study was carried out to investigate the behavior of FRP strengthened prismatic, partial bottle-shaped, and bottle-shaped struts. **Figures 4.5** and **4.6** present the three series of strut specimens and the FRP strengthening systems for each series, respectively.

4.2.1 Axial load capacity of FRP strengthened strut

(a) Prismatic strut

The axial load capacity of a prismatic strut strengthened with transverse FRP sheets and/or longitudinal NSM-FRP rods is contributed by the FRP rods in compression and the concrete confined by transverse FRP reinforcement. It can be expressed as:

$$P_u = 0.85\left[f'_{cc}A_e + f'_{co}(A - A_e)\right] + P_{FRP,r} \tag{4.2}$$

in which

$$A_e = A - \frac{\frac{b}{h}\left(h-2r\right)^2 + \frac{h}{b}\left(b-2r\right)^2}{3} \tag{4.3}$$

where, P_u is the ultimate load capacity of FRP-strengthened prismatic strut; f'_{cc} is the compressive strength of FRP-confined concrete; f'_{co} is the unconfined compressive strength of concrete; A is the gross cross-sectional area of the prismatic strut; A_e is the effective confinement area; b is the width of the section; h is the depth of the section; r is the corner radius of section; $P_{FRP,r}$ is the vertical compressive strength of NSM-FRP rods; and a strength reduction coefficient of 0.85 is used.

Several FRP confinement models have been proposed by various researchers based on their experimental data which are useful in predicting the strength of the FRP-confined concrete struts. Among these, Lam and Teng (2003) proposed a simple model with reasonable accuracy after considering a test database gathered through various research works. This model was subsequently adopted and recommended by ACI 440.2-R08 (2008) with slight modifications for strength evaluation of confined concrete. Based on this model as shown in **Figure 4.7**, the compressive strength of confined concrete f'_{cc} is taken as:

$$f'_{cc} = f'_{co} + 3.3\left(\frac{A_e}{A}\right)\left(\frac{b}{h}\right)^2 f_l \tag{4.4}$$

in which

$$f_l = \frac{2nt_{FRP,s}\varepsilon_{eff}E_{FRP,s}}{D} = \frac{2nt_{FRP,s}\varepsilon_{eff}E_{FRP,s}}{\sqrt{b^2+h^2}} \tag{4.5}$$

where f'_{co} is the unconfined compressive strength of concrete; f_l is the confining pressure; b is the width of the section; h is the depth of the section; r is the corner radius of section; A_e is the effective confinement area; A is the total area of concrete cross-section; n is the number of ply of FRP sheets; $E_{FRP,s}$ is the elastic modulus of FRP sheets; ε_{eff} is the effective strain of FRP sheets, which can be taken as 0.004; D is used to represent the diameter of an equivalent circular cross section for noncircular cross sections, which is the diagonal of the rectangular cross section.

The compressive strength of FRP system is not well established as it seems to vary depending on the type of fiber and resin. In addition, standard test methods are not yet available. Due to micro-buckling of the FRP material, it is anisotropic and not homogeneous (De Luca *et al.*, 2010). Nevertheless, ACI 440 (2008) has suggested that for carbon FRP reinforcement, the compressive strength was 78% of its tensile strength and its elastic modulus was 85% of its tensile modulus of elasticity. The contribution of NSM-FRP rods to the axial load capacity is thus taken as:

$$P_{FRP,r} = 0.85vE_{FRP,r}\varepsilon_{FRP,cu}A_{FRP,r} \leq 0.78vf_{FRP}A_{FRP,r} \tag{4.6}$$

where v is the total number of vertical FRP rods; $A_{FRP,r}$ is the area of one FRP rod; $E_{FRP,r}$ is the elastic modulus of FRP rods; $\varepsilon_{FRP,cu}$ is the compressive strain of FRP rods at ultimate load of strut, which may be taken as 0.002 (Tan 2002); and f_{FRP} is the ultimate tensile strength of the FRP rods.

(b) Partial bottle-shaped strut

If the width , b , of the non-prismatic strut is insufficient for a bottle-shaped strut to develop (i.e. $b<b_{ef}$), as shown in **Figure 4.8(a)**, the strut is described as a partial bottle-shaped strut. The effective width b_{ef} that compressive stresses were assumed to spread laterally in a bottle-shaped strut is taken as:

$$b_{ef} = 0.5H + 0.65a \tag{4.7}$$

where a is the width of the loading area, and H is the height of strut.

Under axial compressive load, a partial bottle-shaped strut member would experience lateral expansion. Transverse FRP reinforcement could restraint the lateral expansion and confine the concrete section. The proposed confinement model for a partial bottle-shaped strut member strengthened with transverse EB-FRP sheets and NSM-FRP rods is presented in **Figure 4.9**. The confined concrete core of the partial bottle-shaped strut would be subjected to biaxial compression with effective lateral confining stresses from FRP sheets and rods. Equilibrium of forces gives the lateral confining pressure, f_l, at failure of the section as:

$$f_l = \left(\frac{2nt_{FRP,s}E_{FRP,s}}{t} + \frac{mA_{FRP,r}E_{FRP,r}}{tL} \right) \varepsilon_{eff} \tag{4.8}$$

where n is the number of ply of FRP sheets per side; m is the number of horizontal FRP rods per side; $t_{FRP,s}$ is the thickness of one layer of FRP sheets; t is the thickness of struts; L is the dispersion length measured on the axis of strut by drawing 45 degree lines from the end of the horizontal FRP rods; $A_{FRP,r}$ is the area of one horizontal FRP rod; $E_{FRP,s}$ and $E_{FRP,r}$ are the elastic modulus of FRP sheets and FRP rods, respectively; and ε_{eff} is the effective FRP strain at failure, which can be taken as 0.004.

Based on the formulation for bi-axially confined concrete given by Tan *et al.* (2013), the confined concrete compressive strength for the partial bottle-shaped strut, as shown in **Figure 4.9b**, can be taken as:

$$f'_{cc} = f'_{co} \left(2.254\sqrt{1 + 7.94\frac{f_l}{f'_{co}}} - 2\frac{f_l}{f'_{co}} - 1.254 \right) \left(1 - 0.8\sqrt{\frac{f_l}{f'_{co}}} \right) \tag{4.9}$$

where f'_{co} is the unconfined strength of concrete; and f_l is the confining pressure.

Hence, the ultimate axial load capacity of the FRP strengthened concrete strut can be evaluated as:

$$P_u = f'_{cc}A_b + P_{FRP,r} \tag{4.10}$$

where, A_b is the loading area of the strut; $P_{FRP,r}$ is the contribution of NSM-FRP rods (given by Equation 4.6).

EC2 (2004) also provides a model for the determination of axial capacity of partial bottle-shaped struts based on the amount of transverse resistance (**Figure 4.4**). In this model, the transverse resistance of the horizontal tie member, F_T, can be considered to be due to the partial contribution of concrete (before cracking) and transverse FRP sheets and rods, as follow:

(a) Before tensile splitting cracking of concrete:

$$F_T = \frac{H}{2} t f_{ct} + \left(\frac{H}{2} 2 n t_{FRP,s} E_{FRP,s} + m A_{FRP,r} E_{FRP,r} \right) \varepsilon \tag{4.11}$$

(b) After tensile splitting cracking of concrete:

$$\begin{aligned} F_T &= \left(\frac{H}{2} 2 n t_{FRP,s} E_{FRP,s} + m A_{FRP,r} E_{FRP,r} \right) \varepsilon \\ &\leq \left(\frac{H}{2} 2 n t_{FRP,s} E_{FRP,s} + m A_{FRP,r} E_{FRP,r} \right) \varepsilon_{eff} \end{aligned} \tag{4.12}$$

where t is the thickness of strut; H is the height of strut; f_{ct} is the tensile strength of concrete before cracking; n is the number of ply of FRP sheets per side; m is the number of horizontal FRP rods per side; $t_{FRP,s}$ is the thickness of one layer FRP sheets; ε is the tensile strain of FRP sheets and rods; $A_{FRP,r}$ is the area of one FRP rod; $E_{FRP,s}$ and $E_{FRP,r}$ are the elastic modulus of FRP sheets and FRP rods, respectively. It was assumed that at cracking, the tensile strain of the transverse FRP sheets and rods was equal to the cracking strain of concrete ($\varepsilon = \varepsilon_{cracking} = 200\times10^{-6}$ mm/mm). At the final stage, the effective tensile strain of the FRP sheets and rods ε_{eff} were assumed to equal to 4000×10^{-6}

mm/mm (Tan 2002; ACI 440 2008). The axial compressive load capacity of the FRP strengthened partial bottle-shaped strut is therefore taken as:

$$P_u = \frac{4F_T b}{b-a} + P_{FRP,r} \tag{4.13}$$

Where F_T is given by Equation 4.12 (with $\varepsilon=\varepsilon_{eff}=0.004$), a is the width of the loading area, b is available width of the concrete strut; $P_{FRP,r}$ is the contribution due to NSM-FRP rods (see Equation 4.6).

(c) Bottle-shaped strut

If the non-prismatic strut is sufficiently wide ($b>b_{ef}$), the strut is described as a full bottle-shaped strut (**Figure 4.8**). In this case, the axial load capacity of the FRP strengthened bottle-shaped strut member can also be evaluated using the Tan's model, as shown in Equation 4.10. The axial compressive load capacity of the FRP strengthened bottle-shaped strut ($b>b_{ef}$) is taken as:

$$P_u = f'_{cc} A_b + P_{FRP,r} \tag{4.10}$$

where f'_{cc} is the confined strength of concrete (see Equation 4.9); A_b is the loading area of the strut; $P_{FRP,r}$ is the contribution due to NSM-FRP rods (see Equation 4.6).

4.3 Test program

In order to verify the applicability and effectiveness of FRP strengthening system on concrete strut members, the performance of plain concrete strut specimens, strengthened with EB-FRP sheets and NSM-FRP rods, were experimentally investigated. The focus was on the enhancement in ultimate load capacity of the FRP-strengthened concrete strut members.

4.3.1 Test specimens

Three series of plain concrete strut specimens, as shown in **Table 4.1** and **Figure 4.5**, were prepared. Series "P" was designed to study the effect of the FRP strengthening system on the load-carrying capacity of prismatic struts. It consisted of four specimens, each having a height *H* of 500 mm and a rectangular cross section of 100 mm in width and 100 mm in thickness. Series "PB" was meant for studying the effect of the FRP strengthening system on the load-carrying capacity of partial bottle-shaped struts. It consisted of fifteen specimens, also having a height *H* of 500 mm but with a rectangular cross section of 300 mm wide and 100 mm thick. Series "B" was used to examine the effect of the FRP strengthening system on the load carrying capacity of full bottle-shaped struts. This series consisted of eight specimens, having a height of 500 mm and cross section measuring 500 mm in width and 100 mm in thickness.

The specimens were designated as "S(A)*xy*(H/V)" where "S" referred to the series name and "*x*" and "*y*" the number of transverse FRP sheets and FRP rods on each opposite side of the specimen, respectively. The prefix "A" referred to specimens with transverse sheet fixed with fiber anchors. The suffix "H" and "V" indicated the direction of NSM-FRP rods. For example, Specimen PB12V had one layer of transverse FRP sheets and two vertical FRP rods on each opposite side of the strut, whereas Specimen

PBA22H had two layers of transverse FRP sheets with FRP anchorages and two horizontal FRP rods on each opposite side of the strut.

4.3.2 Materials

4.3.2.1 Concrete

The concrete cylinder compressive strength at 28 days was targeted at 30 MPa. The concrete mixture composition consisted of 343 kg/m^3 of Ordinary Portland Cement, 240 kg/m^3 of water, 748 kg/m^3 of sand and 898 kg/m^3 of coarse aggregate with maximum size of 10 mm. The specimens were cast in seven batches. Cubes of 100 mm dimension and cylinders (100 mm in diameter and 200 mm in height) were cast along with each batch to assess the compressive and tensile splitting strengths of concrete at the time of testing. As shown in **Table 4.2**, the concrete cylinder compressive strength for the seven batches were 34.0MPa, 23.8MPa, 29.6MPa, 42.2 MPa, 38.7 MPa, 36.2 MPa and 39.5 MPa each based on the average value of six cylinders.

4.3.2.2 FRP materials

The physical and mechanical properties of the carbon FRP sheets and carbon FRP rods according to the supplier’s specifications are shown in **Table 4.3**. The unidirectional carbon FRP sheets had a thickness of 0.176 mm with a weight of 330 g/m^2, and had a specified tensile strength of 3800 MPa, with a tensile elastic modulus of 240 GPa and an ultimate elongation to rupture of 1.55 percent. A three-part resin was used to install the FRP sheets. The carbon FRP rods measured 10 mm by 1.4 mm in cross-section, and had a specified tensile strength of 1000 MPa at 0.6% strain, elastic modulus of 165 GPa, and ultimate elongation of 0.8 to 1.0 percent.

4.3.3 Specimen preparation

Figure 4.5 shows the dimensions of the strut specimens. Wooden moulds were fabricated for the casting of specimens. After the wooden moulds were oiled, the concrete were mixed and poured into the wooden moulds. The formwork was removed after one day, and the specimens were then covered with damp gunny sacks for a week. Thereafter, the specimens were then placed in the laboratory conditions for 28 days under ambient conditions until the time of testing. Accompanying cylinders and cubes were cast and cured in the same manner. All test specimens were white washed before the test in order to trace the crack patterns.

4.3.4 Installation of FRP strengthening systems

Figure 4.6 shows the FRP strengthening systems for the strut specimens. EB-FRP sheets and NSM-FRP rods were applied in the transverse direction for bottle-shaped struts so as to increase the confined compressive strength of the concrete.

The specimens were cured for 28 days before the strengthening system was installed. A three-part resin was used to bond the FRP sheets on to the concrete. The FRP sheets were cut to the required length and width using an ordinary cutting blade. The concrete surface was ground to remove dust, grease, disintegrated materials, loose particles and other bond inhibiting materials before the sheets were bonded. The resin was applied on the entire required surface using a roller, followed by application of the carbon FRP sheets. To ensure proper bonding, a steel roller was used to press the carbon FRP sheets down. The procedure was repeated after each ply of carbon FRP sheets had been applied. The carbon FRP flat rods with a width of 10 mm and a thickness of 1.4 mm were installed into slots at both faces of strut members. A concrete saw was used to cut slots approximately 5 mm wide and 15 mm deep into the substrate. The slots were filled with the epoxy adhesive, and the FRP rods were pressed into the slots.

For EB-FRP sheets, a serious impairment of strengthening effectiveness comes from separation of the FRP sheet from the concrete surface by de-bonding. Therefore, in order to more fully utilize the tensile capacity of the FRP sheet, some form of additional anchorage was considered, that is, fiber anchors as shown in **Figure 4.6**. Series PBA and BA were thus prepared to investigate the effectiveness of FRP anchors in preventing de-bonding of FRP sheets.

All FRP anchors were hand-made in the laboratory by rolling carbon fibre sheets measuring 200 mm wide and 90 mm long. The method of installation is summarized as follows: (a) the concrete surface was roughened with a needle scaler which also removed the cement rich surface; (b) drilling of anchor holes at required locations to specific depths followed by cleaning of holes and concrete surface by spraying with compressed air; (c) insertion of preformed anchor dowels into epoxy filled holes followed by one day of curing, (d) insertion of partly dry fibre sheets over the anchor fans protruding from the concrete surface followed by placement of the FRP sheet in a wet lay-up manner; and (e) bending and splaying of the anchor fans fibres and then epoxying onto the sheets surface.

The completed FRP anchors were then allowed to cure for a period of seven days in a controlled laboratory environment of approximately 25 degrees celsius.

4.3.5 Test setup and procedure

As shown in **Figure 4.10**, a stiff universal testing machine with a 1000 kN capacity and operating in a displacement-controlled mode with a slow rate of loading (0.1 mm/min) was used to test the strut specimens. The specimens were loaded in compression using two steel plates symmetrically placed on their top and bottom faces. The plates each had a length of 100 mm, width of 100 mm (that is, the same as the specimen thickness), and thickness of 50 mm. The magnitude of applied load was registered by a load cell.

The axial shortening and the lateral displacements were recorded by several Linear Variable Differential Transducers (LVDTs) of different ranges at the four faces of the specimen, as shown in **Figure 4.10**. They were mounted in the longitudinal direction to measure the longitudinal deformation of the test zone.

Strains were measured by electrical resistance strain gauges attached to the surface of concrete, reinforcing bars and FRP reinforcement. The positions of the strain gauges are shown in **Figure 4.11**. The vertically oriented concrete strain gauges were meant to record the compressive strains across the mid-length so as to ascertain the lateral spread of the bottle-shaped struts in the panels. In some specimens, horizontally oriented concrete strain gauges were used along the axis of the strut to record the distribution of the transverse tensile strains along the strut axis. The measured strains were recorded using a data-logger.

4.4 Test results and discussion

The concrete strengths at the time of testing the specimens are shown in **Table 4.2**. The cylinder compressive strength varied from 23.8 MPa to 42.2 MPa with an average of 34.8 MPa, whereas the cube compressive strength varied from 28.6 MPa to 47.8 MPa with an average of 42.0 MPa. The cracking loads and ultimate loads of all specimens are summarized in **Table 4.4** and the appearance of specimens after testing is shown in **Figure 4.12**.

4.4.1 General behavior and failure modes

In Series P (prismatic strut specimens), the concrete cover of un-strengthened Specimen P00 started to spall off near failure. The specimen failed due to concrete crushing just below the loading plates in the top region as shown in **Figure 4.12a**. For the FRP strengthened specimens, de-bonding of FRP sheet was observed in Specimen P10, which resulted in failure. Whereas Specimens P20 and P22V, strengthened with two layers of FRP sheets, both failed due to rupture of FRP sheets (**Figure 4.12a**). When the FRP sheets were removed for closer observation, it was found that in the areas where de-bonding and rupture occurred, the concrete has crushed. Also, in Specimen P22V where the vertical NSM-FRP rods were installed, two loud sounds were heard during the tests which were accompanied with a great reduction in the load values. After the FRP sheets were removed, it was also found that both the FRP rods had broken and the concrete around the bars had crushed. It was deduced that the vertical FRP rods had buckled and snapped as the surrounding concrete crushed.

In Series PB, all specimens failed in a brittle manner with a very big bang loud. The un-strengthened specimen (PB00) and specimens strengthened with NSM-FRP rods only (PB02V and PB02H) exhibited a similar behavior (**Figures 4.12b** and **4.13**). In the initial stage of loading, a vertical splitting crack was formed approximately at the mid-height of the specimens, and the longitudinal deformation of strut was quite small. When the applied load was further increased, this crack propagated toward the top and bottom loaded faces of the specimens. As the crack reached close to the loading face, it changed direction and curved toward out of the loaded zone. Ultimate failure occurred due to extreme splitting and spalling of concrete at mid-height of the strut (**Figure 4.12b**). On the other hand, for the specimens strengthened with EB-FRP sheets with or without NSM-FRP rods, ultimate failure was initiated by crushing of the concrete near the loading faces (**Figures 4.12c** and **4.13**). No de-bonding of FRP sheets was observed in both Series PB and PBA specimens (**Figures 4.12d-f** and **4.13**) before failure. The role of FRP anchors appeared not to be mobilized.

In Series B, a longitudinal crack formed in the un-strengthened Specimen B00 as expected which resulted in the failure as shown in **Figure 4.12g**. All FRP strengthened specimens in Series B failed by tensile splitting followed by crushing of concrete. When the FRP sheets were removed, longitudinal cracks were observed as illustrated in **Figures 4.12h** and **4.12i** which indicated that the tensile force developed in the strut exceeded the tensile strength of the concrete and the FRP sheets were subsequently mobilized and responsible for the increase in load carrying capacity. De-bonding of FRP sheets was observed especially in the regions immediately below the applied load due to concrete crushing. Again, the effect of FRP anchors was not obvious from the failure characteristics. However, compared with Specimen B21 which suffered a sudden failure due to a severe FRP de-bonding (**Figure 4.12h**), the use of FRP anchors appeared to prevent an abrupt failure in Specimen BA21 (**Figure 4.12j**).

4.4.2 Axial load-deformation relations

For most specimens, the relation between the applied load and the axial deformation was almost linear up to about 90% of the ultimate load. Only some specimens exhibited some form of ductility after the maximum load was reached. They are presented in **Figure 4.14**. It can be seen that these specimens were provided with FRP anchors which would have prevented the abrupt failure as mentioned earlier.

The load-deformation curves exhibited similar behavior among the specimens. At the initial stage, the load increased linearly with deformation until near the ultimate load and a softening response was obtained. The degree of softening upon splitting depended on the amount of FRP reinforcement. Then, the load decreased slowly. All the FRP strengthened specimens had almost the same initial stiffness as the un-strengthened specimen, which indicated that FRP strengthening did not affect the stiffness of struts. The final failure of all specimens was sudden and brittle with a big bang, and failure of the FRP-strengthened specimens was due to tensile splitting cracking or the crushing of concrete in the loading region. The stiffness of the Specimen PBA22V was higher than all other specimens, indicating that the combination of two layers of transverse FRP sheets and two vertical FRP rods per sides was most effective to improve the stiffness of strut specimens.

4.4.3 Effect of width to height ratio

The ratio of the width to the height of strut specimens, *B*/*H*, was an important factor affecting the strengthening effectiveness of FRP systems. To obtain a clearer picture of the effect on the ultimate load of the specimens, the strut efficiency factor was plotted against the width to height ratio in **Figure 4.15**. The strut efficiency factor is defined as $P_u/(0.85 f'_c A_b)$, where P_u is the ultimate load of specimens, f'_c is the concrete cylinder compressive strength, A_b is the loading area of specimens, and 0.85 is a coefficient to account for specimen size and loading rate compared to a standard cylinder.

The specimens were arbitrarily divided into four clusters according to the FRP strengthening systems: control specimens without strengthening (Specimens P00, PB00, B00); specimens with one layer of FRP sheets per side (Specimens P10, PB10, PBA10, B10, BA10); specimens with two layers of FRP sheets per side (Specimens P20, PB20, PBA20, B20-1, B20-2, BA20); and specimens with two layers of FRP sheets and two vertical FRP bars per side (Specimens P22V, PB22V, PBA22V, B22V, BA22V).

From **Figure 4.15**, for each cluster of specimens, with the increase of *B*/*H*, the strut efficiency factor increased first from the case of a prismatic strut to that of a partial bottle-shaped strut then decreased slightly in the case of a full bottle-shaped strut (due to the change of the failure mode), which means FRP strengthening was most effective for partial bottle-shaped struts for which the *B*/*H* was equal to 0.6. For a FRP strengthened bottle-shaped struts with higher width to height ratio, a larger tensile force would be developed in the strut which made the strut more likely to fail by tensile splitting which thus occurred at lower load. The use of fiber anchors did not enhance the ultimate strength of partial bottle-shaped struts. However, it helped in the case of full bottle-shaped struts.

4.4.4 Effect of FRP configurations

Table 4.4 indicates the effect of FRP strengthening systems on the ultimate load of the struts. The ultimate load capacity of strut members was substantially increased by about 20% to 70%, especially in Series PB specimens. The average increase in ultimate strength in FRP strengthened partial bottle-shaped struts was about 50%~70% compared to the un-strengthened struts (PB00). For Series B, the use of FRP systems in various configurations has resulted in a strength increase of more than 20%. The ultimate load capacity of FRP strengthened specimens increased with additional FRP sheets. The transverse FRP reinforcement was efficient in enhancing the ultimate load capacity of struts. No significant improvement in the ultimate capacity was observed for specimens (PB02H, PB02V) strengthened with NSM-FRP rods only, while Series PB and B specimens strengthened with EB-FRP sheets had significantly higher ultimate load than the un-strengthened struts. After being strengthened by EB-FRP sheets, the failure mode of Series PB specimens changed from a tensile splitting failure of concrete to the crushing of concrete at or near the loaded faces, while the failure mode of Series B struts remained as due to the tensile splitting of concrete. The most efficient FRP configuration however consisted of a combination of EB-FRP sheets and vertical NSM-FRP rods (P22V, PB22V, PBA22V, B22V, and BA22V). The use of fiber anchors was found to be beneficial in Series B specimens as mentioned earlier.

To quantify the effectiveness of transverse FRP strengthening in increasing the load-carrying capacity in struts, the normalized ultimate load of the specimens is plotted against the horizontal FRP reinforcement parameter $\omega_{FRP,h}$ in **Figure 4.16**. The horizontal FRP reinforcement parameter is defined as:

$$\omega_{FRP,h} = \frac{2nt_{FRP,s}H}{tH} \cdot \frac{E_{FRP.s}}{E_c} + \frac{2mA_{FRP,r}}{tH} \cdot \frac{E_{FRP.r}}{E_c} \qquad (4.14)$$

where n is the number of ply of FRP sheets per side; m is the number of horizontal FRP rods per side; H is the height of strut; t is the thickness of strut; $A_{FRP,r}$ is the cross-sectional area of one horizontal FRP rods; $E_{FRP,s}$ is the elastic modulus of FRP sheets; $E_{FRP,r}$ is the elastic modulus of FRP rods; E_c is the elastic modulus of concrete.

Figure 4.16 shows that values of ultimate load increase with an increase in the FRP reinforcement parameter. However, the effectiveness of the horizontal FRP reinforcement appears to diminish with FRP reinforcement parameter beyond 0.05.

4.4.5 Load-strain relations

The transverse strains and longitudinal strains at the mid-height of strut specimens are plotted against the applied load in **Figure 4.17**. Also, the load-versus-strain relations of NSM-FRP rods are presented in **Figure 4.18**.

For Series P (**Figure 4.17a**), the FRP strengthened specimens have similar lateral deformation as the un-strengthened specimen, P00, in the initial stage up to the peak load of Specimen P00. The strengthened specimens exhibited an ascending branch beyond that. Larger tensile strains were recorded for Specimen P20 which led to the lower ultimate strength compared to Specimen P10. The use of vertical FRP rods in Specimen P22V resulted in slightly higher ultimate load but lower compressive strain at ultimate.

In Series PB, except for the un-strengthened specimen PB00 which exhibited a linear load-strain relation up to failure, the load-strain curve followed a two-stage behavior for all strengthened specimens with EB-FRP sheets only (**Figures 4.17b-d**). All specimens displayed similar linear increase in transverse strain in the initial stage until the concrete cracked vertically along the loading line due to the tensile resistance of concrete being exceeded. When the concrete cracked, the transverse strain increased rapidly accompanied with the applied load remaining constant. After the cracks had stabilized, for specimens strengthened with EB-FRP sheets (**Figure 4.17b**), the applied load started to pick up again. Then the applied load dropped suddenly at the time of failure. For specimens with a greater area of transverse FRP reinforcement, the increase in transverse strain upon cracking was smaller. The load-compressive strain response of the specimens showed a similar behavior. When the concrete cracked, the loads experienced a small drop which was immediately followed by a linear load-strain response until the peak load.

In Series B (**Figures 4.17e** and **4.17f**), the specimens displayed similar linear response in strain development initially until the concrete cracked due to the concrete tensile strength being exceeded. When the concrete cracked, the specimens experienced softening with the load remaining constant, accompanied by a rapid increase in strain in the FRP sheets. The axial load subsequently increased with further increase in FRP strain in some specimens (Specimens BA10 and B22V). The use of anchors did not result in significant difference in the FRP strains (**Figure 4.17f**).

The load-versus-strain relations in NSM-FRP rods at mid-length of the specimens are presented in **Figure 4.18**. The maximum strain values of FRP rods were usually at the middle of FRP rods. So the strain values shown in **Figure 4.18** were maximum strain of FRP rods and obtained through the strain gauges which were attached to the middle of FRP rods. The behavior was similar for both vertical FRP rods in compression (**Figures 4.18a** and **4.18b**) and horizontal FRP rods in tension (**Figure 4.18c**). Initially, the strains increased linearly with the applied load. Upon concrete cracking, there was a sudden increase in the tensile strains in the case of horizontal FRP rods, followed by a gradual increase in the applied load and strain subsequently. The maximum compressive strains in vertical FRP rods for Series PB and B specimens was about 3000×10^{-6} mm/mm, and the maximum tensile strains in horizontal FRP rods for Series PB specimens was about 4000×10^{-6} mm/mm.

4.4.6 Strain distribution

In order to investigate the system of stress dispersion and the geometry of STM in the test specimens, several strain gauges were placed across the height and the width, as shown in **Figures 4.11a** and **b**. Five strain gauges were placed horizontally and distributed at regular intervals along the longitudinal axis of strut. Three to five gauges were placed vertically at regular intervals along the transverse axis of strut.

Figure 4.19 presents the transverse tensile strain profile along the vertical axis of strut. In most cases, during the initial stages of loading, prior to initiation of tensile splitting crack, the tensile strain was maximum at about mid-height of the strut where the longitudinal splitting crack was initiated. Once the initial crack appeared, the concrete stiffness reduced significantly. With increasing applied load, locations of maximum magnitudes of the transverse tensile strains were observed to shift towards the top and bottom faces of the strut and the transverse tensile strains reach the maximum at the location 150 mm away from the top and the end. This indicated that the strut-and-tie system of strut was changed with loading.

Figure 4.20 presents the longitudinal compressive strain profile along the horizontal axis of strut. In most specimens, the maximum compressive strain was near the vertical centerline of strut. Across the width of strut, compressive strain reduced with distance from the vertical centerline of strut.

As shown in **Figures 4.19** and **4.20**, the observed transverse tensile strains at failure of the strut were about 0.003 to 0.004, while the longitudinal compressive strains were around 0.002. Thus, the assumption of both an effective tensile strain of 0.004 and an effective longitudinal compressive strain of 0.002 in the FRP reinforcement was justified.

4.4.7 Strength provision

The theoretical ultimate load can be predicted based on analytical considerations (Equation 4.2) described in **Section 4.2.1**. For Series P, the experimental and theoretical ultimate loads for specimens, $P_{u,Test}$ and $P_{u,Pred}$ are compared in **Figure 4.21**. The mean and standard deviation values of the ratio of $P_{u,Test}/P_{u,Pred}$ were 1.02 and 0.051 respectively, showing good agreement.

The comparison of experimental and theoretical (Equation 4.10) ultimate load based on Tan's model (2013) for Series PB specimens is shown in **Figure 4.22a**, and the average ratio of test to predicted value $P_{u,Test}/P_{u,Pred}$ is 1.08 with a standard deviation of 0.096, showing good agreement. The comparison of experimental and theoretical (Equation 4.13) ultimate load for Series PB specimens based on EC2 model is shown in **Figure 4.22b**. The agreement is not very good with the mean and standard deviation of the ratio of $P_{u,Test}/P_{u,Pred}$ being 1.37 and 0.217 respectively. One main reason was that the failure mode of FRP strengthened partial bottle-shaped struts was totally different from the tensile splitting failure of concrete, as assumed in the EC2 model.

The axial load capacities of FRP strengthened bottle-shaped struts (Series B) predicted by the Tan's model (Equation 4.10) are compared with the test results in **Figure 4.23**. The average ratio of test to predicted value $P_{u,Test}/P_{u,Pred}$ is 1.02, with a standard deviation of 0.105, showing good agreement.

4.5 Summary

On the basis of the compressive tests carried out in this investigation on plain concrete struts strengthened by various types of FRP strengthening systems, the following conclusions can be drawn.

(a) The ultimate load capacity of strut members was substantially increased when strengthened with FRP sheets. After being strengthened by EB-FRP sheets, the failure mode of partial bottle-shaped struts changed from a tensile splitting failure of concrete to the crushing of concrete at or near the loaded faces, while the failure mode of bottle-shaped struts remained as due to the tensile splitting of concrete. No significant improvement in the ultimate load capacity was observed for partial bottle-shaped strut members strengthened with NSM-FRP rods only. The most effective FRP configuration consisted of a combination of EB-FRP sheets and NSM-FRP rods.

(b) During the initial stages of loading, prior to initiation of the longitudinal splitting crack, the maximum transverse tensile strains were recorded near the mid-height of the struts and, as the loading increased, the locations of the maximum transverse tensile strains shifted towards the loaded faces of the struts.

(c) The observed transverse tensile strains at failure of the strut were about 0.003 to 0.004, while the longitudinal compressive strains were around 0.002.

(d) Analytical methods based on confined concrete models and strut-and-tie models were proposed to predict the axial load capacity of the FRP-strengthened strut members. Good agreement with the test results was observed for bottle-shaped strut using a biaxially confined concrete model proposed by Tan *et al.* (2013).

Table 4.1: Design parameters of specimens

Series	**Specimen designation**	**No. of layers of FRP sheets (per side)**	**No. of FRP rods (per side)**	**FRP anchor**
P (prismatic strut)	P00	0	0	No
	P10	1	0	No
	P20	2	0	No
	P22V	2	2	No
P (Partial Bottle-shaped strut)	PB00	0	0	No
	PB10	1	0	No
	PB20	2	0	No
	PB12V	1	2	No
	PB22V	2	2	No
	PB02V	0	2	No
	PB02H	0	2	No
	PB12H	1	2	No
	PB22H	2	2	No
	PBA10	1	0	Yes
	PBA20	2	0	Yes
	PBA12V	1	2	Yes
	PBA22V	2	2	Yes
	PBA12H	1	2	Yes
	PBA22H	2	2	Yes
B (Bottle-shaped strut)	B00	0	0	No
	B10	1	0	No
	B20-1	2	0	No
	B20-2	2	0	No
	B22V	2	2	No
	BA10	1	0	Yes
	BA20	2	0	Yes
	BA22V	2	2	Yes

Table 4.2: Main properties of concrete

Concrete batch	**Average cube compressive strength (MPa)**	**Average cylinder compressive strength (MPa)**	**Tensile strength (MPa)**	**Elastic modulus (GPa)**
C1 (P00, P10, P20, P22V) (B20-2, B22V, BA22V)	42.3	34.0	2.63	31.8
C2 (PB10, PB10, PB20)	47.8	42.2	3.16	33.9
C3 (PB12V, PB22V) (PBA12V, PBA22V)	47.3	38.7	2.94	33.0
C4 (PB02V, PB02H) (PBA10, PBA20)	45.3	39.5	2.99	33.2
C5 (PB12H, PB22H) (PBA12H, PBA22H)	43.0	36.2	2.78	32.4
C6 (B00, B10, B20-1)	39.9	29.6	2.33	31.8
C7 (BA10, BA20)	28.6	23.8	1.89	28.5

Table 4.3: Main properties of carbon FRP sheet and carbon FRP rod

Carbon FRP fabric	**Tensile strength (MPa)**	**Elastic modulus (GPa)**	**Ultimate elongation**	**Design thickness (mm)**	**Design width (mm)**
Carbon FRP sheet	3800	240	1.55%	0.176	70
Carbon FRP rod	1000 (6‰)	165	8-10‰	1.4	10
	1300 (8‰)				

Table 4.4: Test results and failure modes

Series	**Specimen designation**	**Mean cylinder strength (MPa)**	**Cracking load (kN)**	**Ultimate load (kN)**	**Increase in ultimate load (%)**	**Strut efficiency factor***	**Failure mode#**
P (prismatic strut)	P00	34.0	-	281	-	0.97	CC
	P10	34.0	-	344	22%	1.19	CC/FD
	P20	34.0	-	331	18%	1.15	CC/FR
	P22V	34.0	-	369	31%	1.28	CC/FR
PB (Partial Bottle-shaped strut)	PB00	42.2	343	343	-	0.96	ST
	PB10	42.2	418	530	55%	1.48	CC
	PB20	42.2	387	565	65%	1.58	CC
	PB12V	38.7	391	520	52%	1.58	CC
	PB22V	38.7	431	593	73%	1.80	CC
	PB02V	39.5	295	295	-14%	0.88	ST
	PB02H	39.5	300	324	-5%	0.97	ST
	PB12H	36.2	373	477	39%	1.55	CC
	PB22H	36.2	381	508	48%	1.65	CC
	PBA10	39.5	349	511	49%	1.52	CC
	PBA20	39.5	431	493	44%	1.47	CC
	PBA12V	38.7	450	544	59%	1.65	CC
	PBA22V	38.7	416	589	72%	1.79	CC
	PBA12H	36.2	378	482	41%	1.57	CC
	PBA22H	36.2	390	534	56%	1.73	CC
B (Bottle-shaped strut)	B00	29.6	-	278	-	1.10	ST
	B10	29.6	328	343	23%	1.36	ST/FD
	B20-1	29.6	306	340	22%	1.35	ST/FD
	B20-2	34.0	361	421	51%	1.46	ST/FD
	B22V	34.0	345	467	68%	1.62	ST/FD
	BA10	23.8	290	333	20%	1.65	ST/FD
	BA20	23.8	292	375	35%	1.85	ST/FD
	BA22V	34.0	327	425	53%	1.47	ST/FD

*Strut efficiency factor = Ultimate load/ (0.85 × cylinder strength × bearing area);

#CC: Crushing of concrete;

FD: FRP sheets/rods de-bonding;

FR: FRP sheets/rods rupture;

ST: Splitting tensile crack.

Table 4.5: Comparison between experimental load and theoretical load

Series	Specimen designation	Mean Cylinder strength (MPa)	Ultimate load (kN)	Predicted load (kN)		$P_{u,Test}/P_{u,Pred}$	
P (Prismatic strut)	P00	34.0	281	289		0.97	
	P10	34.0	344	314		1.09	
	P20	34.0	331	340		0.97	
	P22V	34.0	369	355		1.04	
PB (Partial Bottle-shaped strut)	PB00	42.2	343	358*	$341^{\#}$	0.96*	$1.00^{\#}$
	PB10	42.2	530	479	367	1.11	1.44
	PB20	42.2	565	522	392	1.08	1.44
	PB12V	38.7	520	460	347	1.13	1.5
	PB22V	38.7	593	500	372	1.19	1.59
	PB02V	39.5	295	351	326	0.84	0.9
	PB02H	39.5	324	334	334	0.97	0.97
	PB12H	36.2	477	428	337	1.11	1.42
	PB22H	36.2	508	459	362	1.11	1.4
	PBA10	39.5	511	452	348	1.13	1.47
	PBA20	39.5	493	492	374	1.00	1.32
	PBA12V	38.7	544	460	347	1.18	1.57
	PBA22V	38.7	589	500	372	1.18	1.58
	PBA12H	36.2	482	428	337	1.12	1.43
	PBA22H	36.2	534	460	362	1.16	1.47
B (Bottle-shaped strut)	B00	29.6	278	296		0.94	
	B10	29.6	343	352		0.98	
	B20-1	29.6	340	378		0.90	
	B20-2	34.0	421	430		0.98	
	B22V	34.0	467	448		1.04	
	BA10	23.8	333	291		1.15	
	BA20	23.8	375	306		1.23	
	BA22V	34.0	425	448		0.95	

Note: Equation 4.2 for Series P specimens; Equations 4.10* (Tan's model) and $4.13^{\#}$ (EC2 model) for Series PB specimens; Equation 4.10 for Series B specimens.

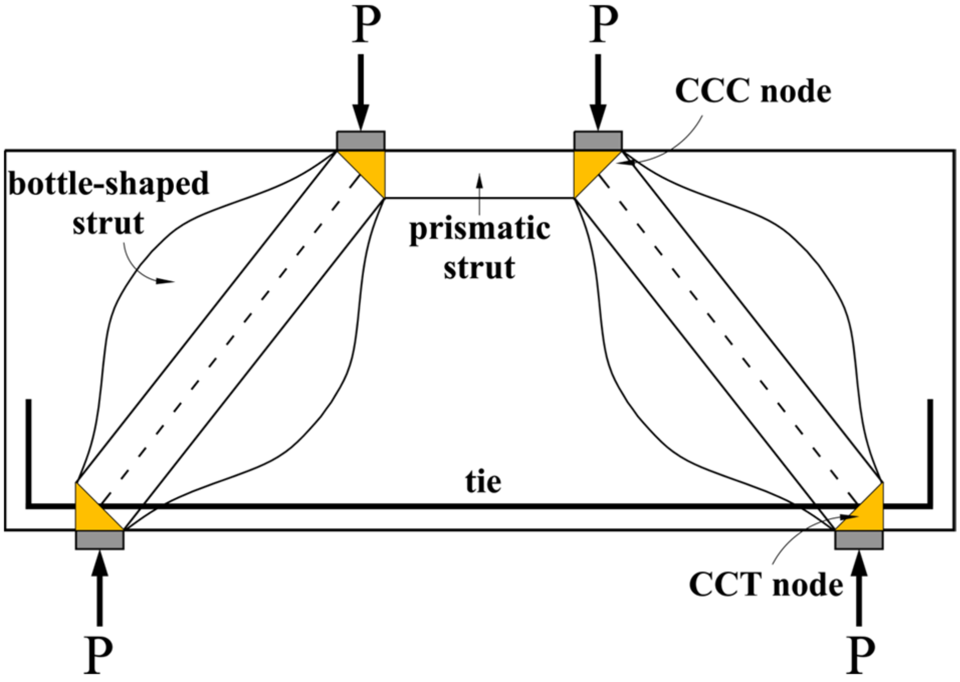

Figure 4.1: Strut-and-tie model for deep beam

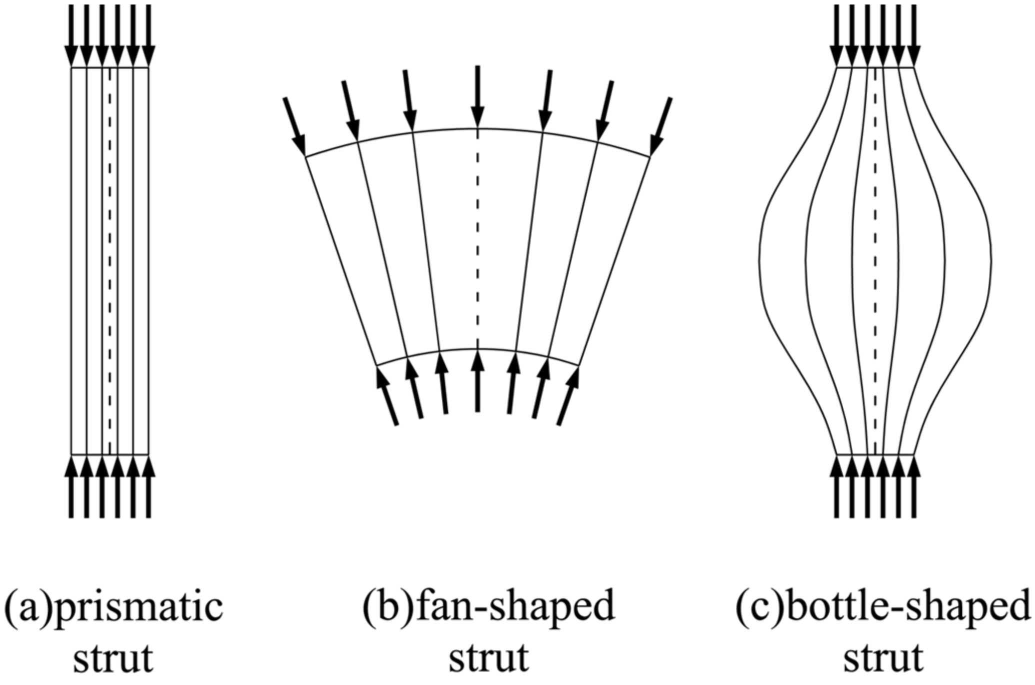

Figure 4.2: Different types of struts

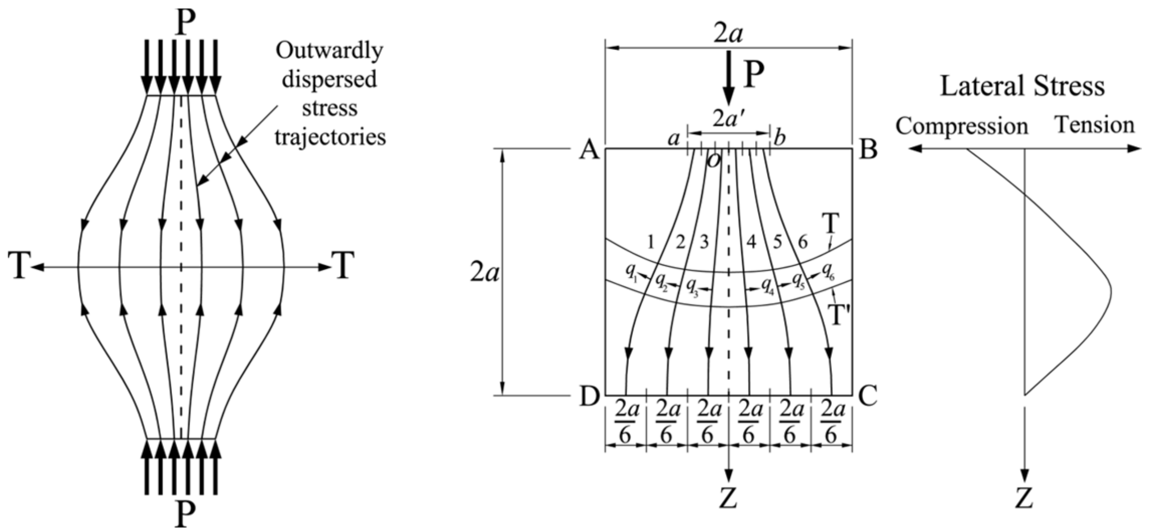

Figure 4.3: Stress trajectories in a bottle-shaped strut (Sahoo *et al.* 2009)

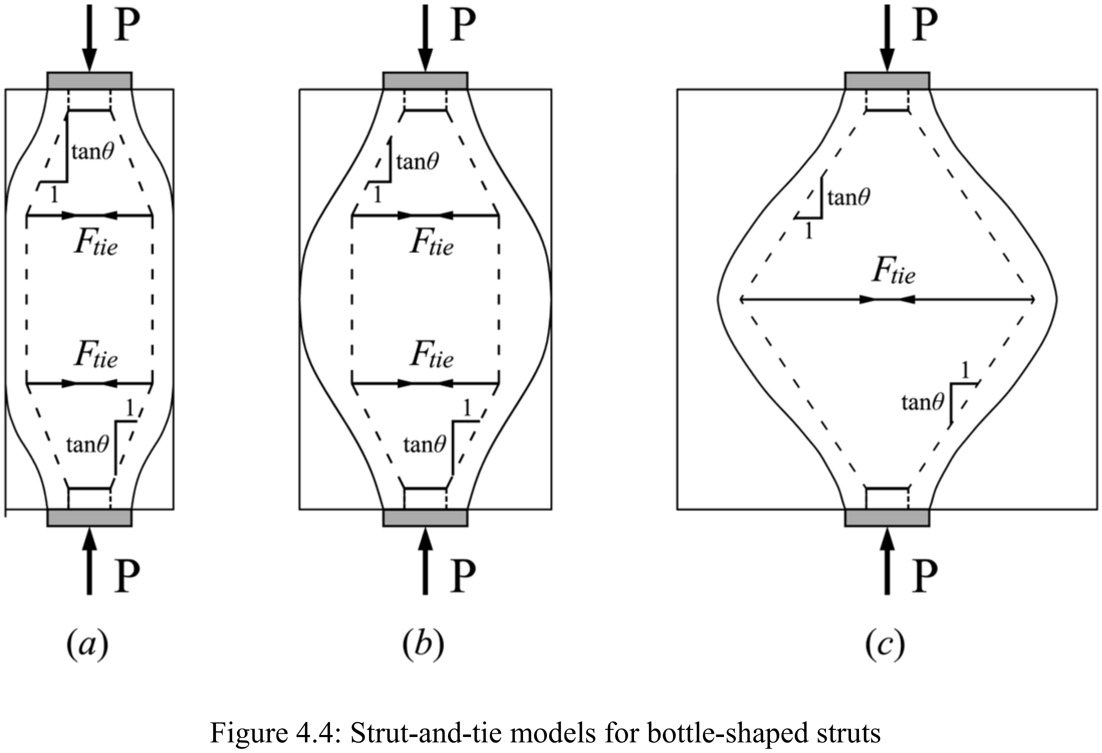

Figure 4.4: Strut-and-tie models for bottle-shaped struts

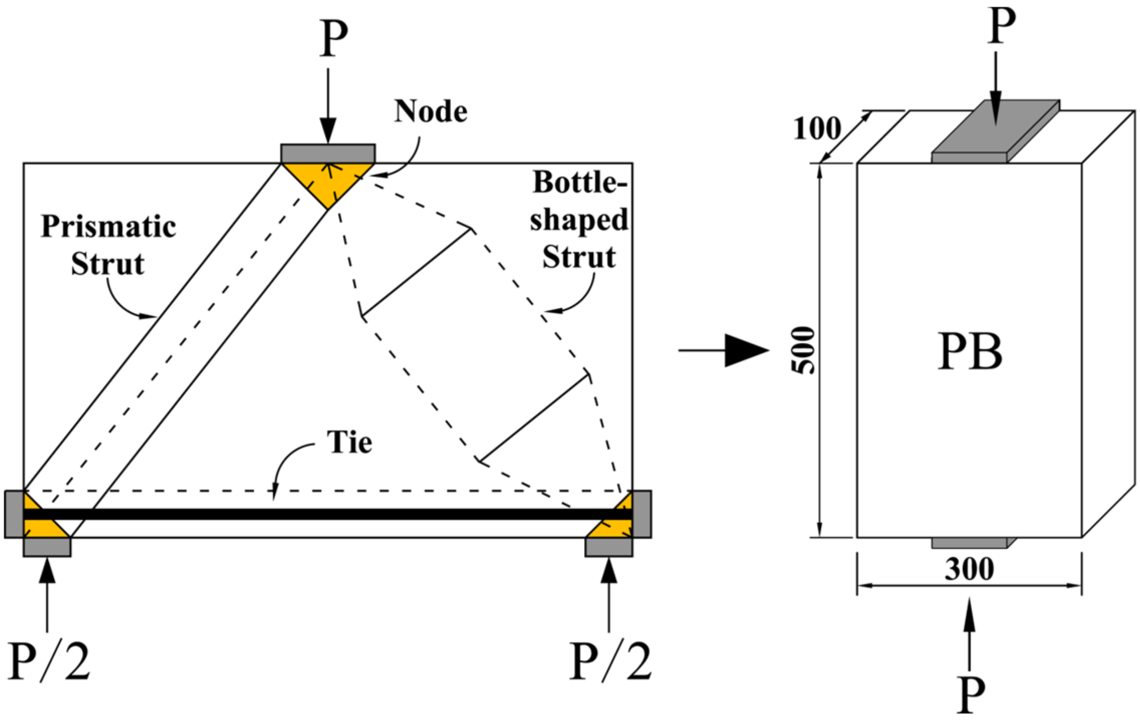

(a) Idealization of strut member

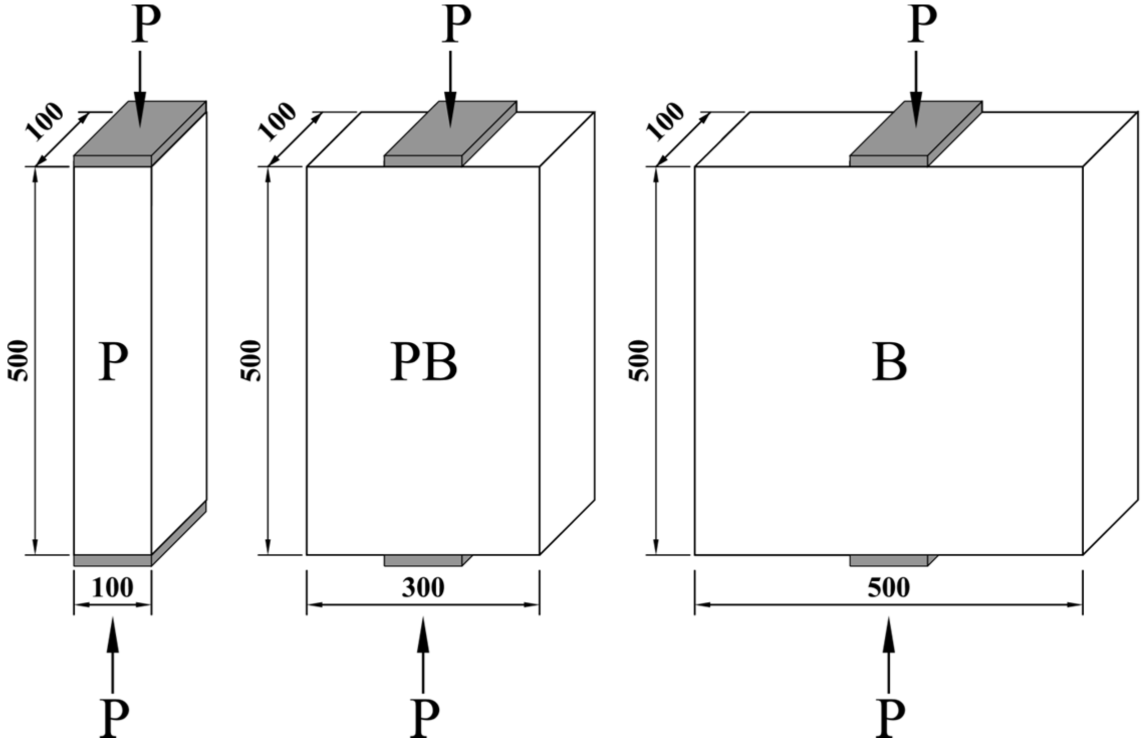

(b) Series P, PB and B

Figure 4.5: Dimensions of test specimens (all dimensions in mm)

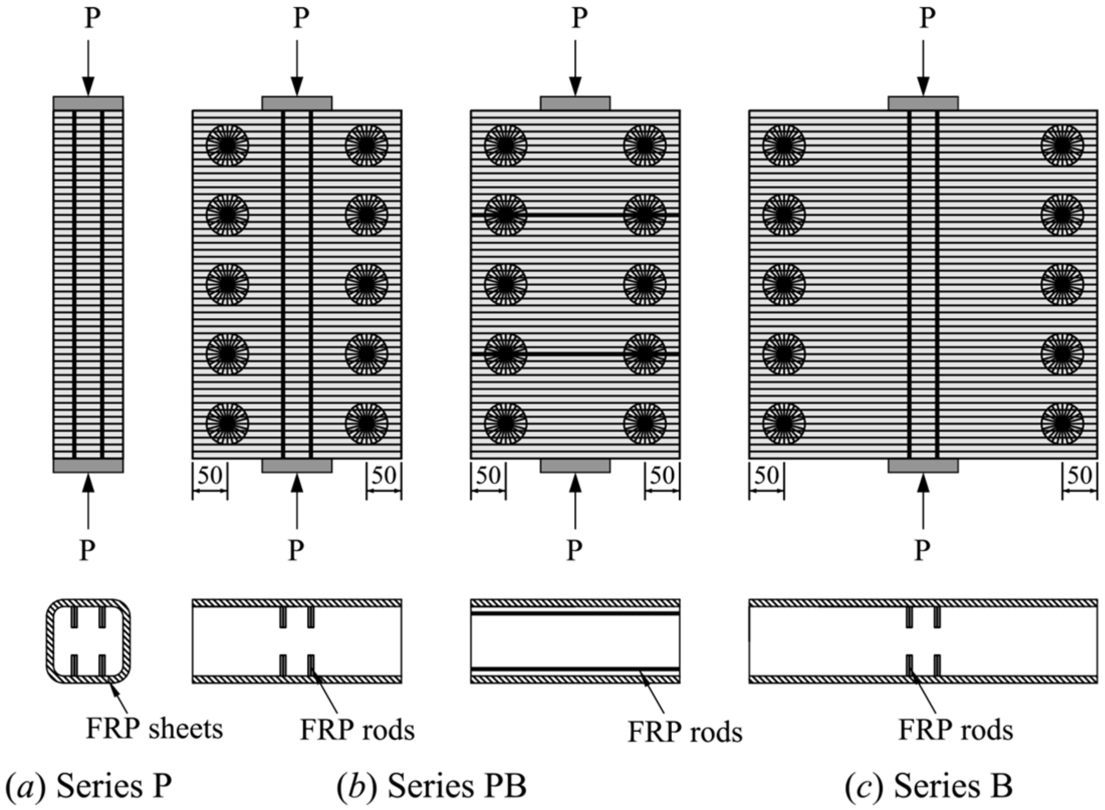

(a) Front view

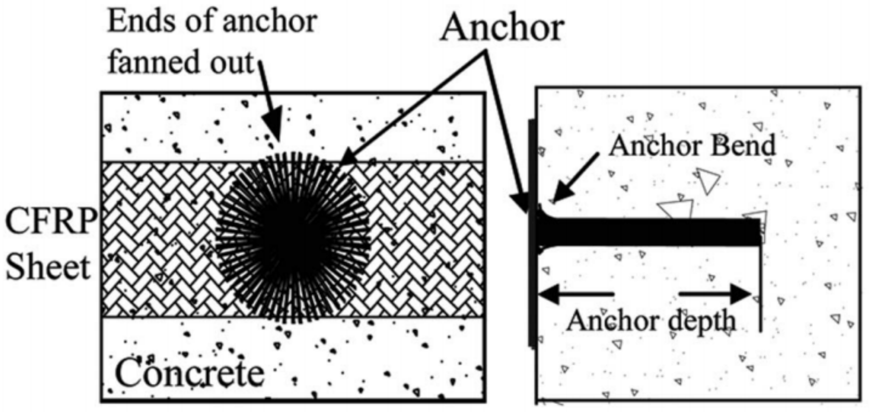

(b) Close-up view of carbon FRP anchor (Orton, Jirsa and Bayrak 2008)

Figure 4.6: FRP strengthening systems

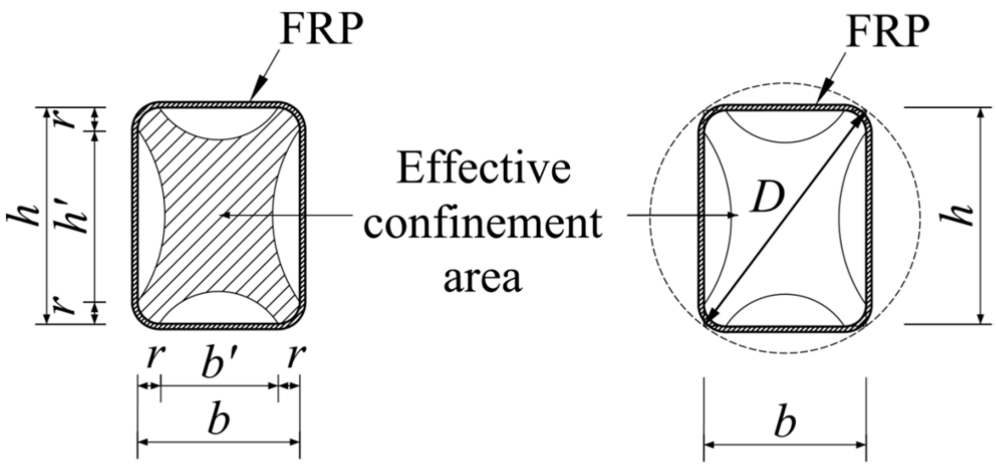

Figure 4.7: FRP-confined rectangular sections (Lam and Teng, 2003)

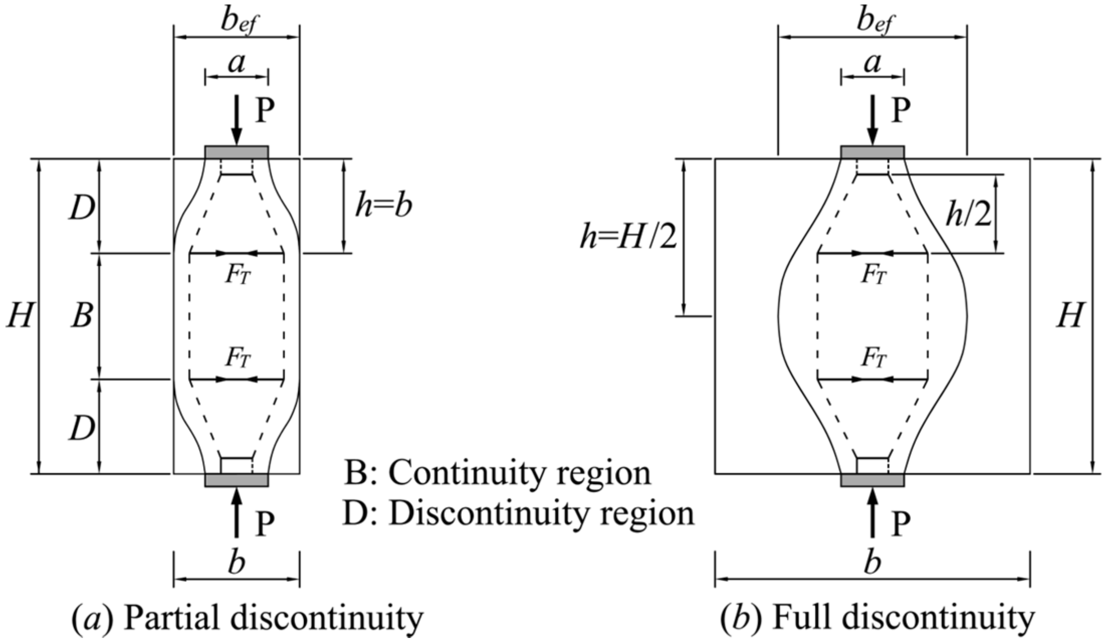

(*a*) Partial discontinuity
(*b*) Full discontinuity

Figure 4.8: Struts with regions of partial and full discontinuity (Eurocode 2 2004)

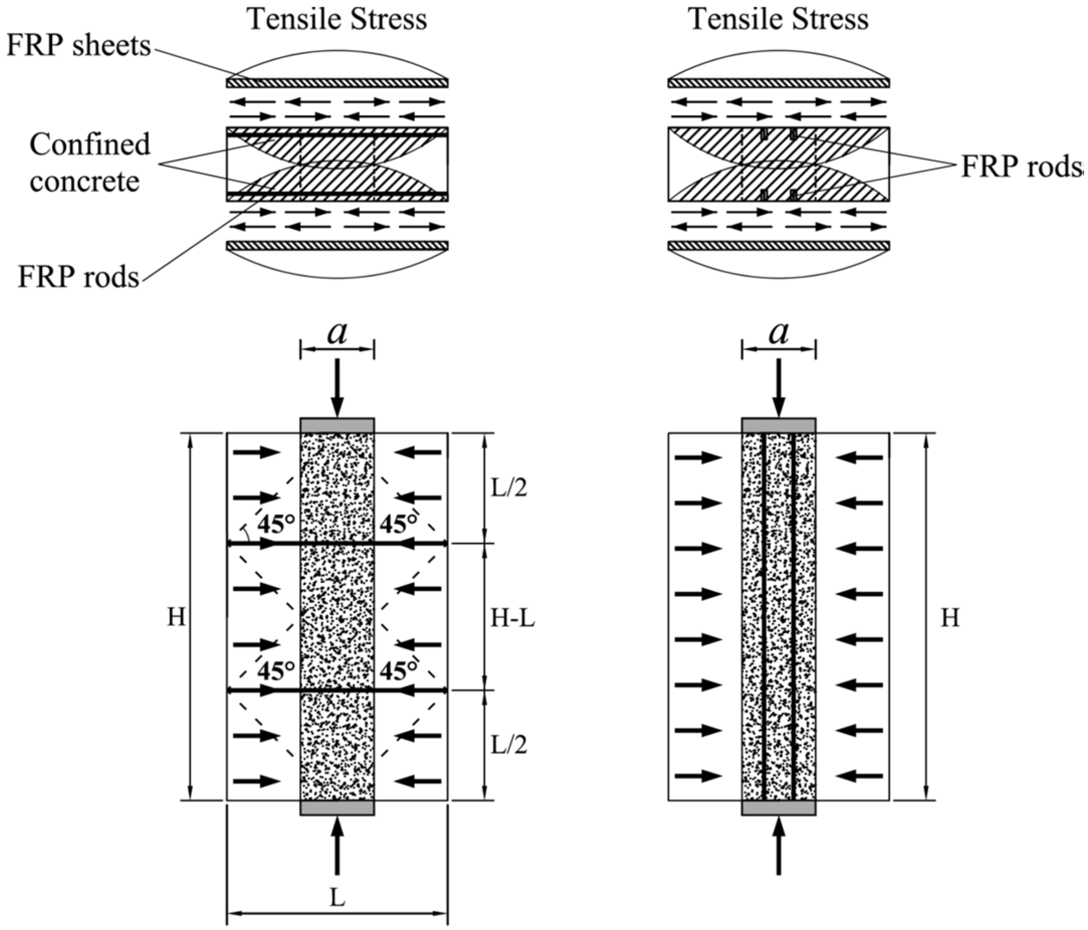

(a) Confinement model

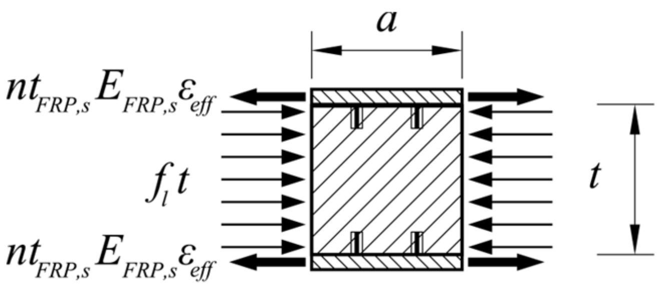

(b) Confinement model

Figure 4.9: Confinement model for FRP strengthened partial bottle-shaped struts

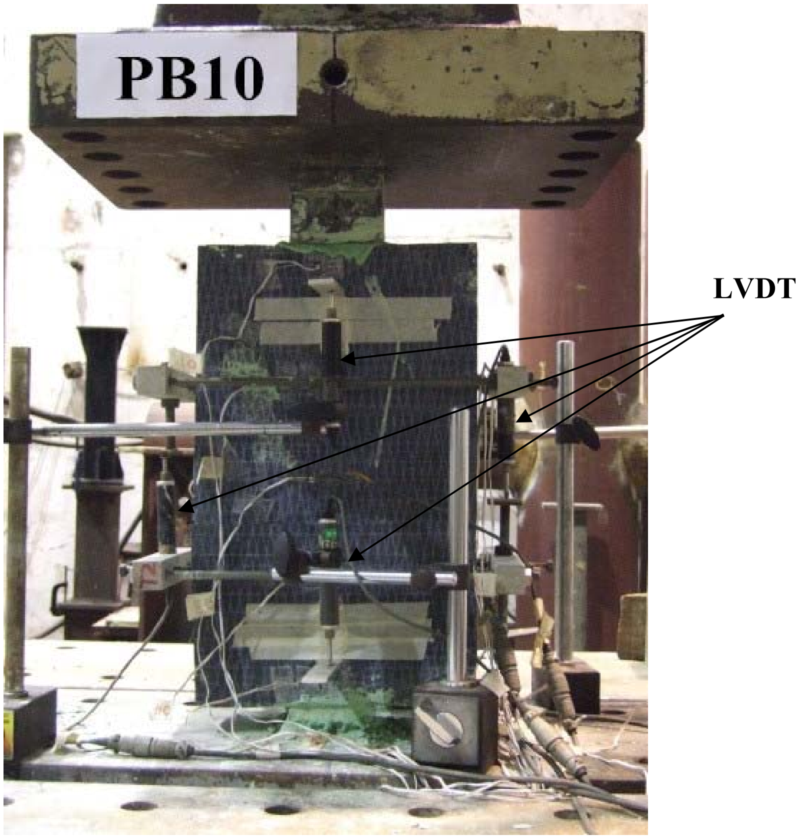

Figure 4.10: Test set up

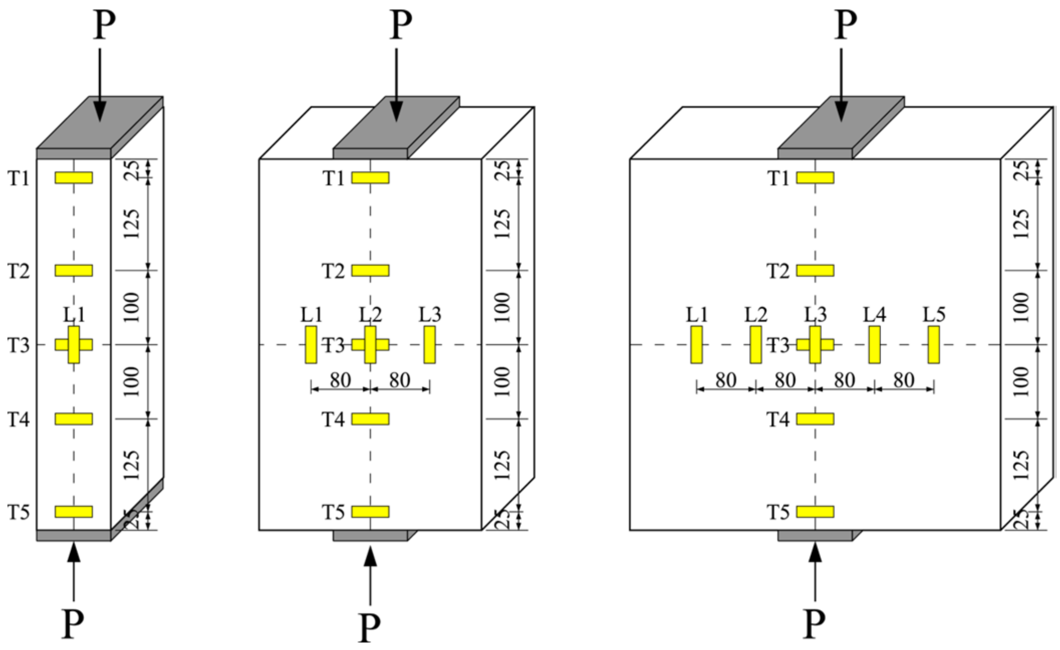

(a) Strain gauges on concrete surface

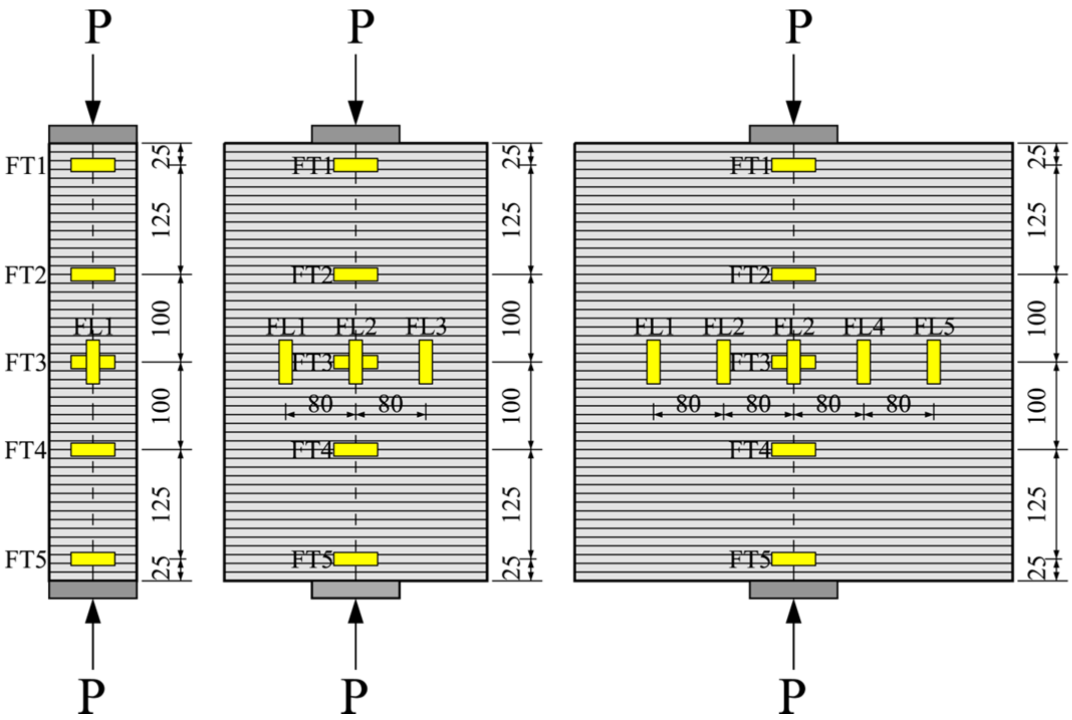

(b) Strain gauges on transverse FRP sheets

Figure 4.11: Locations of strain gauges (cont.)

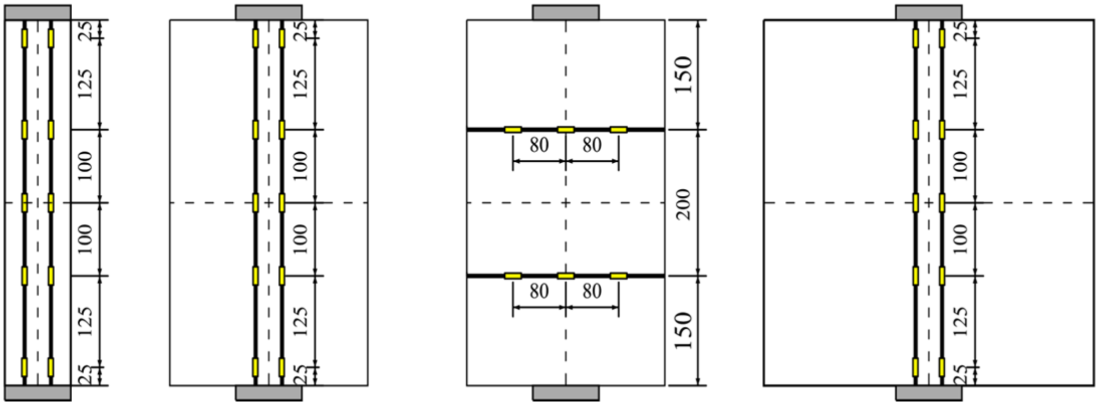

(c) Strain gauges on FRP rods

Figure 4.11: Locations of strain gauges

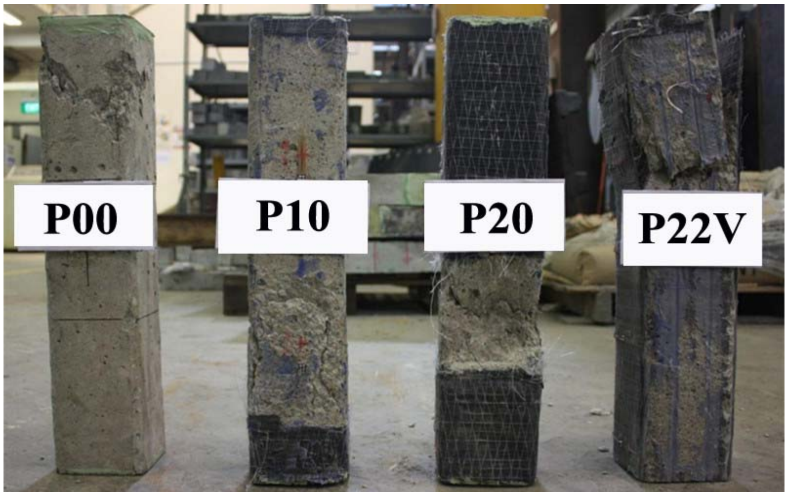

(a) Series P (prismatic strut)

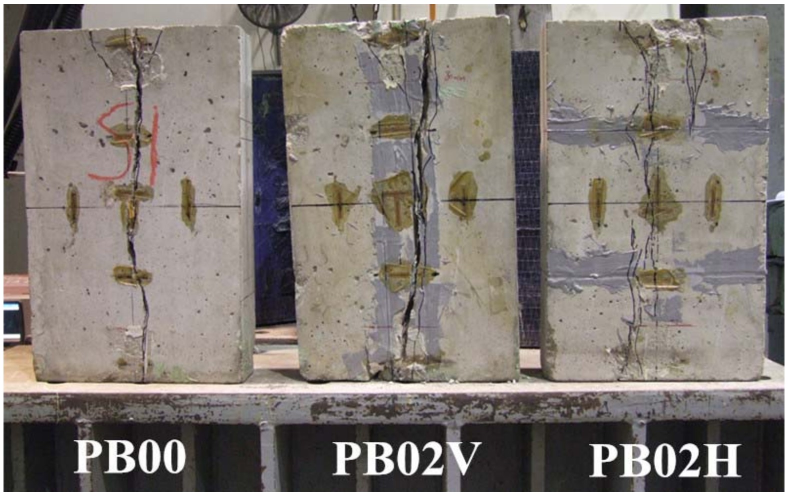

(b) Series PB (partial bottle-shaped strut) with NSM-FRP rods only

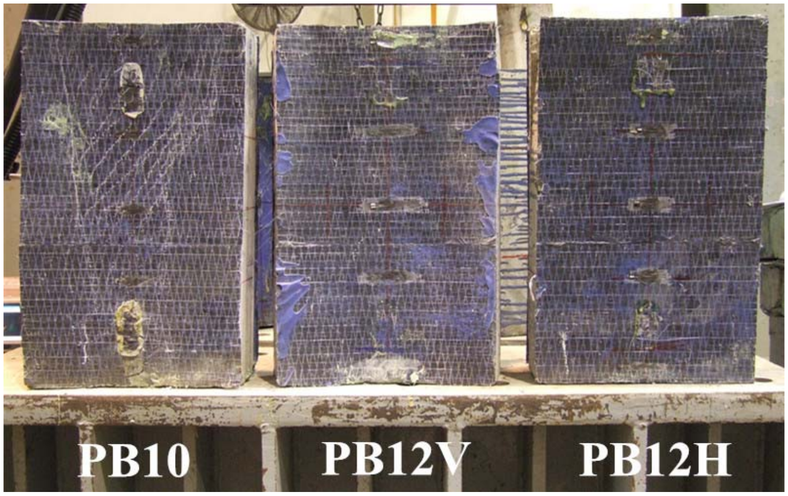

(c) Series PB (partial bottle-shaped strut) with FRP sheets and rods

Figure 4.12: Failure modes of strut specimens (cont.)

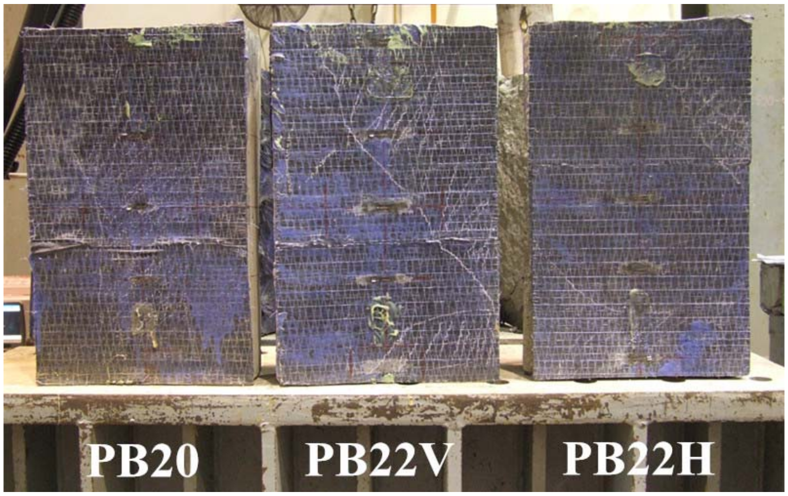

(d) Series PB (partial bottle-shaped strut) with FRP sheets and rods

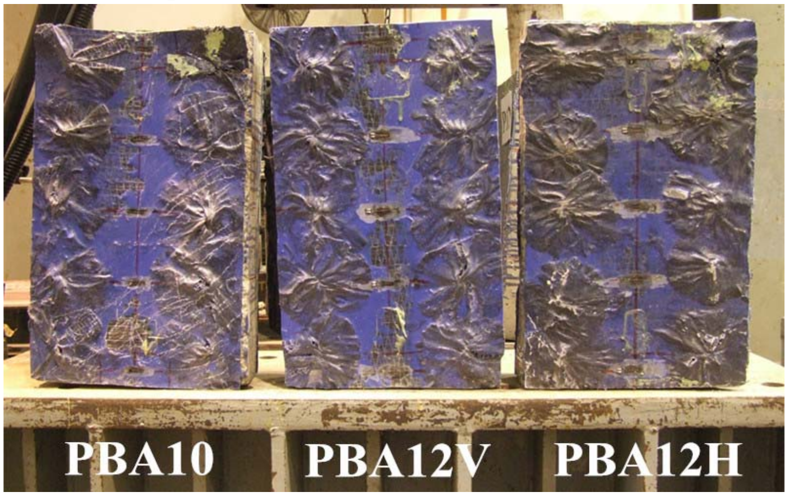

(e) Series PB (partial bottle-shaped strut) with anchored FRP sheets

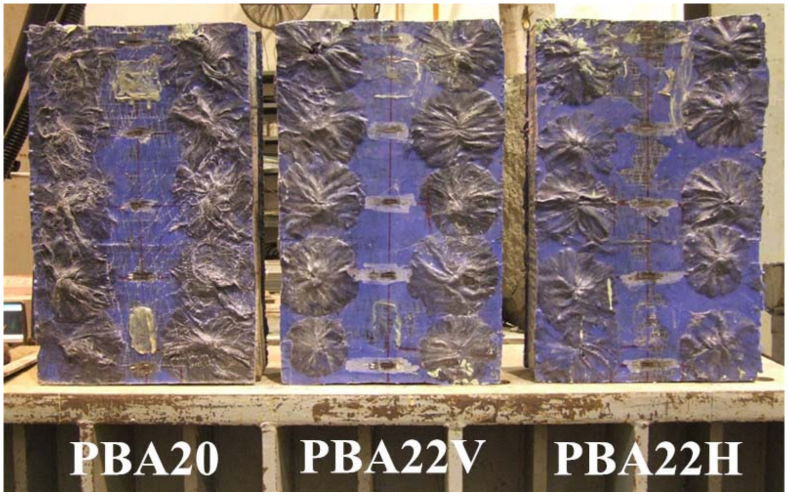

(f) Series PB (partial bottle-shaped strut) with anchored FRP sheets

Figure 4.12: Failure modes of strut specimens (cont.)

(g) Series B (bottle-shaped strut)

(h) Series B (bottle-shaped strut) with FRP sheets and rods

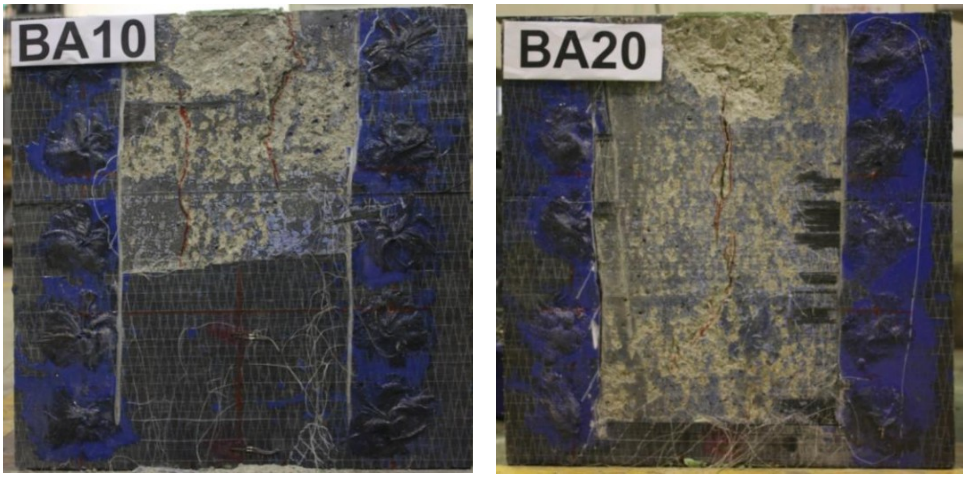

(i) Series B (bottle-shaped strut) with anchored FRP sheets

Figure 4.12: Failure modes of strut specimens (cont.)

(j) Series B (bottle-shaped strut) with FRP sheets and rods

Figure 4.12: Failure modes of strut specimens

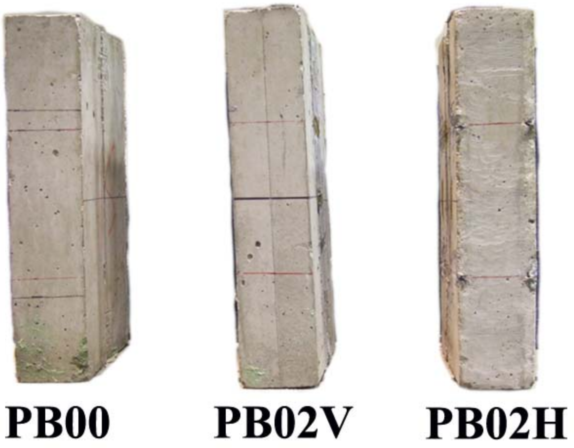

(a) Series PB (partial bottle-shaped strut) with NSM-FRP rods only

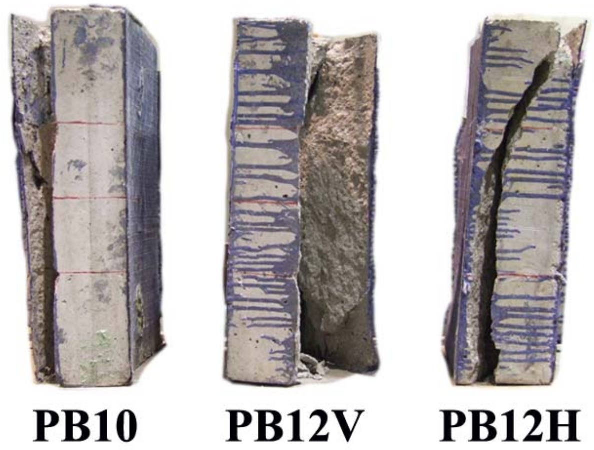

(b) Series PB (partial bottle-shaped strut) with FRP sheets and rods

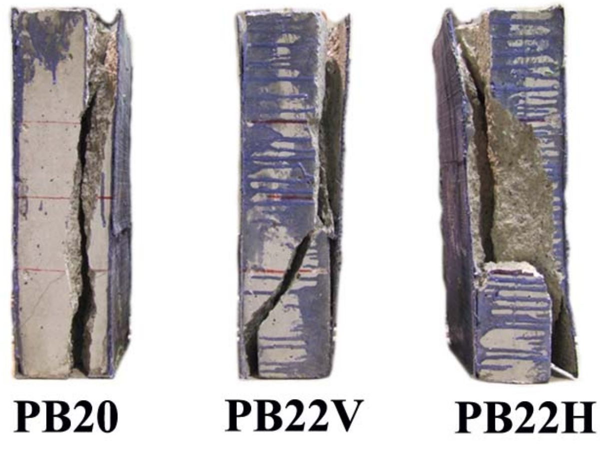

(c) Series PB (partial bottle-shaped strut) with FRP sheets and rods

Figure 4.13: Failure mode of Series PB strut specimens (side view) (cont.)

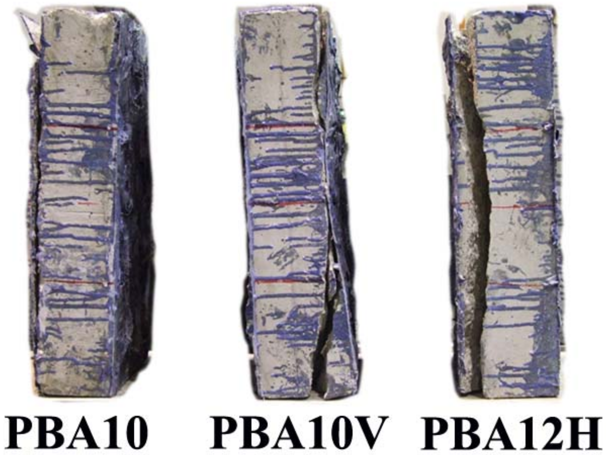

(d) Series PB (partial bottle-shaped strut) with anchored FRP sheets

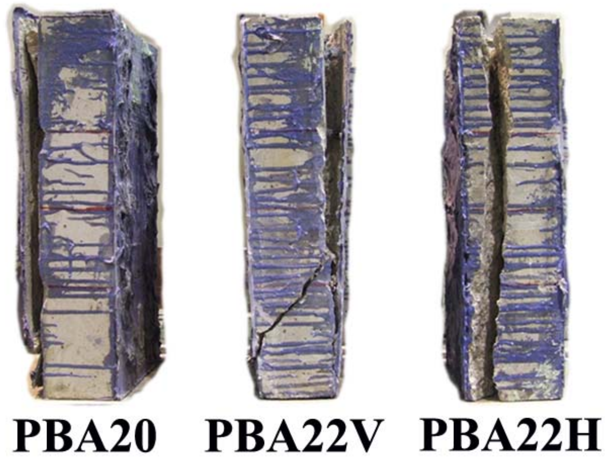

(e) Series PB (partial bottle-shaped strut) with anchored FRP sheets

Figure 4.13: Failure mode of Series PB strut specimens (side view)

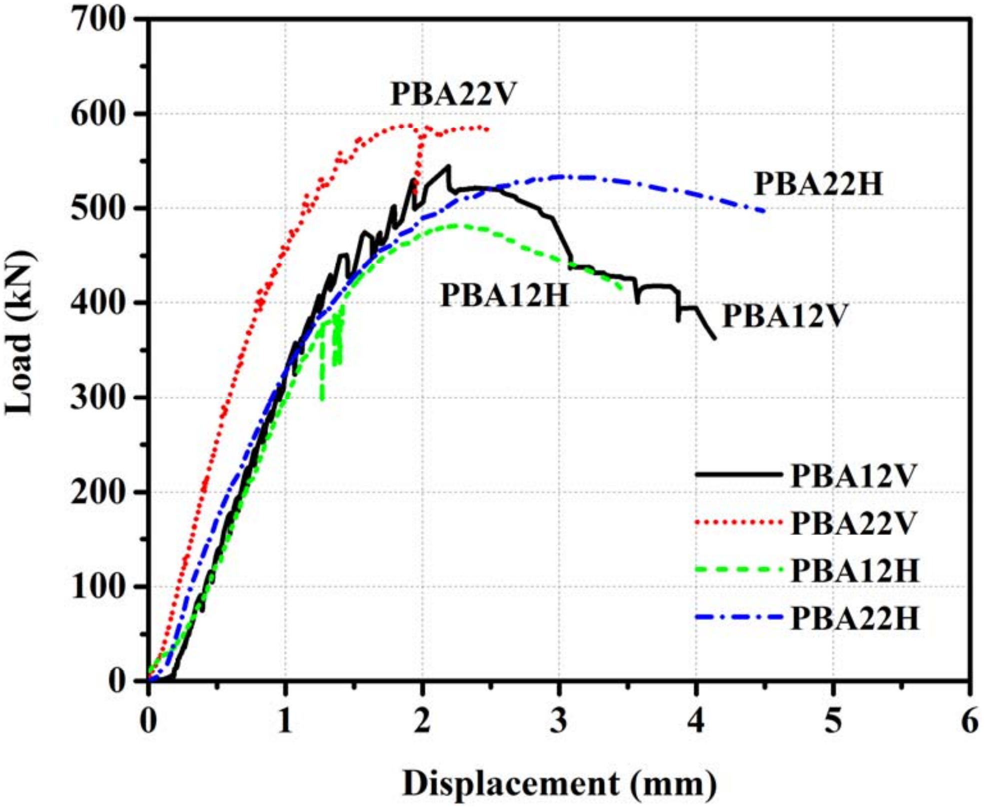

Figure 4.14: Load-deformation relations of specimens

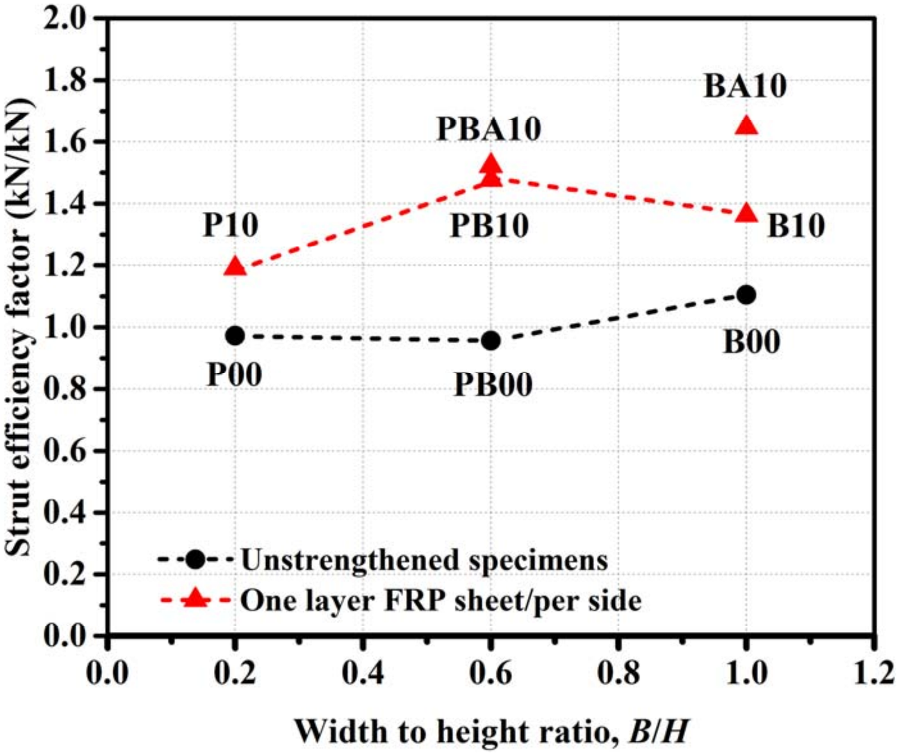

(a) Specimens with one layer FRP sheet/per side

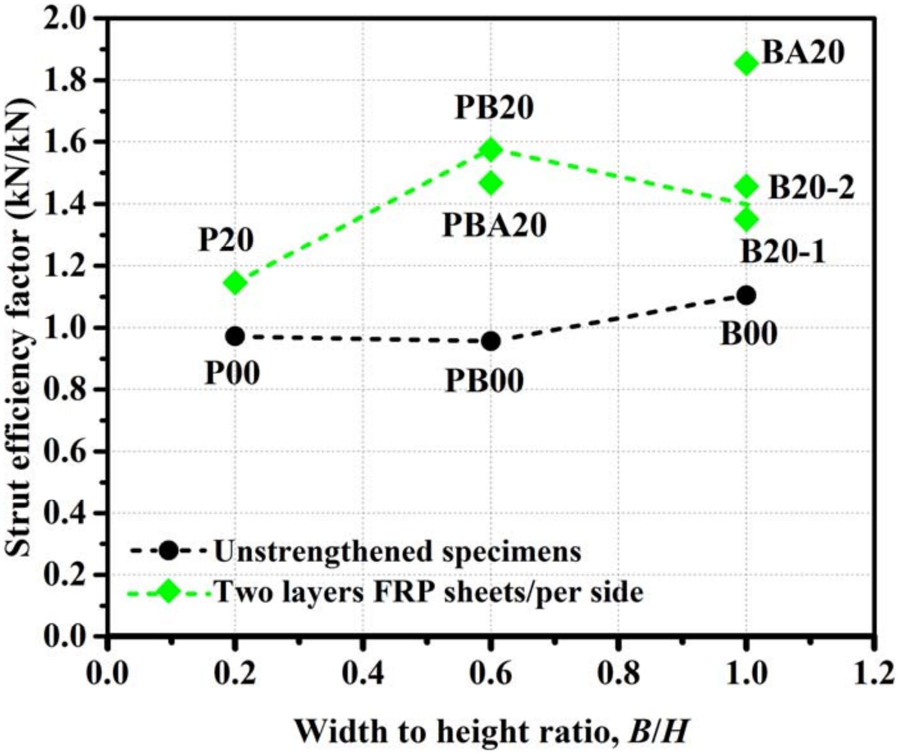

(b) Specimens with two layers FRP sheet/per side

Figure 4.15: Effect of the width to height ratio (cont.)

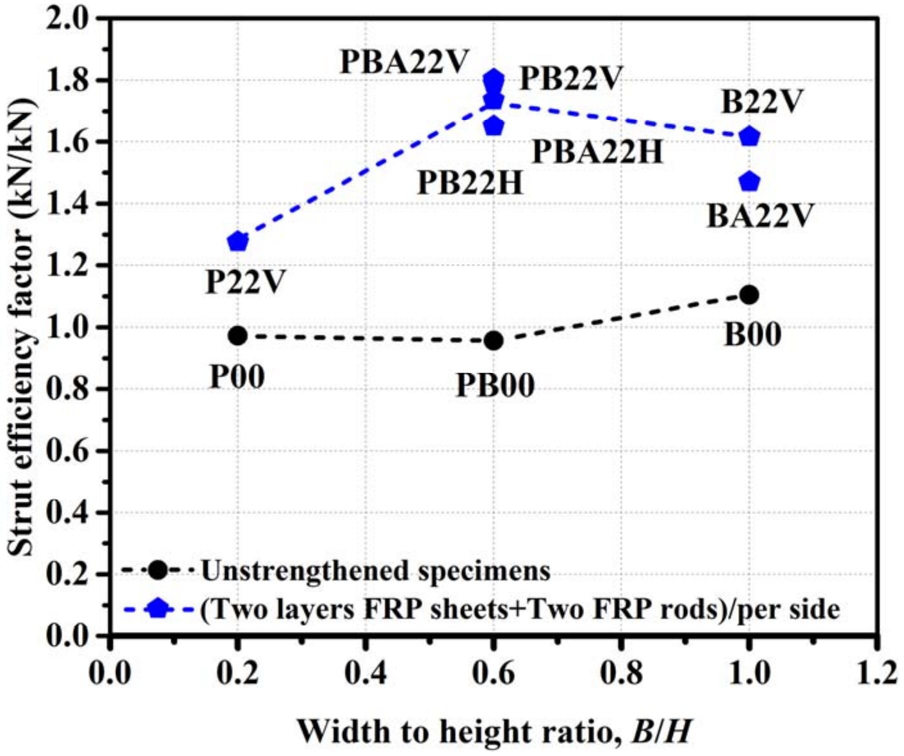

(c) Specimens with two layers FRP sheet and two FRP rods/per side

Figure 4.15: Effect of the width to height ratio

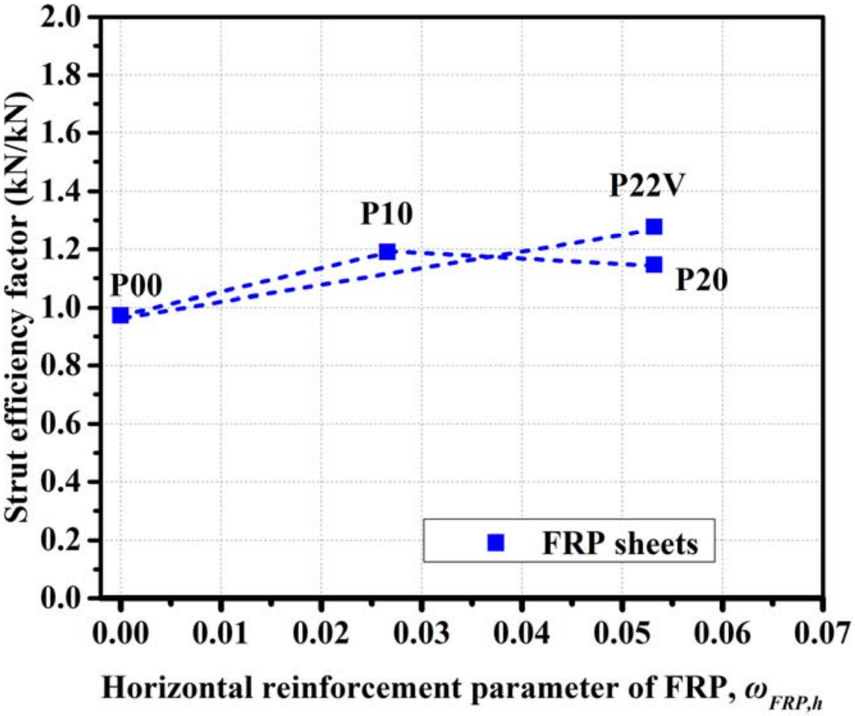

(a) Series P specimens

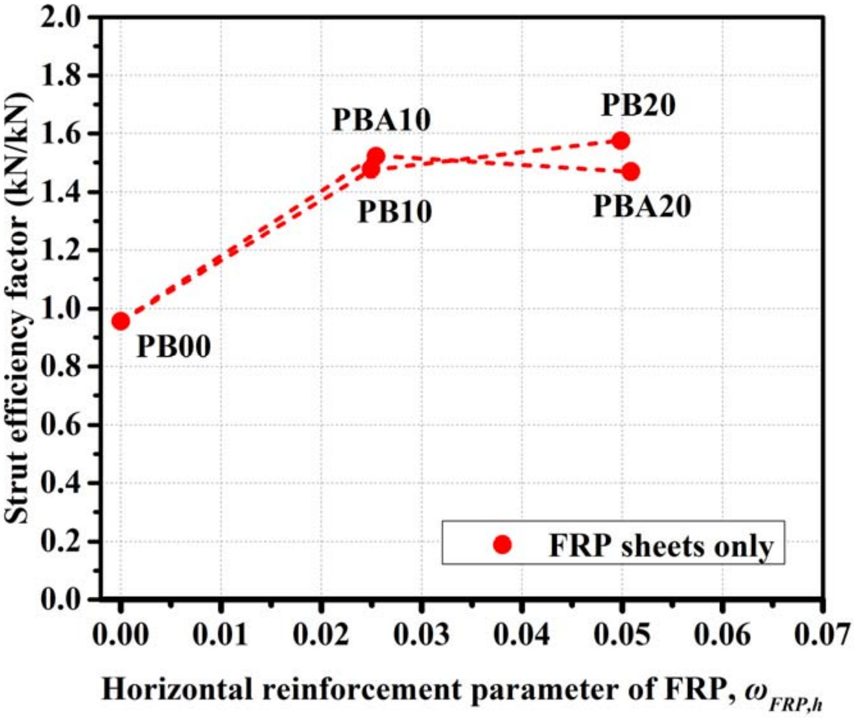

(b) Series PB specimens

Figure 4.16: Relation between normalized ultimate load and the horizontal FRP reinforcement parameter (cont.)

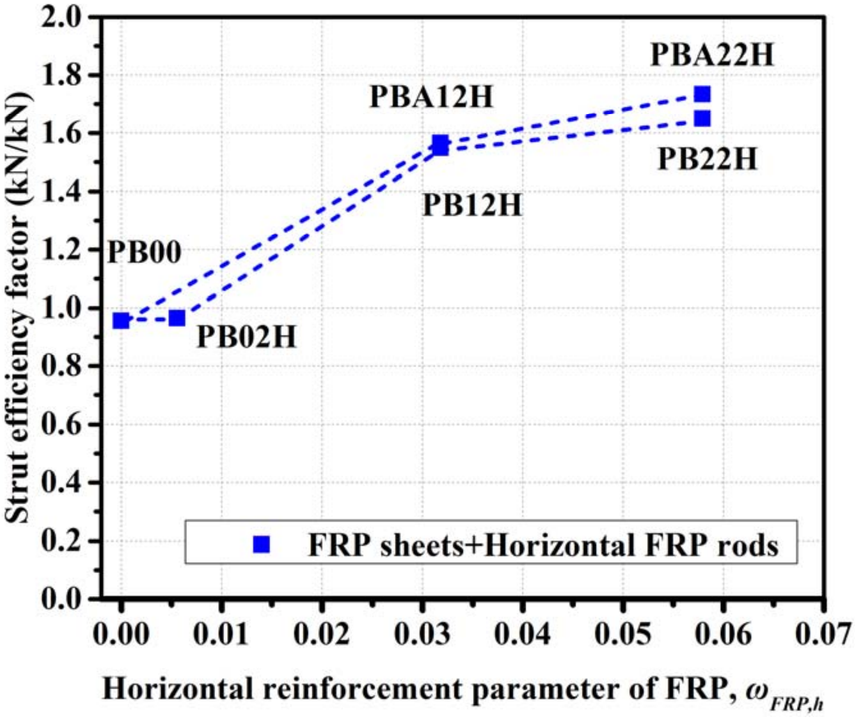

(c) Series PB specimens

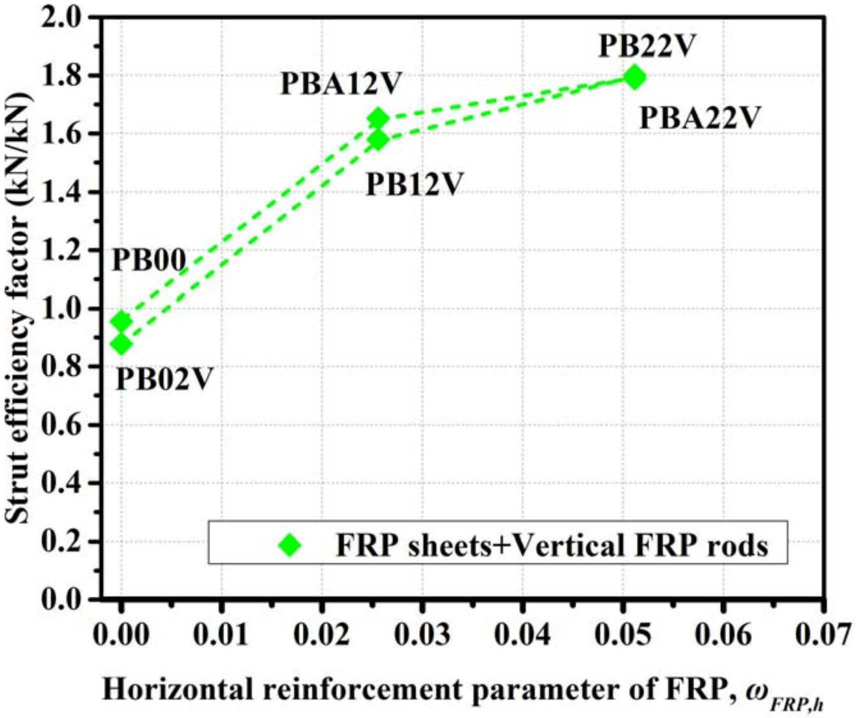

(d) Series PB specimens

Figure 4.16: Relation between normalized ultimate load and the horizontal FRP reinforcement parameter (cont.)

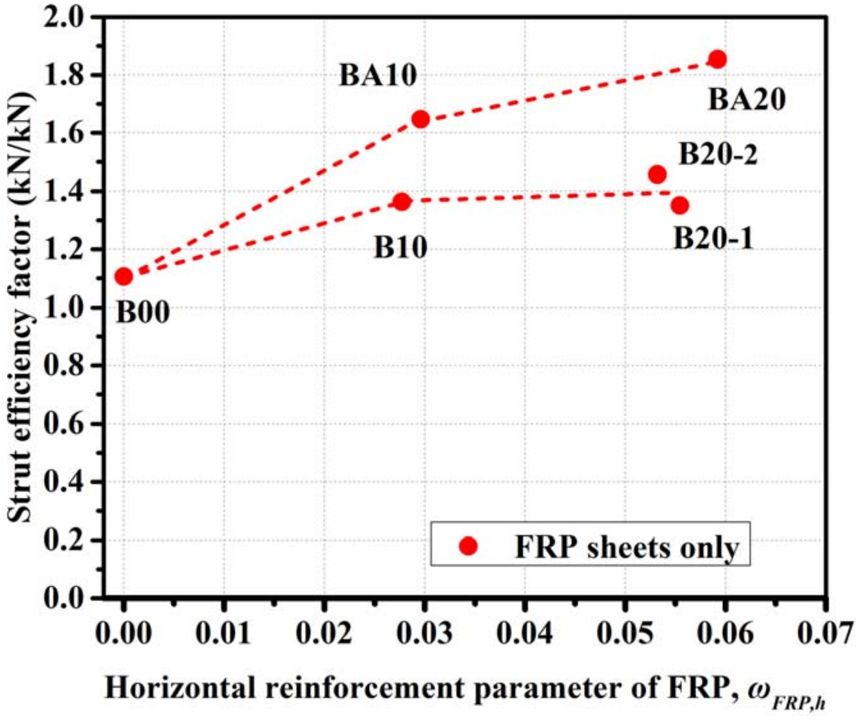

(e) Series B specimens

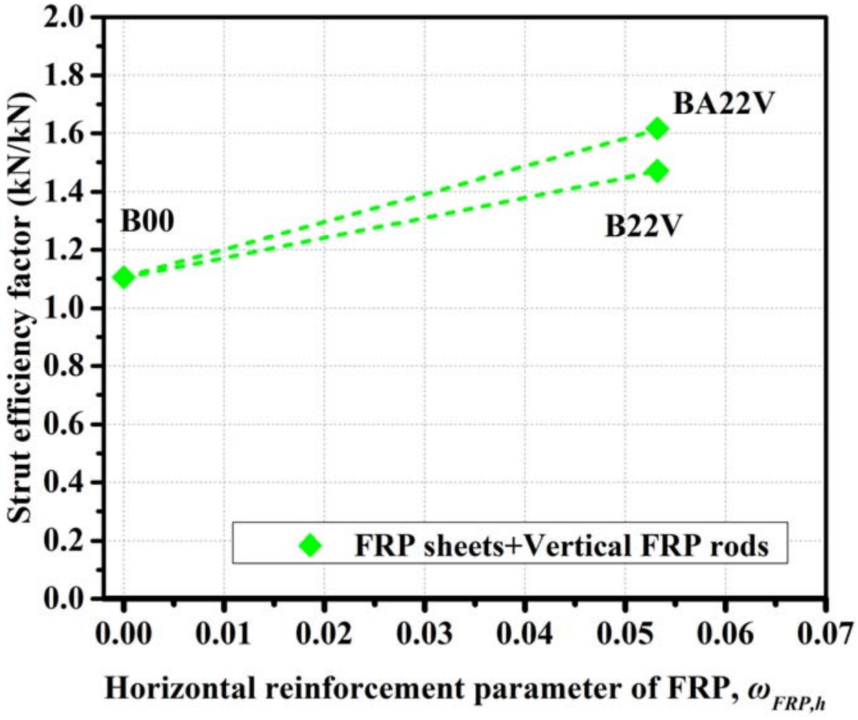

(f) Series B specimens

Figure 4.16: Relation between normalized ultimate load and the horizontal FRP reinforcement parameter

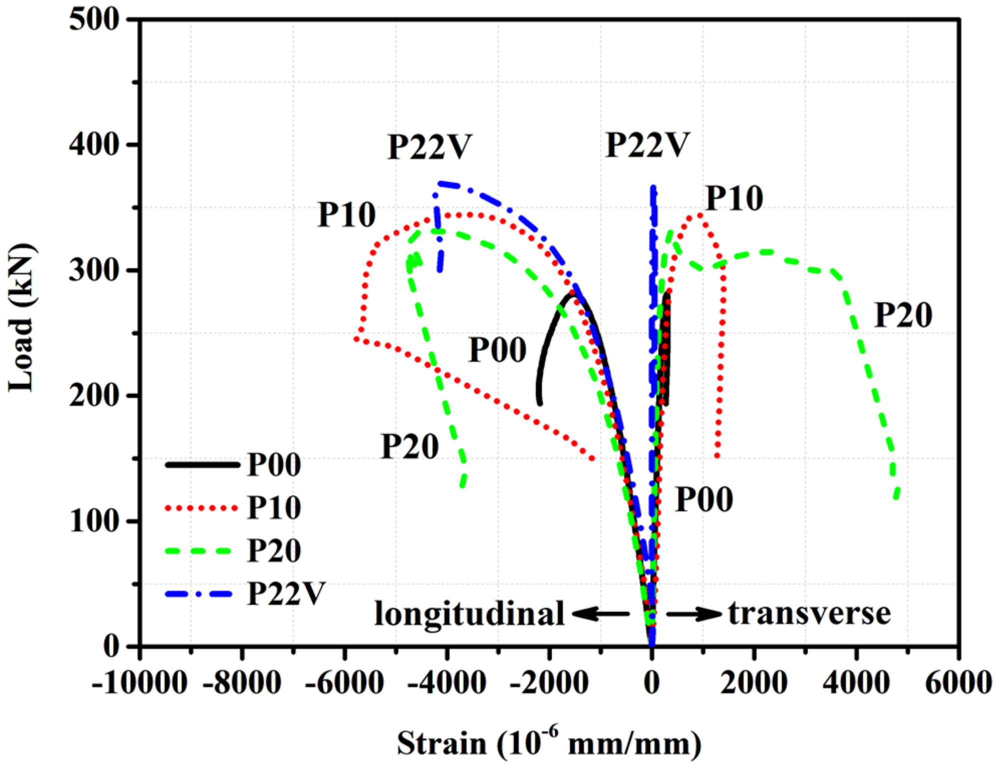

(a) Series P specimens

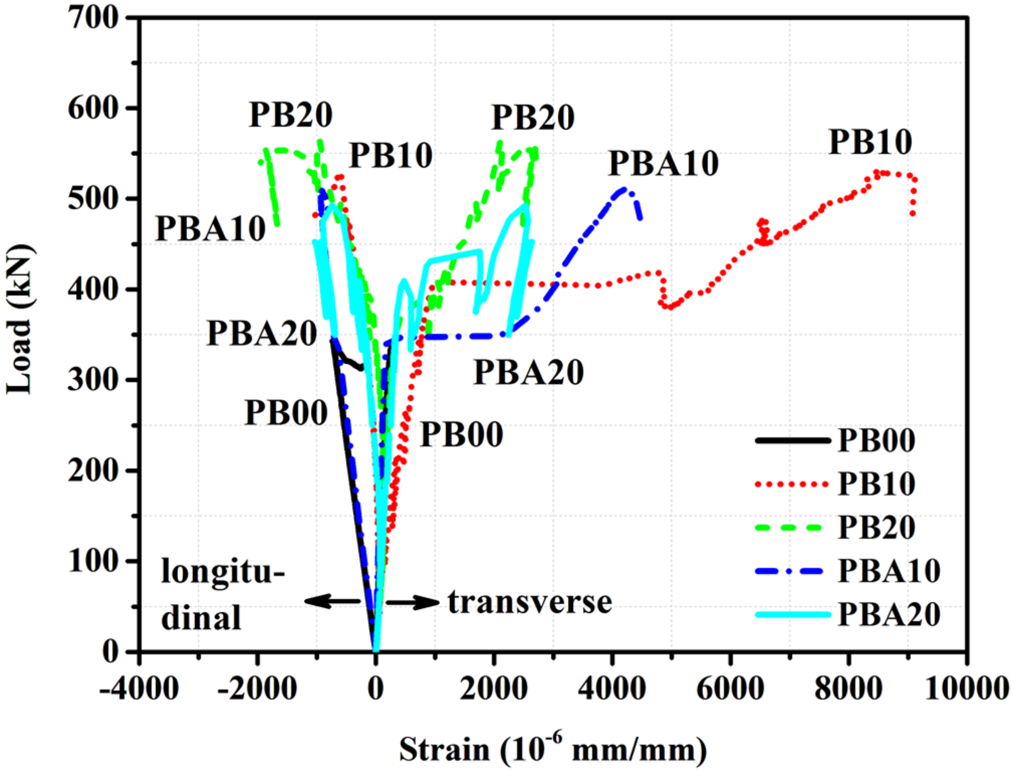

(b) Series PB specimens (with FRP sheets only)

Figure 4.17: Load-strain relations at mid-height of strut (cont.)

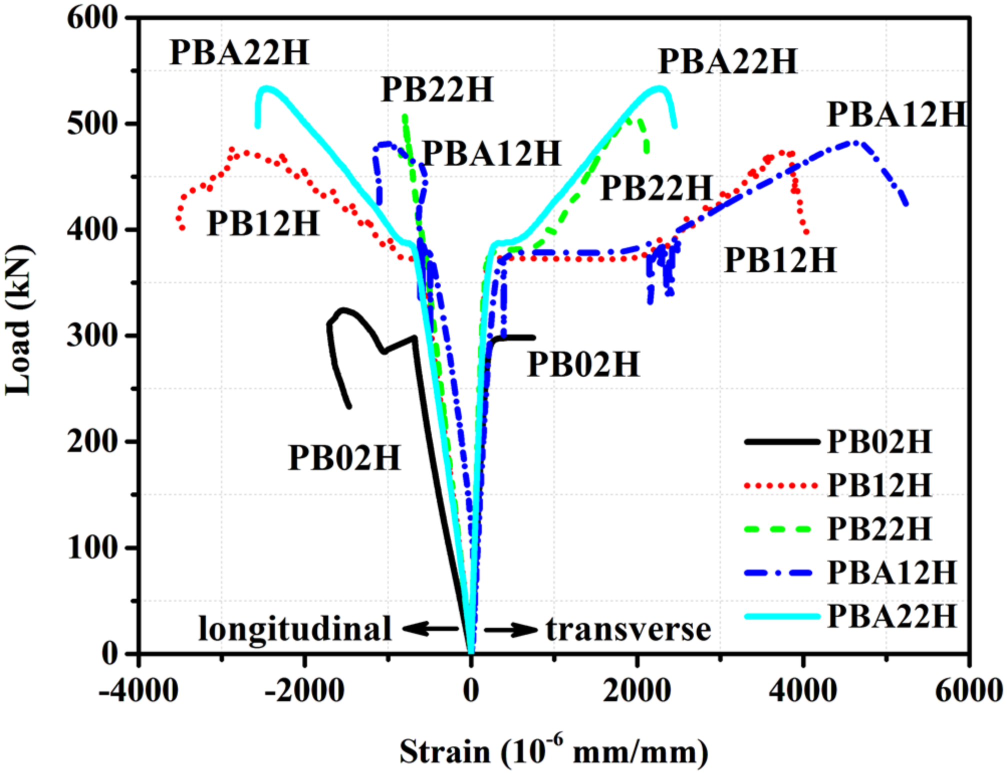

(c) Series PB specimens (with horizontal FRP rods)

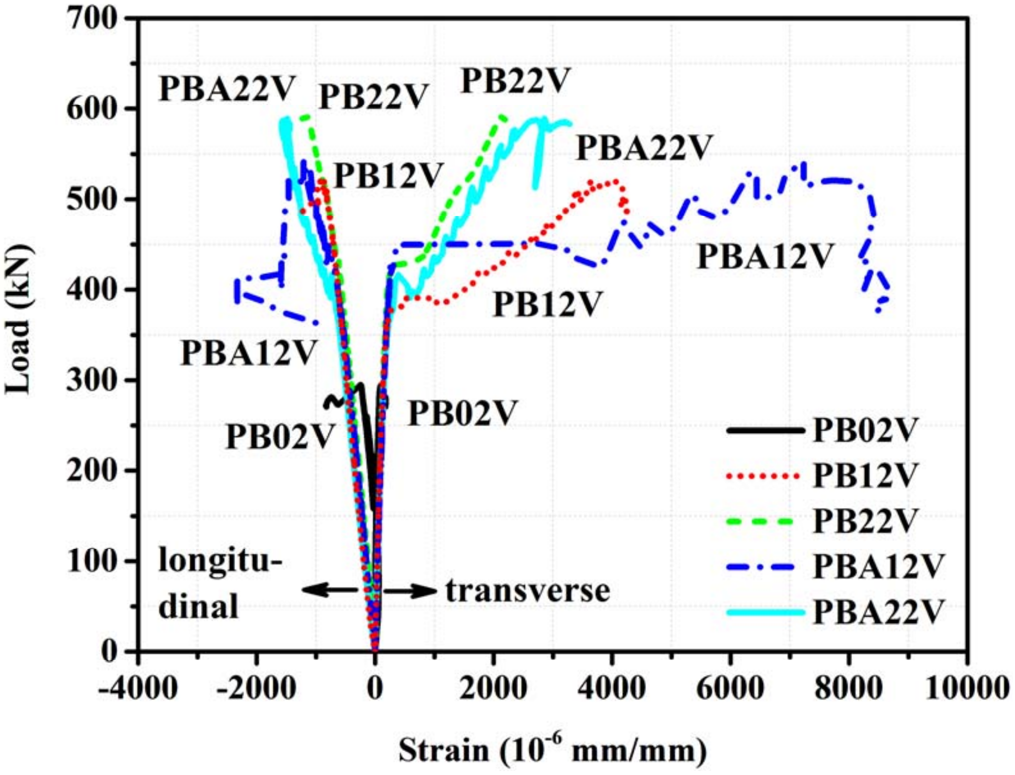

(d) Series PB specimens (with vertical FRP rods)

Figure 4.17: Load-strain relations at mid-height of strut (cont.)

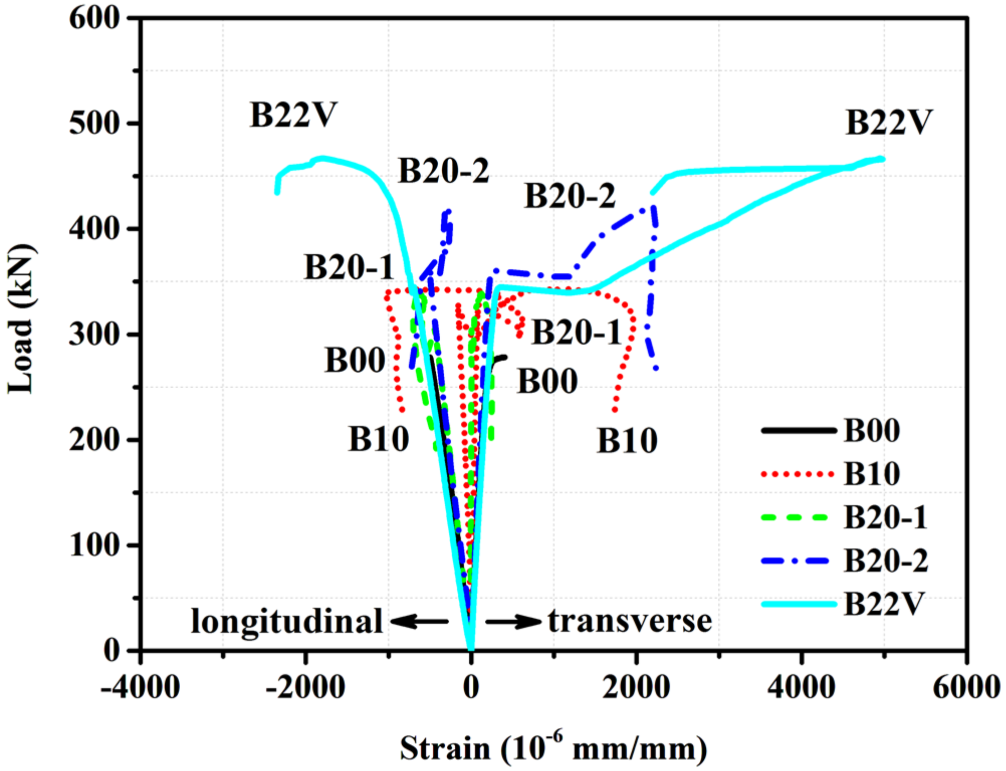

(e) Series B specimens (without anchors)

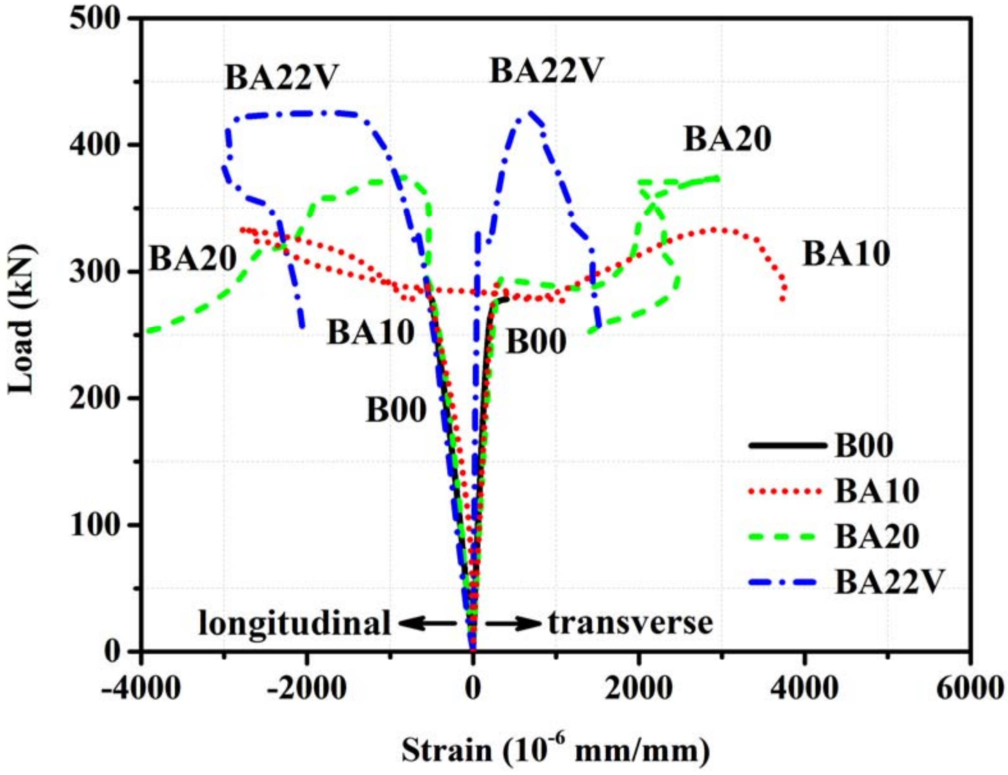

(f) Series B specimens (with anchors)

Figure 4.17: Load-strain relations at mid-height of strut

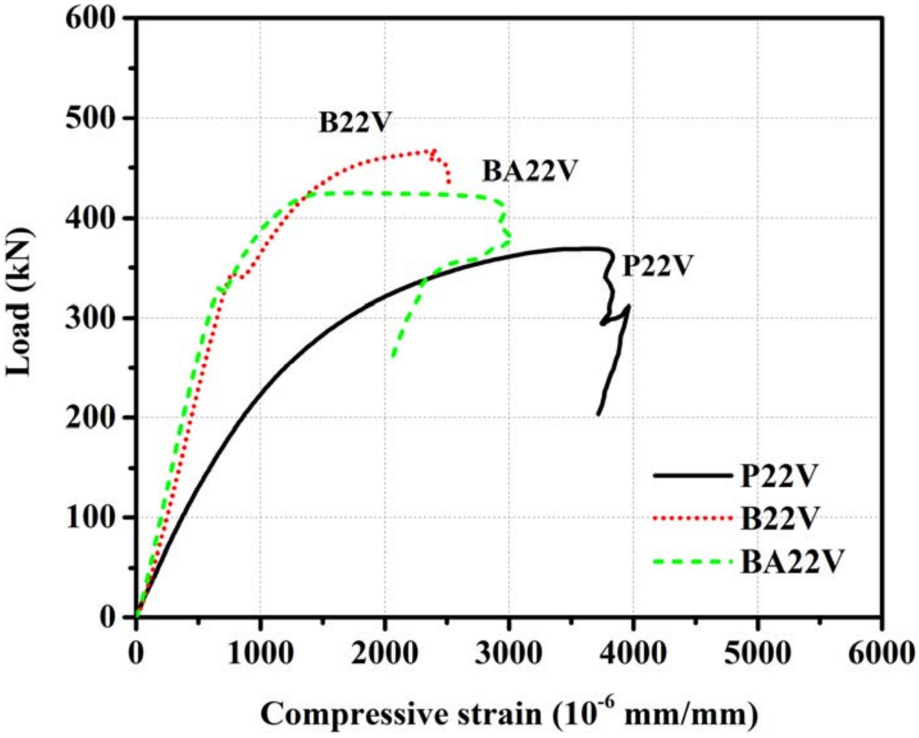

(a) Vertical FRP rods in Series P and B

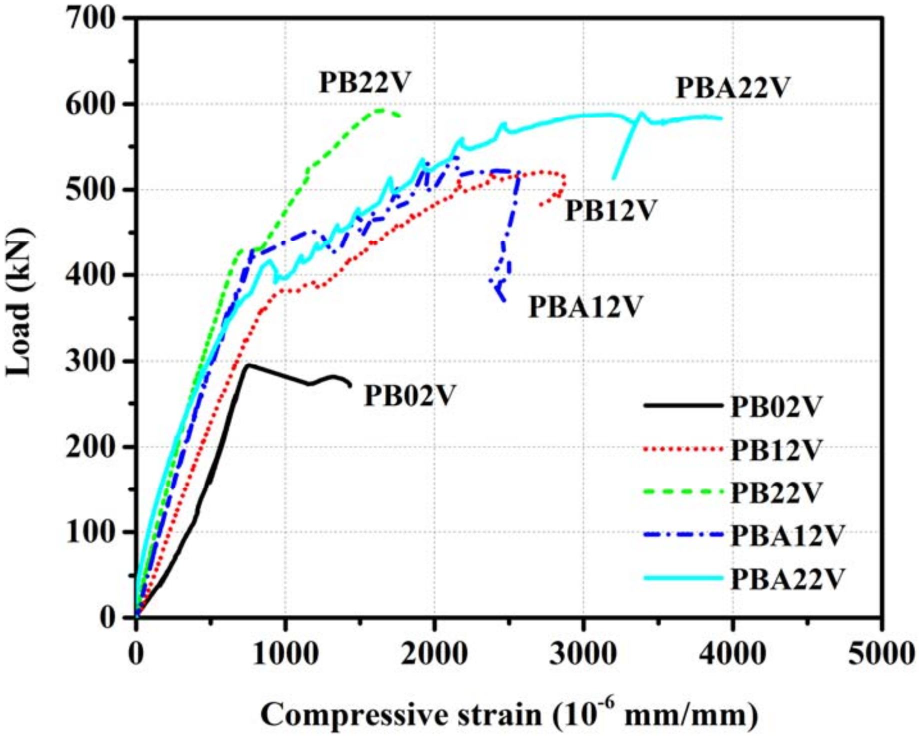

(b) Vertical FRP rods in Series PB

Figure 4.18: Load-strain relations for NSM FRP rods (cont.)

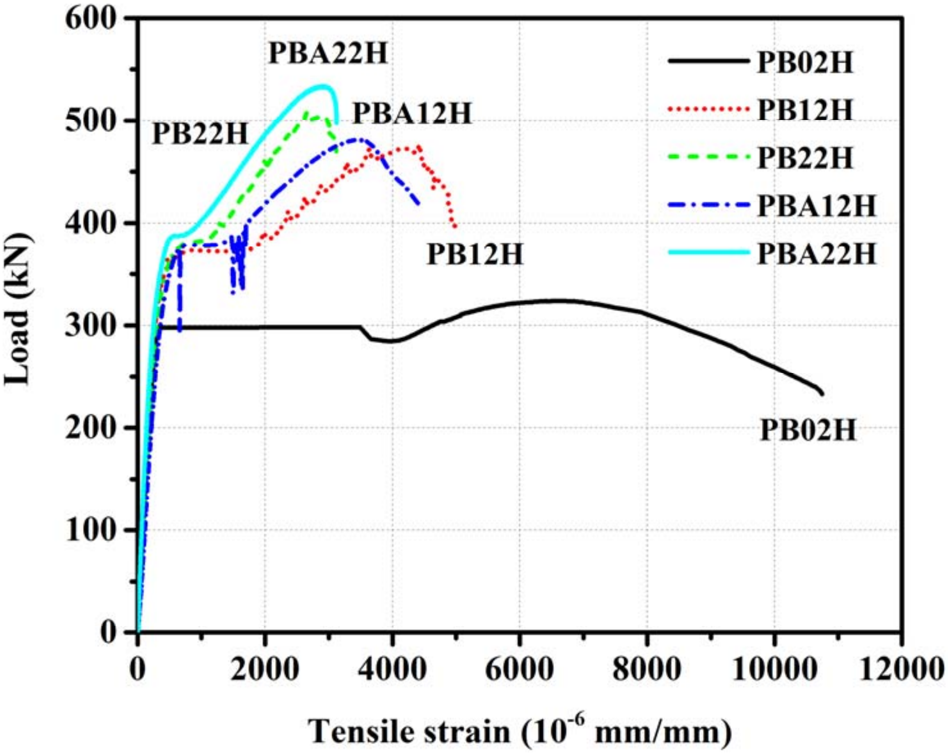

(c) Horizontal FRP rods in Series PB

Figure 4.18: Load-strain relations for NSM FRP rods

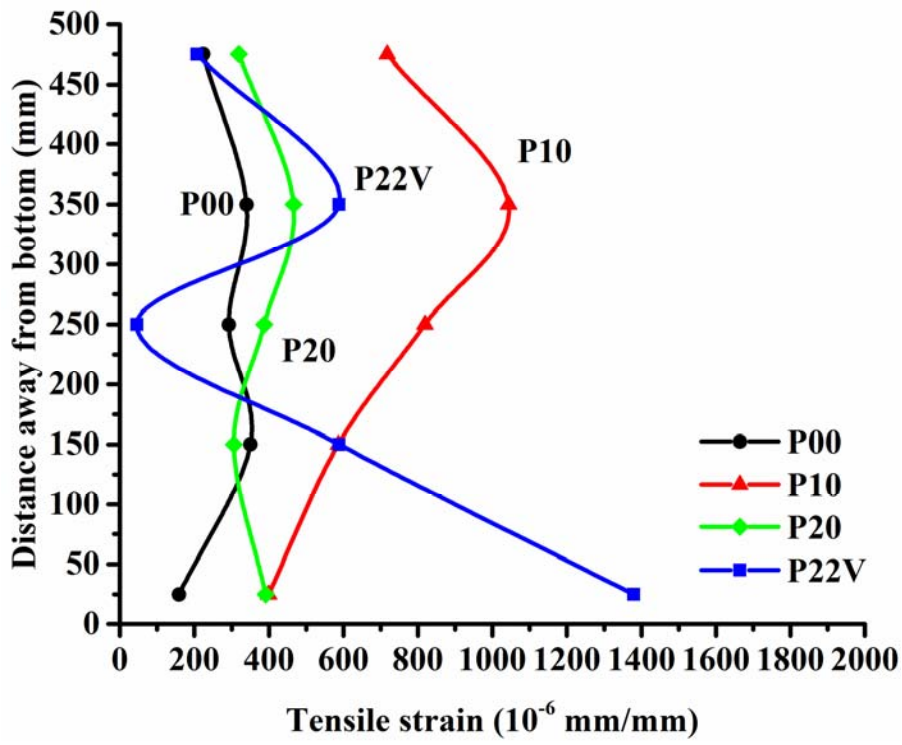

(a) Series P specimens

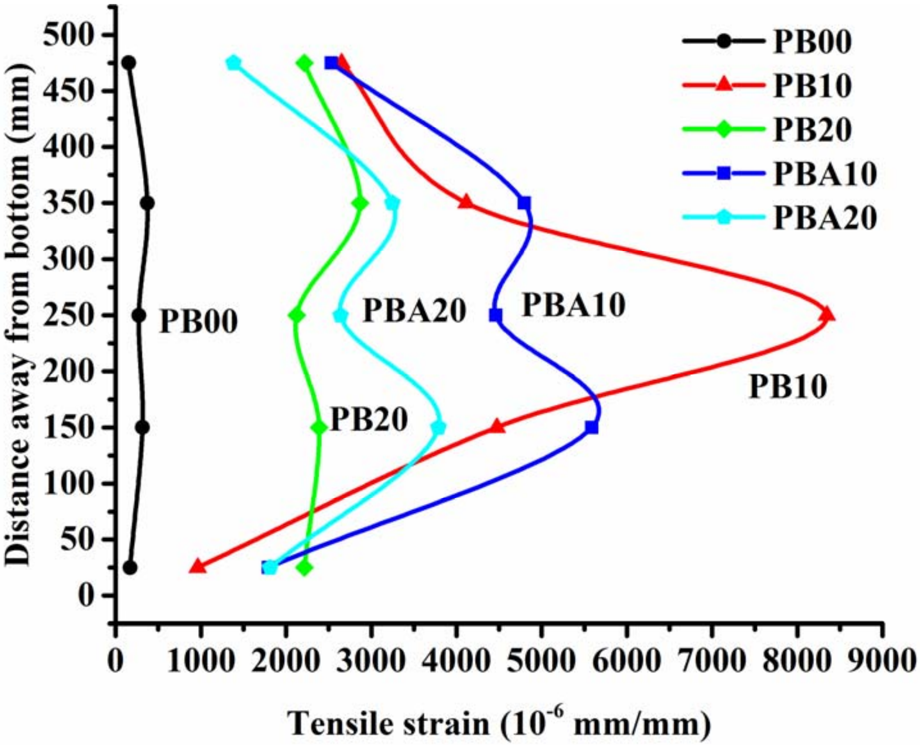

(b) Series PB specimens (with FRP sheets only)

Figure 4.19: The transverse strain distribution of specimens prior to failure (cont.)

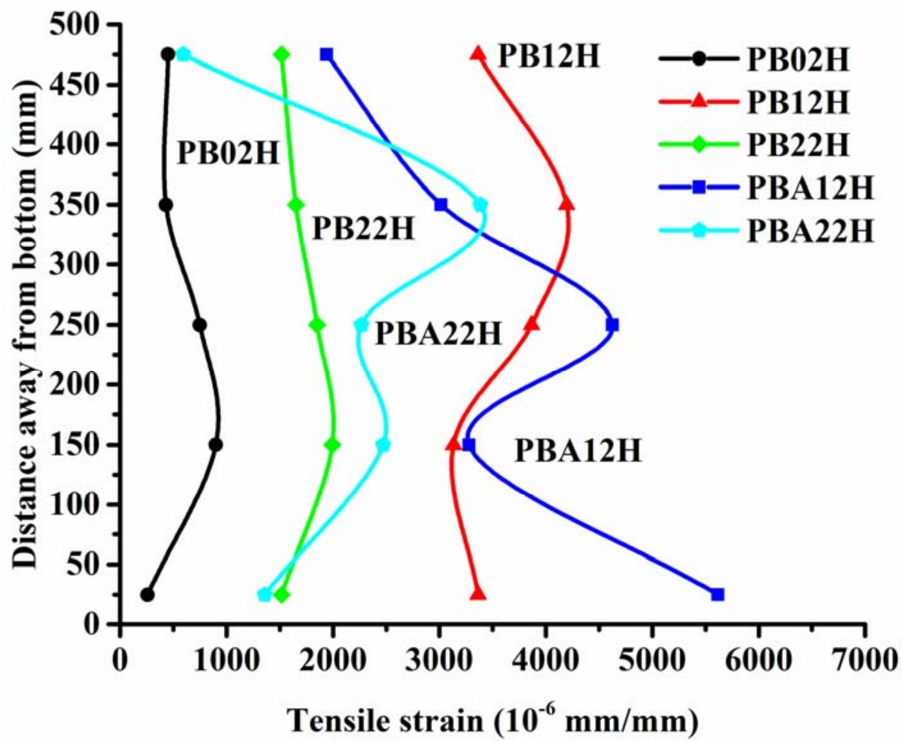

(c) Series PB specimens (with horizontal FRP rods)

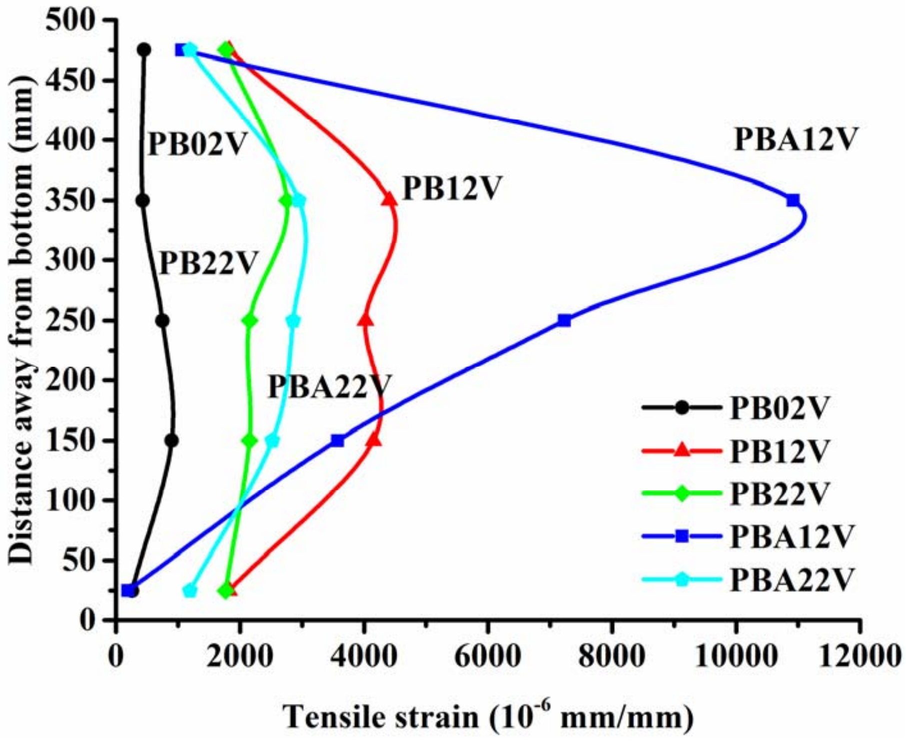

(d) Series PB specimens (with vertical FRP rods)

Figure 4.19: The transverse strain distribution of specimens prior to failure (cont.)

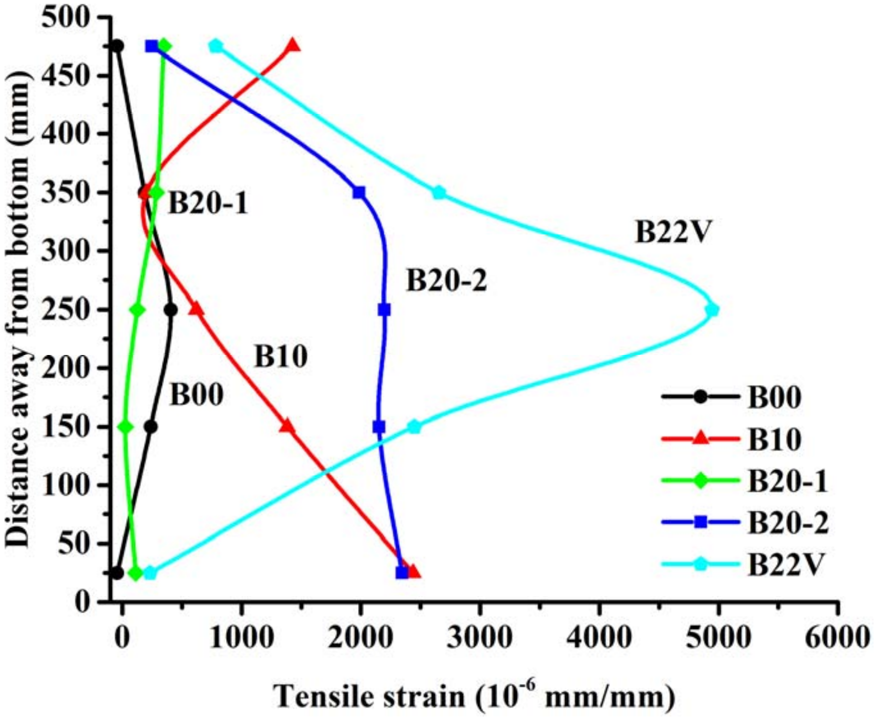

(e) Series B specimens (without anchors)

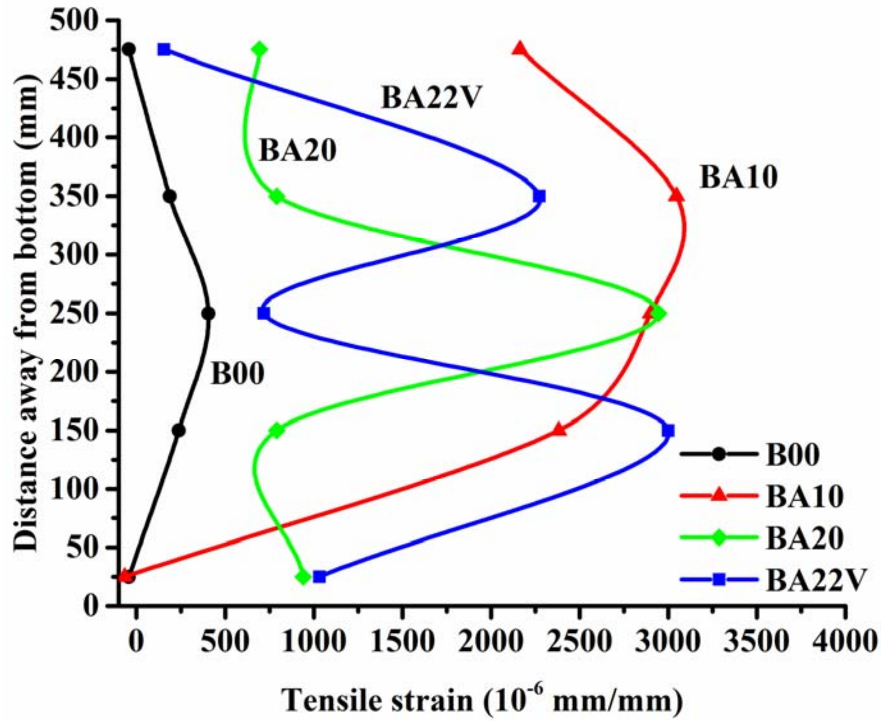

(f) Series B specimens (with anchors)

Figure 4.19: The transverse strain distribution of specimens prior to failure

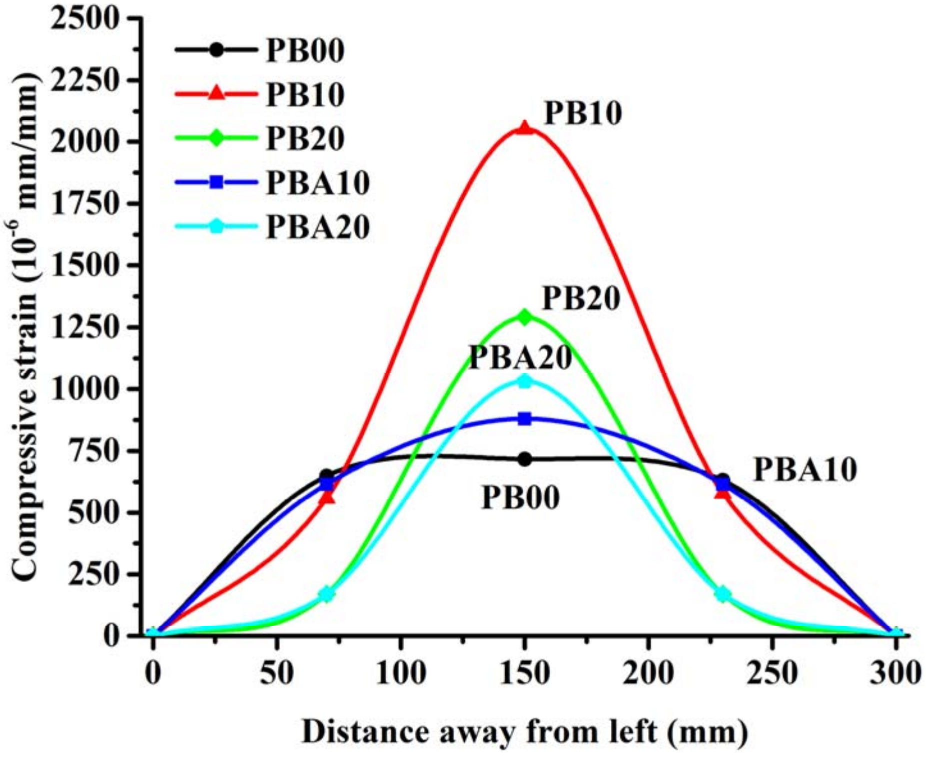

(a) Series PB specimens (with FRP sheets only)

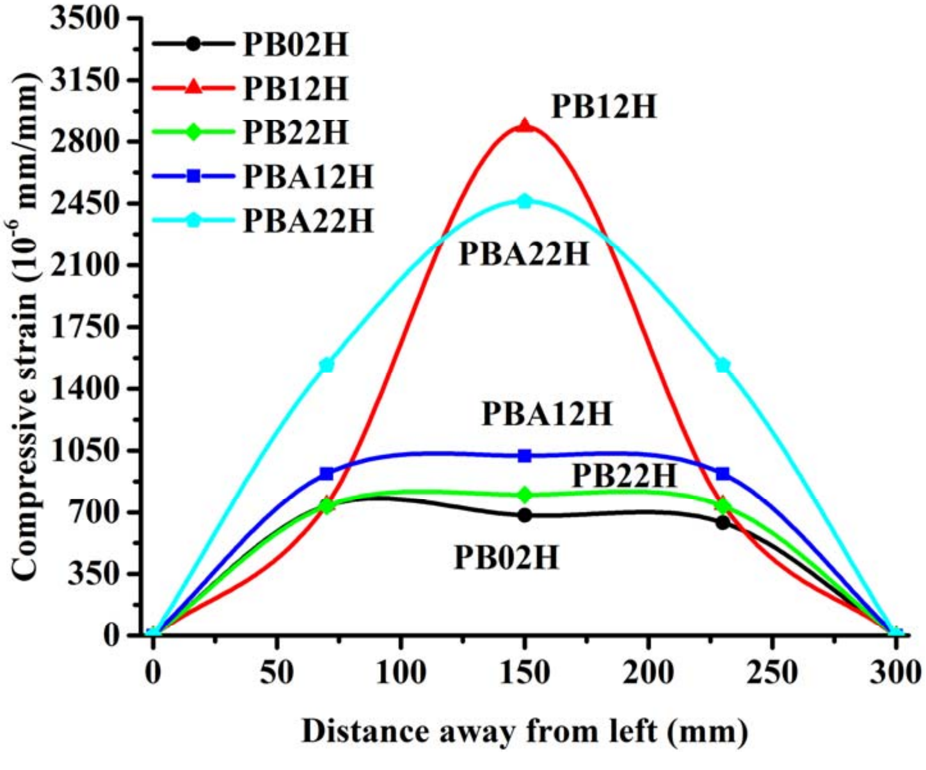

(b) Series PB specimens (with horizontal FRP rods)

Figure 4.20: The longitudinal strain distribution of specimens prior to failure (cont.)

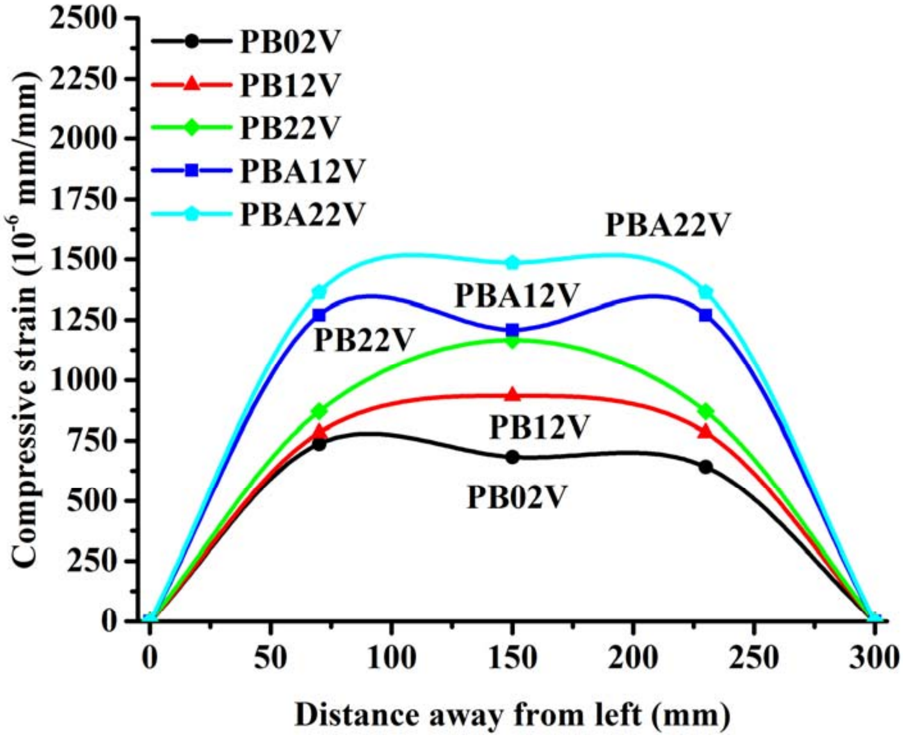

(c) Series PB specimens (with vertical FRP rods)

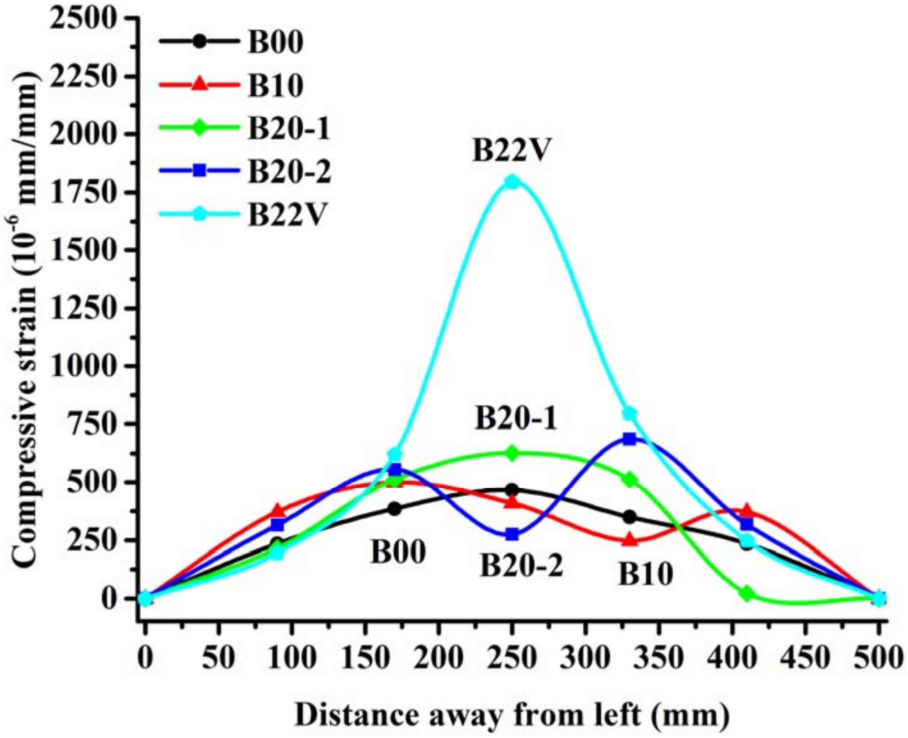

(d) Series B specimens (without anchors)

Figure 4.20: The longitudinal strain distribution of specimens prior to failure (cont.)

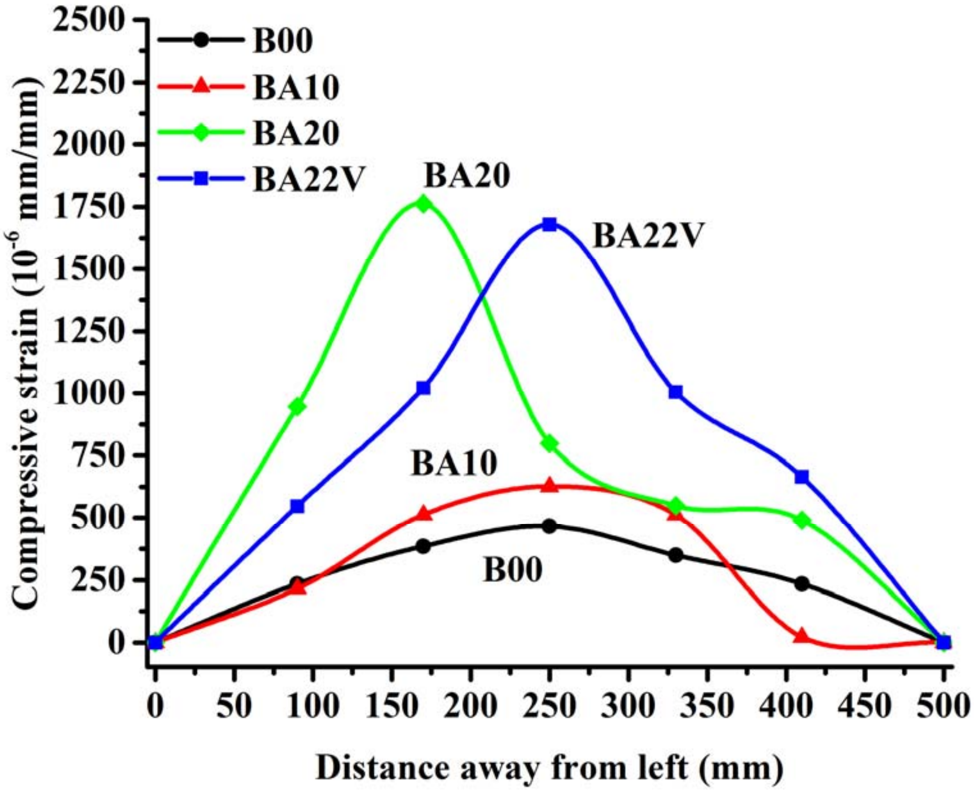

(e) Series B specimens (with anchors)

Figure 4.20: The longitudinal strain distribution of specimens prior to failure

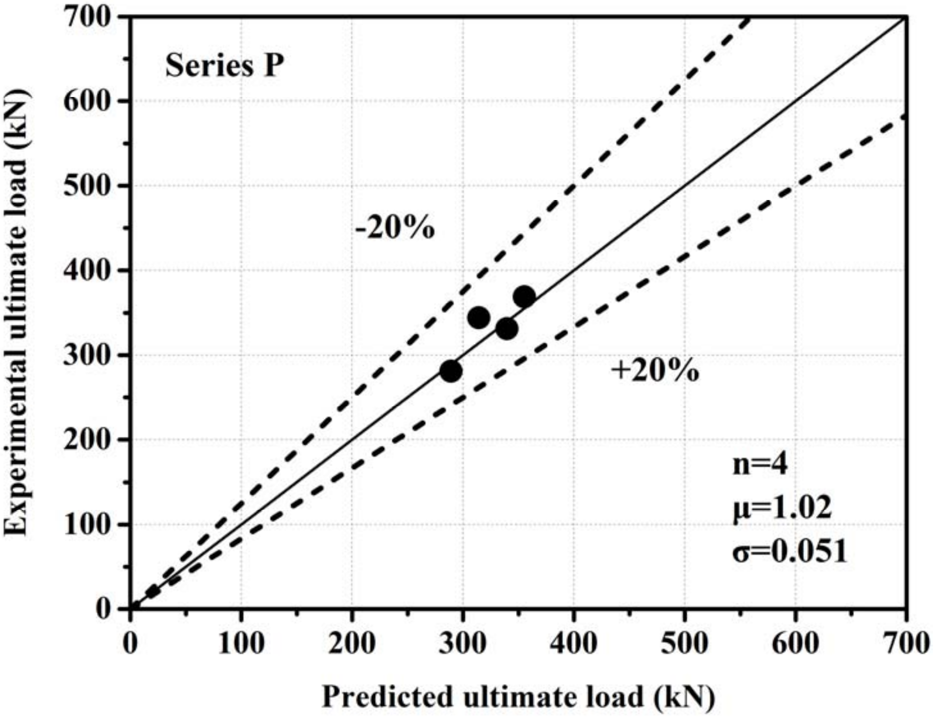

Figure 4.21: Comparison of experimental ultimate load with theoretical prediction for Series P specimens based on Lam and Teng's model

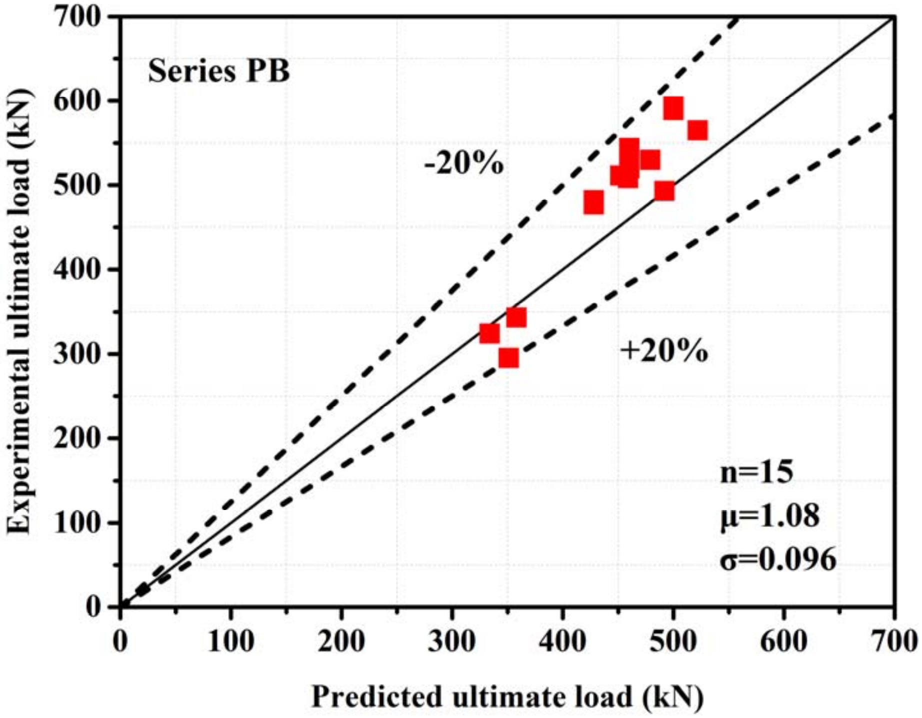

(a) Based on Tan's model

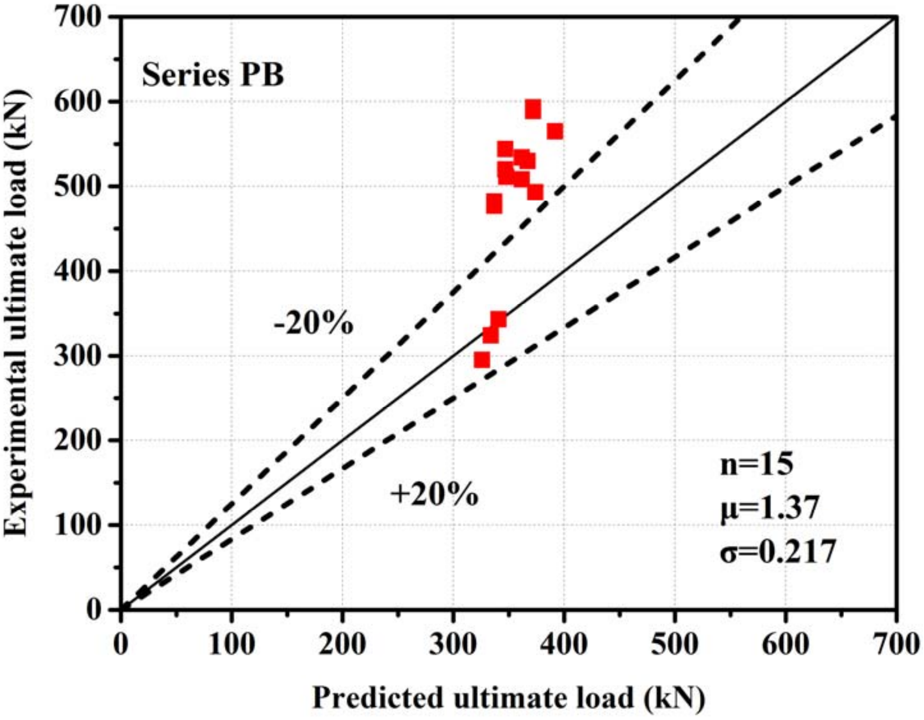

(b) Based on EC 2 model

Figure 4.22: Comparison of experimental ultimate load with theoretical predictions for Series PB specimens

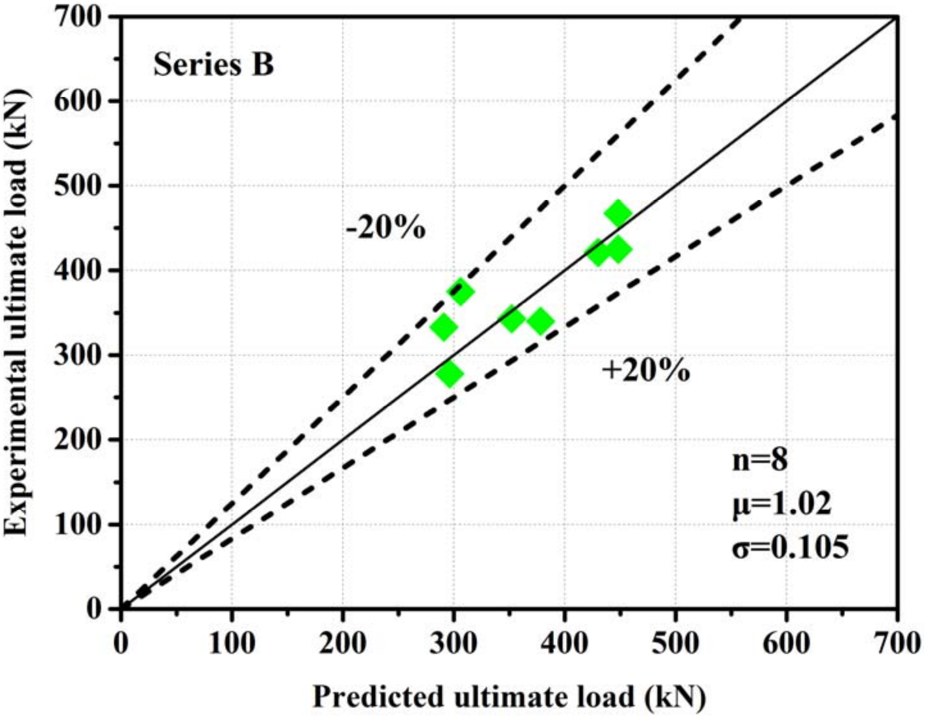

Figure 4.23: Comparison of experimental ultimate load with theoretical prediction based on Tan's model

Chapter 5. FRP Strengthening of RC Corbels

5.1 General

Based on the findings on the behavior and ultimate load of FRP-strengthened tie and strut members reported in Chapters 3 and 4, respectively, a case study on the FRP strengthening of non-flexural RC member, that is a corbel, based on strut-and-tie modelling was carried out and reported in this chapter. Fourteen specimens, either deficient in concrete strength or internal steel reinforcement, were strengthened with FRP reinforcement and tested to failure under vertical loading. The experimental investigation analyzed the effect of FRP strengthening systems on the ultimate load capacity of specimens. The applicability of the proposed strengthening design procedure based on Chapters 3 and 4 was also evaluated from the case study.

5.2 Analytical considerations

A corbel is a short structural element (**Figure 5.1a**) that cantilevers out from a column/wall to support loads, and is subject to relatively high shear. The strut-and-tie model for corbels shown in an inverted position is illustrated in **Figure 5.1b**. On the basis of previous experimental results obtained and the crack patterns observed at failure, it appears reasonable to substitute the cracked continuum with an equivalent single strut member. The strut-and-tie model for corbels therefore constitutes a diagonal strut member of compressed concrete (inclined at an angle θ with respect to the horizontal direction) and a horizontal tie member representative of the main steel. It is possible to obtain the ultimate load using the equilibrium of forces by considering failure of the tensile tie member or of the compressive concrete strut members (refer **Figure 5.1c**), based on the findings reported in Chapters 3 and 4.

Case 1(a): Failure of tie member without FRP strengthening:

$$P_u = 2F_{tie}\tan\theta = 2\cdot f_y A_s \cdot \tan\theta \tag{5.1}$$

Case 1(b): Failure of tie member with FRP strengthening (**Figure 5.2**):

$$P_u = 2F_{tie}\tan\theta = 2\cdot(f_y A_s + 2nE_{FRP,s}\varepsilon_{eff}t_{FRP,s}w_{FRP,s} + 2mE_{FRP,r}\varepsilon_{eff}A_{FRP,r})\cdot\tan\theta \tag{5.2}$$

where P_u is the ultimate load and F_{tie} is the strength of tie member; f_y is the yield strength of main steel; A_s is the area of steel reinforcement; n is the number of ply of FRP sheets per side; m is the number of horizontal FRP rods per side; $t_{FRP,s}$ is the thickness of one layer of FRP sheets; $w_{FRP,s}$ is the width of FRP sheets; ε_{eff} is the effective tensile strain of FRP reinforcement; Based on the study in Chapter 3, the effective FRP strain at failure can be taken as: ε_{eff} =0.004. $E_{FRP,s}$ and $E_{FRP,r}$ are the elastic modulus of FRP sheets and FRP rods, respectively; $A_{FRP,r}$ is the area of one FRP rod; and θ is the inclination of the diagonal strut.

Case 2(a): Failure of strut member without FRP strengthening (following EC2 code):

$$P_u = 2F_{strut}\sin\theta = 2\cdot K\cdot\nu'\cdot f_c'\cdot A_{strut}\cdot\sin\theta \tag{5.3}$$

where F_{strut} is the strength of the diagonal strut member; f_c' is the strength of concrete; A_{strut} is the effective area of the strut; K=0.6 for cracked compression struts, and $\nu' = \left(1 - f_c'/250\right)$.

The effective area of the cross-section of the inclined strut is defined as:

$$A_{strut} = w_{strut}\cdot t \tag{5.4}$$

where w_{strut} is the effective width of diagonal strut and t is the thickness of the diagonal strut (which was equal to 100 mm in this case study). The width of a strut is determined by the equation $w_{strut} = l_b \cos\theta + t \sin\theta$, where l_b is the width of the support bearing plate; and t is the thickness of compression strut. In dimensioning the width of a strut where support or load plate is not used, l_b is assumed to be t.

Case 2(b): Failure of strut member with FRP strengthening:

As shown in **Figures 5.1** and **5.3**, due to the sloping face of the corbels, the width of struts is insufficient for a full bottle-shaped strut to develop, so the struts in the corbels are considered as a partial bottle-shaped strut and Tan's model (Tan *et al.* 2013) was used which showed good agreement with the test results in Chapter 4. The ultimate load capacity of corbels can be taken by:

$$P_u = 2F_{strut} \sin\theta = 2 \cdot f'_{cc} \cdot A_{strut} \cdot \sin\theta \tag{5.5}$$

where f'_{cc} is the confined compressive strength of strut. The proposed confinement model for a corbel with the strut member strengthened with EB-FRP sheets and NSM-FRP rods is presented in **Figure 5.3**.

Transverse FRP reinforcement restraints the lateral expansion and confines the concrete section. The confined concrete core of the strut would be subjected to biaxial compression with effective lateral confining stresses from FRP sheets. Based on the equations given by Tan *et al.* (2013) and as described in Chapter 4, the confined concrete strut strength for rectangular sections subjected to confining pressures, f_l, as shown in **Figure 5.3b**, is:

$$f'_{cc} = f'_{co}\left(2.254\sqrt{1+7.94\frac{f_l}{f'_{co}}}-2\frac{f_l}{f'_{co}}-1.254\right)\left(1-0.8\sqrt{\frac{f_l}{f'_{co}}}\right) \tag{5.6}$$

where f'_{co} is the unconfined strength of concrete; f'_{cc} is the confined concrete compressive strength; f_l is the confining pressures. Equilibrium of forces gives the confining pressure, f_l, at failure of the section as:

$$f_l = \left(\frac{2nt_{FRP,s}E_{FRP,s}}{t}+\frac{mA_{FRP,r}E_{FRP,r}}{tL}\right)\varepsilon_{eff} \tag{5.7}$$

where n is the number of ply of FRP sheets per side; m is the number of transverse FRP rods per side; t is the thickness of struts; $t_{FRP,s}$ is the thickness of one layer of FRP sheets; L is the dispersion length measured on the axis of the strut by drawing 45 degree lines from the end of the horizontal FRP rods; $A_{FRP,r}$ is the area of one FRP rod; $E_{FRP,s}$ and $E_{FRP,r}$ are the elastic modulus of FRP sheets and FRP rods respectively; ε_{eff} is the effective FRP strain at failure. Based on the study in Chapter 4, the effective FRP strain at failure can be taken as: $\varepsilon_{eff}=0.004$.

Based on the above analytical considerations in this section, the design of FRP strengthening systems for corbels based on strut-and-tie modelling can be carried out. The FRP strengthening systems was based on analyzing corbels using strut-and-tie model with all possible arrangements of strut and tie members and then applying the FRP reinforcement to the obtained ties and struts to increase the ultimate load capacity of tie and strut members respectively.

(a) FRP strengthening of tie member:

$$F_{tie} = P_{u,d} \big/ 2\tan\theta = f_y A_s + 2nE_{FRP,s}\varepsilon_{eff} t_{FRP,s} w_{FRP,s} + 2mE_{FRP,r}\varepsilon_{eff} A_{FRP,r} \tag{5.8}$$

$$2nE_{FRP,s} t_{FRP,s} w_{FRP,s} + 2mE_{FRP,r} A_{FRP,r} = \left(P_{u,d} \big/ 2\tan\theta - f_y A_s\right) \big/ \varepsilon_{eff} \tag{5.9}$$

Where $P_{u,d}$ is the design ultimate load of corbel, and F_{tie} is the design strength of FRP strengthened tie member; ε_{eff} is the effective FRP strain at failure, which can be taken as: ε_{eff} =0.004. Based on these equations, the required amount of FRP reinforcement can be obtained.

(b) FRP strengthening of strut member:

$$F_{strut} = P_{u,d} \big/ 2\sin\theta = f'_{cc} \cdot A_{strut} \tag{5.10}$$

where F_{strut} is the design strength of FRP strengthened strut member; f'_{cc} is the design confined concrete compressive strength; A_{strut} is the effective area of strut (Equation 5.4). After obtaining the design compressive strength of concrete, based on the Equations 5.6 and 5.7, the required amount of FRP reinforcement can be calculated.

5.3 Test program

In order to verify the effectiveness and validity of the FRP strengthening approach based on strut-and-tie modelling, the strength and performance of reinforced concrete corbels, strengthened with EB-FRP sheets and NSM-FRP rods, were experimentally investigated. The focus of the experimental research was the restoration of ultimate load bearing capacity of reinforced concrete corbels either deficient in concrete strength or internal steel area by FRP strengthening of tie members or strut members, respectively. In the real field cases, the corbels designed according to code should be with stirrups. In order to assess the contribution of the FRP strengthening systems on the load capacity of tie members and strut members more clearly, there were no stirrups in the corbel specimens in this chapter. Stirrups are provided to resist the shear forces and diagonal tension stresses in the corbels and provide confinement to the interior concrete core. If there were stirrups in the corbels, the corbels should resist higher load.

5.3.1 Test specimens

The test specimens consisted of fourteen reinforced concrete corbels with two different shear span to depth ratios (*a*/*d*=0.50, *a*/*d*=1.0) classified into two Series, C50 and C100, as shown in **Tables 5.1** and **5.2**. The strengthening methods for corbel specimens deficient in internal steel area (namely specimens with prefix CA) was FRP strengthening of tie members, whereas it was FRP strengthening of strut members for the corbel specimens deficient in concrete strength (namely specimens with prefix CB). Three types of steel reinforcement were used, and two different concrete strengths were investigated. The main reinforcement of Series C50 specimens were two 10 mm and two 13 mm diameter deformed reinforcing steel bar, whereas they were two 13 mm and two 16 mm diameter bars for the corbel Series C100 specimens. The test was performed under monotonically increasing vertical load.

Each specimen consisted of a short column with two corbels arranged symmetrically on both sides as shown in **Figure 5.4**. The cross-section dimension of the 500 mm long rectangular column was 225 mm by 100 mm, and four 13 mm diameter deformed bars were used as column longitudinal reinforcement, whereas 6 mm diameter plain bars at a spacing of 55 mm were used as hoop reinforcement. The overall depth of each corbel was 400 mm at the interface with the column and 325 mm (Series C50) or 275 mm (Series C100) at the cantilever end. In all specimens, the thickness of corbels t was 100 mm, and the height h was 400 mm, resulting in an effective depth d of 350 mm.

The specimen designation can be interpreted as follows: the first two letters indicated the FRP strengthening systems ("CA" for specimens with FRP strengthening of tie members and "CB" for specimens with FRP strengthening of strut members). The shear span to depth ratios (a/d) of the specimens were shown in the next field; that was "50" for a/d=0.50 and "100" for a/d=1.0. The main reinforcement ratio for Specimens CA50, CB50, CA100 and CB100 was ρ=0.45%, ρ=0.76%, ρ=0.76% and ρ=1.15% respectively. The last number in the specimen name represented FRP strengthening system applied to the corbels: "1" means strengthening with only EB-FRP sheets and "2" means strengthening with both EB-FRP sheets and NSM-FRP rods.

5.3.2 Materials

The concrete mix was designed for a 28-day cylinder strength of 30 MPa for Series CA specimens and 60 MPa for Series CB specimens. A mix proportion of 1.0: 2.18: 2.62: 0.69 by weight of Ordinary Portland Cement, natural sand, crushed granite of a maximum size of 10 mm and water was adopted for Series CA specimens. The mix proportion consisting of Ordinary Portland Cement (OPC), fine aggregates, coarse aggregates (10mm) and water in the mix ratio of 1: 1.83: 1.51: 0.35 was used for Series CB specimens. Compressive tests on cylinders and cubes were carried out by means of a universal testing machine operating in displacement-control mode. Test results were listed in **Table 5.3**.

The results of direct tensile tests carried out on steel bars (three for each bar diameter) are given in terms of mean values of yield strength and ultimate strength in **Table 5.4**. The yield strength of deformed longitudinal reinforcements, f_y , were 541 MPa for H10 bar, 584 MPa for H13 bar and 569 MPa for H16 bar respectively. The modulus of elasticity for H10, H13 and H16 bars were 184.6 GPa, 181 GPa and 173GPa, respectively.

The properties of the FRP sheets/rods and epoxy resin used in the strengthened specimens are given in **Tables 5.5** and **5.6**. The unidirectional carbon FRP sheets had a thickness of 0.176 mm with a weight of 330 g/m^2, and had a specified tensile strength of 3800 MPa, with a tensile elastic modulus of 240 GPa and an ultimate elongation to rupture of 1.55 percent. A three-part resin was used to install the FRP sheets. The carbon FRP rods measured 10 mm by 1.4 mm in cross-section, and had a specified tensile strength of 1000 MPa at 0.6% strain, elastic modulus of 165 GPa, and ultimate elongation of 0.8 to 1.0 percent.

5.3.3 Specimen preparation

As shown in **Figure 5.5**, two wooden moulds were fabricated for casting of the specimens. The steel bars were first cut and bent. The reinforcement cages for the specimens were then assembled with the bars held in position by short transverse bars of 6 mm diameter and welded together. Before casting, several 10 mm strain gauges (Type FLA-10-11) were fixed on the longitudinal bars and water-proofed using silicone. Lead wires were soldered to the gauges and guided along the reinforcement bar out to the exposed top of formwork. The reinforcement cages were placed after the wooden moulds were oiled. Then concrete were mixed and poured into the wooden moulds. For each batch of concrete, six companion cubes of 100mm dimension and six cylinders (100 mm diameter with 200 mm height) were prepared to determine the concrete strengths at the time of test.

The formwork was removed after one day, and specimens were then cured by covering with damp gunny sacks for a week. Thereafter, the specimens were left in the laboratory under ambient conditions until the time of testing, which was 28 days after casting. Accompanying cylinders and cubes were cured in the same manner. All test specimens were white washed before the test so as to trace the crack pattern.

5.3.4 Installation of FRP strengthening systems

In order to verify the FRP strengthening design approach based on strut-and-tie modelling as discussed in Chapters 3 and Chapter 4, some corbel specimens were strengthened only in tie members, while some only in the compressive strut (**Figure 5.6**). Based on the different FRP strengthening system, specimens were classified in to two fundamental series: Series CA with FRP strengthening of tie members and Series CB with FRP strengthening of strut member.

For FRP strengthening of tie members, the orientation of FRP sheets and rods was parallel with the steel reinforcement and the location of FRP sheets and rods coincided with the internal main steel bar. For FRP strengthening of strut members, the FRP sheets and rods were placed perpendicular to the axis of strut member. The amount of FRP sheets and rods was calculated based on the previous study in Chapters 3 and 4 to restore the loss of ultimate load capacity of RC corbels due to deficient in internal steel reinforcement or concrete strength respectively. One or two layer of EB-FRP sheets and two or four NSM-FRP rods for were applied to strengthen the strut members or tie members.

The carbon FRP sheets were applied on fully cured, surface-dry specimens. The residue on concrete surface was removed and aggregates were exposed by using a brush and vacuum cleaner before FRP strengthening was carried out. The FRP sheets were cut to the predetermined width and length using an ordinary pair of scissors and their surface was kept clean using a cotton brush. A three-component epoxy was weighed, mixed and applied to the concrete surface and carbon FRP sheets concurrently, within the FRP manufacturer's specified pot-time. Then, the coated sheets were applied to the specimens and aluminum rollers were used to press the carbon FRP sheets down for even and proper bonding of carbon FRP to the concrete surface. The procedure was repeated after each ply of carbon FRP sheet had been applied. The carbon FRP flat rods with a width of 10 mm and a thickness of 1.4 mm were bonded into slots at both faces of tie members. A concrete saw was used to cut slots approximately 5 mm wide and 15 mm deep into the substrate. The slots were filled with the epoxy adhesive, and the carbon FRP rods were pressed into the slots.

5.3.5 Test setup and procedure

All the corbel specimens were simply supported and loaded through the column as shown in **Figure 5.7**. The test specimens, which were inverted columns with two protruding corbels, were seated on one roller supports. Bearing plates were used at the loading point and the supports. The vertical load was applied onto the column via a roller support and measured by a load cell. All test specimens were loaded in a rigid frame to failure using a 1000 kN capacity displacement-control hydraulic actuator. It was assumed that the vertical load was equally divided between the two corbels. To make sure that “equal division of the applied load”, the corbels were seated on supports symmetrically and the distances from the column face to the supports, *a*, were the same for the two corbels. The corbels were seated on roller support set at distances of 175 mm and 350 mm from the column face, yielding *a*/*d* ratios of 0.50 and 1.0 respectively. The vertical load, *P*, was increased monotonically until the failure of the corbel on either side of the specimen was reached. The failure was defined as the sudden and excessive loss of load bearing capacity of the test specimens.

Each specimen was instrumented to measure mid-span deflection and strains, as shown in **Figures 5.7** and **5.8**. Deflection and strains of concrete and carbon FRP sheet and rods were measured with a transducer (LVDT) and strain gauges, respectively. The strain gauges were mounted onto the concrete surface, steel reinforcement (prior to casting the specimens) and carbon FRP sheets and rods at the section of maximum moment (at the interface with the column), as shown in **Figure 5.8**. After each increment of loading, deflection and strain gages readings were recorded by a data logger. The development of cracks was also carefully observed and marked on the specimens.

5.4 Test results and discussion

In this following section, the observed behavior and mode of failure of each specimen is described and discussed. The concrete strengths at the time of testing the specimens are shown in **Table 5.3**. For the Batch H concrete, the cylinder compressive strength varied from 66.3 MPa to 69.5 MPa with an average of 67.3 MPa, whereas the cube compressive strength varied from 75.7 MPa to 82.5 MPa with an average of 78.5 MPa. For the Batch L concrete, the cylinder compressive strength varied from 34.3 MPa to 39.3 MPa with an average of 36.6 MPa, whereas the cube compressive strength varied from 39.9 MPa to 48.4 MPa with an average of 44.3 MPa. The test results are summarized in **Tables 5.7** and **5.8**.

5.4.1 Overall behavior and failure modes

The appearance of the specimens after being tested to failure is shown in **Figures 5.9** to **5.13**. The behavior of reinforced concrete corbels was mainly influenced by the shear span to effective depth ratio, the concrete strength, FRP strengthening system and the corbel geometry. The failure of all specimens was very sudden and explosive with a big bang. The cracks indicated two main patterns as shown in **Figure 5.9a**: (a) Cracks near the corbel-column interface. (b) Cracks developed from the support to the corbel-column interface. Cracks near the corbel-column interface never caused the corbel failure.

5.4.1.1 Control specimens

The ultimate load of the control specimens (C50 and C100) were 613 kN and 496 kN, respectively. In these two specimens, in the initial stage of loading, the first major crack (**Figure 5.9)** appeared as a vertical crack at the column face at 110 kN and 87 kN respectively (which were at about 18% of the respective ultimate failure loads). On further loading, a diagonal crack formed near the support. Increasing the load led to the creation of new diagonal cracks which propagated rapidly until failure. Failure of these two specimens happened when a large crack that initiated at the support suddenly extended to the column face and vertically along the column interface as shown in **Figures 5.9b** and **5.9c**. In the case of Specimen C100, the failure of the strut due to tensile splitting was clearly seen. Then the concrete at the compression zone of the struts and the nodal zones crushed and spalled off from the side and bottom of the corbels.

5.4.1.2 Un-strengthened specimens

The ultimate load of the specimens with “insufficient” steel reinforcement (CA50-0 and CA100-0) were 439.5 kN and 262.7 kN, respectively (i.e. the ultimate load decreased by about 28.3% and 47.1% of control specimen ultimate load, respectively). The crack pattern was almost identical to the respective control specimens. A diagonal crack was observed at 140 kN and 110 kN, respectively (which were at 31.8% and 41.9% of the ultimate failure loads, respectively). With increasing applied load, other cracks appeared. Before failure, the diagonal cracks propagated and extended from the support towards the intersection point of the corbel inclined surface and column face, as shown in **Figures 5.10a** and **5.12a**. Failure happened by diagonal tensile splitting of the strut member.

The ultimate load failure of the specimens with low concrete strength (CB50-0 and CB100-0) were 444.1 kN and 164.5 kN, respectively (i.e. the ultimate load decreased by about 27.6% and 66.8% of control specimen ultimate load, respectively). Similar cracking behavior as before was observed, although the crack inclination in CB100-0 was different from the other specimens as shown in **Figure 5.13a**. In these two specimens, local cracking near the support area was observed. The major crack was observed at 58 kN and 90 kN, respectively (that were 13.1% and 54.7% of the ultimate failure loads, respectively). Diagonal cracks formed and propagated slowly with increasing applied load. The failure resulted from crack propagation from the support to the corbel-column interface. The failure was similar to the diagonal splitting failure mode.

5.4.1.3 FRP-strengthened specimens

For FRP strengthened specimens, FRP strengthening of tie members and strut members not only delayed the formation of the diagonal cracks effectively but also reduced the width of diagonal cracks. Propagation of cracks was slower than for the control specimens. FRP strengthening of tie members also caused an increased in tie capacity, and converted the flexural yielding of tie to a tensile splitting or concrete crushing of strut in the Specimens CA50-1, CA50-2, CA100-1, and CA100-2. On the other hand, for the corbels with FRP strengthening of strut members, the failure modes were changed from tensile splitting of strut to concrete crushing of strut (Specimens CB50-1, CB50-2, CB100-1, and CB100-2). No de-bonding of FRP was observed before failure.

The crack patterns of FRP-strengthened specimens and failure modes are shown in **Figures 5.10~5.13**. The behavior of the corbels was generally associated with the behavior of the strut and tie members. The possible failure modes were either due to tensile splitting of concrete strut (TS) in un-strengthened specimens, the concrete crushing in the struts and nodal zones (CC) in FRP-strengthened specimens or yielding of the main reinforcement (SY). The failure of the corbels occurred in the following manner: First, the cracks appeared from the tensile face near the corbel-column interface. Then, the cracks between the bearing plate and the corbel-column interface with an average orientation 70°~80° with respect to the horizontal axis appeared and propagated. Almost all the specimens experienced diagonal tensile splitting or crushing of strut (with or without yielding of steel reinforcement), with crushing of concrete at the nodal zones. The failure modes were changed relative to the configuration of FRP strengthening. FRP strengthening of tie members caused an increased in tie capacity, and converted the flexural yielding of tie to a tensile splitting or concrete crushing of strut in the Specimens CA50-1, CA50-2, CA100-1, and CA100-2. Moreover, for the behavior and failure mode of corbels with FRP strengthening of strut members, the failure modes were changed from tensile splitting of strut to concrete crushing of strut (Specimens CB50-1, CB50-2, CB100-1, and CB100-2). When the specimen failed in tensile splitting or crushing of concrete strut without steel yielding, the failures were very brittle with a loud bang, and excessive deflection and large cracks was observed along with a sharp decrease in load. While, for specimens that failed in yielding of the tension tie, the load remained almost constant with increasing deflection at ultimate, indicating a more ductile behavior.

5.4.2 Ultimate load capacity

As shown in **Table 5.7** and **Figure 5.14**, test results revealed that the loss in ultimate load capacity of RC corbels due to deficiency in concrete strength or internal steel reinforcement could be restored by FRP strengthening system with EB-FRP sheets and NSM-FRP rods based on strut-and-tie modelling. The ultimate load of the specimens with FRP strengthening of tie members (CA50-1, CA50-2, CA100-1 and CA100-2) were 585.9

kN, 637.1 kN, 467.8 kN and 549.0 kN, respectively (i.e. 95.6%, 103.9%, 94.3% and 110.7% of the reference ultimate load, respectively). The ultimate load of the specimens with FRP strengthening of strut members (CB50-1, CB50-2, CB100-1 and CB100-2) were 621.5 kN, 668.0 kN, 461.5 kN and 521.9 kN, respectively (i.e. 101.4%, 108.9%, 93% and 105.2% of the reference ultimate load, respectively).

The strengthening of tie member with EB-FRP sheets only resulted in 33% and 78% ultimate load capacity increase in Specimens CA50-1 and CA100-1, compared to control Specimens CA50-0 (ρ=0.45%) and CA100-0 (ρ=0.76%) respectively. With the same amount of FRP reinforcement parameter but using both EB-FRP sheets and NSM-FRP rods, the strengthening of tie member resulted in an increase of 45% and 108% for the specimen CA50-2 and CA100-2. This indicated that the strengthening effectiveness of EB-FRP sheets combined with NSM-FRP rods was better than using EB-FRP sheets alone.

For Specimens CB50-1 and CB100-1, which were strengthened with EB-FRP sheets only, the increase resulting in ultimate load capacity were 39% and 184% respectively, compared to the control Specimens CB50-0 (ρ=0.76%) and CB100-0 (ρ=1.15%). With a larger FRP reinforcement parameter, a large increase of 50% and 234% was obtained for Specimens CB50-2 and CB100-2 which were strengthened with both EB-FRP sheets and NSM-FRP rods. This indicated that the ultimate load capacity of strut member increased with increasing FRP reinforcement parameter.

5.4.3 Load-versus-midspan deflection relations

Figures 5.15 and **5.16** show the load-versus-midspan deflection curves for Series C50 and C100 specimens. For each specimen, there was a short setting-in stage, during which the bearing plates were brought in contact with the specimen faces. After the setting-in stage, the load increased linearly with the mid-span deflection up to near the ultimate load. For all specimens, the load decreased abruptly upon reaching the ultimate value and failure was brittle. Also, all FRP strengthened specimens had almost the same stiffness as the un-strengthened specimens. The maximum deflection at collapse was small, ranging from about 5 to 15 mm.

5.4.4 Steel strains

Figures 5.17 and **5.18** present the measured steel strains in the tension reinforcement. It was evident that all specimens exhibited a trilinear behavior in the load-steel strain relation. In the first region, the steel strains increased linearly with the applied load until the first crack was observed. In the second region, the strains continued to increase at a faster rate until the yielding of main steel bar. The rate of strain increase was however lower in FRP strengthened specimens. During this region, the load would experience some small drops when cracks appeared. In the third region, the steel strains developed rapidly with slight or no increase in load until failure.

The state of main steel strains at the ultimate load level can be determined from **Figures 5.17 and 5.18**. For Specimens C50, CA50-0, CA50-1, CA50-2, C100, CA100-1 and CA100-2, the steel strains at ultimate load exceeded the yield strains of the steel bars, indicating that yielding of the tension reinforcement had occurred before ultimate failure. For specimens with FRP-strengthened struts, steel yielding was not observed before the ultimate load was reached.

5.4.5 Load-FRP strain relations

The tensile strains of steel bars, FRP sheets and rods were measured at the section of maximum moment. It was observed that the load versus tensile strain response for all specimens yielded trilinear behavior as well, as shown in **Figure 5.19**. The first kink in slope of the response usually corresponded to the occurrence of the first flexural crack at the corbel-to-column boundary. The second kink in the slope indicated the yielding of the main steel bar. For Specimens CA50-1, CA50-2, CA100-1 and CA100-2, the main steel bar, FRP sheets and FRP rods had similar tensile strains at the same load level which indicated that the bond among concrete, steel and FRP was good and both EB-FRP sheets and NSM-FRP rods were effective in strengthening the tie members. The maximum tensile strains in FRP reinforcement for Specimens CA50-1 and CA100-1 was about 3000×10^{-6} mm/mm, while for Specimens CA50-2 and CA100-2, it was around 5000×10^{-6} mm/mm due to the different strengthening configuration. The maximum tensile stress in all carbon FRP sheets and rods was less than its ultimate tensile capacity, even though de-bonding did not occur. The use of an effective tensile strain of 4000×10^{-6} mm/mm for the carbon FRP reinforcement in the design approach was also justified.

The compressive strains along the axis of the strut members in specimens with FRP strengthened struts are plotted against the applied load in **Figure 5.20**. The compressive strain increased linearly with the applied load in the initial stage, upon diagonal cracking (that was tensile splitting of struts), the compressive strain increased at a higher rate with increasing load. At failure, the FRP compressive strains in strut members were significantly increased from 1500×10^{-6} mm/mm in the un-strengthened Specimen CB50-0 to 1750~2750 ×10^{-6} mm/mm for Specimens CB50-1 and CB50-2. For Specimens CB100-1 and CB100-2, the FRP compressive strains in strut members were increased from 300×10^{-6} mm/mm in Specimen CB100-0 to 1400~1600×10^{-6} mm/mm. The effective compressive strain was therefore in the order of 2000×10^{-6} mm/mm.

The transverse tensile strains at mid-length of the strut members for specimens with FRP strengthened struts are shown in **Figure 5.21**. It was observed that the development of tensile strain of FRP with the applied load was similar to that of longitudinal compressive strain. The tensile strains in the struts at ultimate load of the specimens members were significantly increased from 200×10^{-6} mm/mm (Specimen CB50-0) to 2000~4000×10^{-6} mm/mm for Specimens CB50-1 and CB50-2. For Specimens CB100-1 and CB100-2, the tensile strains in strut members were increased from 200×10^{-6} mm/mm (Specimen CB100-0) to 1800~2800×10^{-6} mm/mm. The effective tensile strain was therefore in the order of 3000×10^{-6} mm/mm to 4000×10^{-6} mm/mm.

5.4.6 Comparison with design ultimate load

The design load capacities of FRP strengthened corbels were set to be equal to the ultimate load of the control specimens. The amount of FRP sheets and rods for FRP strengthening of tie member and strut member were calculated using an effective strain of 0.004 based on the finding in Chapters 3 and 4. Note that safety factors were not considered in the design load. The design ultimate loads of FRP-strengthened struts are compared with the observed failure loads in **Table 5.8** and **Figure 5.22**. The observed ultimate load carrying capacity of corbels was found to be within 20 percent of the design value, except for Specimens CB100-0 which failed prematurely due to spalling of concrete. The mean and standard deviation values of the ratio of $P_{u,Test}/P_{u,d}$ of the 13 specimens were 1.18 and 0.163 respectively, showing good agreement between the design failure load and observed failure load. In general, the observed failure loads were higher than the design loads, which was expected since the strut-and-tie model was a lower bound approach.

5.5 Summary

On the basis of the tests carried out on RC corbels strengthened by various combinations of externally bonded FRP sheets and near-surface-mounted FRP rods, the following conclusions can be drawn:

(a) The loss of ultimate load capacity of RC corbels due to low concrete strength or low steel reinforcement could be restored by FRP strengthening using EB-FRP sheets and/or NSM-FRP rods based on strut-and-tie modelling.

(b) The effectiveness of FRP strengthening of strut member increased with increasing FRP strengthening parameter. The most efficient FRP configuration for tie member consisted of a combination of EB-FRP sheets and NSM-FRP rods, even for the same reinforcement parameter. The actual stress in all the carbon FRP sheets and rods was less than its ultimate tensile capacity.

(c) All of the corbels showed a brittle mode of failure with little warning. The stiffness of corbel specimens was not increased by FRP reinforcement.

(d) The analytical models proposed in Chapters 3 and 4 to design the FRP strengthening systems and evaluate the strength of FRP-strengthened tie and strut members were verified. The design approach led to good agreement between the design ultimate load and the observed values, with the latter exceeding the design values for most specimens.

Table 5.1: Design parameters of specimens

Series		**Specimens**	***f'*$_c$ (MPa)**	***a*/*d***	**Steel reinforcement ratio, *ρ* (%)**	**Design of FRP strengthening system**
C50	Control specimens	C50	60	0.5	0.76 (2×13)	-
	FRP strengthening of tie member	CA50-0	60	0.5	0.45 (2×10)	-
		CA50-1				EB-FRP sheets only
		CA50-2				EB-FRP sheets +NSM-FRP rods
	FRP strengthening of strut member	CB50-0	30	1.0	0.76 (2×13)	-
		CB50-1				EB-FRP sheets only
		CB50-2				EB-FRP sheets +NSM-FRP rods
C100	Control specimens	C100	60	1.0	1.15 (2×16)	-
	FRP strengthening of tie member	CA100-0	60	0.5	0.76 (2×13)	-
		CA100-1				EB-FRP sheets only
		CA100-2				EB-FRP sheets +NSM-FRP rods
	FRP strengthening of strut member	CB100-0	30	1.0	1.15 (2×16)	-
		CB100-1				EB-FRP sheets only
		CB100-2				EB-FRP sheets +NSM-FRP rods

Table 5.2: Dimensions of specimens

Series	***θ* (degree)**	***a* (mm)**	***d* (mm)**	***b*$_1$ (mm)**	***b*$_2$ (mm)**
C50	41°	175	350	225	100
C100	54°	350			

Note: (refer to **Figures 5.2** and **5.4**)

θ = Angle between strut and tie;

a = Effective shear span from support from face of column stump;

d = Effective corbel depth at the corbel-column interface;

b_1 = Width of loading plate;

b_2 = Width of support.

Table 5.3: Main properties of concrete

Concrete batch	**Average cube compressive strength (MPa)**	**Average cylinder compressive strength (MPa)**	**Tensile strength (MPa)**	**Elastic modulus (GPa)**
H1 (C50, C100)	82.5	69.5	4.67	39.4
H2 (CA50-0, CA100-0)	77.9	66.8	4.54	38.9
H3 (CA50-1, CA100-1)	77.7	66.6	4.53	38.8
H4 (CA50-2, CA100-2)	75.7	66.3	4.51	38.8
L1 (CB50-0, CB100-0)	39.9	34.3	2.66	31.9
L2 (CB50-1, CB100-1)	44.6	36.2	2.78	32.4
L3 (CB50-2, CB100-2)	48.4	39.3	2.98	33.2

Table 5.4: Main properties of reinforcing steel

Reinforcing bar	**Diameter, d (mm)**	**Cross-sectional area, A_s (mm^2)**	**Elastic modulus, E_s (GPa)**	**Yield strength, f_y**		**Ultimate strength, f_u**	
				MPa	kN	MPa	kN
H10	10	78.5	184.6	541	42.5	662	52
H13	13	132.7	186.1	584	77.5	666	88.4
H16	16	201.1	173.1	569	114.4	649	130.55

Table 5.5: Main properties of carbon FRP sheet

Carbon FRP sheet	
Elastic modulus (GPa)	240
Tensile strength (MPa)	3800
Design thickness (mm)	0.176
Ultimate tensile force per 100mm width (kN)	21.1
Fiber weight (g/m²)	300
Elongation at rupture	1.55%

Table 5.6: Main properties of carbon FRP rod

Carbon FRP rod	
Elastic modulus (GPa)	165
Design dimension (mm x mm)	10 x 1.4
Rupture strain (%)	1.2
Tensile strength (MPa)	(6‰) 1000
	(6‰) 1300

Table 5.7: Test results and failure modes

Type	**Specimen**	**FRP reinforcement/per side**	**Ultimate load, P_u (kN)**	**Failure mode***
Control specimens	C50	-	613.1	SY/CC
FRP strengthening of tie	CA50-0	-	439.5	SY/TS
	CA50-1	two layer FRP sheets with 75 mm width	585.9	SY/CC
	CA50-2	one layer FRP sheets with 95 mm width and two FRP bars	637.1	SY/CC
FRP strengthening of strut	CB50-0	-	444.1	TS
	CB50-1	two layer FRP sheets	621.47	CC
	CB50-2	two layer FRP sheets and four FRP bars	667.98	CC
Control specimens	C100	-	496.0	SY/CC
FRP strengthening of tie	CA100-0	-	262.7	SY/TS
	CA100-1	two layer FRP sheets with 126 mm width	467.8	SY/CC
	CA100-2	two layer FRP sheets with 97 mm width and two FRP bars	549.0	SY/CC
FRP strengthening of strut	CB100-0	-	164.5	TS
	CB100-1	two layer FRP sheets	461.5	CC
	CB100-2	two layer FRP sheets and four FRP bars	521.9	CC

*CC: Crushing of concrete strut

TS: Tensile splitting of concrete strut

SY/CC: Steel bar yielding followed by crushing of concrete strut

SY/TS: Steel bar yielding followed by tensile splitting of concrete strut

Table 5.8: Comparison between actual and design failure load

Specimen	**Concrete cylinder strength f'_c (MPa)**	**Design ultimate load, $P_{u,d}$ (kN)**	**Actual failure load, $P_{u,Test}$ (kN)**	$P_{u,Test}/P_{u,d}$
C50	69.5	487.1	613.1	1.26
CA50-0	66.8	286.5	439.5	1.53
CA50-1	66.6	487.1	585.9	1.20
CA50-2	66.3	487.1	637.1	1.31
CB50-0	34.3	355.1	444.1	1.25
CB50-1	36.2	487.1	621.5	1.28
CB50-2	39.3	535.8	668.0	1.25
C100	69.5	453.5	496.0	1.09
CA100-0	66.8	307.2	262.7	0.86
CA100-1	66.6	453.5	467.8	1.03
CA100-2	66.3	453.5	549.0	1.21
CB100-0	34.3	355.1	164.5[#]	0.46
CB100-1	36.2	453.5	461.5	1.03
CB100-2	39.3	498.8	521.9	1.21

[#] Premature crack due to spalling of concrete (**Figure 5.13a**).

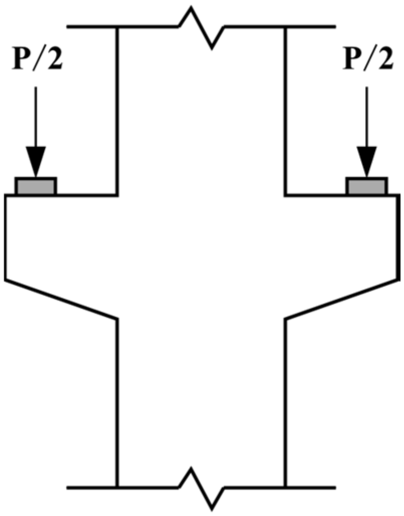

(a) Column with corbels

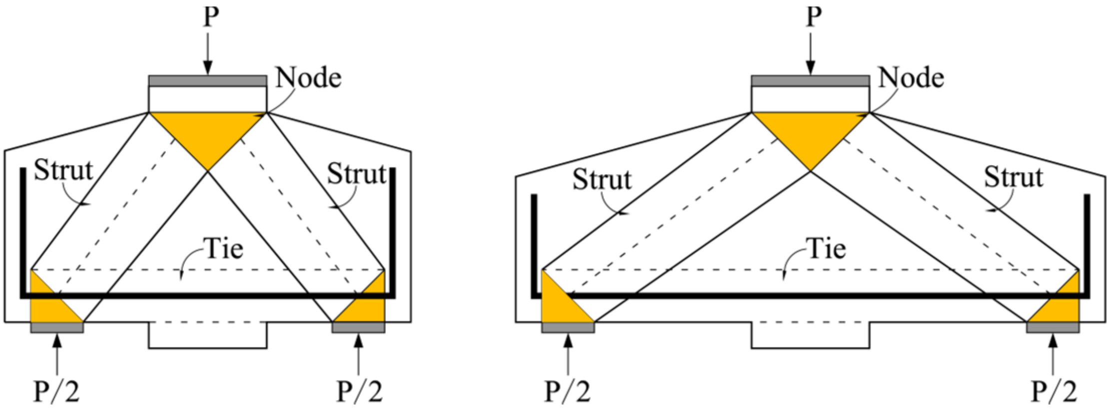

(b) Strut-and-tie model for corbels in inverted position

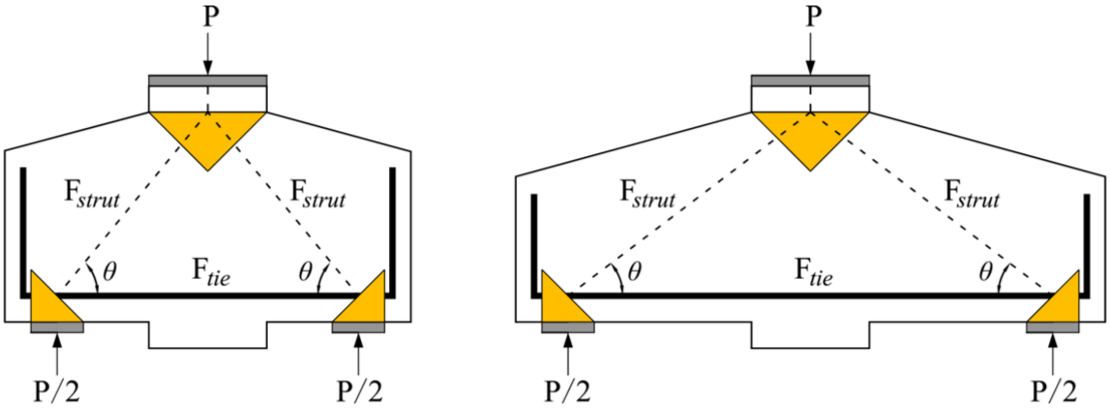

(c) Forces in strut and tie members

Figure 5.1: Strut-and-tie model for corbels

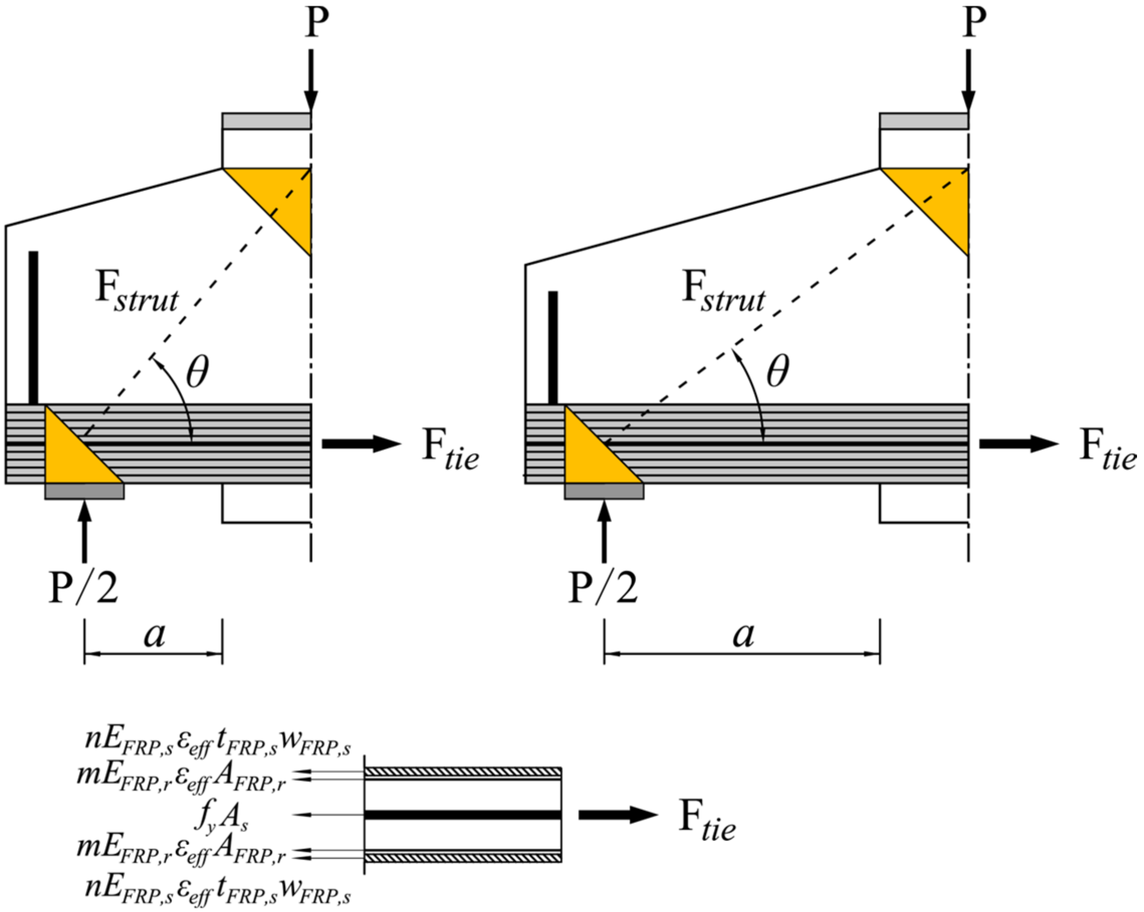

Figure 5.2: Analytical model for corbels with FRP strengthened ties

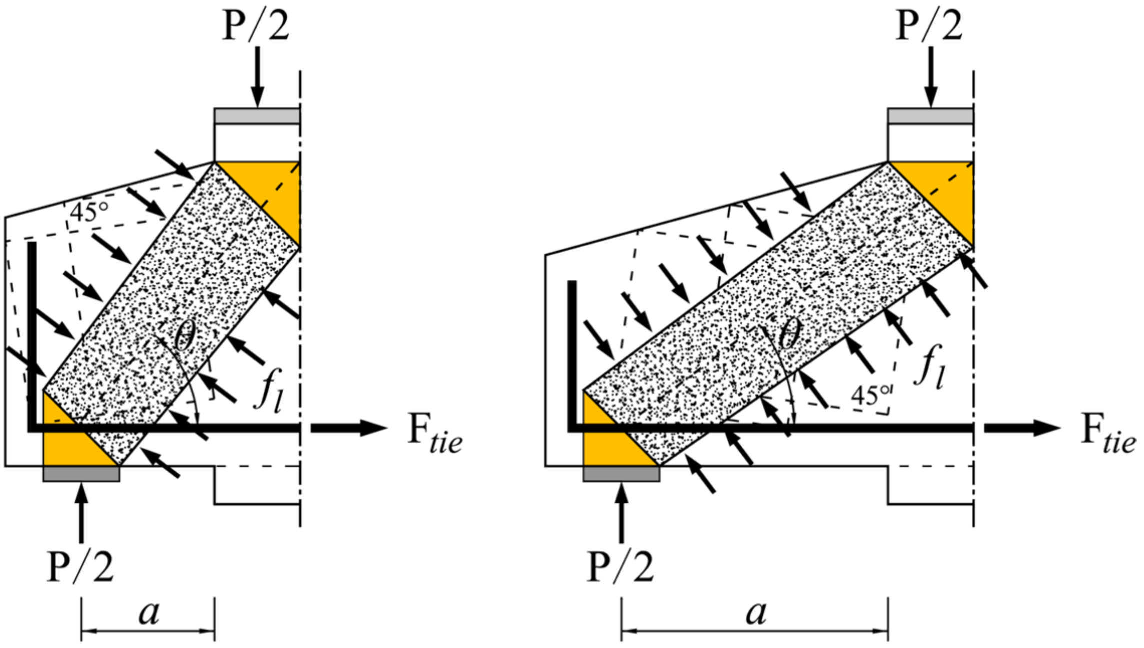

(a) Model for FRP strengthened struts

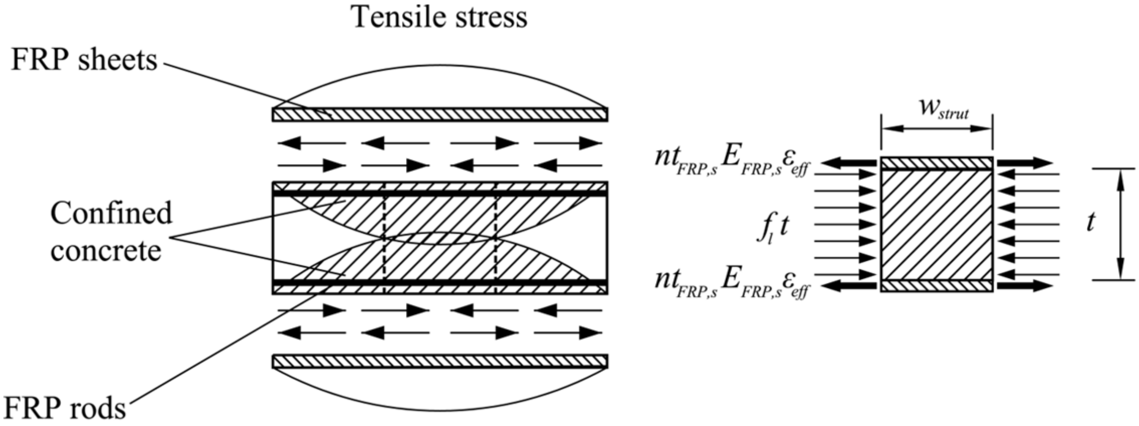

(b) Analytical model

Figure 5.3: Analytical model for corbels with FRP strengthened struts

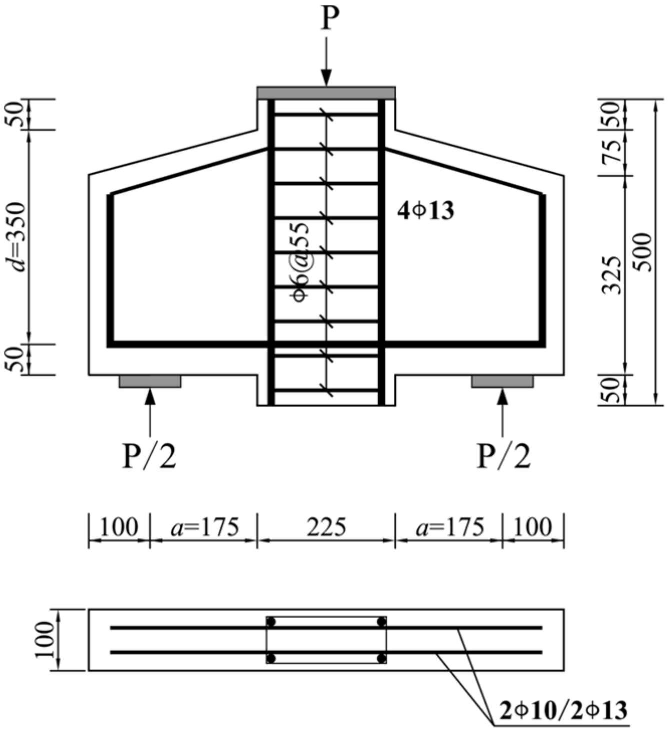

(a) Series C50

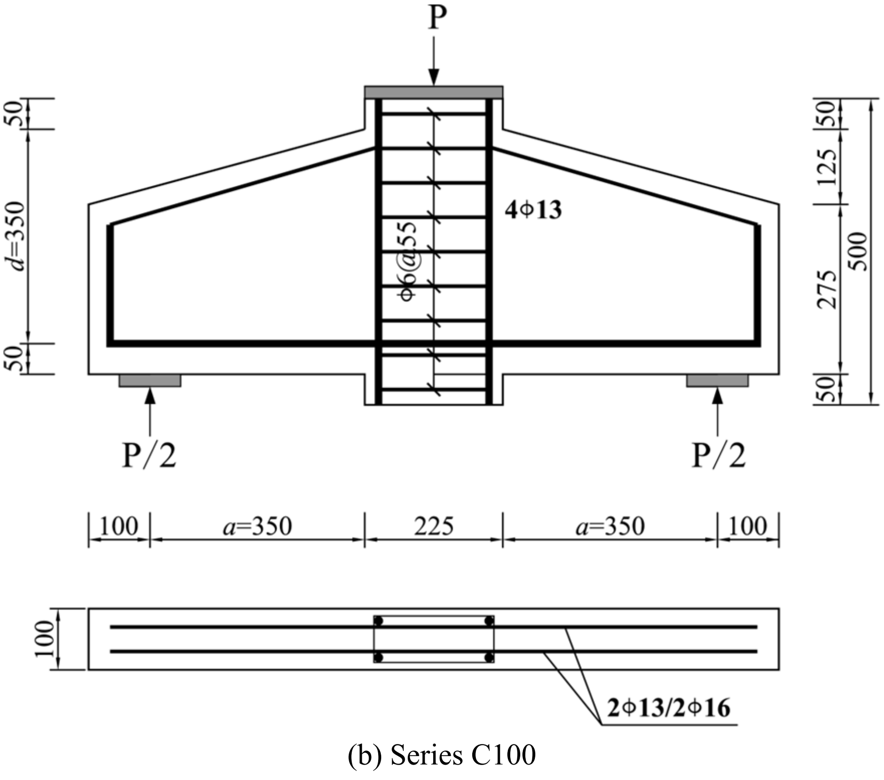

(b) Series C100

Figure 5.4: Size and reinforcement details of test specimens (all dimensions in mm)

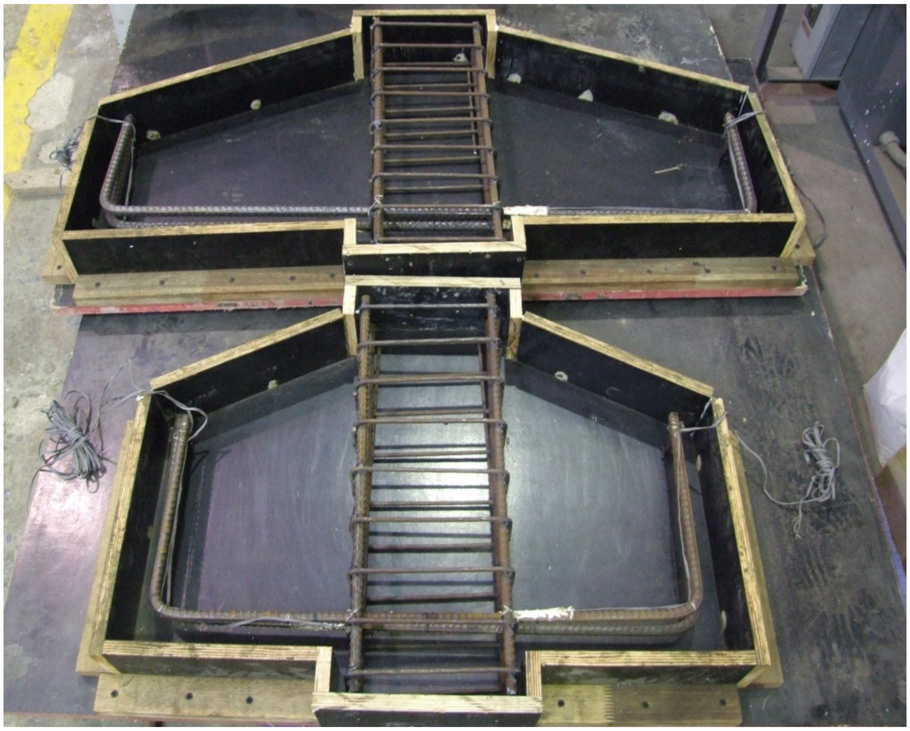
(a) Wooden moulds for corbel specimens


(b) Casting of corbel specimens

Figure 5.5: Specimens preparation

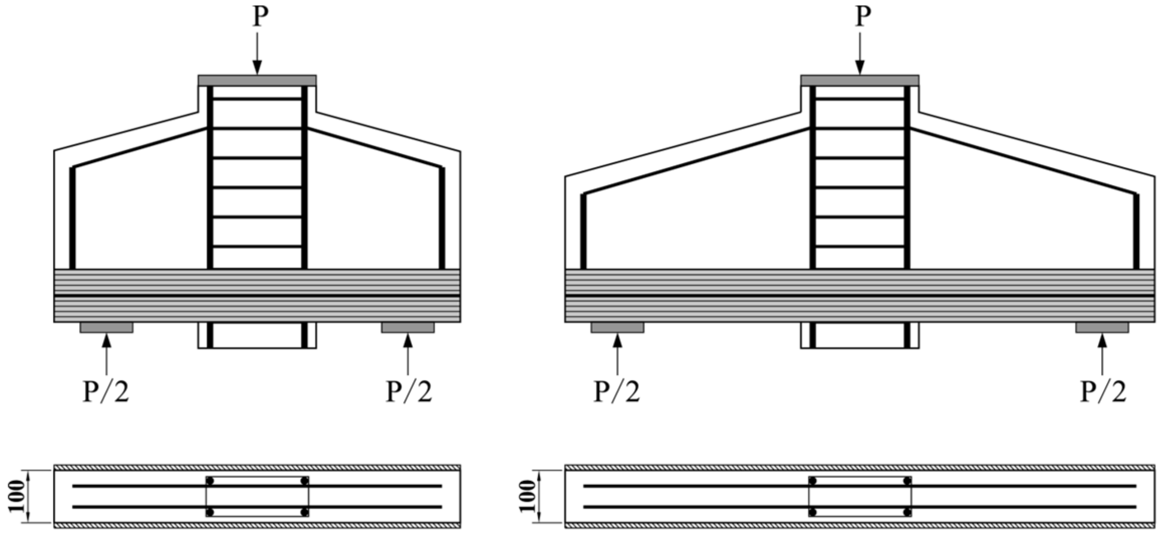

(a) FRP strengthening of tie members

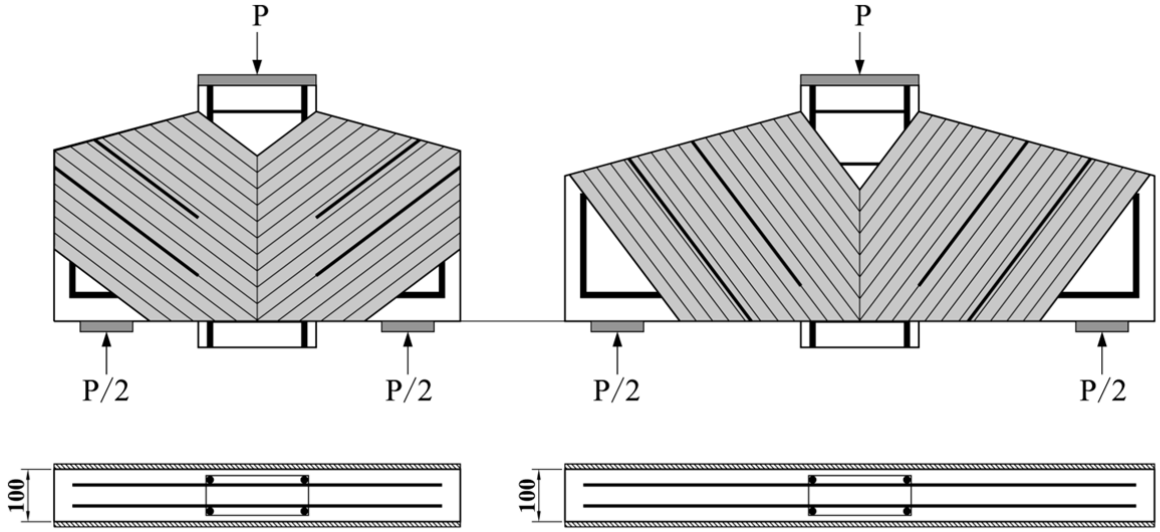

(b) FRP strengthening of strut members

Figure 5.6: FRP strengthening systems

Figure 5.7: Test setup

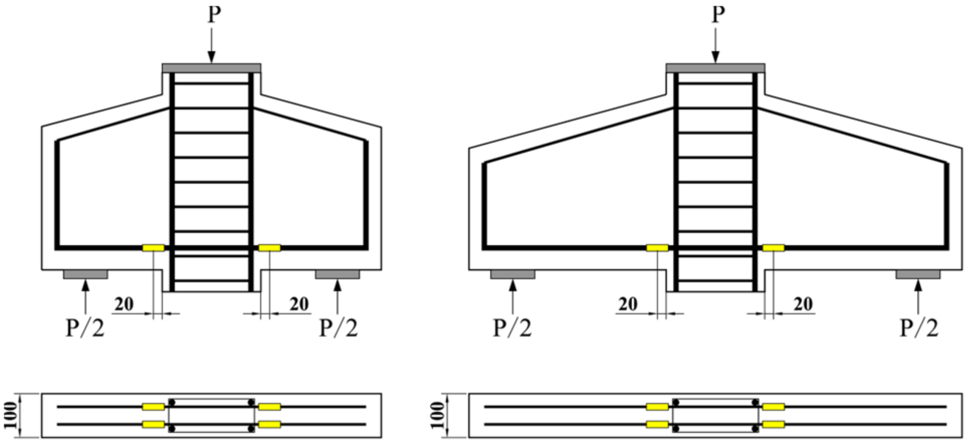

(a) Strain gauges on steel bars

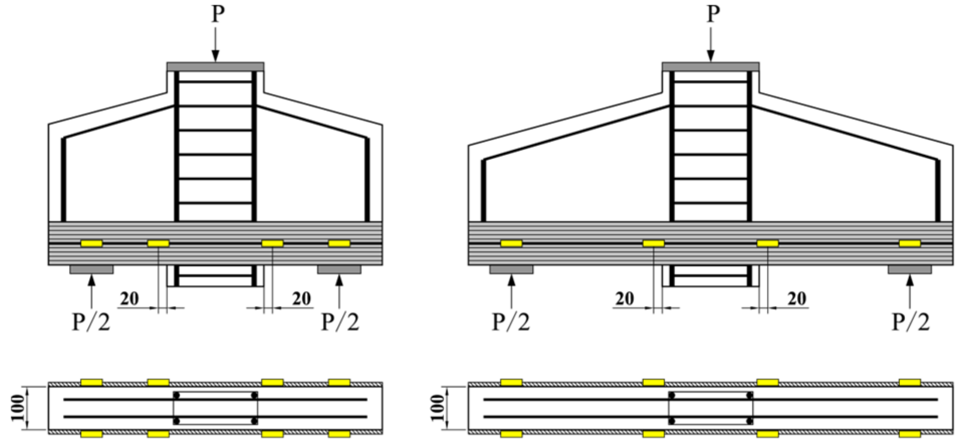

(b) Strain gauges on FRP rods

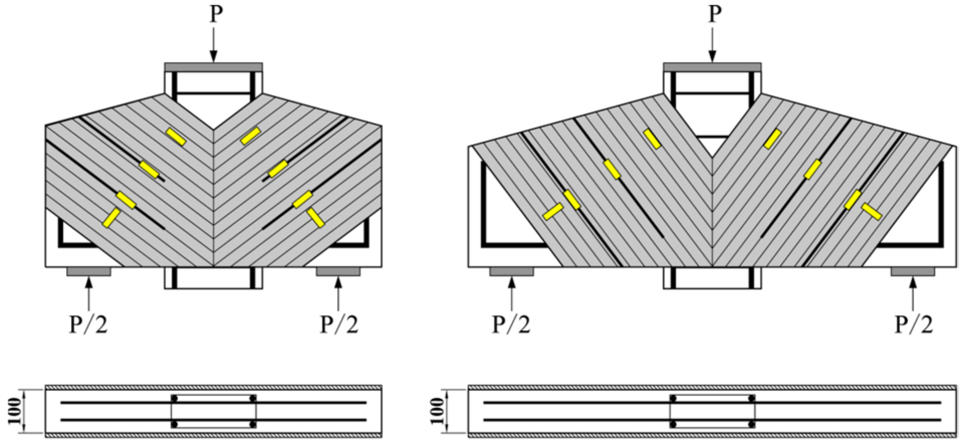

(c) Strain gauges on FRP sheets

Figure 5.8: Arrangement of strain gauges

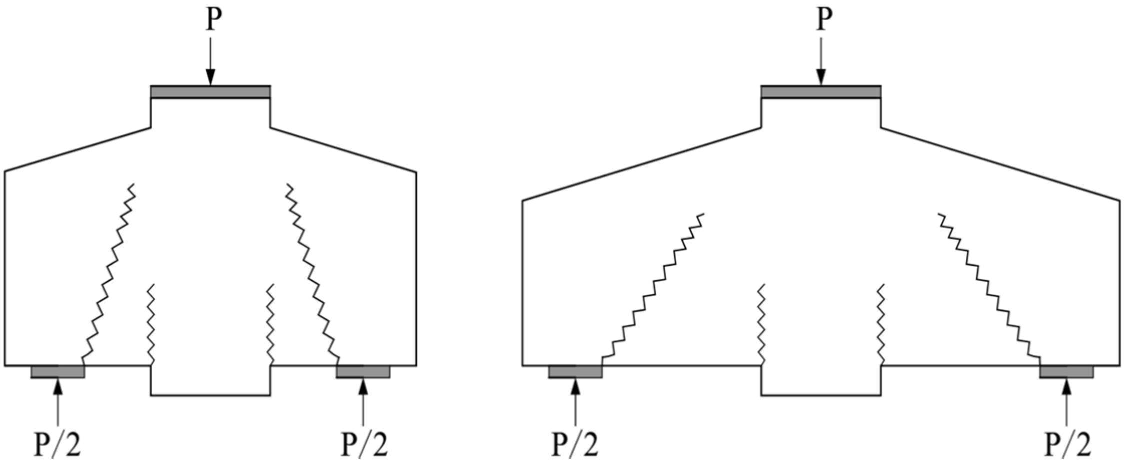

(a) Typical crack patterns

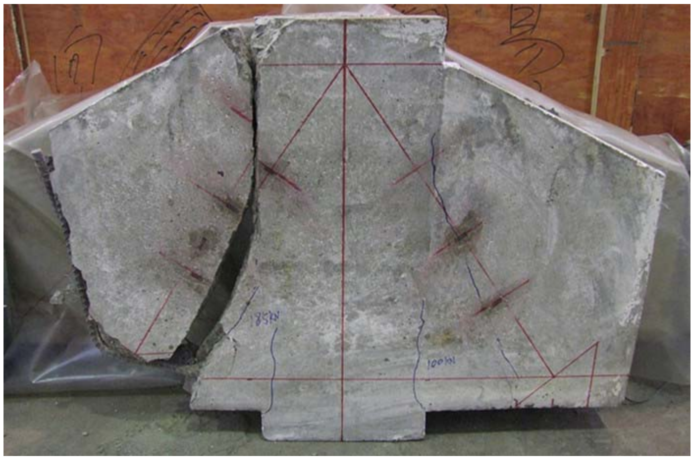

(b) C50

(c) C100

Figure 5.9: Failure modes of control specimens

(a) CA50-0

(b) CA50-1

(c) CA50-2

Figure 5.10: Failure modes of CA50 specimens

(a) CB50-0

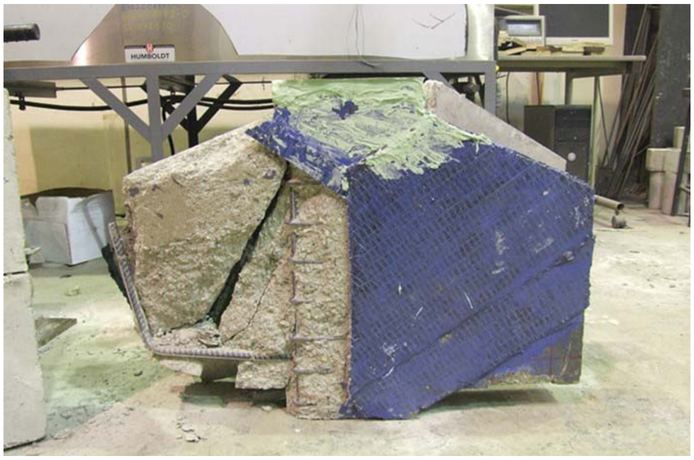

(b) CB50-1

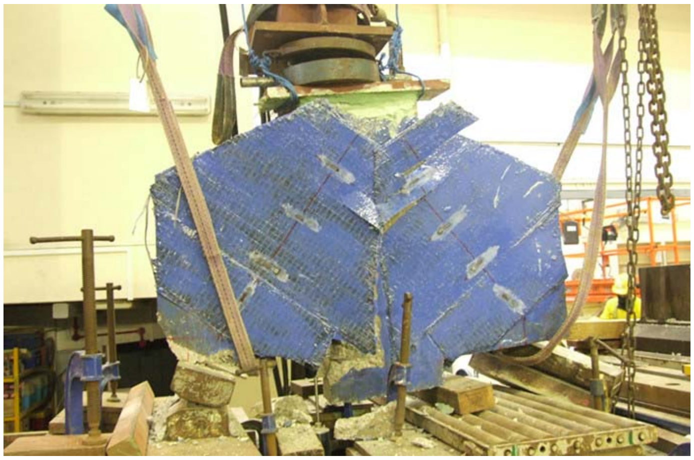

(c) CB50-2

Figure 5.11: Failure modes of CB50 specimens

(a) CA100-0

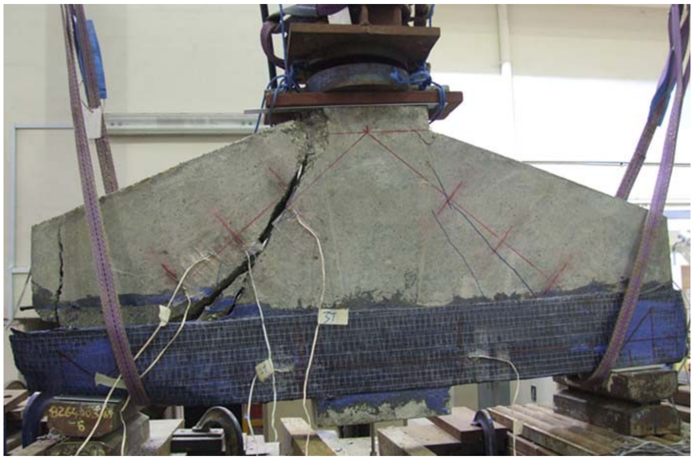

(b) CA100-1

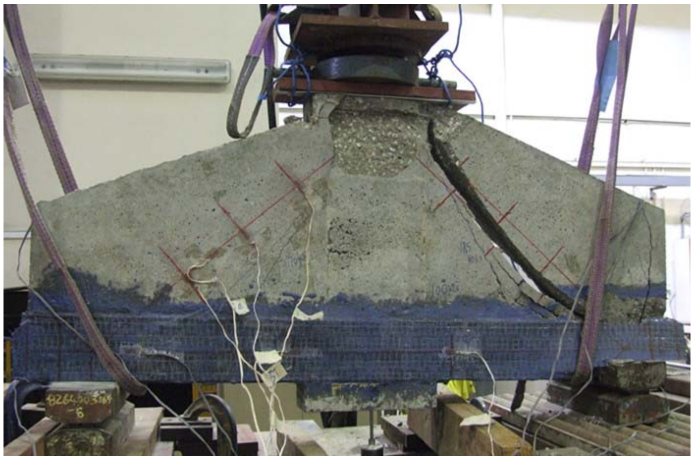

(c) CA100-2

Figure 5.12: Failure modes of CA100 specimens

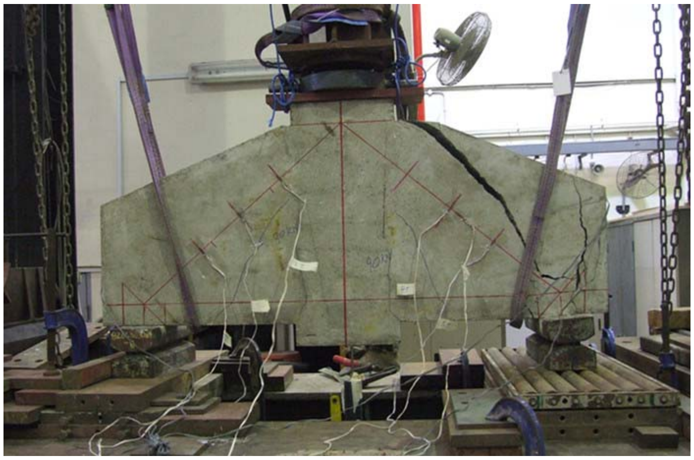

(a) CB100-0

(b) CB100-1

(c) CB100-2

Figure 5.13: Failure modes of CB100 specimens

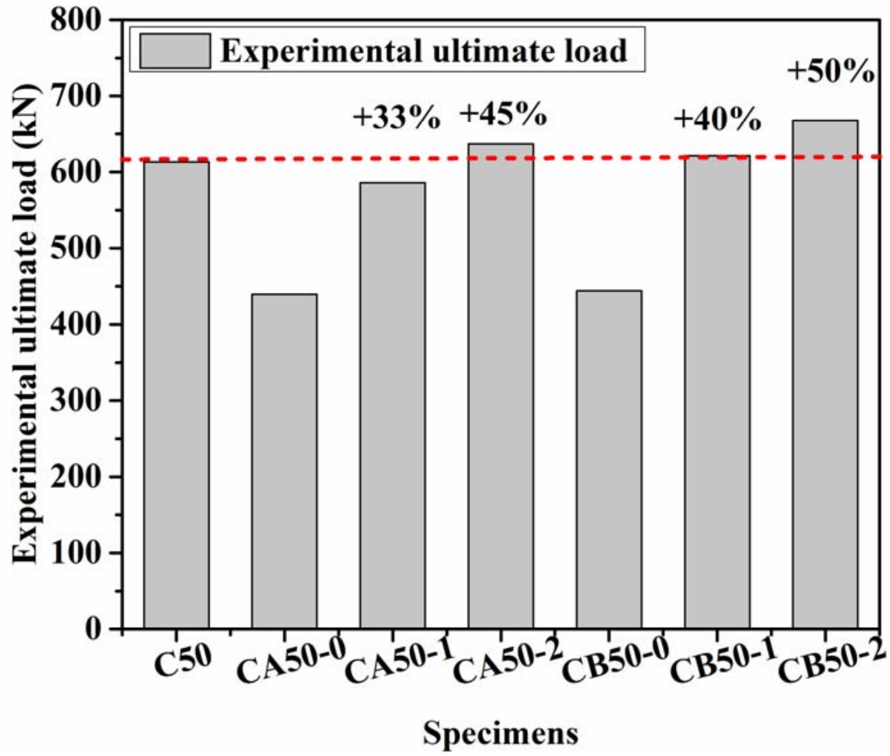

(a) Series C50 specimens (*a*/*d*=0.5)

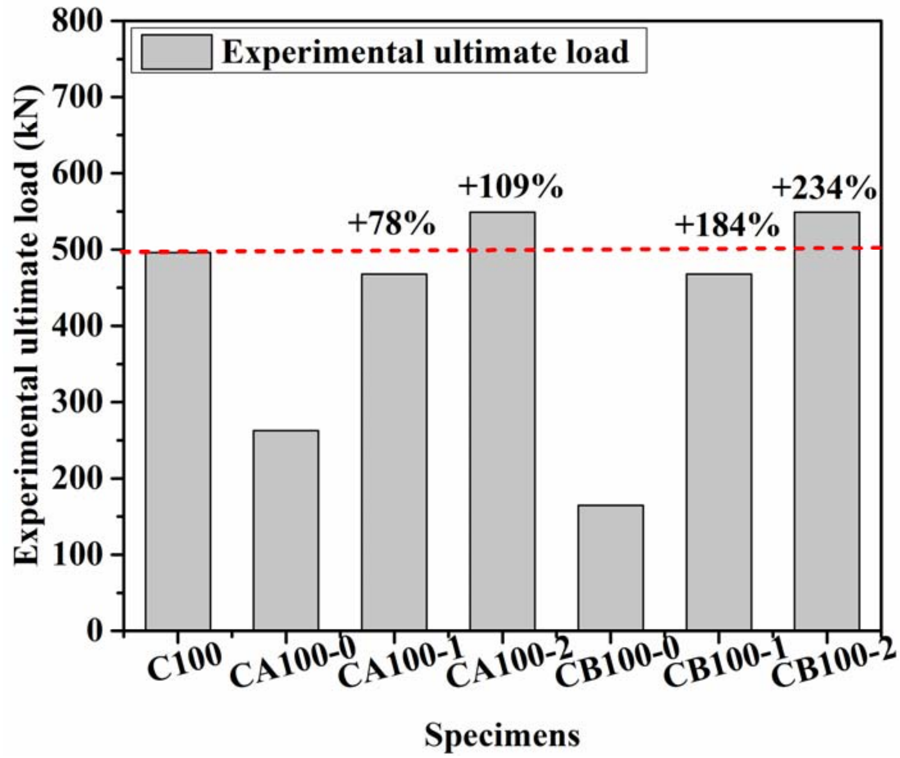

(b) Series C100 specimens (*a*/*d*=1.0)

Figure 5.14: Ultimate load capacity

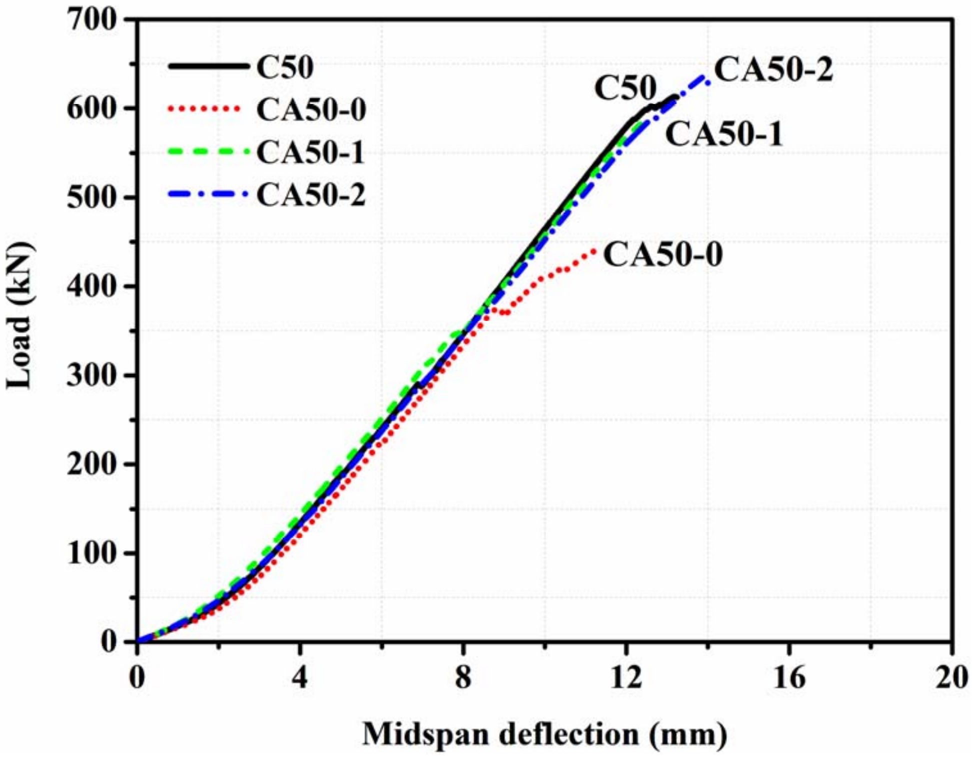

(a) Specimens with FRP strengthened tie members

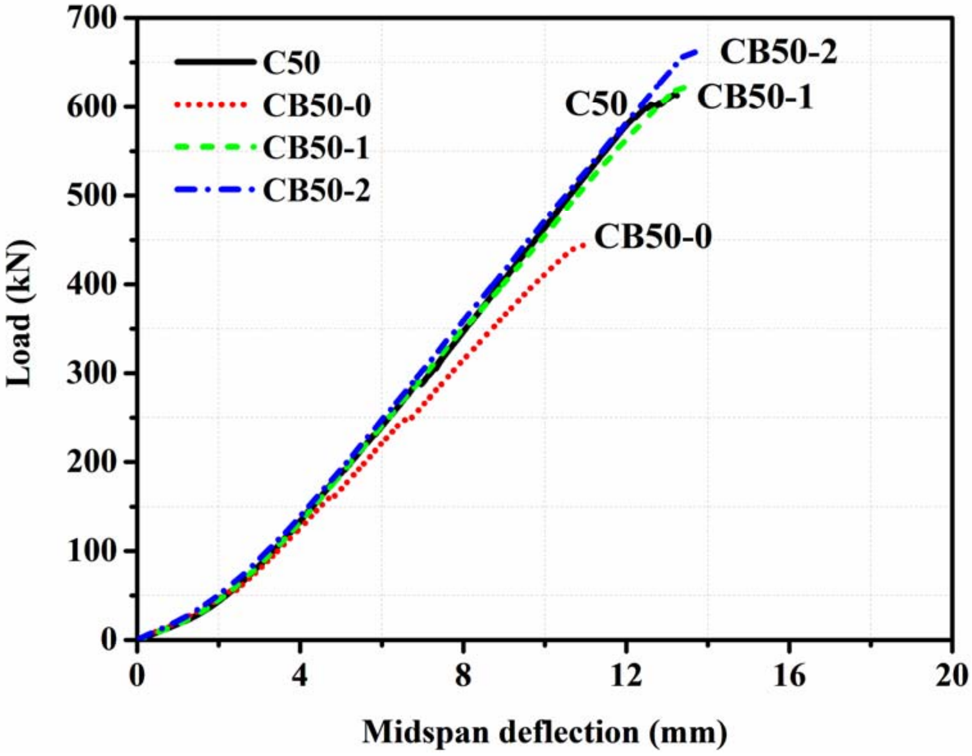

(b) Specimens with FRP strengthened strut members

Figure 5.15: Load-deflection relations of Series C50 specimens (*a*/*d*=0.5)

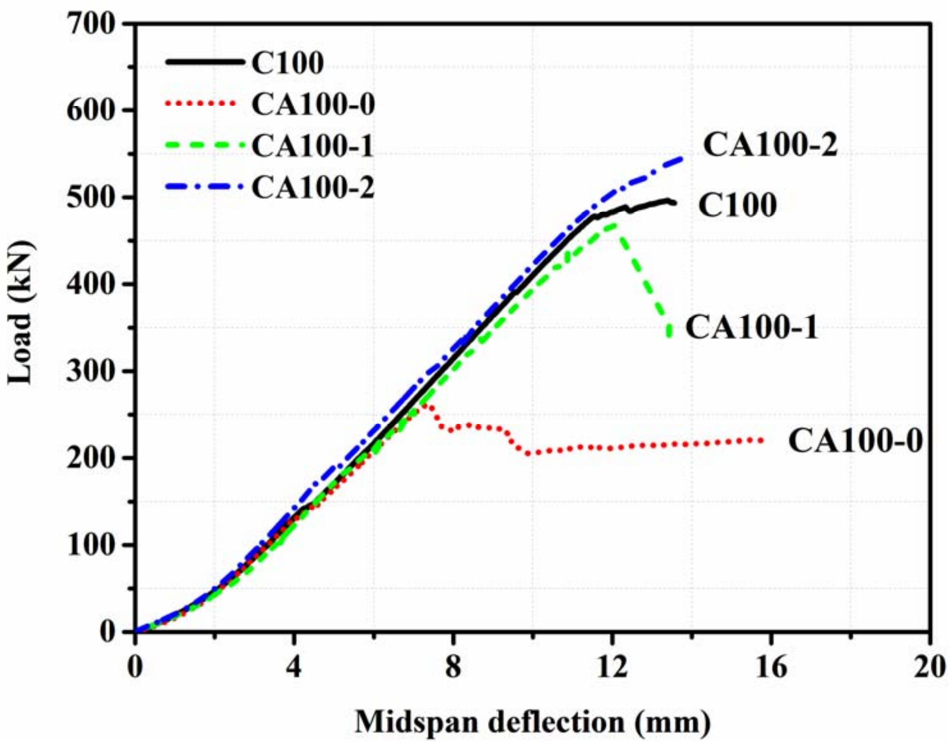

(a) Specimens with FRP strengthened tie members

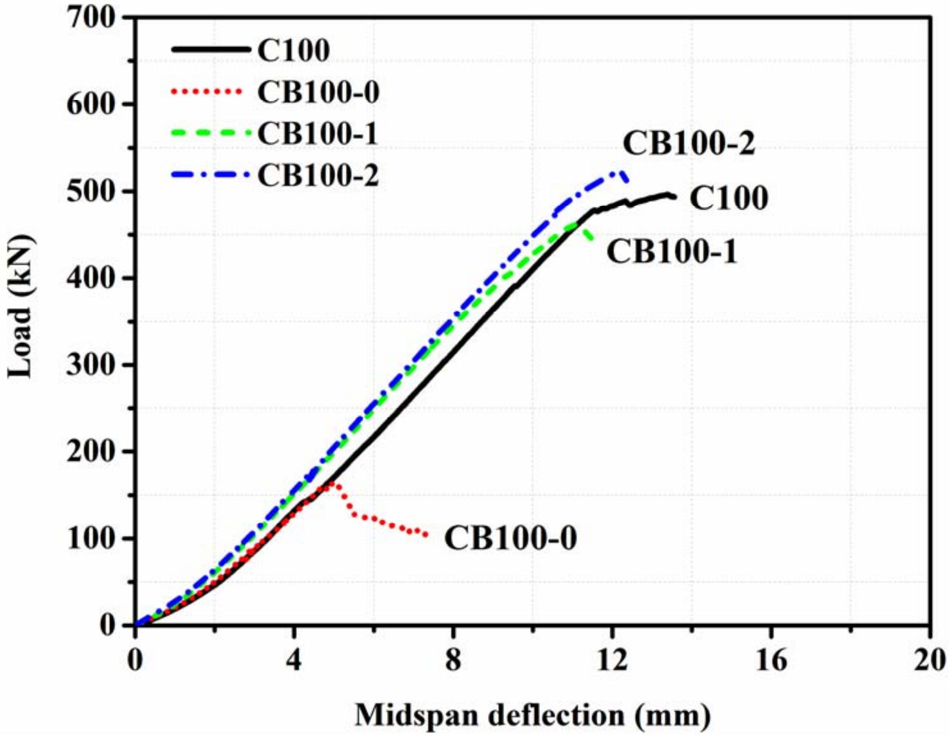

(b) Specimens with FRP strengthened strut members

Figure 5.16: Load-deflection relations of Series C100 specimens (*a*/*d*=1.0)

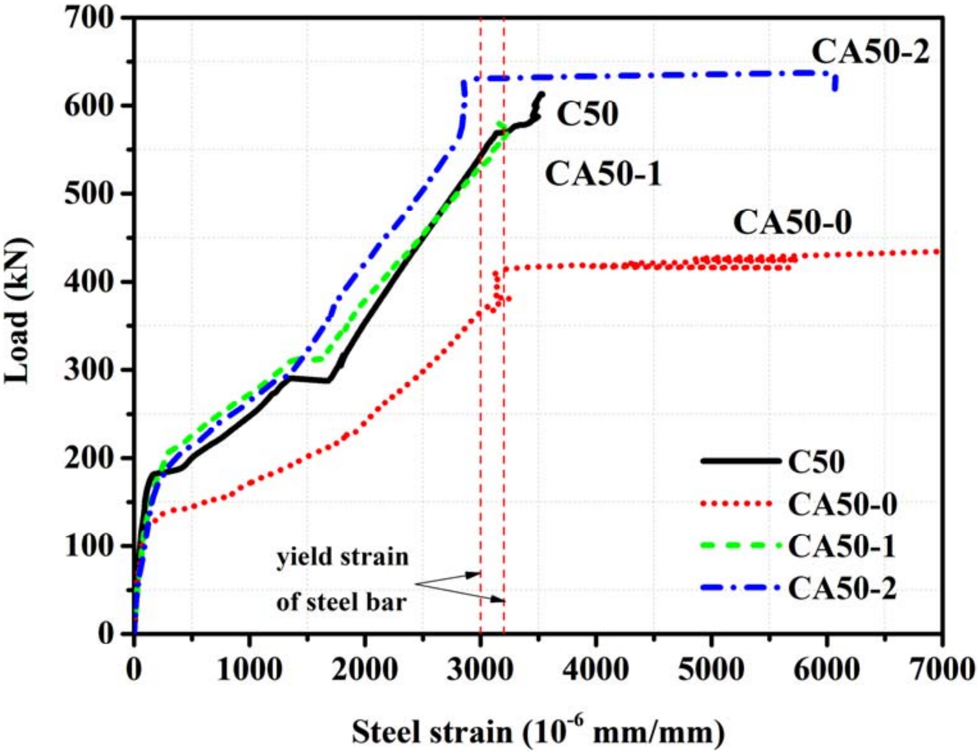

(a) Specimens with FRP strengthening of tie members

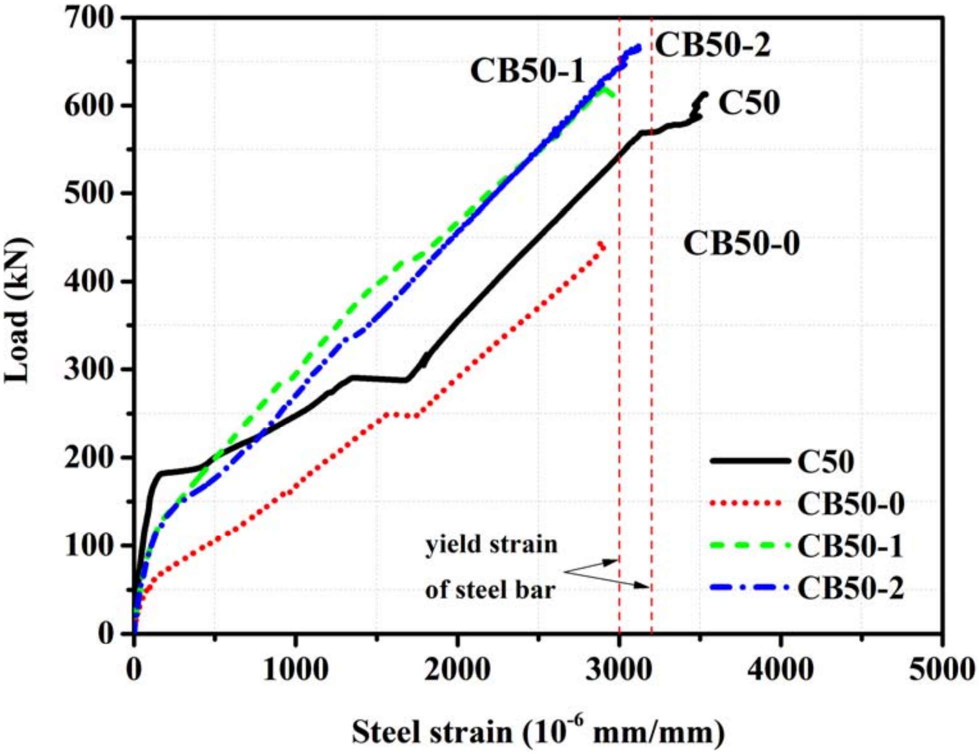

(b) Specimens with FRP strengthening of strut members

Figure 5.17: Steel strain of Series C50 specimens (*a*/*d*=0.5)

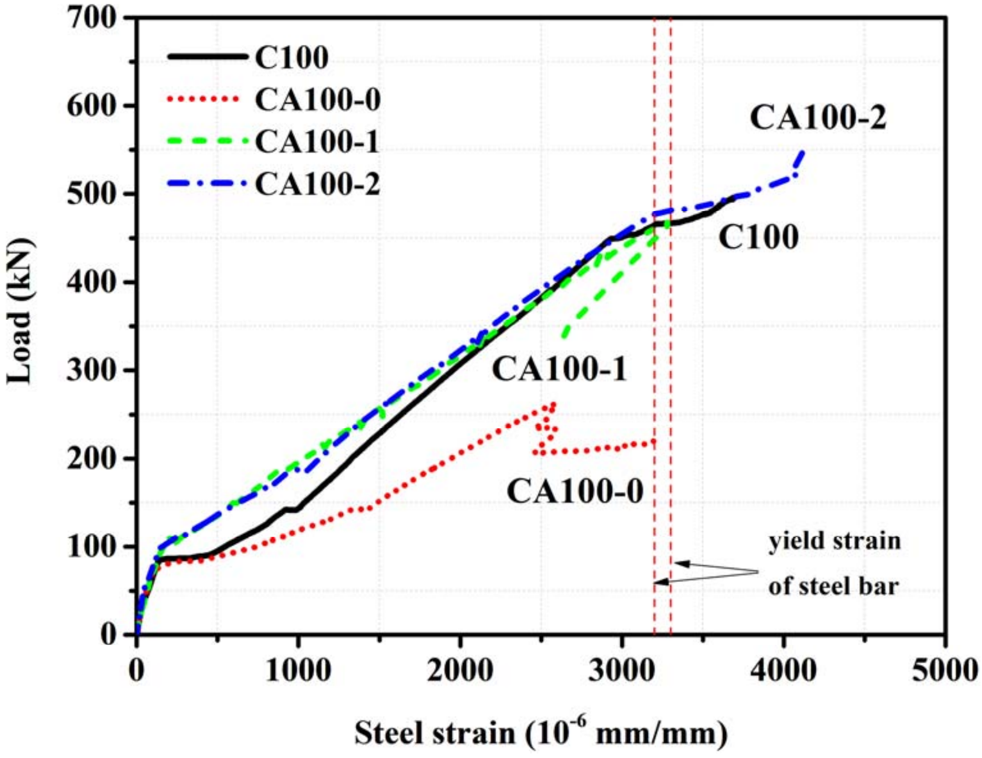

(a) Specimens with FRP strengthening of tie members

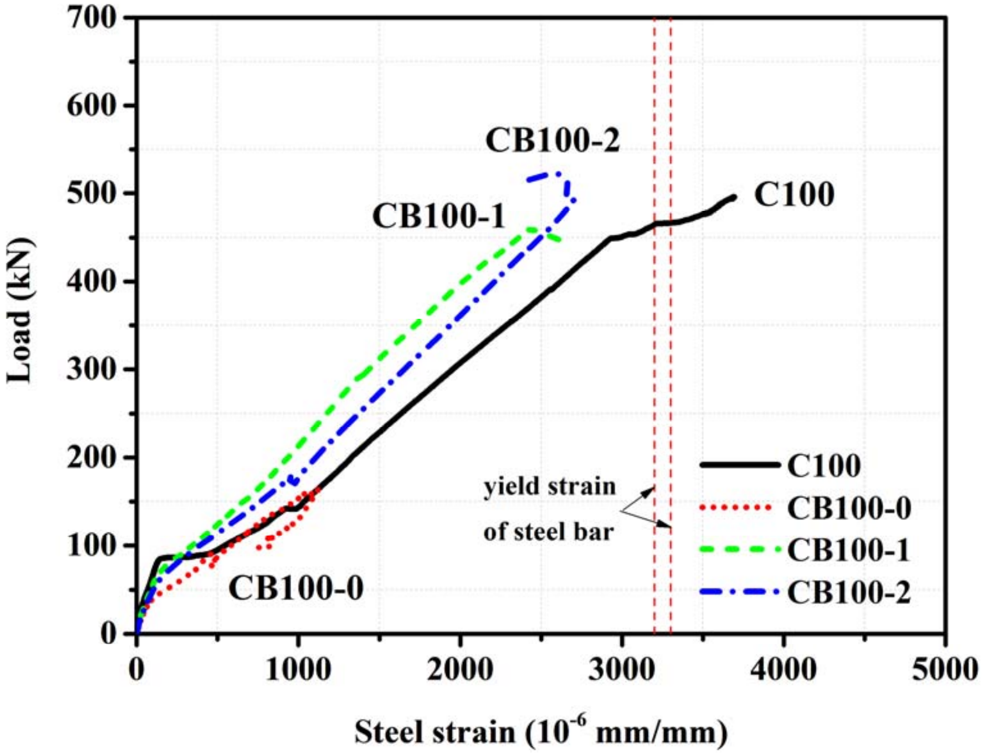

(b) Specimens with FRP strengthening of strut members

Figure 5.18: Steel strain of Series C100 specimens (*a*/*d*=1.0)

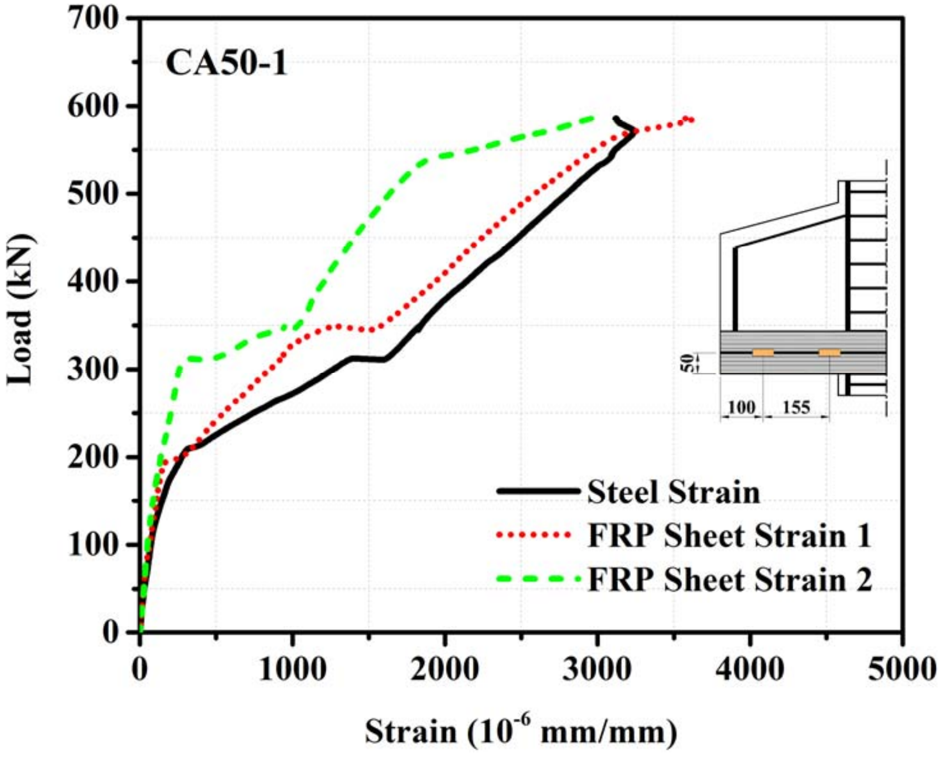

(a) CA50-1

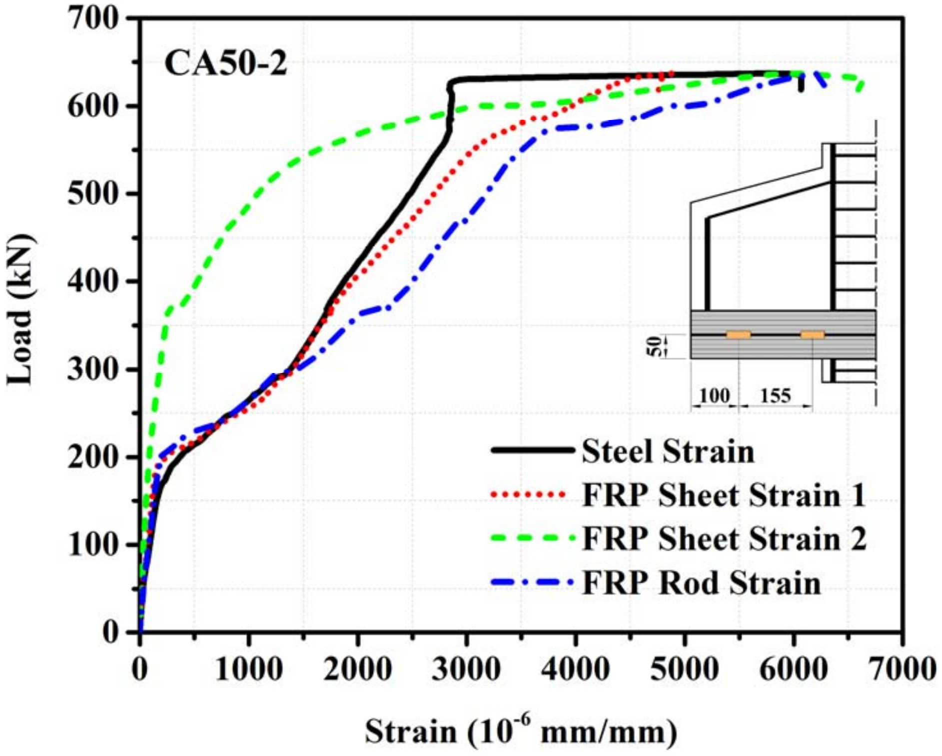

(b) CA50-2

Figure 5.19: Tensile strain of Series CA specimens (at tie member) (cont.)

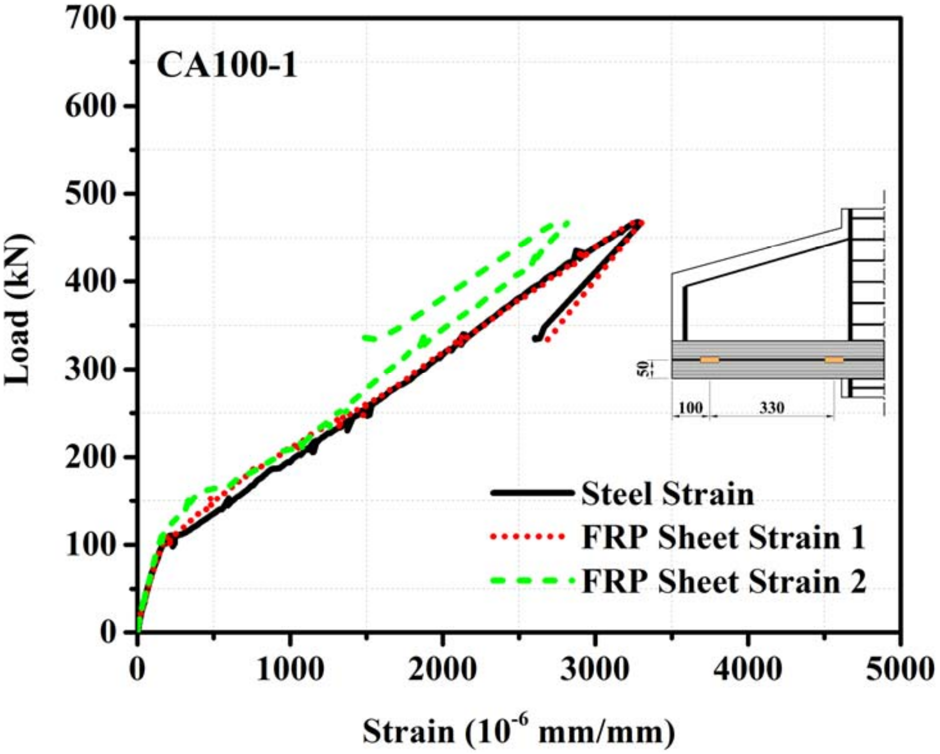

(c) CA100-1

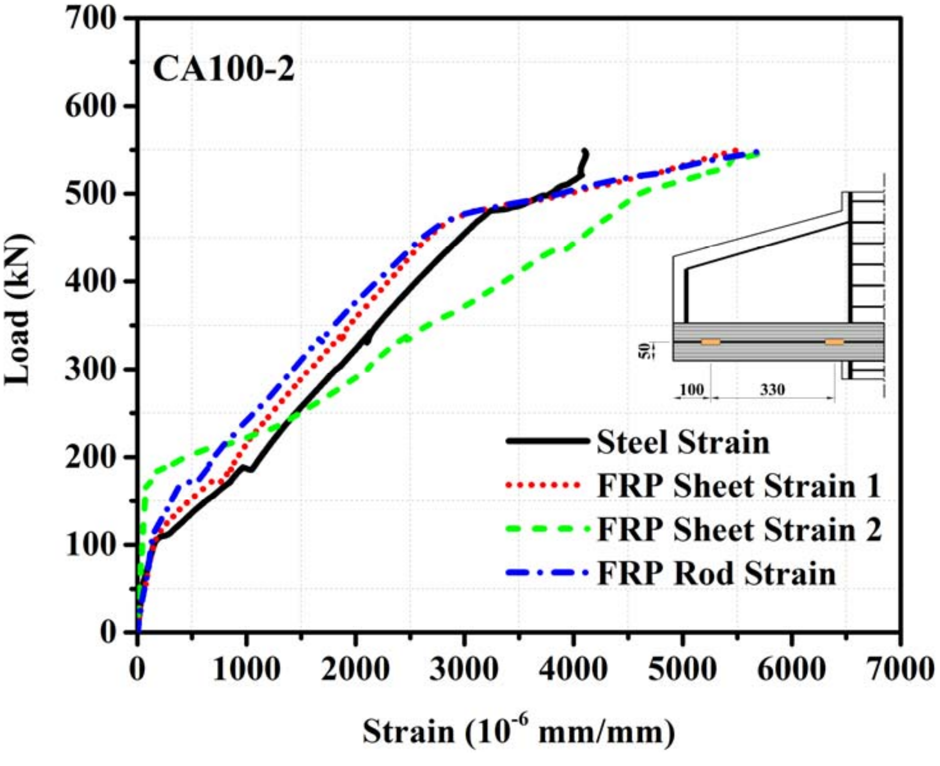

(d) CA100-2

Figure 5.19: Tensile strain of Series CA specimens (at tie member)

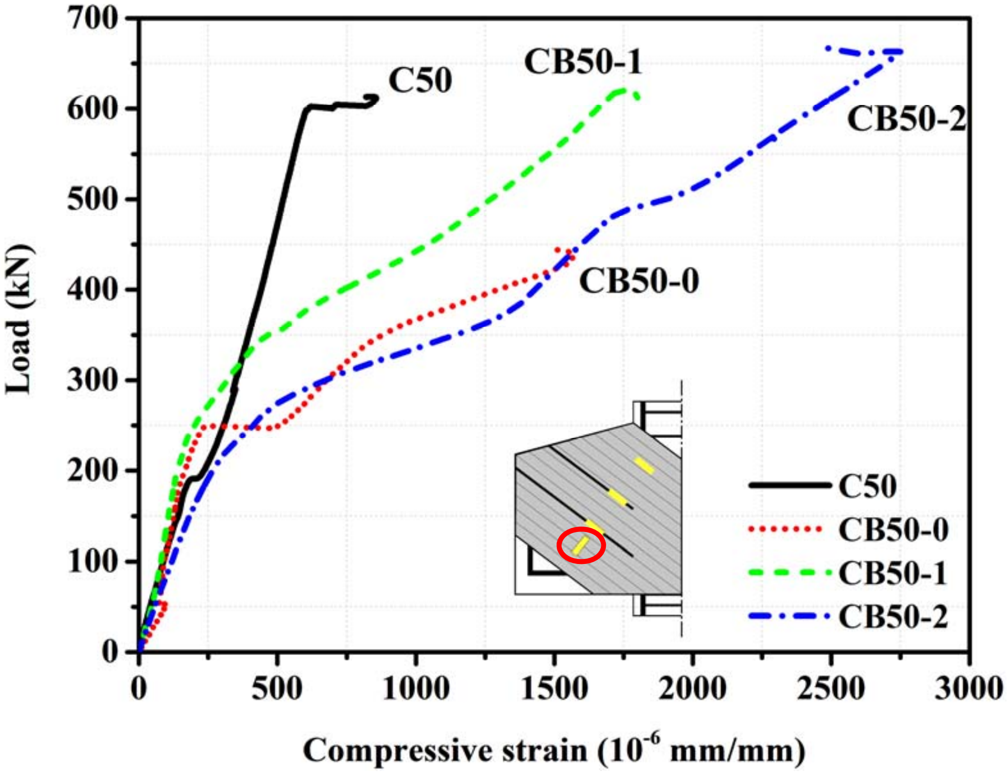

(a) Series C50 specimens

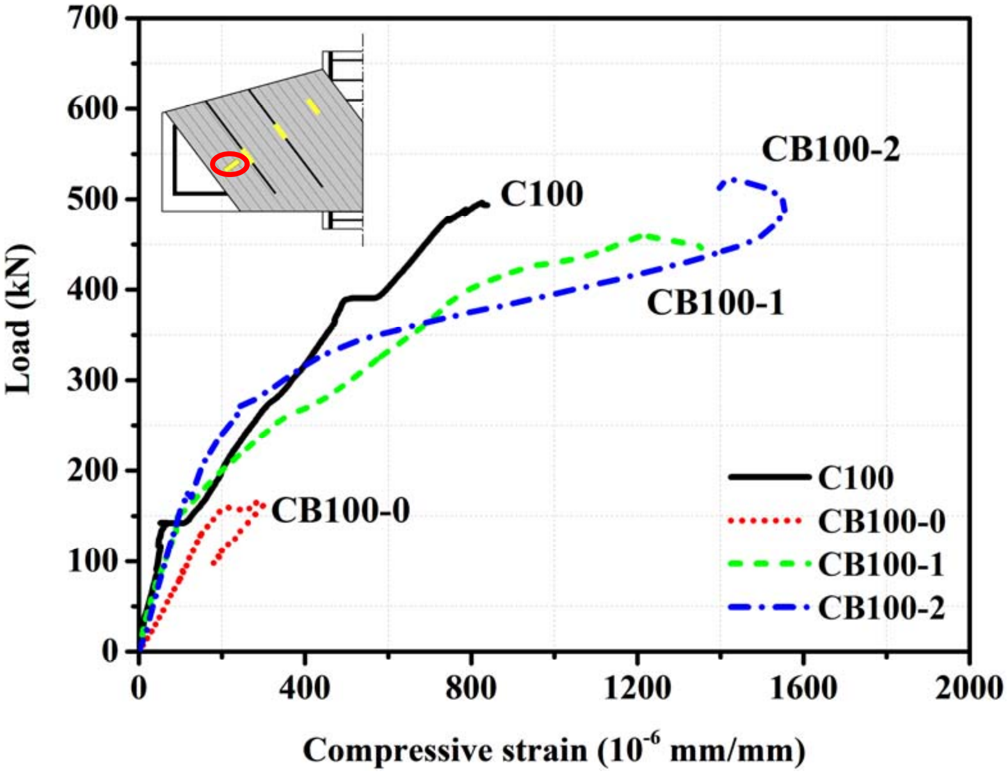

(b) Series C100 specimens

Figure 5.20: Longitudinal compressive strain in struts of Series C50 and C100 specimens

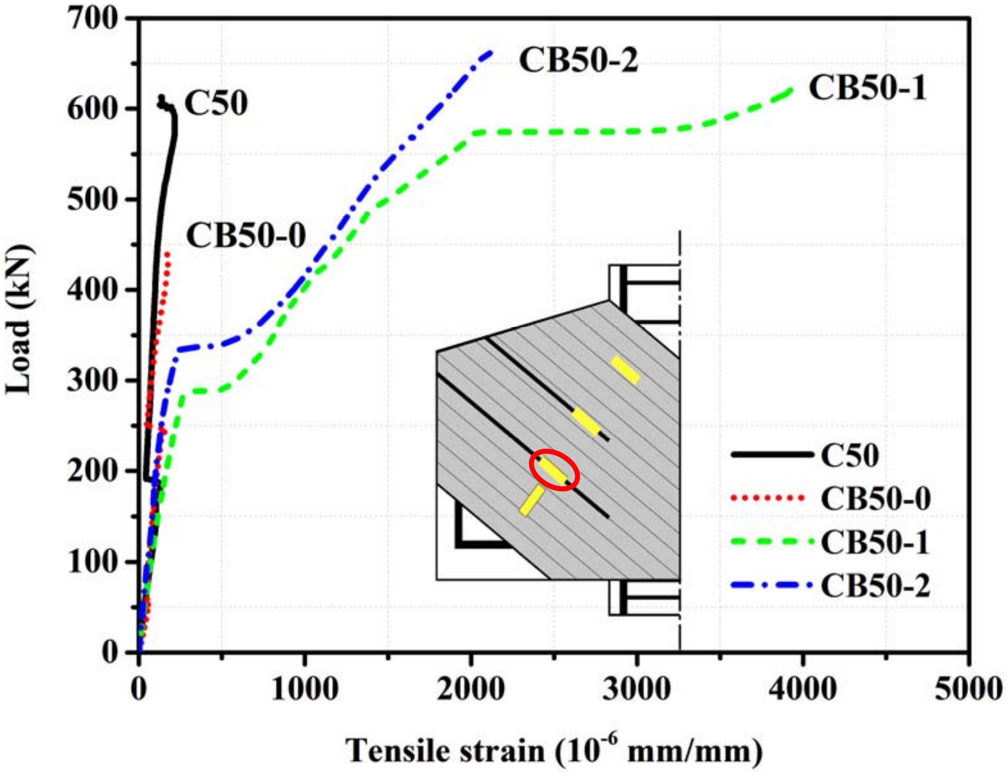

(a) Series C50 Specimens

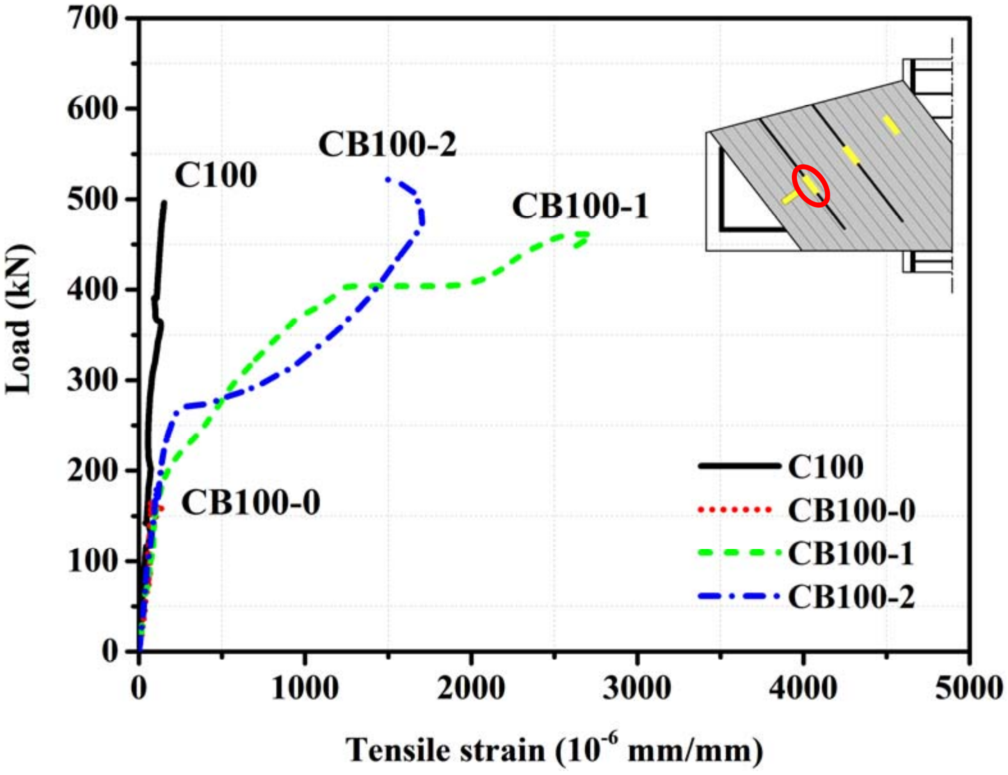

(b) Series C100 specimens

Figure 5.21: Transverse tensile strain in struts of Series C50 and C100 specimens

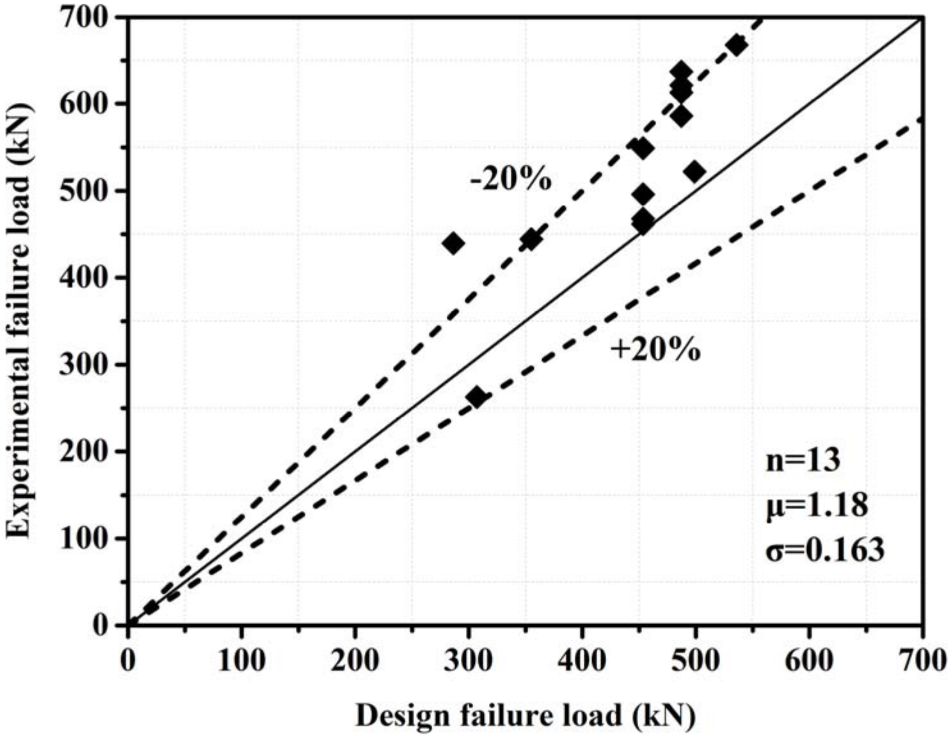

Figure 5.22: Comparison between experimental failure load and predicted failure load

Chapter 6. Conclusions and Recommendations

6.1 Review of work

This study was carried out to evaluate the strut-and-tie method for FRP strengthening of non-flexural reinforced concrete structural members. A comprehensive literature survey was first conducted on the strengthening of non-flexural members such as deep beams, dapped beams, beams with openings, corbels and others using FRP systems. Focus was placed on the use of strut-and-tie modelling in such strengthening works. In order to increase the loading-carrying capacity of non-flexural members, it would be necessary to consider strengthening the strut and/or tie members in the strut-and-tie model. The study therefore consisted of three parts.

In the first part, eight short tie and seven long tie specimens were fabricated and tested to failure under direct tension. The behavior and ultimate tensile load capacity of FRP-strengthened RC tie member were observed, and the effect of FRP strengthening systems was analyzed. An analytical model was proposed to determine the ultimate tensile load capacity of FRP-strengthened RC tie members, and the predictions were compared with experimental values.

In the second part, a total of twenty-seven plain concrete strut specimens were fabricated and tested to failure under axial quasi-static compressive loading. The behavior and ultimate load of FRP-strengthened strut members were investigated. The effect of FRP strengthening systems on prismatic, partial bottle-shaped and full bottle-shaped struts was analyzed. An analytical model was also proposed to calculate the ultimate axial load capacity of strut members strengthened by FRP reinforcement, and the predicted ultimate loads were compared with experimental values.

In the third part, in order to verify the validity of the proposed strengthening approach based on strut-and-tie modelling for non-flexural RC members, a case study on RC corbels was carried out. Fourteen corbel specimens either deficient in concrete strength or internal steel reinforcement were fabricated, strengthened with FRP systems following the findings of part 1 and 2 of the study and tested to failure under vertical loading.

6.2 Summary of main findings

From the studies carried out on FRP strengthening of non-flexural RC members based on strut-and-tie modelling, the following conclusions can be drawn.

1. FRP strengthening of tie members

(a) Longitudinal elongation and crack widths in tie members were reduced by FRP reinforcement. The ultimate tensile load capacity was substantially increased. Failure of the FRP-strengthened tie specimens was sudden and non-ductile due to de-bonding and rupture of FRP reinforcement.

(b) The effective strain in the FRP reinforcement was found to be about 0.003 to 0.005.

(c) The strengthening effectiveness of NSM-FRP rods was better than EB-FRP sheets while the most effective FRP strengthening system consisted of a combination of NSM-FRP rods and EB-FRP sheets.

(d) The theoretical load-strain curves based on de-bonding of FRP reinforcement matched the test results well, although the axial stiffness was higher than observed.

(e) The gain in the ultimate load due to FRP strengthening systems was proportional to the FRP reinforcement parameter.

2. FRP strengthening of strut members

(a) The ultimate load capacity of strut members was substantially increased when strengthened with FRP sheets. After being strengthened by EB-FRP sheets, the failure mode of partial bottle-shaped struts changed from a tensile splitting failure of concrete to the crushing of concrete at or near the loaded faces, while the failure mode of bottle-shaped struts remained as due to the tensile splitting of concrete. No significant improvement in the ultimate load capacity was observed for partial bottle-shaped strut members strengthened with NSM-FRP rods only. The most effective FRP configuration consisted of a combination of EB-FRP sheets and NSM-FRP rods.

(b) During the initial stages of loading, prior to initiation of the longitudinal splitting crack, the maximum transverse tensile strains were recorded near the mid-height of the struts and, as the loading increased, the locations of the maximum transverse tensile strains shifted towards the loaded faces of the struts.

(c) The observed transverse tensile strains at failure of the strut were about 0.003 to 0.004, while the longitudinal compressive strains were around 0.002.

(d) Analytical methods based on confined concrete models and strut-and-tie models were proposed to predict the axial load capacity of the FRP-strengthened strut members. Good agreement with the test results was observed for bottle-shaped strut using a biaxially confined concrete model proposed by Tan *et al.* (2013).

3. Verification of proposed approach for FRP strengthening of corbel

(a) The loss of ultimate load capacity of RC corbels due to low concrete strength or low steel reinforcement could be restored by FRP strengthening using EB-FRP sheets and NSM-FRP rods based on strut-and-tie modelling.

(b) All corbels showed a brittle mode of failure with little warning. The stiffness of corbel specimens was not increased by the presence of FRP reinforcement.

(c) The analytical models proposed in Chapters 3 and 4 to design the FRP strengthening systems and evaluate the strength of FRP-strengthened tie and strut members were verified. The design approach led to good agreement between the design ultimate load and the observed values, with the latter exceeding the design values on most specimens.

4. The effective tensile and compressive strain of the FRP reinforcement

Following ACI 440 (2008)’s recommendation, to ensure integrity of the confined concrete, the effective FRP strain at failure can be taken as: $\varepsilon_{eff} = 0.004 \leqslant 0.75\varepsilon_{FRP,ru}$, where $\varepsilon_{FRP,ru}$ is the rupture strain of FRP reinforcement. 0.004 and 0.002 were adopted as the effective tensile strain and effective compressive strain of the FRP reinforcement in the equations and predictions. In Chapter 3, the observed effective tensile strain in the FRP reinforcement was found to be about 0.003 to 0.005. In Chapter 4, the observed transverse tensile strains at failure of the strut were about 0.003 to 0.005, while the observed longitudinal compressive strains were around 0.002 to 0.003. In Chapter 5, the effective tensile strain of FRP was in the order of 0.003 to 0.004 and the effective compressive strain was therefore in the order of 0.002. Thus, the assumption of both an effective tensile strain of 0.004 and an effective longitudinal compressive strain of 0.002 in the FRP reinforcement was justified. The effectiveness of the value, 0.004 and 0.002, had also been confirmed by comparison "theoretical" predictions with experimental results.

Taking into account the complex bond behavior of the concrete-FRP interface, it would be necessary in the future to study the effective FRP strain at failure in greater depth and broaden the experimental database. This might make it possible to set a future code for FRP strengthening technique.

6.3 Recommendations for further research

Some recommendations for further research in the area of FRP strengthening of non-flexural RC members based on strut-and-tie modelling are also suggested below.

1. This study assumes that the nodal zones are sufficiently strong to carry the additional load due to strengthening. Further study may be carried out to investigate the strength of nodal zones and methods to strengthen these zones.

2. This study demonstrated the validity of the proposed strengthening design approach based on strut-and-tie modelling. Future study could be carried out on other types of non-flexural RC members, such as deep beams, and beams with openings.

3. Numerical modeling by FEM would be an interesting and powerful method to check the accuracy of the recorded strains. The FEM model could be used to better calibrate the equations adopted for prediction by conducting a small parametric study in the future study.

References

Adebar, P. and Zhou, L. (1996). “Design of deep pile caps by strut-and-tie models.” *ACI Structural Journal*, 93(4), 437-448.

Afefy, H. M. E., Mahmoud, M. H. and Fawzyneering, T. M. (2013). “Rehabilitation of defected RC stepped beams using CFRP.” *Engineering Structures*, 49, 295-305.

Alshegeir, A. and Ramirez, J. A. (1992). “Strut-tie approach in pre-tensioned deep beams.” *ACI Structural Journal*, 89(3), 296-304.

American Concrete Institute (ACI). (2011). “Building code requirements for structural concrete and commentary”. *ACI 318-11*, Farmington Hills, Michigan.

American Concrete Institute (ACI). (2008). “Guide for the design and construction of externally bonded FRP systems for strengthening concrete structures.” *ACI 440.2R-2008*, Farmington Hills, Michigan.

American Association of State Highway and Transportation Officials (AASHTO). (2008). “AASHTO LRFD Bridge Design Specifications. 4th Edition—2008 Interim Revisions.” Washington, DC: AASHTO.

Arabzadeh1, A., Aghayari, R., Rahai, A. R. (2012). “A new model for predicting the effective strength in reinforced concrete bottle-shaped struts.” *International Journal of Civil Engineering*, 10(4), 253-262.

Australian Standard Committee BD/2. (1994). “Concrete structures (AS 3600-1994).” Standards Association of Australia.

Bergmeister, K., Breen, J. E., and Jirsa, J. O. (1991). “Dimensioning of the nodes and development of reinforcement.” Report of the IABSE Colloquium on Structural Concrete. IABSE Stuttgart, Germany, 551-556.

Brown, M. D., Sankovich, C. L., Bayrak, O. and Jirsa, J. O. (2006). “Behavior and efficiency of bottle-shaped struts.” *ACI Structural Journal*, 103(3), 348-355.

Brown, M. D. and Bayrak, O. (2006). “Minimum transverse reinforcement for bottle-shaped struts.” *ACI Structural Journal*, 103(6), 813-821.

Brown, M. D. and Bayrak, O. (2008). “Design of deep beams using strut-and-tie models—Part II: design recommendations.” *ACI Structural Journal*, 105(4), 142-149.

Canadian Standards Association (CSA). (1994). “Design of concrete structures (CAN3-A23.3M94).” Structural Design, Rexdale.

Collins, M.P. and Mitchell, D. (1986). “A rational approach to shear designd the 1984 Canadian Code Provisions.” *ACI Journal*, 83(6), 925-933.

Comité Euro International du Béton.(1993). “CEB-FIP Model Code 1990: Design Code, 1st edition.” Thomas Telford, London.

Concrete Design Committee. (1995). “The design of concrete structure (NZS3101: Part 1 and 2: 1995).” New Zealand Standard.

De Luca, A., Matta, F., and Nanni, A. (2010). “Behavior of full-scale glass fiber-reinforced polymer reinforced concrete columns under axial load.” ACI Structural Journal, 107(5), 589.

Elgwady, M. A., Rabie, M., and Mostafa, M. T. (2005). “Strengthening of corbels using CFRP, an experimental program.” Cairo University, Giza, Egypt.

European Committee for Standardizations (CEN). (2004). “Eurocode 2: Design of concrete structures: Part1-1: General rules and rules for buildings.” *EN 1992-1-1:2004*, Brussels.

Foster, S. J., Powell, R. E., and Selim, H. S. (1996). “Performance of high-strength concrete corbels.” *ACI Structural Journal*, 93(5), 555-563.

Foster, S. J. and Gilbert, R. I. (1997). “Strut-and-tie modeling of non-flexural members.” *Australian Civil/Structural Engineering Transactions*, CE39 (2, 3), 87-94.

Foster, S. J. and Malik, A. R. (2002). “Evaluation of efficiency factor models used in strut-and-tie modeling of non-flexural members.” *Journal of Structural Engineering*, 128(5), 569-577.

Huang, P. C. and Nanni, A. (2006). “Dapped-end strengthening of full-scale prestressed double tee beams with FRP composites.” *Advances in Structural Engineering*, 9(2), 293-308.

Islam, M. R., Mansur, M. A. and Maalej, M. (2005). “Shear strengthening of RC deep beams using externally bonded FRP systems.” *Cement & Concrete Composites*, 27, 413-420.

Jirsa, J. O., Breen, J. E., Bergmeister, K., Barton, .D, Anderson, R. and Bouadi, H. (1991). “Experimental studies of nodes in strut-and-tie models.” *Report of the IABSE Colloquium on Structural Concrete*, Stuttgart, Germany, 525-532.

Kupfer, H. (1964). Erweiterung der Mörsch’schen Fachwerkanalogie mit Hilfe des Prinzips vom Minimum der Formänderungsarbeit. “Expansion of Marsch's Truss analogy by application of the principle of minimum strain energy.” CEB-Bulletin, 40.

Lam, L., and Teng, J. G. (2003). "Design-oriented stress-strain model for FRP-confined concrete in rectangular columns." *Journal of Reinforced Plastics and Composites*, 22(13),1149-1186.

Leondardt, F. (1965). "Reducing the shear reinforcement in reinforced concrete beams and slabs." Magazine of Concrete Research, 17(53), 187-198.

Lim, W. K. (2006). "Strengthening of beams with opening using FRP systems." Bachelor thesis, National University of Singapore, Singapore.

Low, S. H. (2013). "FRP strengthened strut for strut-and-tie modeling of structural concrete." Bachelor thesis, National University of Singapore, Singapore.

MacGregor, J. G. (1997). "Reinforced concrete: mechanics and design. 3rd edition." Upper Saddle River NJ. Prentice-Hall.

Marti, P. (1985). "Truss models in detailing." *Concrete International*, 7(12), 66-73.

Maxwell, B. S. and Breen, J. E. (2000). "Experimental evaluation of strut-and-tie model applied to deep beam with opening." *ACI Structural Journal.* 97(1), 142-148.

Mitchell, D., Collins, M. P., Bhide, S. B., and Rabbat, B. G. (2004). "AASHTO LRFD Strut-and-Tie Model Design Examples." Portland Cement Association.

Mörsch, E. (1920, 1922). "Der Eisenbetonbau-seine Theorie und Anwendung (Reinforced concrete construction-Theory and application)." Vol. 1, Part 1 1920, Part 2 1922. Konrad Wittwer, Stuttgart.

Muhammad, F. B. M. J. (2007). "Strut-and-tie method for structural strengthening." Bachelor thesis, National University of Singapore, Singapore.

Nagy-György, T., Sas, G., Dăescu, A.C., Barros, J.A.O. and Stoian, V. (2012). "Experimental and numerical assessment of the effectiveness of FRP-based strengthening configurations for dapped-end RC beams." *Engineering Structures*, 44, 291-303.

Nielsen, M. P., Braestrup, M. W., Jensen, B. C., and Bach, F. (1978). "Concrete plasticity, beam shear-shear in joints-punching shear." Special Publication of the Danish Society of Structural Science and Engineering, Technical University of Denmark, Copenhagen.

Orton, S. L., Jirsa, J. O., and Bayrak, O. (2008). "Design considerations of carbon fiber anchors." *Journal of Composites for Construction*, 12(6), 608-616.

Ozden, S., and Atalay, H. M. (2011). "Strengthening of reinforced concrete corbels with GFRP overlays." *Science and Engineering of Composite Materials*, 18(1-2), 69-77.

Park, S. and Aboutaha R. S. (2009). “Strut-and-tie method for CFRP strengthened deep RC members.” *Journal of Structural Engineering*, 135(6), 632-643.

Pimanmas, A. (2010). “Strengthening R/C beams with opening by externally installed FRP rods: Behavior and analysis.” *Composite Structures*, (92), 1957-1976.

Rausch, E. (1929). “Berechnung des Eisenbetons gegen Verdrehung (Design of reinforced concrete in torsion).” Technische Hoechschule, Berlin: Springer, Germany.

Richart, F. E. and Larsen, T. J. (1927). “An investigation of web stresses in reinforced concrete beams.” University of Illinois Engineering Experimental Station Bulletin, 166 .

Ritter, W. (1899). “Die Bauweise Hennebique (Hennebiques Construction Method).” 33(7), 59-61.

Rogowsky, D. M. and MacGregor, J. G. (1986). “Design of reinforced concrete deep beams.” *Concrete International: Design and Construction*, 8(8), 49-58.

Sahoo, D. K., Gautam, R. K., Singh, B. and Bhargava, P. (2008). “Strength and deformation characteristics of bottle-shaped struts.” *Magazine of Concrete Research*, 60(2), 137-144.

Sahoo, D. K., Singh, B. and Bhargava P. (2009a), “An appraisal of the ACI strut efficiency factors.” *Magazine of Concrete Research*, 61(6), 445-456.

Sahoo, D. K., Singh, B. and Bhargava, P. (2009b) “Investigation of dispersion of compression in bottle-shaped struts.” *ACI Structural Journal*, 106(2), 178-186.

Sahoo, D. K., Singh, B., and Bhargava, P. (2011). “Minimum reinforcement for preventing splitting failure in bottle-shaped struts.” *ACI Structural Journal*, 108(2), 206-216.

Sas, G., Dăescu, C., Popescu, C., and Nagy-György, T. (2014). “Numerical optimization of strengthening disturbed regions of dapped-end beams using NSM and EBR CFRP.” *Composites Part B: Engineering,* 67, 381-390.

Schlaich, J., Schäfer, K. and Jennewein, M. (1987). “Toward a consistent design of structural concrete.” *PCI Journal*, 32(3), 74-150.

Schlaich, J. and Schäfer, K. (1991). “Design and detailing of structural concrete using strut-and-tie models.” *The Structural Engineer*, 69(6), 113-125.

Slater, W. A., Lord, A. R. and Zipprodt, R. R. (1927). “Shear tests of reinforced concrete beams.” Technical Papers, *US Bureau of Standards*, 314 .

Su, R. K. L. and Chandler, A. M. (2001). “Design criteria for unified strut-and-tie models.” *Progress in Structural Engineering and Materials*, 3, 288-298.

Tan, K. H. (2001). “Shear strengthening of dapped beams using FRP systems.” *FRPRCS-5*, Thomas Telford, London, 1, 249-258.

Tan, K. H. (2002). “Strength enhancement of rectangular reinforced concrete columns using fiber-reinforced polymer.” *Journal of Composites for Construction*, 6(3), 175-183.

Tan, K. H. (2004). “Design of non-prismatic RC beams using strut and tie models.” *Journal of Advanced Concrete Technology– Japan Concrete Institute*, 2, 249-256.

Tan, K. H., Bhowmik, T., and Balendra, T. (2013). “Confinement model for FRP-bonded capsule-shaped concrete columns.” *Engineering Structures*, 51, 51-59.

Teng, J. G., Chen, J., Smith, S. and Lam, L. (2002). “FRP-strengthened RC structures.” Wiley, Chichester, U.K.

Warwick, W., and Foster, S. J. (1993). “Investigation into the efficiency factor used in non-flexural member design.” UNICIV Report No R-320, School of Civil Engineering, University of New South Wales, Kensington.

Wight, J. K. and MacGregor, J. G. (2011). “Reinforced concrete: mechanics and design. 6th edition.” Prentice-Hall, Upper Saddle River, New Jersey.

Appendix

Typical load-strain curve figures (the portion 0.00 to 0.01) of FRP strengthened tie members were shown in **Figure A-1** to see the contribution of the FRP strengthening systems more clearly.

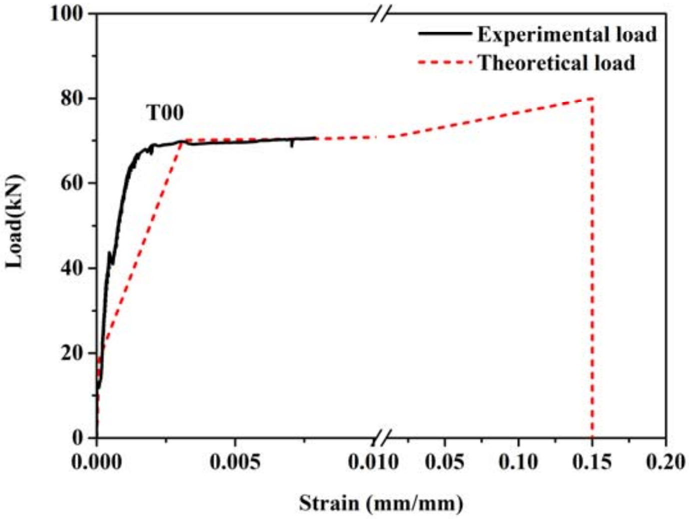

(a) Specimen T00

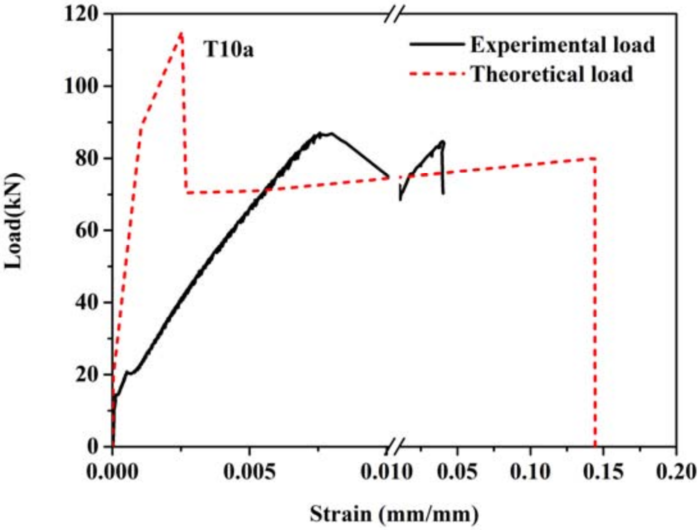

(b) Specimen T10a

Figure A-1: Comparison between experimental load-strain curves and theoretical load-strain curves (cont.)

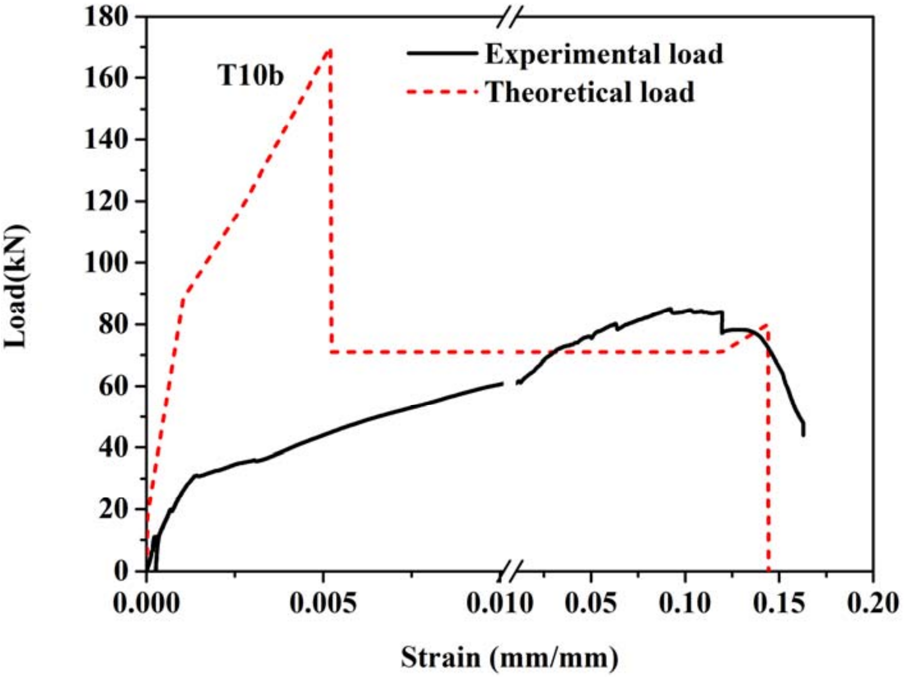

(c) Specimen T10b

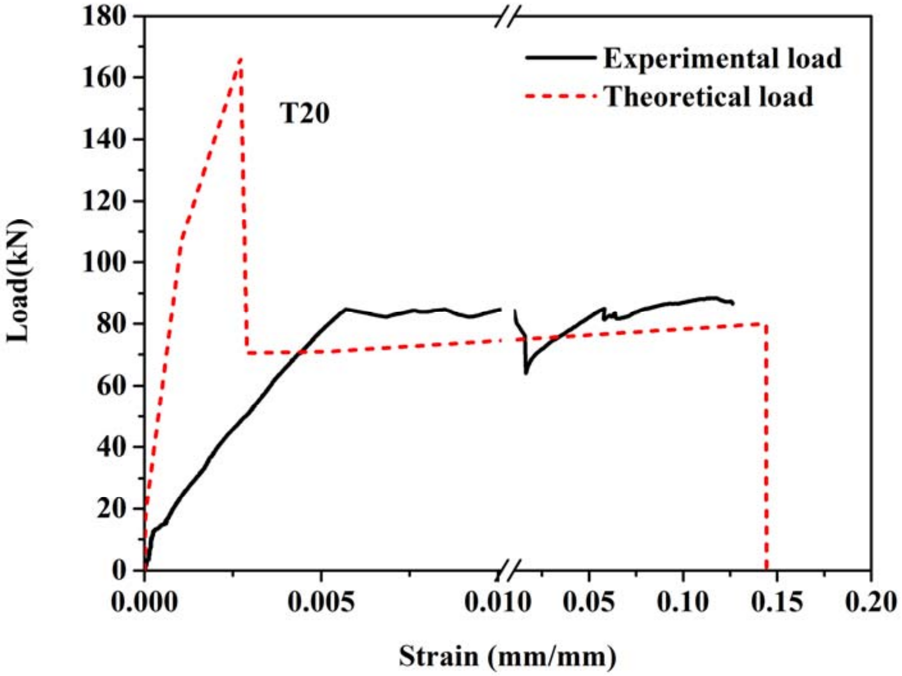

(d) Specimen T20

Figure A-1: Comparison between experimental load-strain curves and theoretical load-strain curves (cont.)

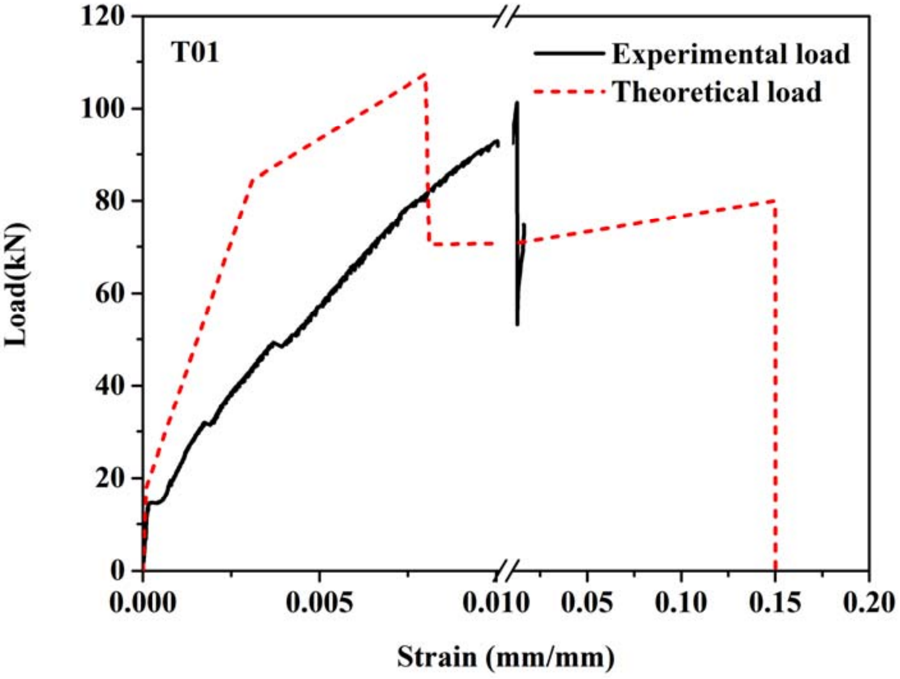

(e) Specimen T01

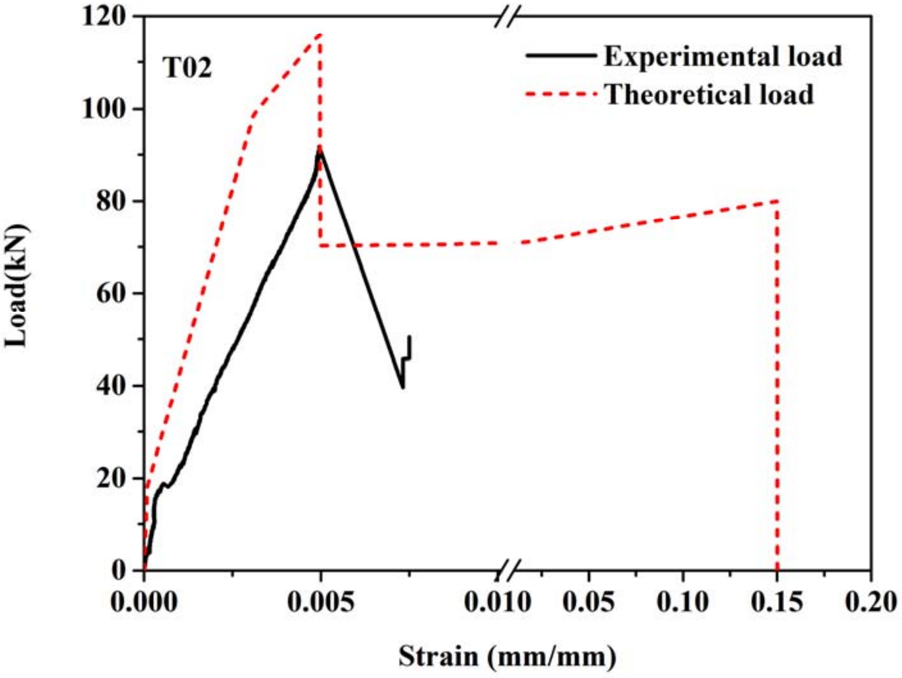

(f) Specimen T02

Figure A-1: Comparison between experimental load-strain curves and theoretical load-strain curves (cont.)

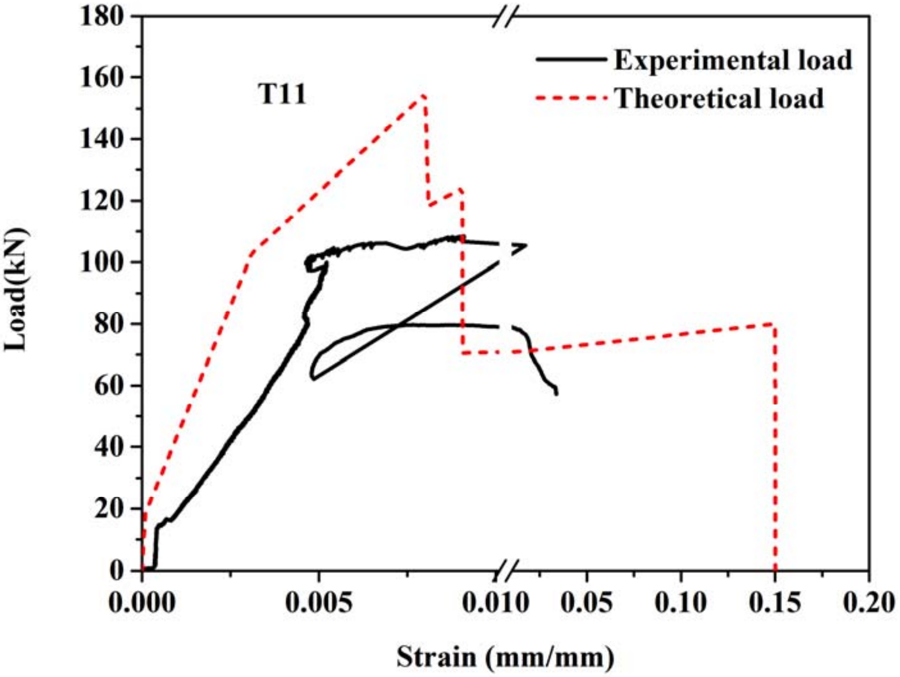

(g) Specimen T11

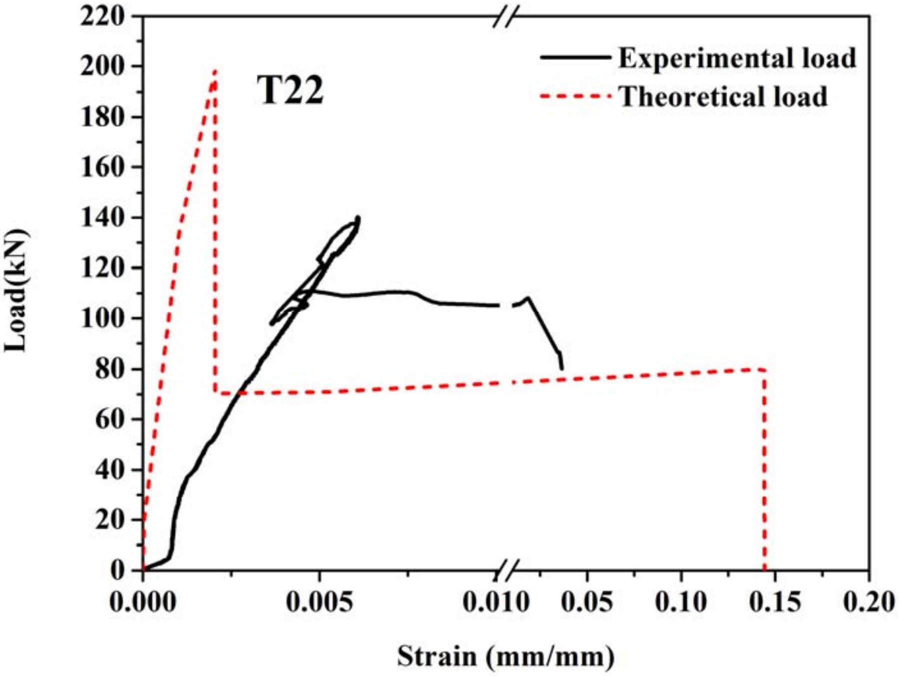

(h) Specimen T22

Figure A-1: Comparison between experimental load-strain curves and theoretical load-strain curves (cont.)

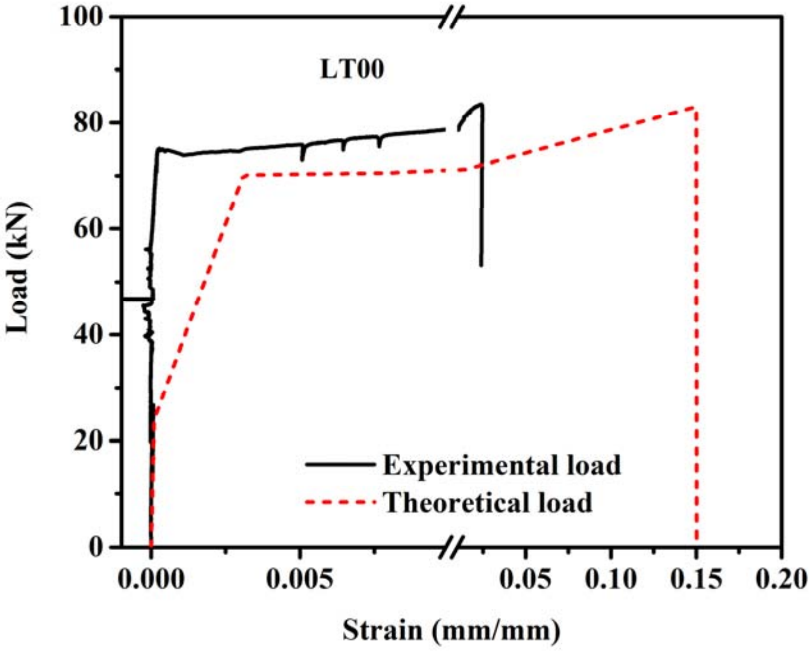

(i) Specimen LT00

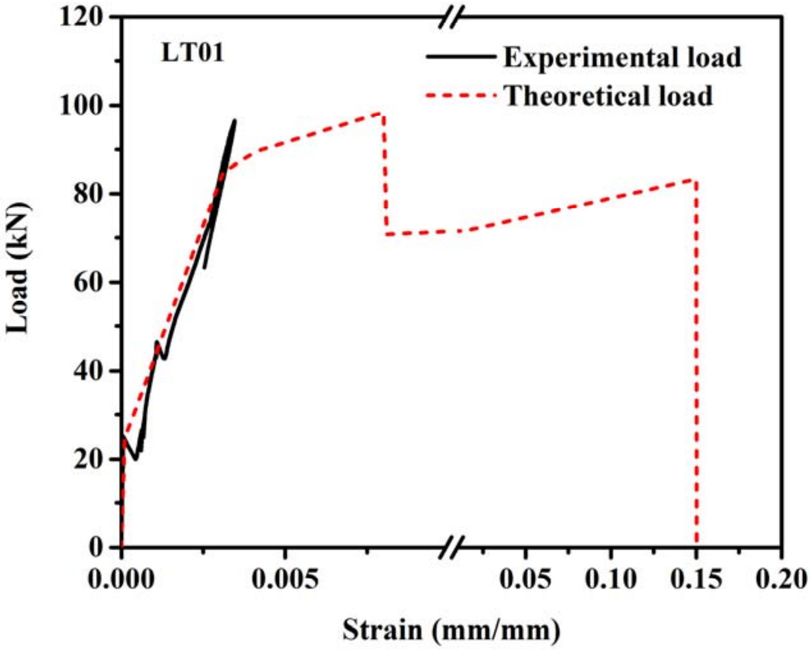

(j) Specimen LT01

Figure A-1: Comparison between experimental load-strain curves and theoretical load-strain curves (cont.)

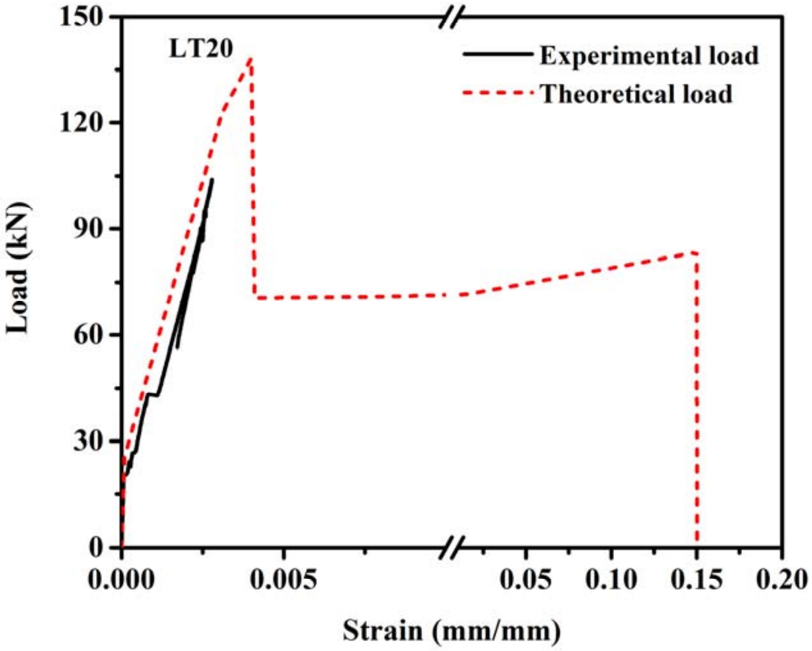

(k) Specimen LT20

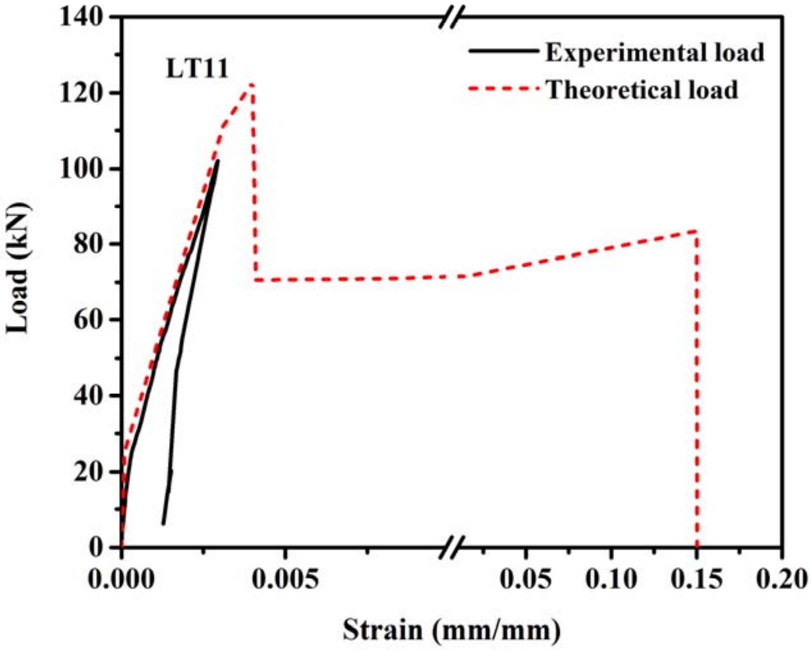

(l) Specimen LT11

Figure A-1: Comparison between experimental load-strain curves and theoretical load-strain curves (cont.)

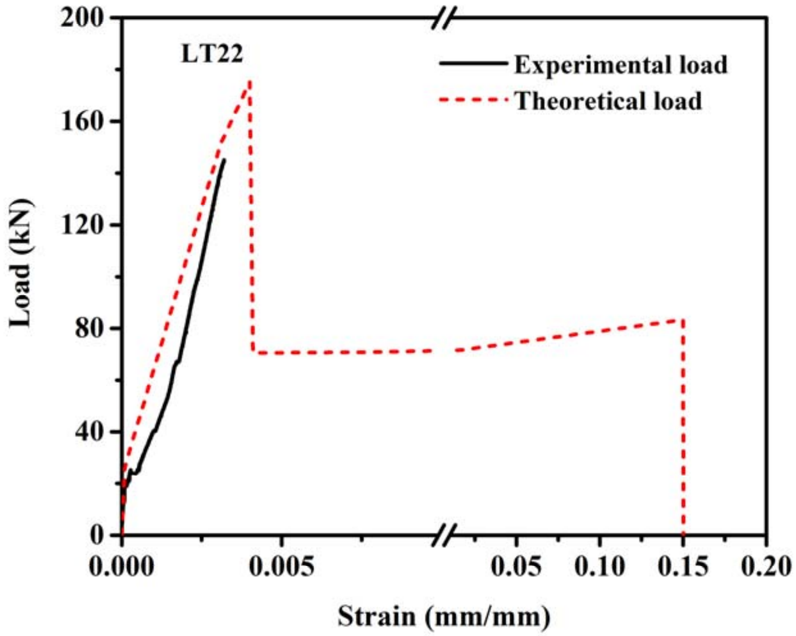

(m) Specimen LT22

Figure A-1: Comparison between experimental load-strain curves and theoretical load-strain curves

Typical figures correspond to the transverse strain distribution of FRP strengthened strut members at different load levels were shown in **Figure A-2** to show the trend as described in the last paragraph on page 117, which reads "With increasing applied load, locations of the maximum magnitudes of the transverse tensile strains were observed to shift towards the top and bottom faces of the strut …".

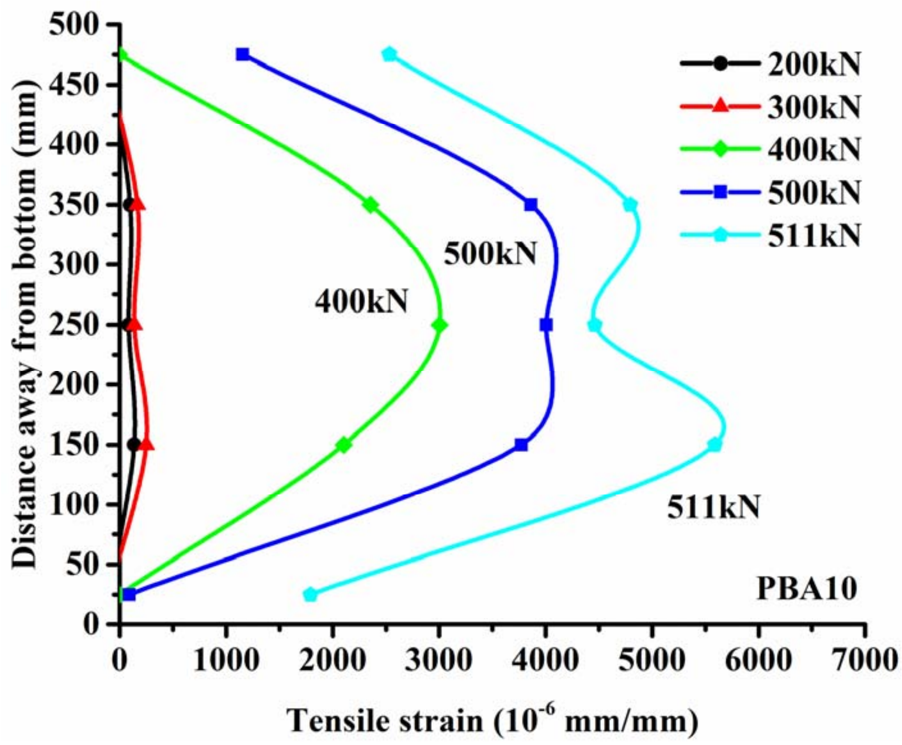

(a) Specimen PBA10

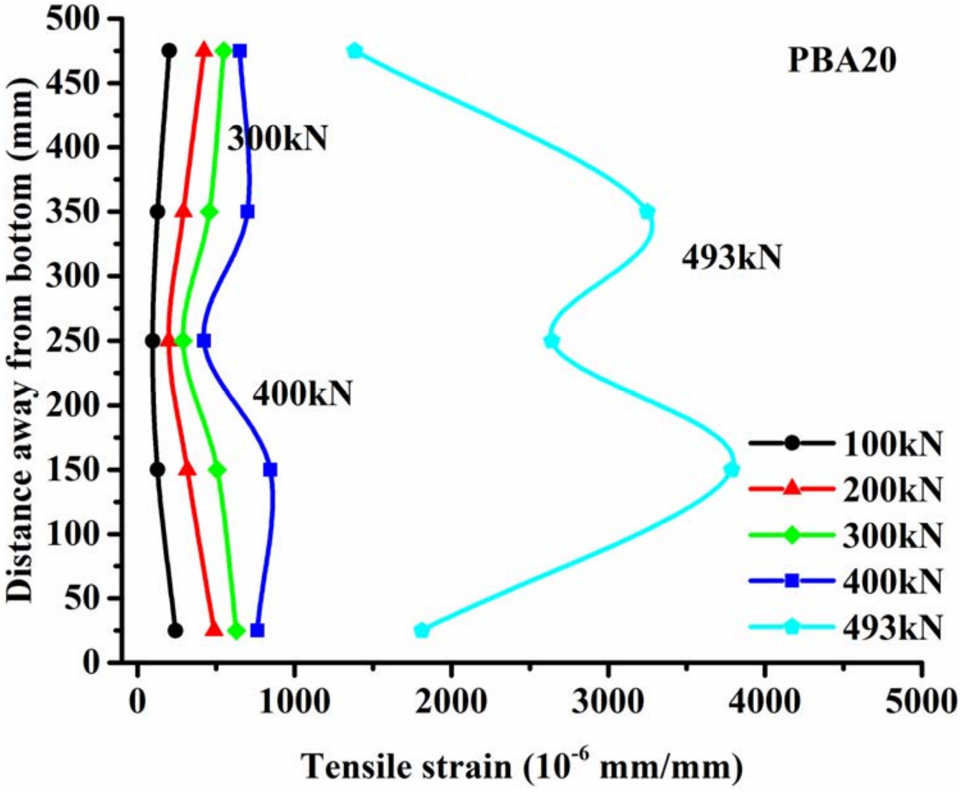

(b) Specimen PBA20

Figure A-2: The transverse strain distribution of specimens at different load levels (cont.)

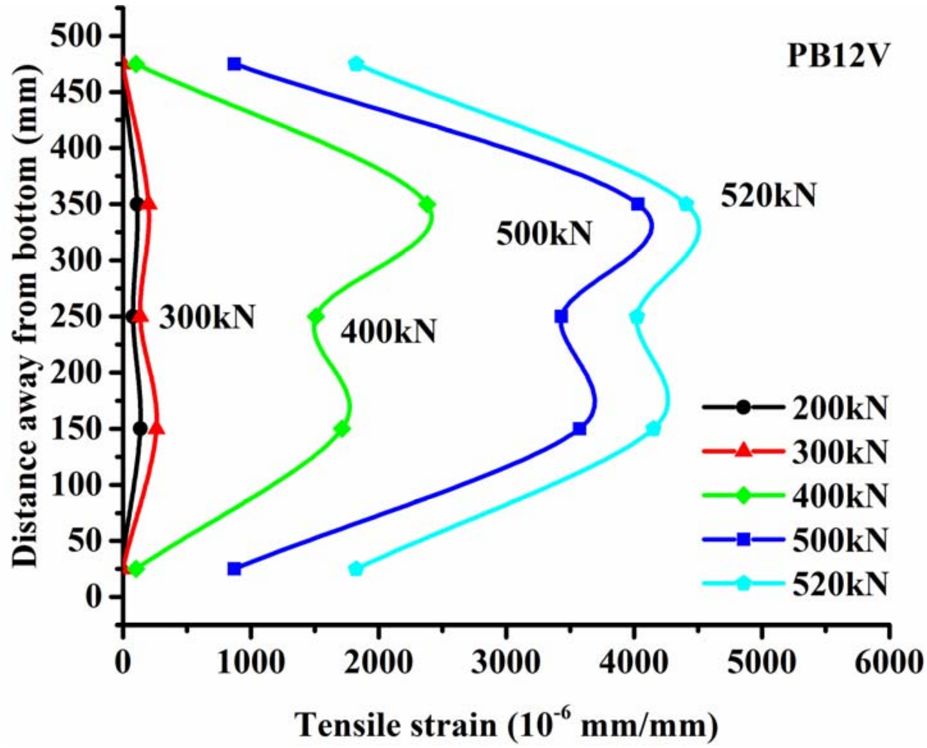

(c) Specimen PB12V

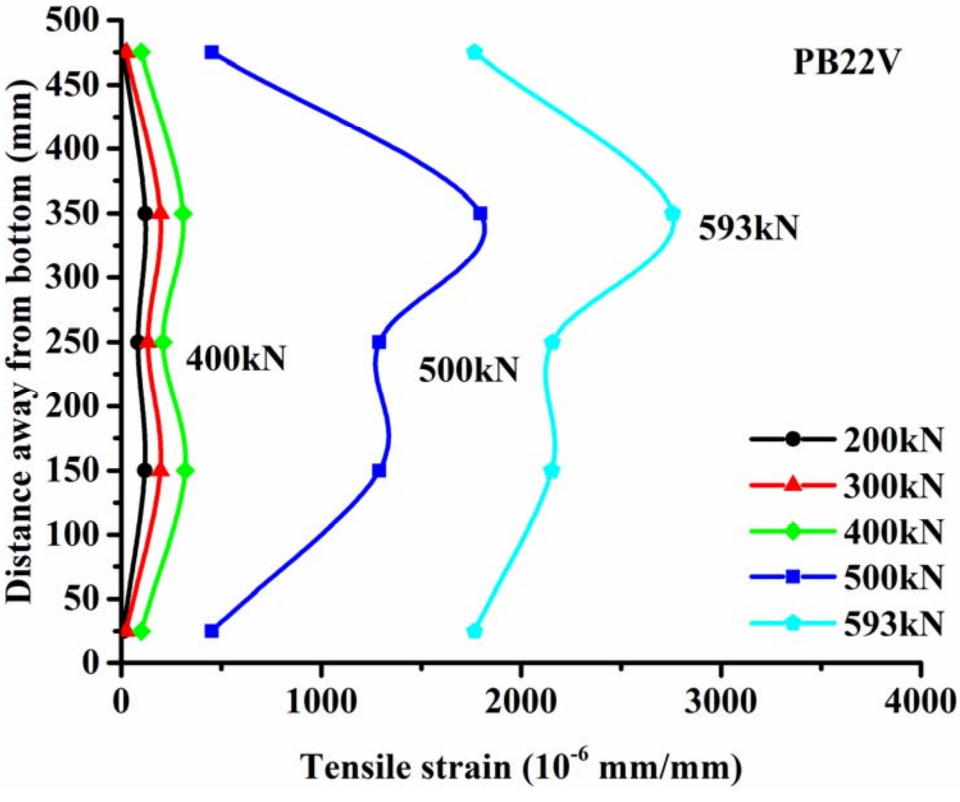

(d) Specimen PB22V

Figure A-2: The transverse strain distribution of specimens at different load levels (cont.)

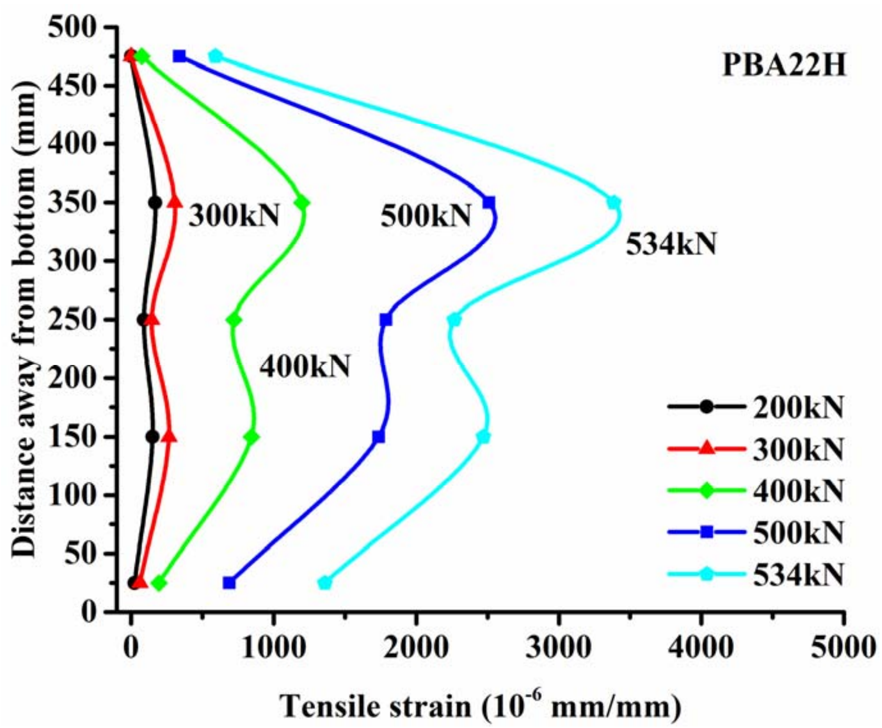

(e) Specimen PBA22H

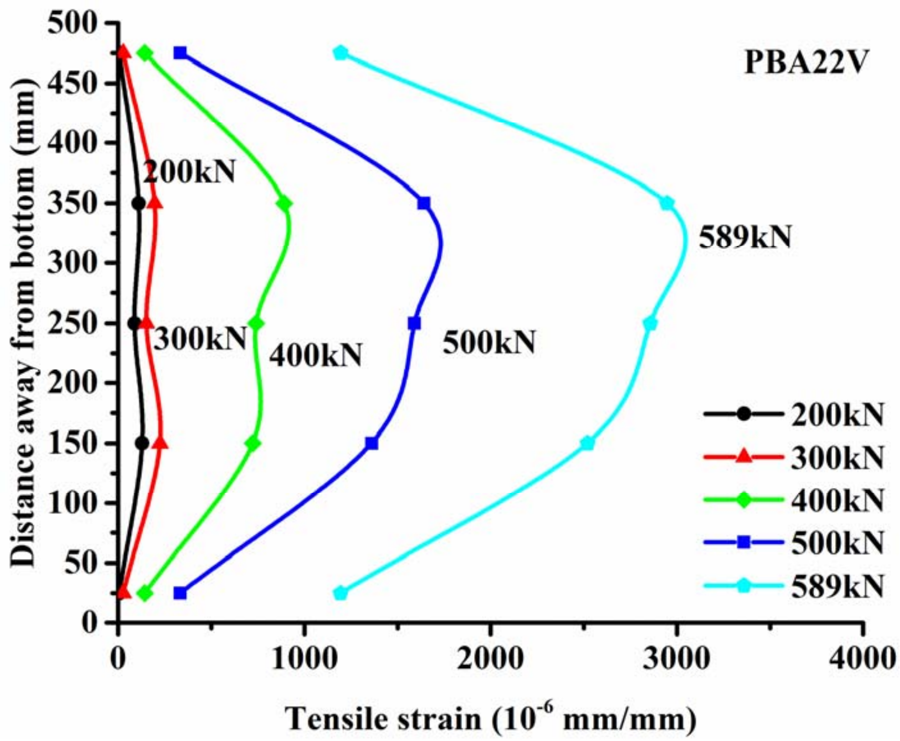

(f) Specimen PBA22V

Figure A-2: The transverse strain distribution of specimens at different load levels